

AD-778 756

A STUDY OF LOAD-DEFORMATION AND  
BUCKLING RELATIONSHIPS FOR RETICULATED  
SHELLS

H. Dean Bartel

Air Force Weapons Laboratory  
Kirtland Air Force Base, New Mexico

April 1974

DISTRIBUTED BY:

**NTIS**

National Technical Information Service  
U. S. DEPARTMENT OF COMMERCE  
5285 Port Royal Road, Springfield Va. 22151

AIR FORCE WEAPONS LABORATORY  
Air Force Systems Command  
Kirtland Air Force Base  
New Mexico 87117

When US Government drawings, specifications, or other data are used for any purpose other than a definitely related Government procurement operation, the Government thereby incurs no responsibility nor any obligation whatsoever, and the fact that the Government may have formulated, furnished, or in any way supplied the said drawings, specifications, or other data, is not to be regarded by implication or otherwise, as in any manner licensing the holder or any other person or corporation, or conveying any rights or permission to manufacture, use, or sell any patented invention that may in any way be related thereto.

DO NOT RETURN THIS COPY. RETAIN OR DESTROY.


UNCLASSIFIED

Security Classification

DOCUMENT CONTROL DATA - R &amp; D

AD 778 756

(Security classification of title, body of abstract and indexing annotation must be entered when the overall report is classified)

1. ORIGINATING ACTIVITY (Corporate author)		2a. REPORT SECURITY CLASSIFICATION	
Air Force Weapons Laboratory (DEV) Kirtland Air Force Base, New Mexico 87117		UNCLASSIFIED	
3. REPORT TITLE		2b.	
A STUDY OF LOAD-DEFORMATION AND BUCKLING RELATIONSHIPS FOR RETICULATED SHELLS			
4. DESCRIPTIVE NOTES (Type of report and inclusive dates)			
15 March 1973 through 31 March 1974			
5. AUTHOR(S) (First name, middle initial, last name)			
H. Dean Bartel			
6. REPORT DATE	7a. TOTAL NO. OF PAGES	7b. NO. OF REFS	
April 1974	244	37	
8a. CONTRACT OR GRANT NO.	9a. ORIGINATOR'S REPORT NUMBER(S)		
b. PROJECT NO. WDNS3411	AFWL-TR-74-87		
c. Subtask Y99QAXSC157	9b. OTHER REPORT NO(S) (Any other numbers that may be assigned this report)		
d.			
10. DISTRIBUTION STATEMENT			
Approved for public release; distribution unlimited.			
11. SUPPLEMENTARY NOTES		12. SPONSORING MILITARY ACTIVITY	
Reproduced from best available copy. 		Defense Nuclear Agency Washington, DC 20305	
13. ABSTRACT			
(Distribution Limitation Statement A)			
<p>The objectives of this research were to determine the theoretical and experimental load-deformation response and buckling loads of reticulated shells and to study the growth of imperfections in reticulated shell models. Two types of theoretical analyses (elastic material behavior was assumed) of reticulated shells were conducted to predict load-deformation relationships. A "split rigidity" concept was used in which equivalent membrane and bending thicknesses were calculated. The second technique was a space frame analyses using the NASTRAN computer code. Three spherical reticulated shell models (two brass and one plastic) were fabricated and tested experimentally. Results of the study indicated that the NASTRAN code predicted the deflection patterns well and identified the final buckle locations. The assumption of elastic material behavior precluded predicting the exact deflection magnitudes due to material yielding. Buckling loads were closely predicted using a theory by Buchert. This theory included the effects of large deflections and employed the split rigidity approach. Plasticity reduction factors were applied to the predicted results to account for material nonlinearities.</p>			
<p>Reproduced by NATIONAL TECHNICAL INFORMATION SERVICE U S Department of Commerce Springfield VA 22151</p>			

DD FORM 1473  
1 NOV 65

UNCLASSIFIED

Security Classification

**Security Classification**

14

## KEY WORDS

**LINK A**

**LINK B**

**LINK C**

NAME	ROLE
Mr. J. Edgar Hoover	Director
Mr. Clegg	Chief of Bureau
Mr. Glavin	Chief of Bureau
Mr. Ladd	Chief of Bureau
Mr. Nichols	Chief of Bureau
Mr. Rosen	Chief of Bureau
Mr. Tracy	Chief of Bureau
Mr. Carson	Chief of Bureau
Mr. Egan	Chief of Bureau
Mr. Gurnea	Chief of Bureau
Mr. Hendon	Chief of Bureau
Mr. Pennington	Chief of Bureau
Mr. Quinn	Chief of Bureau
Mr. Nease	Chief of Bureau
Mr. Gandy	Chief of Bureau

WT

[illegible]

WT

[illegible]

WT

Shells  
Reticulated shells  
Imperfections  
Buckling  
Experimental  
Split rigidity  
NASTRAN

ia

UNCLASSIFIED

**Security Classification**

A STUDY OF LOAD-DEFORMATION  
AND BUCKLING RELATIONSHIPS FOR RETICULATED SHELLS

H. Dean Bartel

Final Report for Period 15 March 1973 through 31 March 1974

Approved for public release; distribution unlimited.

FOREWORD

The research was performed under Program Element 62704H, Project WDNS3411, Subtask Y99QAXSC157, and was funded by the Defense Nuclear Agency.

Inclusive dates of research were 15 March 1973 through 31 March 1974. The report was submitted 2 April 1974 by the Air Force Weapons Laboratory Project Officer, Captain H. Dean Bartel (DEV).

This report was prepared as a dissertation in partial fulfillment of the requirements for the degree of Doctor of Philosophy at the University of Missouri.

The author wishes to express his sincere appreciation to Dr. Kenneth P. Buchert, dissertation supervisor, for his technical assistance throughout the conduct of this research effort. The efforts of Dr. James W. Baldwin during the experimental and data reduction portions of the study are also appreciated.

This technical report has been reviewed and is approved.

*H. Dean Bartel*

H. DEAN BARTEL  
Captain, USAF  
Project Officer

*John J. Osborn*

JOHN J. OSBORN  
Lt Colonel, USAF  
Chief, Facility Survivability  
Branch

*William B. Liddicoet*

WILLIAM B. LIDDICOET  
Colonel, USAF  
Chief, Civil Engineering Research  
Division

## ABSTRACT

## (Distribution Limitation Statement A)

The objectives of this research were to determine the theoretical and experimental load-deformation response and buckling loads of reticulated shells and to study the growth of imperfections in reticulated shell models. Two types of theoretical analyses (elastic material behavior was assumed) of reticulated shells were conducted to predict load-deformation relationships. A "split rigidity" concept was used in which equivalent membrane and bending thicknesses were calculated. The second technique was a space frame analysis using the NASTRAN computer code. Three spherical reticulated shell models (two brass and one plastic) were fabricated and tested experimentally. Results of the study indicated that the NASTRAN code predicted the deflection patterns well and identified the final buckle locations. The assumption of elastic material behavior precluded predicting the exact deflection magnitudes due to material yielding. Buckling loads were closely predicted using a theory by Buchert. This theory included the effects of large deflections and employed the split rigidity approach. Plasticity reduction factors were applied to the predicted results to account for material nonlinearities.

## TABLE OF CONTENTS

CHAPTER	PAGE
I. INTRODUCTION	1
1.1 General	1
1.2 Previous Research	2
1.2.1 Analytical Work	2
1.2.2 Experimental Studies	5
1.3 Object and Scope	6
II. THEORY AND ANALYSIS	8
2.1 The Split Rigidity Method	8
2.1.1 Theory	8
2.1.2 Test Model Analysis	13
2.2 Analysis by the Stiffness Method	17
2.2.1 General	17
2.2.2 The B2 Model	17
2.2.3 The PRET Test Model	22
2.3 Reticulated Shell Buckling	25
2.3.1 Buckling Theories	25
2.3.2 Application to Experimental Models	28
III. EXPERIMENTAL PROCEDURES	34
3.1 General	34
3.2 Fabrication of the Models	35
3.2.1 Brass	35
3.2.2 Plastic	42
3.3 Testing Apparatus and Test Setup	42
3.3.1 Pressure Vessel	42
3.3.2 Easterby Apparatus	49
3.3.3 DCDT Device	49
3.3.4 Pressure Measurement	51
3.4 Test Procedure	51
3.5 Data Reduction	56
3.6 Materials Testing	58
3.6.1 Brass	58
3.6.2 Plastic	60
IV. RESULTS AND COMPARISONS	61
4.1 Experimental Results	61
4.1.1 Materials Testing	61
4.1.2 B2 Model Deflections	68
4.1.3 B1 Model Deflections	80
4.1.4 PRET Model Deflections	80



## TABLE OF CONTENTS - Continued

## PAGE

## CHAPTER

4.2	Theoretical Predictions	103
4.2.1	B2 Model Predictions	103
4.2.2	PRET Model Predictions	112
4.3	Comparison of Predicted and Experimental Results	112
4.3.1	B2 Model Deflections	112
4.3.2	PRET Model Deflections	128
4.3.3	Discussion of Deflection Results	136
4.4	Buckling Results	139
4.4.1	Parameter Variations	139
4.4.2	Buckling of the B2 Model	143
4.4.3	Buckling of the B1 Model	151
4.4.4	Buckling of the PRET Model	156
V.	SUMMARY AND CONCLUSIONS	161
5.1	Summary	161
5.2	Conclusions	163
APPENDIX A	THE SPLIT RIGIDITY ANALYSIS METHOD	168
A.1	Assumptions	168
A.2	Bending Deflection Theory	168
A.2.1	General	168
A.2.2	Equilibrium	169
A.2.3	Strains and Curvature Changes	171
A.2.4	Forces and Bending Moments	173
A.2.5	Differential Equation Solution	173
A.2.6	Final Expressions	179
A.3	Boundary Conditions	181
A.3.1	Deflection Compatibility	181
A.3.2	Rotation Compatibility	183
A.3.3	Simply Supported Edge	184
A.3.4	Fixed Edge	184
APPENDIX B	STATIC ANALYSIS BY THE STIFFNESS METHOD	185
B.1	Assumptions and Definitions	185
B.2	General Problem Flow	187
B.3	NASTRAN Solution Procedure	187

## TABLE OF CONTENTS - Continued

CHAPTER	PAGE
APPENDIX C    LEAST-SQUARES SPHERICAL FIT COMPUTER PROGRAM	195
C.1    General	195
C.2    Theory of the Least-Squares Fit	195
C.3    Mainline Program Flow Chart	200
C.4    Subroutines	202
C.4.1    Subroutine REDUCE	202
C.4.2    Subroutine ITER	205
C.5    Program Input and Output	207
C.5.1    Input Data	207
C.5.2    Typical Program Output	209
PROGRAM PRINT-OUT	211
REFERENCES	222
DISTRIBUTION	225

## LIST OF FIGURES

FIGURE		PAGE
2.1	Free-Body Diagram of a Shell Element	10
2.2	Displacement of a Point	11
2.3	Compatibility Restoring Forces	13
2.4	Cross Section of Brass H-Section	14
2.5	PRET Model Edge Ring Geometry	16
2.6	Coordinate Systems	19
2.7	Model Theoretical Grid	20
2.8	PRET Model Theoretical Grid	24
2.9	B2 Model: Equation 2.26	29
2.10	B1 Model: Equation 2.26	32
2.11	PRET Model: Equation 2.26	33
3.1	Scribing the Pattern Mold	36
3.2	Bending the Brass Members	36
3.3	Flange Trimming	37
3.4	Soft-Solder Technique	37
3.5	Adding the Edge Ring	38
3.6	Completed B2 Test Model	38
3.7	Completed B1 Test Model	41
3.8	Vacuum-Forming Device	43
3.9	Molded PRET Model	43
3.10	Cutting the PRET Model	44

## LIST OF FIGURES - Continued

FIGURE	PAGE
3.11 Completed PRET Test Model	45
3.12 Test Pressure Vessel	47
3.13 Membrane-Stretching Device	47
3.14 Mounting a Test Model	48
3.15 The Original Easterby Apparatus	50
3.16 Radial Arm Assembly	50
3.17 Spring-loaded Tip Assembly	52
3.18 Attaching the Easterby Apparatus	52
3.19 Pressure-measuring Devices	53
3.20 Data Recording Devices	55
3.21 Tensile Test Specimens	59
4.1 Stress vs Strain for S-Type Brass Specimen	62
4.2 Stress vs Strain for T-Type Brass Specimen	63
4.3 Stress vs Strain for O-Type Brass Specimen	64
4.4 Stress vs Strain for Plastic Material	65
4.5 Creep Test on Plastic Material	67
4.6 B2 Model Experimental Grid	69
4.7 B2 Model Initial Imperfections	71
4.8a B2 Model: .15 to 1.0 psi	72
4.8b B2 Model: 1.0 to 1.5 psi	73
4.8c B2 Model: 1.5 to 2.0 psi	74
4.8d B2 Model: 2.0 to 2.5 psi	75
4.8e B2 Model: 2.5 to 3.0 psi	76
4.8f B2 Model: 1.0 to 2.0 psi	77

## LIST OF FIGURES - Continued

FIGURE	PAGE
4.8g B2 Model: 1.0 to 2.5 psi	78
4.8h B2 Model: 1.0 to 3.0 psi	79
4.8i B2 Model: Imperfections Plus Deflections at 3.0 psi	81
4.9 B1 Model Experimental Grid	82
4.10 B1 Model Initial Imperfections	83
4.11a B1 Model: .15 to 1.0 psi	84
4.11b B1 Model: 1.0 to 2.0 psi	85
4.11c B1 Model: 2.0 to 3.0 psi	86
4.11d B1 Model: 3.0 to 4.0 psi	87
4.11e B1 Model: 4.0 to 5.0 psi	88
4.11f B1 Model: 5.0 to 6.0 psi	89
4.11g B1 Model: 1.0 to 3.0 psi	90
4.11h B1 Model: 1.0 to 4.0 psi	91
4.11i B1 Model: 1.0 to 5.0 psi	92
4.11j B1 Model: 1.0 to 6.0 psi	93
4.11k B1 Model: Imperfections Plus Deflections at 6.0 psi	94
4.12 PRET Experimental Grid	95
4.13 PRET Model Initial Imperfections	96
4.14a PRET Model: .15 to 1.0 psi	97
4.14b PRET Model: 1.0 to 2.0 psi	98
4.14c PRET Model: 2.0 to 3.0 psi	99
4.14d PRET Model: .15 to 2.0 psi	100
4.14e PRET Model: .15 to 3.0 psi	101
4.14f PRET Model: Imperfections Plus Deflections at 3.0 psi	102

## LIST OF FIGURES - Continued

FIGURE		PAGE
4.15a	B2 Model: 1.0 to 1.5 psi	104
4.15b	B2 Model: 1.5 to 2.0 psi	105
4.15c	B2 Model: 2.0 to 2.5 psi	106
4.15d	B2 Model: 2.5 to 3.0 psi	107
4.15e	B2 Model: 1.0 to 2.0 psi	108
4.15f	B2 Model: 1.0 to 2.5 psi	109
4.15g	B2 Model: 1.0 to 3.0 psi	110
4.15h	B2 Model: Imperfections Plus Deflections at 3.0 psi	111
4.16a	PRET Model: .15 to 1.0 psi	113
4.16b	PRET Model: 1.0 to 2.0 psi	114
4.16c	PRET Model: 2.0 to 3.0 psi	115
4.16d	PRET Model: .15 to 2.0 psi	116
4.16e	PRET Model: .15 to 3.0 psi	117
4.16f	PRET Model: Imperfections Plus Deflections at 3.0 psi	118
4.17a	B2 Model: 1.0 to 1.5 psi	119
4.17b	B2 Model: 1.5 to 2.0 psi	120
4.17c	B2 Model: 2.0 to 2.5 psi	121
4.17d	B2 Model: 2.5 to 3.0 psi	122
4.17e	B2 Model: 1.0 to 2.0 psi	123
4.17f	B2 Model: 1.0 to 2.5 psi	124
4.17g	B2 Model: 1.0 to 3.0 psi	125
4.17h	B2 Model: Imperfections Plus Deflections at 3.0 psi	126
4.18a	PRET Model: .15 to 1.0 psi	130
4.18b	PRET Model: 1.0 to 2.0 psi	131

## LIST OF FIGURES - Continued

FIGURE		PAGE
4.18c	PRET Model: 2.0 to 3.0 psi	132
4.18d	PRET Model: .15 to 2.0 psi	133
4.18e	PRET Model: .15 to 3.0 psi	134
4.18f	PRET Model: Imperfections Plus Deflections at 3.0 psi	135
4.19	Plastic Analysis of B2 Buckled Area	137
4.20	Effect of the Plasticity Reduction Factor	144
4.21	Buckled B2 Test Model	145
4.22a	B2 Model: Load-Deflection Without Imperfections	146
4.22b	B2 Model: Load-Deflection with Global Imperfections	147
4.22c	B2 Model: Load-Deflection with Local Imperfections	148
4.23	Buckled B1 Test Model	152
4.24a	B1 Model: Load-Deflection without Imperfections	153
4.24b	B1 Model: Load-Deflection with Global Imperfections	154
4.24c	B1 Model: Load-Deflection with Local Imperfections	155
4.25	Buckled PRET Test Model	257
4.26a	PRET Model: Load-Deflection without Imperfections	158
4.26b	PRET Model: Load-Deflection with Global Imperfections	159
4.26c	PRET Model: Load-Deflection with Local Imperfections	160
A.1	Free-Body Diagram of a Shell Element	170
A.2	Shell Displacements	172
A.3	Shell Edge Forces	174
A.4	Damping of the Edge Effects	177
A.5	Angular Variables	178
A.6	Displacement of a Point	180

## LIST OF FIGURES - Continued

FIGURE		PAGE
A.7	Compatibility Restoring Forces	181
B.1	NASTRAN Coordinate Systems	186
B.2	General Problem Flow	188
C.1	Coordinate System for Spherical Fit	196
C.2	Solution of Equation C.6	199
C.3	Mainline Program Flow Chart	201
C.4	Subroutine REDUCE Flow Chart	203
C.5	Schematic of Radial Arm Assembly	204
C.6	Subroutine ITER Flow Chart	206



## LIST OF TABLES

TABLE		PAGE
2.1	Shell Model Summary	13
4.1	Model and Material Property Summary	68
4.2	Change in Radius of Buckle Area with Increase in Pressure	141
4.3	Summary of Predicted Buckling Loads	150

## LIST OF SYMBOLS

$a, b$	edge beam eccentricities (see Figure 2.3)
$A$	cross-sectional area of a member
$A_b$	cross-sectional area of edge beam
$A_i, B_i, C_i$	rectangular to spherical transformation coefficients
$C$	a constant defined in Equation 2.6
$d_i$	initial imperfection at point $i$
$D_b$	flexural rigidity
$E$	Young's modulus
$E_s$	secant modulus
$E_t$	tangent modulus
$F$	factor in Buchert buckling equation defined in Equation 2.26
$F_i$	point load applied to joint $i$
$F_H, F_v$	compatibility restoring forces due to membrane forces at edge beam
$F_H''$	compatibility restoring force due to bending moment at edge beam
$G_m$	multipoint constraint set
$I$	moment of inertia of a member cross-section
$K_{gg}$	global stiffness method
$L$	member length
$M_p$	plastic moment capacity of a member
$M_\phi$	meridional bending moment
$M_\theta$	circumferential bending moment
$N_\phi$	meridional membrane force

$N_\theta$	circumferential membrane force
$P$	external applied pressure
$P_{cr}$	critical buckling pressure
$P_g$	global load matrix
$Q_\phi$	meridional shear force
$r_g$	radius of gyration of a member cross-section
$r_i$	radial distance from the center of the best-fit sphere to point $i$
$r_0$	radius of best-fit sphere to experimental data
$R$	spherical shell radius
$\Delta R$	drift in recording apparatus readings
$R_i$	experimental radius to a gage point from the center of the Easterby apparatus spherical pivot
$R_g$	matrix of constraint coefficients
$S$	summation defined in Equation C.4
$S_1, S_2$	radial arm dimensions (see Figure C.5)
$t_b$	equivalent bending thickness
$t_m$	equivalent membrane thickness
$u_g$	global displacement matrix
$u_m$	matrix of independent degrees of freedom
$u_n$	matrix of dependent degrees of freedom
$U$	arbitrary variable equal to $RQ_\phi$
$v$	deflection tangent to shell surface
$V$	angle of rotation of a tangent to a meridian
$V_T$	rotational flexibility of edge beam
$V_R$	voltmeter reading converted to inches

$w$	deflection normal to shell surface
$w_b$	bending deflection normal to shell surface
$x, y, z$	rectangular coordinate system axes
$X_0, Y_0, Z_0$	center coordinates of best-fit sphere to experimental data
$Y_s$	enforced displacement vector
$Z$	external load applied normal to shell
$\alpha$	angle measured from the shell springing
$\gamma$	phase angle
$\delta$	horizontal deflection of a point on the shell surface
$\Delta$	maximum value of $w$
$\epsilon_\theta$	circumferential membrane strain
$\epsilon_\phi$	meridional membrane strain
$\eta$	plasticity reduction factor
$\theta$	circumferential angle
$\kappa$	split rigidity constant
$\rho$	radial component in spherical coordinates
$\nu$	Poisson's Ratio
$\phi$	meridional angle
$\phi_s$	opening angle of spherical shell
$\chi_\theta$	circumferential curvature
$\chi_\phi$	meridional curvature

## CHAPTER I

### INTRODUCTION

#### 1.1 GENERAL

Recent trends in architectural and structural design have led to widespread use of shell-type structures. Their aesthetic appeal and the minimum requirement for internal supporting members has popularized their use in sports stadia, auditoriums, shopping malls, etc. Earlier shells and domes were primarily continuous structures of reinforced concrete, with the material providing structural strength and serving as covering for the structures.

More recently, however, certain advantages over continuous shells and domes have been attained through the use of reticulated shells. These structures are formed by approximating shell surface with a framework of relatively short linear structural members. A membrane-type covering is attached to provide thermal and acoustic barriers and for protection against environmental effects. The construction problems associated with scaffolding and formwork are thereby reduced or eliminated, and the aesthetic and practical advantages of a variety of covering materials can be incorporated into the design. Spurred by the popularity of this type of structure and by several spectacular failures of dome-type buildings, a demand has been created for improved analysis and design techniques. The large size of many of these buildings has presented design problems entirely new to structural engineers. The preponderance of the theoretical work currently

available in the literature has logically concentrated on continuous shells. With the advent of the high-speed digital computer, however, recent publications have presented structural analysis techniques and buckling theories for reticulated domes. The necessary experimental work on which to formulate and verify analytical techniques is, unfortunately, extremely limited. Many continuous shell theories have been modified to the case of reticulated domes without an adequate data base to justify their use.

The purpose of this paper was to study the load-deflection relationships and buckling characteristics of several model reticulated shells. The experimental data thus generated can hopefully be used to investigate the adequacy of current theoretical procedures.

## 1.2 PREVIOUS RESEARCH

1.2.1 Analytical Work. Analytical techniques using stiffness and flexibility methods have been formulated in numerous recent studies (1,2,3,4,5,6,7,8) of reticulated domes and other space frames. Two of the more recent computer codes developed and in wide practical use are NASTRAN<sup>(7)</sup> and FRAN<sup>(8)</sup>. NASTRAN (acronym for NASA Structural Analysis) was developed during the advent of the space program under the direction of the National Aeronautics and Space Administration. This code employs the stiffness method of analysis and will allow linear elastic analyses of space frameworks and numerous other structural assemblies to be performed. Output consists of grid point displacements, applied loads at grid points, forces at constrained grid points, element forces, and element stresses. FRAN is also a linear elastic code for

complex structures. Numerous external loading conditions can be applied and joint connection rigidities can be varied. Structures with up to 15,000 members and 2,000 joints can be analyzed.

Substructuring a large problem to aid in determining the stiffness matrix inverse and to simplify the bookkeeping procedures is also possible in FRAN.

Continuum analyses <sup>(9,10,11,12)</sup> of shells and domes were formulated earlier. Only recently, however, have there been attempts to modify these elastic continuum theories to the analysis and design of reticulated domes. A paper by Wright <sup>(13)</sup> presented a shell analogy in which member axial forces were related to shell membrane forces. Elastic constants and effective thicknesses were given for homogeneous isotropic and anisotropic continuous shells which were equivalent to various reticulated shell grids. Equivalent meant that when a reticulated shell was analyzed as a continuum, the continuum elastic properties were assumed such that the load-deformation behavior was very nearly that of the actual framework. Wright <sup>(14)</sup> also presented a continuum analysis for double-layer space frame shells. A double-layer shell consists of two reticulated shell grids separated by an assemblage of members having a shear-carrying capacity. The elastic constants of an anisotropic homogeneous continuum possessing the same deformational characteristics were given. Member forces were found from the stress resultants of the continuum. Benard <sup>(15)</sup> studied the relationship between lattice (reticulated) and continuous structures and included grid systems with both asymmetrical and symmetrical patterns. Equilateral triangular, isosceles triangular,

and square lattices were studied and their equivalent continuum elastic constants were presented. The study included several direct comparisons with Wright's work. Mitchell (16) presented a shell analogy for a framed dome and made comparisons with a relaxation solution. The Dome of Discovery in Britain was studied as a model. Lane (17) compared a truss solution, Wright's method, and a diamond-element method to determine bar forces in a triangon network. He found that the finer the network, the better the agreement between the truss solution and the shell analogy. Others (18,19) have made similar studies.

Buckling theories as applied to reticulated frameworks have been developed primarily within the past decade. Buchert (20) has reported experimental results on a series of stiffened plastic shells to substantiate his theoretical development. The test shells consisted of a continuous plastic outer shell fastened to an inner "stiffening" shell having a reticulated member pattern. The theory was developed by calculating the deflections during loading and prior to buckling using a large deflection stability approach. The tests agreed well with the theory and confirmed that the shell edges could be stiffened and relatively high buckling loads obtained by increasing the meridional curvature near the edge of the shell. Buchert (21) also developed general buckling equations for doubly curved latticed structures. Expressions for the effect of edge conditions, deviations from a perfect sphere, and material yield strength were discussed. Lind (22) did extensive work on local buckling and snap-through instability for regular triangulated single layer domes.



Buchert<sup>(23)</sup> derived plasticity reduction factors and conducted model tests to verify his buckling theories which included the effects of plasticity and large deflections. McCutcheon and Dickie<sup>(24)</sup> used energy considerations to develop buckling criteria for large dome frameworks. Experimental investigations were conducted using a portion of a dome. Tezcan and Ovunc<sup>(25)</sup> used an iteration procedure to determine buckling loads of space structures and accounted for nonlinear behavior. The matrix approach was used with the addition of considering geometry changes. Wright<sup>(13)</sup> formulated criteria for the buckling of individual members and a criteria was proposed for snap-through buckling. A criteria was proposed for overall instability of reticulated shells based upon the use of equivalent continuum thicknesses and elastic constants. The Bucharest Dome collapse was predicted and estimates of buckling loads for other large reticulated structures were given.

1.2.2 Experimental Studies. In addition to the experimental work mentioned above, other investigators<sup>(26,27,28,29,30)</sup> have performed much needed experimental studies. Makowski and Pippard<sup>(27)</sup> performed experiments on a braced (reticulated) dome similar to the Dome of Discovery. Models of 1/8-inch diameter steel wire were built and Maxwell's Reciprocal Theorem was used to calculate displacements. The experimental results compared well with the theoretical predictions. Bayley<sup>(29)</sup> reported experimental work on a model dome with a three-way framing system, and compared the results with theoretical predictions. A 1/15th scale of a 143-foot diameter prototype was investigated. Uniform, half-uniform, and apex loading

cases were investigated. The effect of introducing limited joint and support rigidity was discussed. Little (30) documented work on the methods and problems of model testing and studied the use of model testing in the design of full-scale structures.

### 1.3 OBJECT AND SCOPE

An examination of the above literature revealed a lack of theoretical and experimental information on the load-deformation relationships of a reticulated dome from initial loading to the final buckled configuration. Also, several theories were postulated that reticulated shells can be analyzed, designed, and will behave as continuous domes. The lack of an adequate experimental data base to check these theories and to identify the causes of buckling in a reticulated dome thus initiated this study.

Two theoretical analyses to predict the load-deflection response of reticulated shells were employed, namely the split rigidity approach and the NASTRAN stiffness method. These analyses were based on the assumption of linear elastic material behavior. The NASTRAN predictions, however, included the effects of geometric nonlinearities. An experimental program to check these predictions was performed. Three model spherical reticulated domes were fabricated, one of plastic and two of brass. Hydrostatic water pressure loading was applied and radial deflections under each were measured using a highly accurate sensing device. The models were incrementally loaded to their respective buckling loads, and the buckling load was compared with the predictions of several current buckling theories. A least-squares curve-fitting technique was

developed to reduce the experimental deflection data. Detailed comparisons between theoretical and experimental deflections were made by comparing contour plots of the deflected shape and by comparing deflections along selected reference lines through the location of the final buckle. No stress or strain measurements were made on the models to check stresses.

## CHAPTER II

## THEORY AND ANALYSIS

The theoretical approach to the objectives of this study was a two-pronged effort: 1) to predict the deflections of a spherical reticulated shell as it deformed under load, and 2) to use these deflections to predict the buckling load of the shell. Two types of deflection analyses, the split rigidity approach and a conventional space frame analysis, are described in this section. A detailed theoretical development of each of these theories is presented in the appendices. A summary of these theories together with their application to several experimental shell models is given here. Buckling theories of reticulated shells are then presented and applied to the test models.

## 2.1 THE SPLIT RIGIDITY METHOD

2.1.1 Theory. A relatively new approach to predicting the deflections of reticulated shells has been the split rigidity technique.<sup>(20)</sup> This concept introduced the idea of an equivalent continuum membrane thickness  $t_m$  to account for membrane action in the shell, and an equivalent continuum bending thickness  $t_b$  to represent bending behavior. By considering different rigidities for membrane and bending action, this "split rigidity" theory took advantage of the available and relatively simple closed-form shell equations, provided the following basic assumptions were met:

(1) The shell material behaved in a linear elastic manner.

(2) The member grid pattern was a relatively uniform square grid such that single constant equivalent thicknesses could be established in both membrane and bending behavior. For this particular study, the theory was also restricted to a spherical reticulated shell subjected to a uniform radial load.

Upon writing three basic equilibrium equations for the spherical shell element in Figure 2.1 and making appropriate substitutions for the forces and moments therein, the problem was reduced to the solution of two ordinary differential equations:

$$\frac{d^2 Q_\phi}{d\phi^2} = - E t_m V \quad 2.1$$

$$\frac{d^2 V}{d\phi^2} = \frac{R^2 Q_\phi}{D_b} \quad 2.2$$

where  $Q_\phi$  = the meridional shear force

$E$  = Young's modulus for the material

$V$  = the angle of rotation of a tangent to a meridian

$R$  = the spherical shell radius.

The flexural rigidity quantity  $D_b$  was defined as

$$D_b = \frac{E t_b^3}{12(1-\nu^2)} \quad 2.3$$

where  $\nu$  is Poisson's Ratio. Equations 2.1 to 2.3 provided for both bending and membrane behavior, thus originating the term "split rigidity."

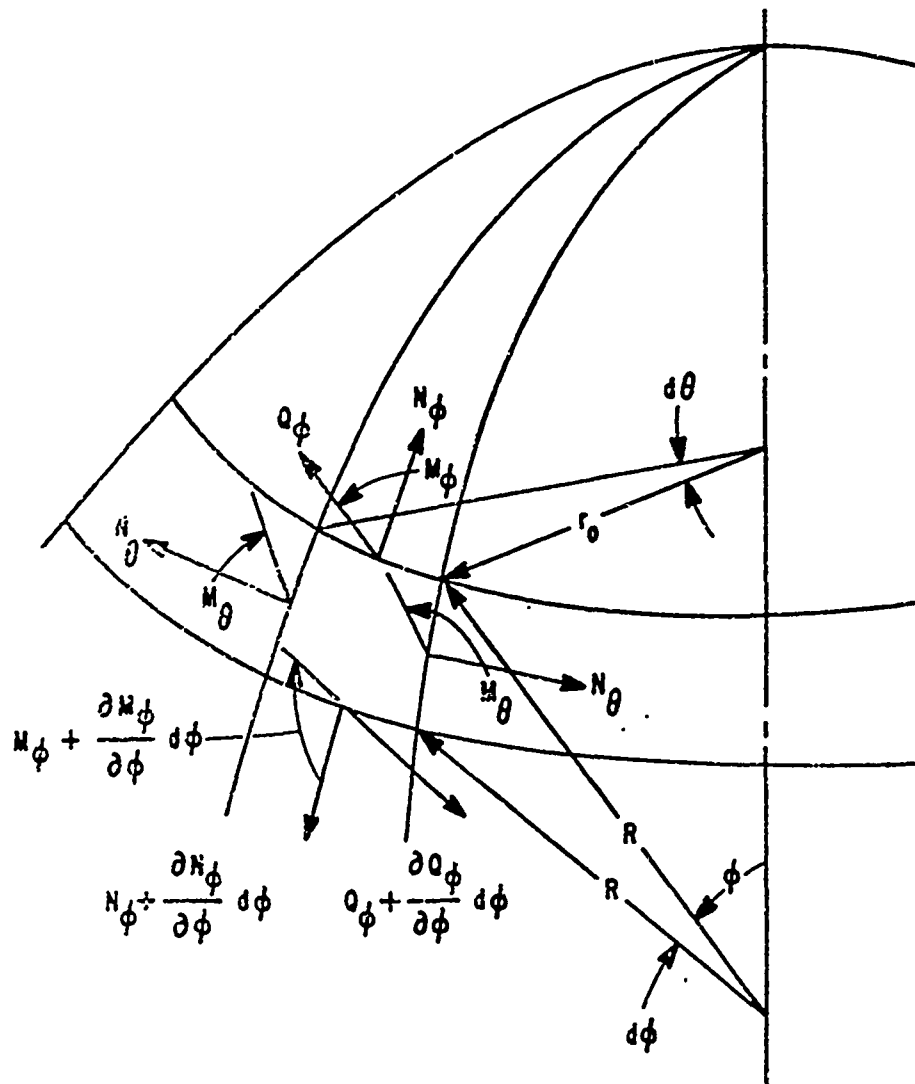


Figure 2.1 Free-Body Diagram of a Shell Element

By eliminating  $Q_\phi$  from the above equations a single fourth order differential equation resulted.

$$\frac{d^4 V}{d\phi^4} + 4\kappa^4 V = 0 \quad 2.4$$

$$\text{where } \kappa^4 = \frac{3R^2(1 - \nu^2)t_m}{t_b^3}$$

Reproduced from  
best available copy.

Equation 2.4 is known as the Gekeler (31) equation when  $t_m = t_o = t$ .

After solving this equation, expressions for the forces  $N_\phi$ ,  $N_\theta$ ,  $Q_\phi$  and the bending moments  $M_\phi$  and  $M_\theta$  were obtained. These internal forces were the quantities required to determine the deflection  $w$  normal to the shell surface (see Figure 2.2). The deflection  $w$  was the final objective for this analytic approach, and due to bending effects alone was

$$w_b = - \frac{RC}{\sqrt{2} \kappa} e^{-\kappa\alpha} \sin(\kappa\alpha + \gamma - \frac{3\pi}{4}) \quad 2.5$$

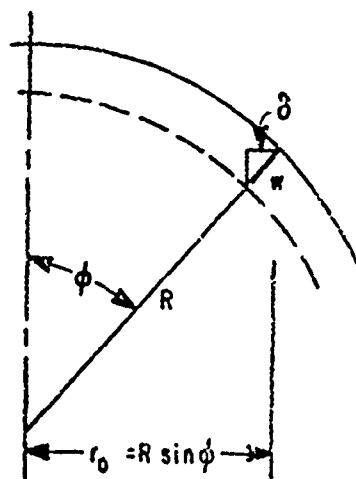


Figure 2.2 Displacement of a Point

where the constant  $C$  and the phase angle  $\gamma$  were to be determined from boundary conditions.

The first boundary condition for deflection compatibility at the edge beam (also called the shell springing) gave

$$C = \frac{-2\kappa^2 \left[ \frac{N_{\theta s}}{t_m} + N_{\phi s} \left( \frac{r_o \cos \phi_s}{A_b} - \frac{v}{t_m} \right) \right]}{E \left[ \sqrt{2} \kappa \sin \left( \gamma - \frac{3\pi}{4} \right) + \frac{r_o t_m}{A_b \sin \phi_s} \sin \left( \gamma - \frac{\pi}{2} \right) \right]} \quad 2.6$$

where  $A_b$  was the edge beam cross-sectional area and the subscript "s" referred to the subscripted quantities evaluated at the shell springing. By enforcing rotation compatibility at the edge beam a second boundary condition resulted.

$$\begin{aligned} \frac{C \sin \gamma}{V_{\tau}} &= N_{\phi s} (-a \cos \phi_s + b \sin \phi_s) \\ &+ \frac{\sqrt{2} \kappa D_b C}{R} \left[ -\sin \left( \gamma - \frac{\pi}{4} \right) + \frac{a\sqrt{2} \kappa}{R \sin \phi_s} \sin \left( \gamma - \frac{\pi}{2} \right) \right] \end{aligned} \quad 2.7$$

where  $V_{\tau}$  was the rotational flexibility of the edge beam. Other geometric quantities in the above equation are shown in Figure 2.3.

Therefore, simultaneous solution of Equations 2.6 and 2.7 for  $C$  and  $\gamma$  produced the desired normal deflection  $w$  which includes both bending and membrane action:

$$w = -\frac{R}{Et_m} [N_{\theta} - vN_{\phi}] - \frac{RC}{\sqrt{2} \kappa} e^{-\kappa \alpha} \sin \left( \kappa \alpha + \gamma - \frac{3\pi}{4} \right) \quad 2.8$$



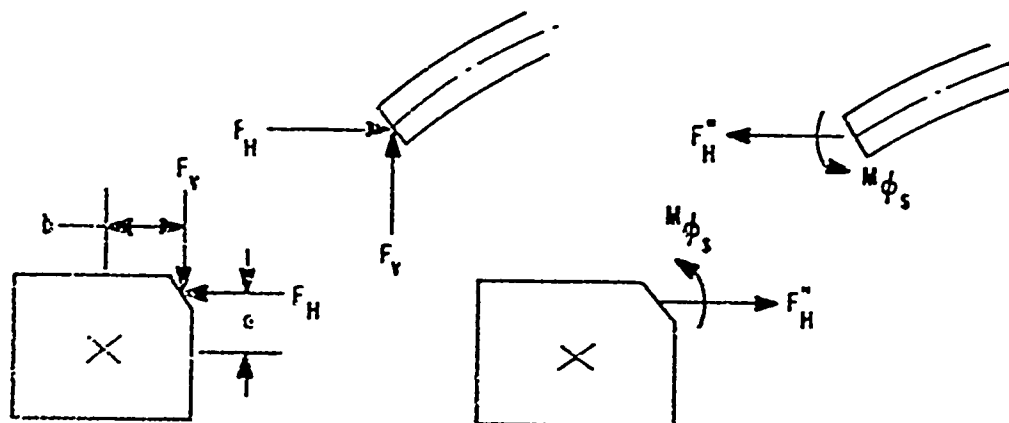


Figure 2.3 Compatibility Restoring Forces

Only a summary of the split rigidity approach to the prediction of deflections has been presented here. A complete development of the theory is given in Appendix A.

2.1.2 Test Model Analysis. Application of the split rigidity approach was made to three model reticulated domes. A summary of the models and their geometries is presented in Table 2.1. Full details

TABLE 2.1

Model	Grid Spacing	Material	Member Cross-Section
B2	2"	Brass	H
B1	1"	Brass	H
PRET	2"	Plastic	Rectangular

of the models and their fabrication are given in Chapter 3, and pertinent dimensions and other quantities necessary to solve Equation 2.8 are extracted therefrom. The analysis of each model follows.

Model B2. Brass members with the dimensions shown in Figure 2.4

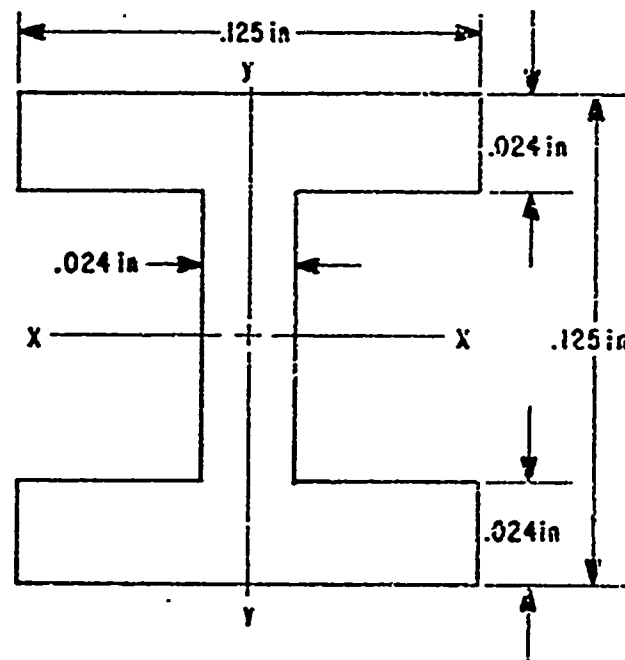


Figure 2.4 Cross-Section of Brass H-Section

were used in this model. The member properties were:

$$\text{Area} = A = .00785 \text{ in}^2$$

$$I_{xx} = .0000165 \text{ in}^4$$

$$I_{yy} = .0000079 \text{ in}^4$$

A solid circular brass edge ring having a quarter-inch diameter cross-section provided the following properties:

$$\text{Area} = .04909$$

$$I = .0001917$$

Young's modulus for the brass material was found to be  $10 \times 10^6$  psi (see part 4.1). A Poisson's Ratio of 0.33 was assumed. The B2 model radius (determined from a fit to experimental data as described in part 3.5) was 16.17 inches, and an opening angle of  $47^\circ$  was used.

This opening angle, designated  $\phi_s$ , was the angle between the vertical axis of the shell and a line from the sphere center to the shell springing, as shown later in Figure A.5. Using these known quantities it was found that  $\kappa = 13.28$  and  $D_b = 82.51$  lb-in. Roark<sup>(32)</sup> gave the edge beam rotational flexibility as  $R^2/EI$ , or .136 rad/lb for the B2 model. For a square grid approximation the membrane thickness  $t_m$  was equal to  $A/d$  where  $d$  was the member spacing, and the bending thickness  $t_b$  was given by

$$t_b = \sqrt[3]{\frac{12I(1 - \nu^2)}{d}} \quad 2.9$$

Thus  $t_m = .00393$  inches and  $t_b = .0445$  inches. Solving Equations 2.6 and 2.7 simultaneously for  $\gamma$  and  $C$  gave  $36^\circ$  and  $-.00404$  p, respectively. Here  $p$  was the external uniform pressure load applied radially. The final expression for combined membrane and bending deflections for the B2 model was therefore

$$w = -.00348pe^{-\kappa\alpha} \sin(\kappa\alpha - 81^\circ) - .00223 p \quad 2.10$$

The deflection was taken to be positive for an outward movement. The pressure  $p$  was a positive quantity.

B1 Model. Corresponding quantities were computed for the B1 test model. The same member cross-section and edge ring were used. In this case  $R = 16.40$  inches,  $\kappa = 13.39$ ,  $D_b = 164.4$  lb-in,  $V = .1403$  rad/lb,  $t_m = .00785$  inches, and  $t_b = .0560$  inches. From the boundary condition equations,  $\gamma = 37^\circ$  and  $C = -.00235$  p. The combined membrane and bending deflection equation for the B1 model was

$$w = -.00204 p e^{-\kappa\alpha} \sin(\kappa\alpha - 82^\circ) - .00115 p \quad 2.11$$

PRET Model. The plastic reticulated model shell had members whose cross section averaged .214 inches in depth and one-half inch in width. This gave section properties of  $A = .107 \text{ in}^2$  and  $I = .000406 \text{ in}^4$ . The edge beam condition for the PRET model is illustrated in Figure 2.5. Due to this geometry a very flexible edge beam was assumed, meaning  $\gamma = \pi/4$ . Young's modulus for the plastic material was measured to be 187,000 psi, and a Poisson's Ratio of 0.30 was assumed. The PRET model radius was 15.60 inches, and its opening angle was  $50.6^\circ$ . The edge beam area was taken as  $.113 \text{ in}^2$ . Thus  $\kappa = 11.22$ ,  $t_m = .0534$  inches,  $t_b = .1307$  inches, giving  $C = -.0403 p$  from Equation 2.6. For the PRET model the split rigidity equation for the deflection  $w$  was

$$w = -.0396 p e^{-\kappa\alpha} \sin(\kappa\alpha - \frac{\pi}{2}) - .00853 p \quad 2.12$$

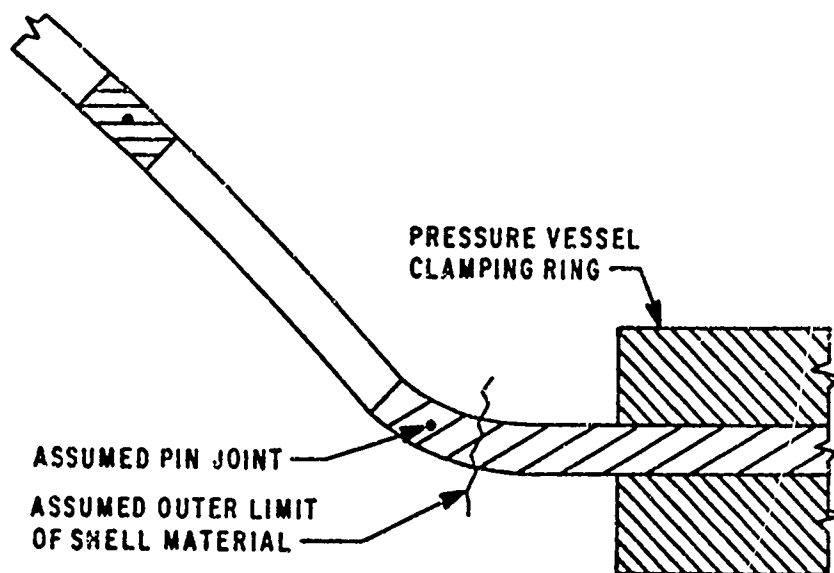


Figure 2.5 PRET Model Edge Ring Geometry

The split rigidity equations given here are plotted in part 4.3 against experimental results.

## 2.2 ANALYSIS BY THE STIFFNESS METHOD

2.2.1 General. In addition to the split rigidity analysis just described, a conventional space frame analysis was conducted using the NASTRAN<sup>(7)</sup> (acronym for NASA STRuctural ANalysis) computer code. Using the stiffness method a series of calculations was conducted for static incremental loadings for two of the three test shell models. The coordinate systems, grid point selection, members and their cross-sectional and material properties, loads, and the boundary conditions assumed in the NASTRAN analyses are described in the following section.

The assumption of linear elastic material behavior was made in the analyses described here. An accurate prediction of any potential plastic behavior was therefore not expected either in this type of analysis or in the previously described split rigidity technique. Prediction of any nonlinear behavior due to geometric imperfections was the objective of the NASTRAN analyses. It should be noted that no NASTRAN analyses were conducted for the B1 test model. Since experimental instrumentation was not provided at each joint, the exact determination of all the necessary joint coordinates was not possible for this model.

2.2.2 The B2 Model. A full description of the B2 model and its fabrication is presented in part 3.2.1. This model was constructed of curved brass H-sections in a grid pattern intended to simulate a two-inch spacing of the members in both the circumferential and

meridional directions. A solid quarter-inch diameter brass edge ring provided support at its base.

Coordinate Systems. The origin of both coordinate systems employed was located at the center of the spherical test model, as shown in Figure 2.6. The "basic" coordinate system (using NASTRAN terminology) was rectangular, while the "local" system was defined in spherical coordinates to take advantage of the shell geometry.

Grid Point Selection. The location of member joints was denoted by specifying the experimental radius and the design meridional and circumferential angles with respect to the local coordinate system. Since the edge ring itself was not instrumented radially, joint locations around its circumference were determined by linear extrapolation of the radial values of gage points located one and two inches meridionally from the desired location.

The grid used in the analysis is shown in Figure 2.7. This grid appears as it would if viewed from the shell center. The members in the actual model of Figure 4.6 not appearing in the analysis grid were assumed to provide load transfer only, with negligible contribution to the structural stiffness. Joint locations of these members were not all instrumented, so their true radial locations were not known.

Incidentally, a subtlety of the NASTRAN code required locating the crown joint .001 degrees both meridionally and circumferentially from the vertical axis of the coordinate system. Ambiguities in vector definitions would result if this procedure were not followed.

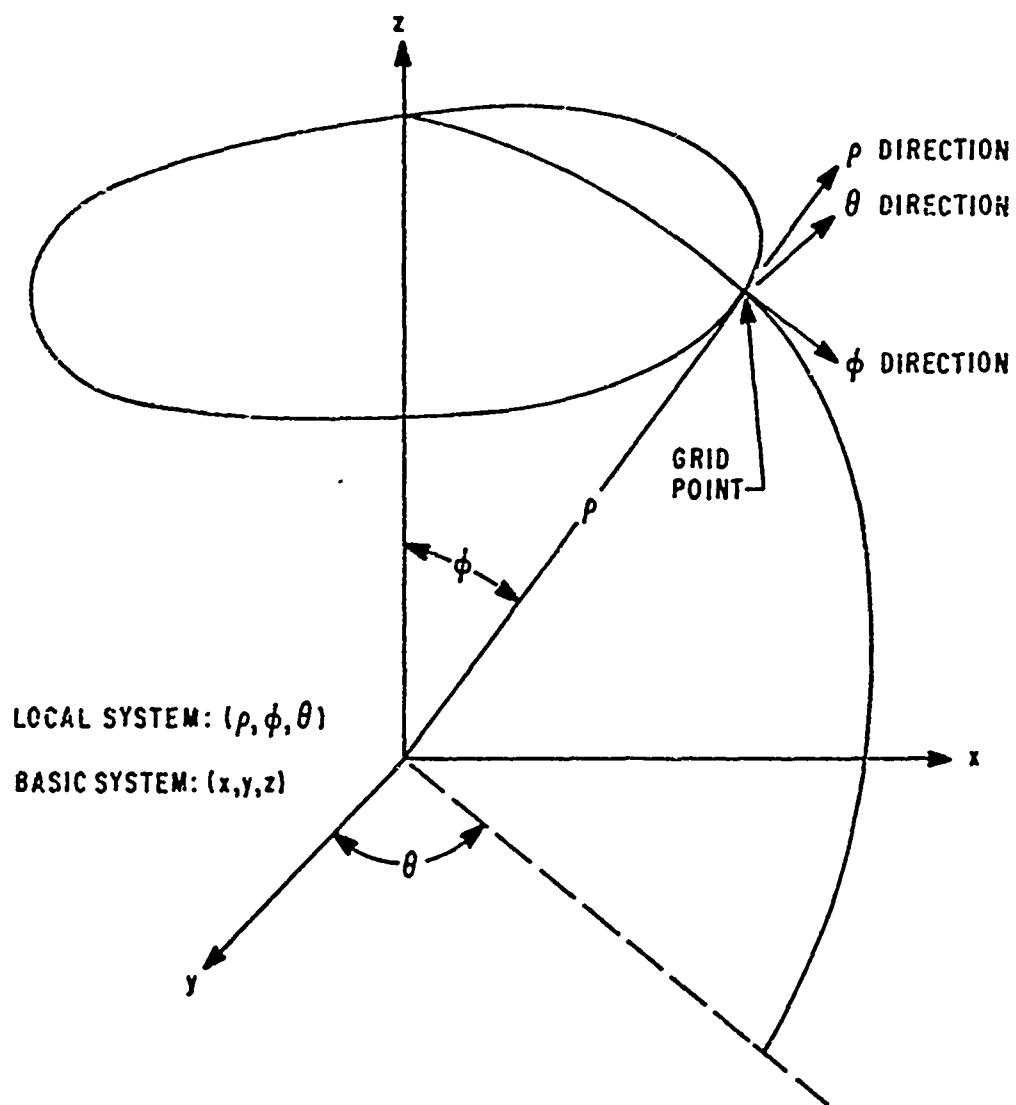


Figure 2.6 Coordinate Systems

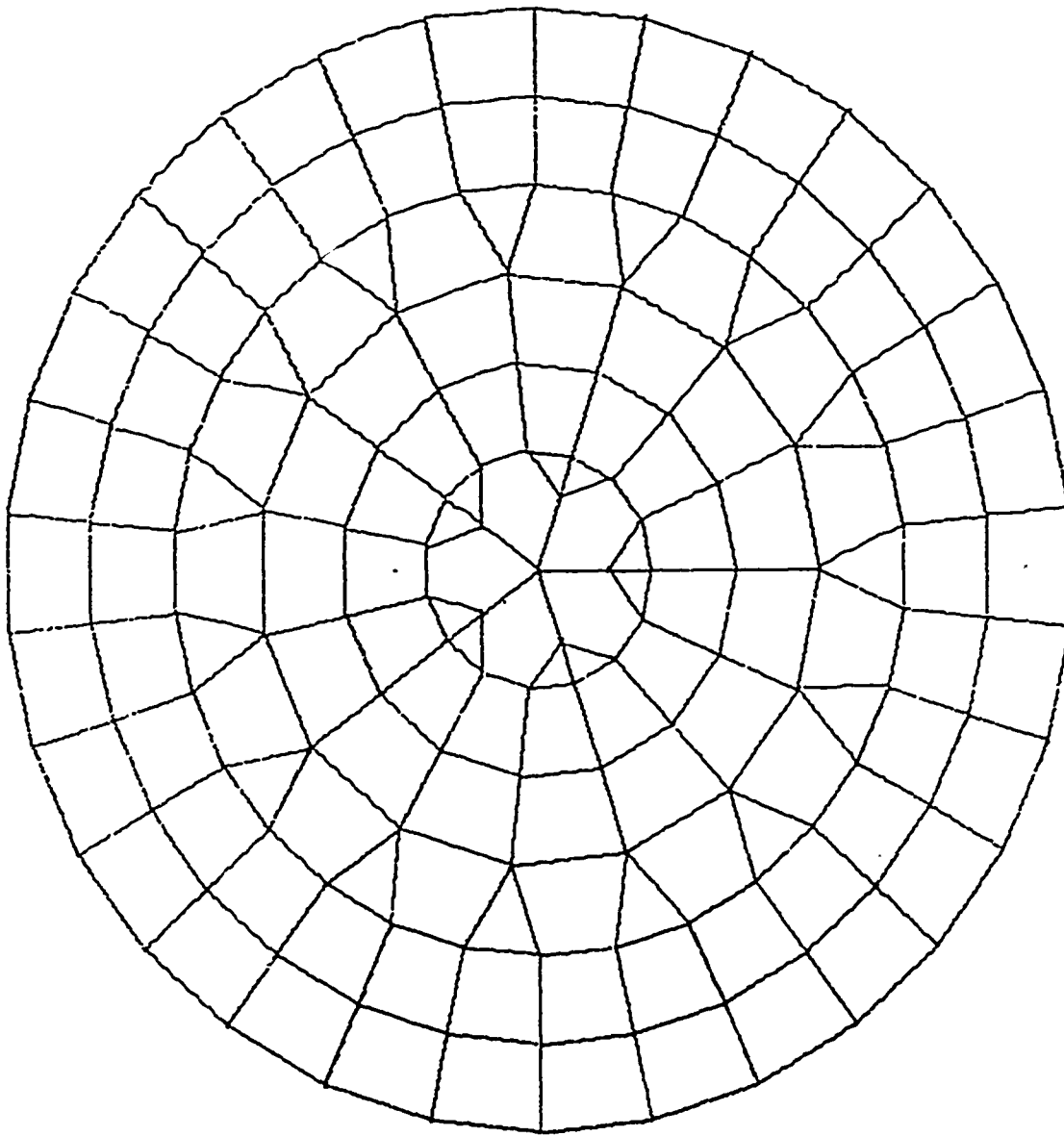


Figure 2.7 B2 Model Theoretical Grid



Bar Elements and Member Properties. The brass H-sections used in the model were assumed to be straight members between the joint locations. The member properties were given previously in part 2.1.2.

Material Properties. Based on results of the tensile tests as described in 3.6.1 and 4.1.1, the elastic modulus for the brass material was taken as  $10 \times 10^6$  psi. A Poisson's Ratio of 0.33 was assumed.

Loads. An option for applying a pressure distribution along a bar member was not available in NASTRAN. A series of radial point loads applied to each joint was therefore assumed. For most joints the loads were calculated as follows. The surface area for the circular segment lying between two parallel circles was computed as

$$\text{AREA} = 2\pi (\cos\phi_T - \cos\phi_B) R^2 \quad 2.13$$

These parallel circles were located on either side of a circular ring of joints and midway meridionally to the adjoining ring of joints. This area was then multiplied by the external pressure and divided by the number of joints around a ring, or,

$$F_i = \frac{2\pi P}{N} (\cos\phi_T - \cos\phi_B) R^2 \quad 2.14$$

where

$F_i$  = point load applied to joint  $i$

$P$  = external pressure load

$N$  = number of joints around a ring

$\phi_T, \phi_B$  = meridional angles bounding the segment above

and below, respectively

$R$  = "best-fit" radius of experimental data.  $R$  for the B2 model was 16.17 inches.

For the crown joint and the five adjoining joints, the contributing load was proportioned as follows. One-third of the load between the crown and the adjoining parallel circle of joints was applied at the crown. The remainder of the load was distributed equally to the remaining five joints.

Boundary Conditions. The boundary conditions for the B2 model required setting the vertical displacement of the edge ring to zero. This was accomplished in NASTRAN by applying the following constraint:

$$w \cos \phi_s - v \sin \phi_s = 0 \quad 2.15$$

where  $\phi_s$  was the shell opening angle. Here  $w$  was the radial and  $v$  the meridional displacements. To prevent rigid body displacement the crown joint was restrained against horizontal displacement, and one edge ring joint was restrained circumferentially to avoid rigid body rotation.

2.2.3 The PRET Test Model. The fabrication of the PRET model is detailed in part 3.2.2. It was designed as a spherical reticulated shell having quarter-inch thick members of a plastic material, with a two-inch grid spacing. The model was constrained at its base by clamping it at the pressure vessel edge.

Coordinate Systems. As in the B2 model analyses the origins of both the local and basic coordinate systems were located at the sphere center.

Grid Point Selection. Joint coordinates were specified by the radial distance from the spherical center (as determined by a

"best-fit" to the experimental data) and by the design values for meridional and circumferential angles. Locations of joints outside the range of the measuring device were extrapolated with a curve through the measurable data on the same parallel circle.

The analysis grid for the PRET model is given in Figure 2.8, and duplicates that of the actual model. The view is from the spherical center. The crown node was located slightly off-center, again to prevent ambiguous geometric definitions in NASTRAN.

Bar Elements and Member Properties. Straight members were assumed for the PRET analyses. Member properties for the model were determined from individual thickness measurements taken on each member. The thicknesses varied because of the vacuum-forming method of fabrication and ranged from typical values of .22 to .25 inches near the springing to .19 to .20 inches near the crown.

Material Properties. Based on results of the material property tests described in parts 3.6.2 and 4.1.1, an elastic modulus of 187,000 psi was used in the analyses. Poisson's Ratio was taken as 0.30 for the plastic material.

Loads. Radial point loads were assumed acting at each member joint and were calculated in a manner identical to that for the B2 model. Note, however, that the first parallel circle of joints next to the PRET model crown contained six rather than five joints among which the load was equally divided.

Boundary Conditions. The existing edge ring geometry of the PRET model was shown previously in Figure 2.5. The shaded areas represent circumferential members seen when cutting a meridional

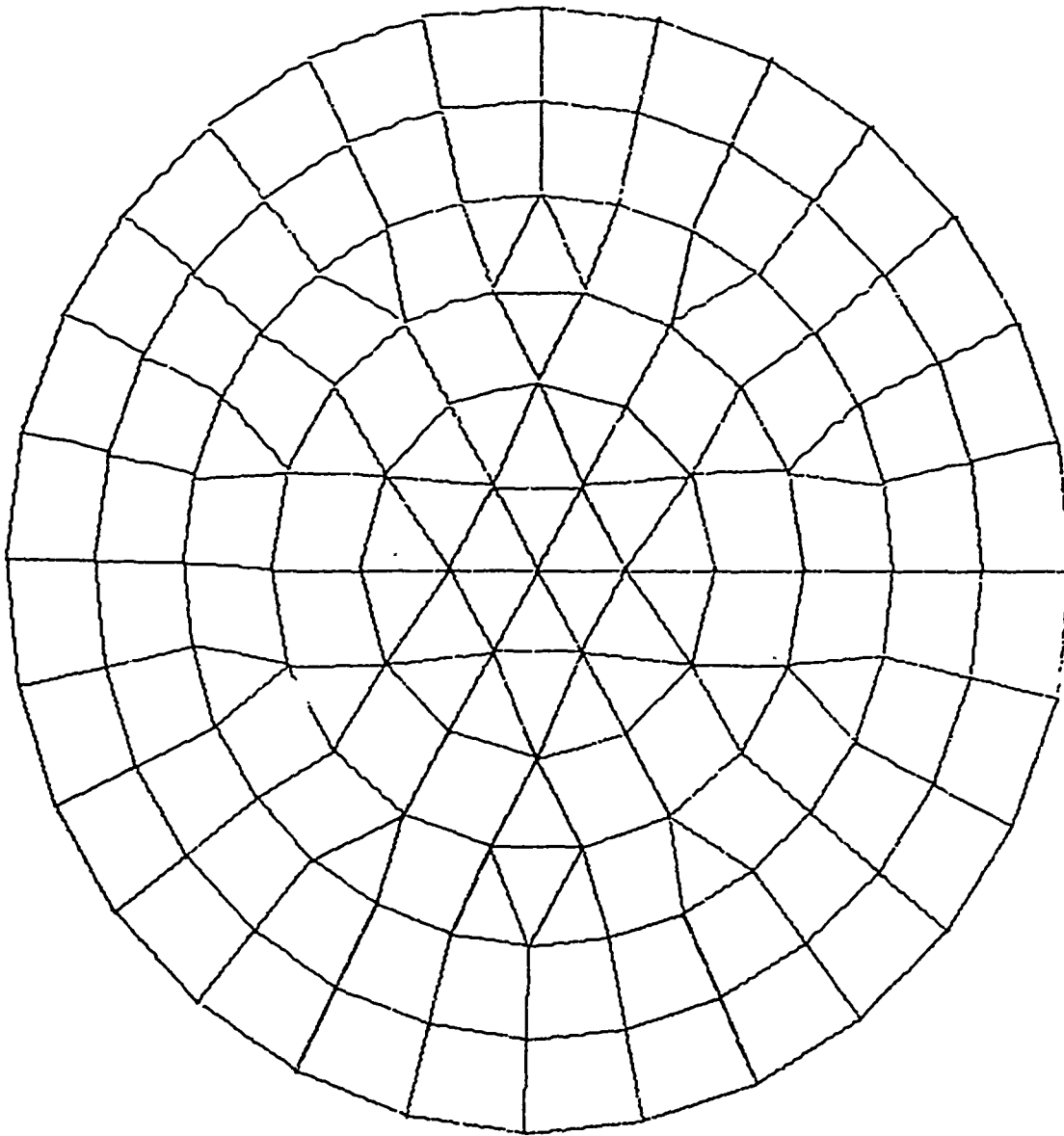


Figure 2.8 PRET Model Theoretical Grid

section through the shell between two meridional members. Joints located on the edge ring were assumed to be free to rotate in any direction but displacements were prevented. The edge ring was therefore taken as a regular size member with the actual model material outside this member ignored. This assumption was deemed reasonable considering the low bending stiffness of the quarter-inch plastic material protruding from the pressure vessel clamping ring.

To prevent rigid body motion in the PRET analyses, the crown joint was constrained horizontally and an edge ring joint was constrained circumferentially.

### 2.3 RETICULATED SHELL BUCKLING

When designing a reticulated shell several types of buckling must be considered. General buckling over a large portion of the shell is a prime consideration. Local snap-through buckling, when a joint is loaded and deflects through such that the local curvature is reversed, can also occur. The possibility of member column buckling between joints must also be examined.

In the following section each of the above buckling types was investigated. Appropriate theories are presented and then are applied to the experimental models previously described.

2.3.1 Buckling Theories. Two different theories for general buckling are given here. The effects of live load deflections were included in Buchert's theory<sup>(20)</sup>, while material and member properties only were considered for Von Karman-type buckling<sup>(33, 34, 35)</sup>.

General Buckling (Buchert). Buchert<sup>(20)</sup> developed a general buckling theory by calculating deflections during loading and prior

to buckling and using a large deflection stability approach. Equation 2.4, the differential equation for secondary edge effects, formed the basis of this theory.

By maximizing the deflection predicted by Equation 2.8 and considering a simply supported edge, the result was

$$w_{MAX} = -\frac{RCe^{-3\pi/4}}{2\kappa} - \frac{R}{Et_m} (N_\theta - \nu N_\phi) \quad 2.16$$

Buchert presented the results of this theory in the following form. Let  $\Delta = |w|_{MAX}$ . For small deflections, or for  $\Delta/t_m \ll 1$

$$P_{cr_E} = \frac{2Et_m^2}{R^2} \left[ 0.41 \left( \frac{t_b}{t_m} \right)^{3/2} - 0.81 \frac{\Delta}{t_m} \right] \quad 2.17$$

If  $\Delta/t_m$  was not much less than 1.0, or for large deflections, the following expression was used:

$$P_{cr_E} = \frac{2Et_m^2}{R^2} \left\{ -0.54 \frac{\Delta}{t_m} - 0.145 \sqrt{9.9 \left( \frac{\Delta}{t_m} \right)^2 + 3.08 \left( \frac{t_b}{t_m} \right)^3} \right. \\ \left. + \sqrt{1.09 \left( \frac{\Delta}{t_m} \right)^2 - 0.03 \frac{\Delta}{t_m} \sqrt{9.9 \left( \frac{\Delta}{t_m} \right)^2 + 3.08 \left( \frac{t_b}{t_m} \right)^3} + 0.359 \left( \frac{t_b}{t_m} \right)^3} \right\} \quad 2.18$$

Linear elastic material behavior was assumed in the above equation, as noted by the subscript E. Buchert<sup>(23)</sup> derived plasticity reduction factors for this equation in the event inelastic material response was anticipated. In that case the plastic buckling pressure was given by

$$P_{cr_p} = \eta P_{cr_E} \quad 2.19a$$

where

$$\eta = \frac{3}{4E} (E_t \pm \frac{E_s}{3}) \quad 2.19b$$

In this expression,

$E_s$  = the secant modulus, and

$E_t$  = the tangent modulus associated with the maximum membrane stress.

General Buckling (Von Karman). Von Karman-type buckling<sup>(33)</sup> when incorporated with the concept of split rigidities<sup>(34)</sup> was expressed as

$$P_{cr_E} = CE \left(\frac{t_m}{R}\right)^2 \left(\frac{t_b}{t_m}\right)^{3/2} \quad 2.20$$

Wright<sup>(13)</sup> recommended a value for the constant C of 0.38, while Buchert<sup>(35)</sup> found C to be 0.365. (These values of C do not include a safety factor.)

Local Snap Buckling. Crocker and Buchert<sup>(36)</sup> have given the criteria for local snap-through buckling as follows:

If

$$\frac{R}{L^2} \sqrt{\frac{I}{A}} \leq .10 \quad 2.21$$

then the local snap buckling can occur. In the above, L is the member length. Wright<sup>(13)</sup> gave the criteria for local buckling as:

If

$$\frac{R}{L^2} \sqrt{\frac{I}{A}} \leq .092 \quad 2.22$$

then buckling would occur for inextensible supports, and if

$$\frac{R}{L^2} \sqrt{\frac{I}{A}} \leq .132 \quad 2.23$$

then buckling would occur for extensible supports.

Euler Column Buckling. For a uniform radial pressure  $p$ , the membrane forces were  $pR/2$  throughout the shell. The member forces, assuming a square grid with straight members, were thus equal to  $pRL/2$ . Using the Euler column buckling load the critical pressure  $p_{cr}$  was

$$P_{cr_E} = \frac{2\pi^2 EI}{RL^2} \quad 2.24$$

Even with rigid joints the possibility of antisymmetrical buckling existed; thus the straightforward Euler load was used.

2.3.2 Application to Experimental Models. Each of the previous buckling equations was applied to the prediction of the buckling load for the experimental shell models. The following is a summary of these predictions.

The B2 Model. The general buckling formula derived by Buchert (Equation 2.18) was expressed in the following form

$$P_{cr_E} = \frac{2Et_m^2}{R^2} \cdot F \quad 2.25$$

where

$$F = 0.54 \frac{\Delta}{t_m} - 0.145 \sqrt{9.9 \left(\frac{\Delta}{t_m}\right)^2 + 3.08 \left(\frac{t_b}{t_m}\right)^3} + \sqrt{1.09 \left(\frac{\Delta}{t_m}\right)^2 - .03 \frac{\Delta}{t_m} \sqrt{9.9 \left(\frac{\Delta}{t_m}\right)^2 + 3.08 \left(\frac{t_b}{t_m}\right)^3} + 0.359 \left(\frac{t_b}{t_m}\right)^3} \quad 2.26$$

From the previously defined properties of the B2 model,  $t_b/t_m = .0445/.00393 = 11.3$ ,  $R = 16.17$  inches and  $E = 10 \times 10^6$  psi. A non-dimensional plot of the factor  $F$  versus the deflection term  $\Delta/t_m$  is shown in Figure 2.9. This family of curves demonstrated the sensitivity



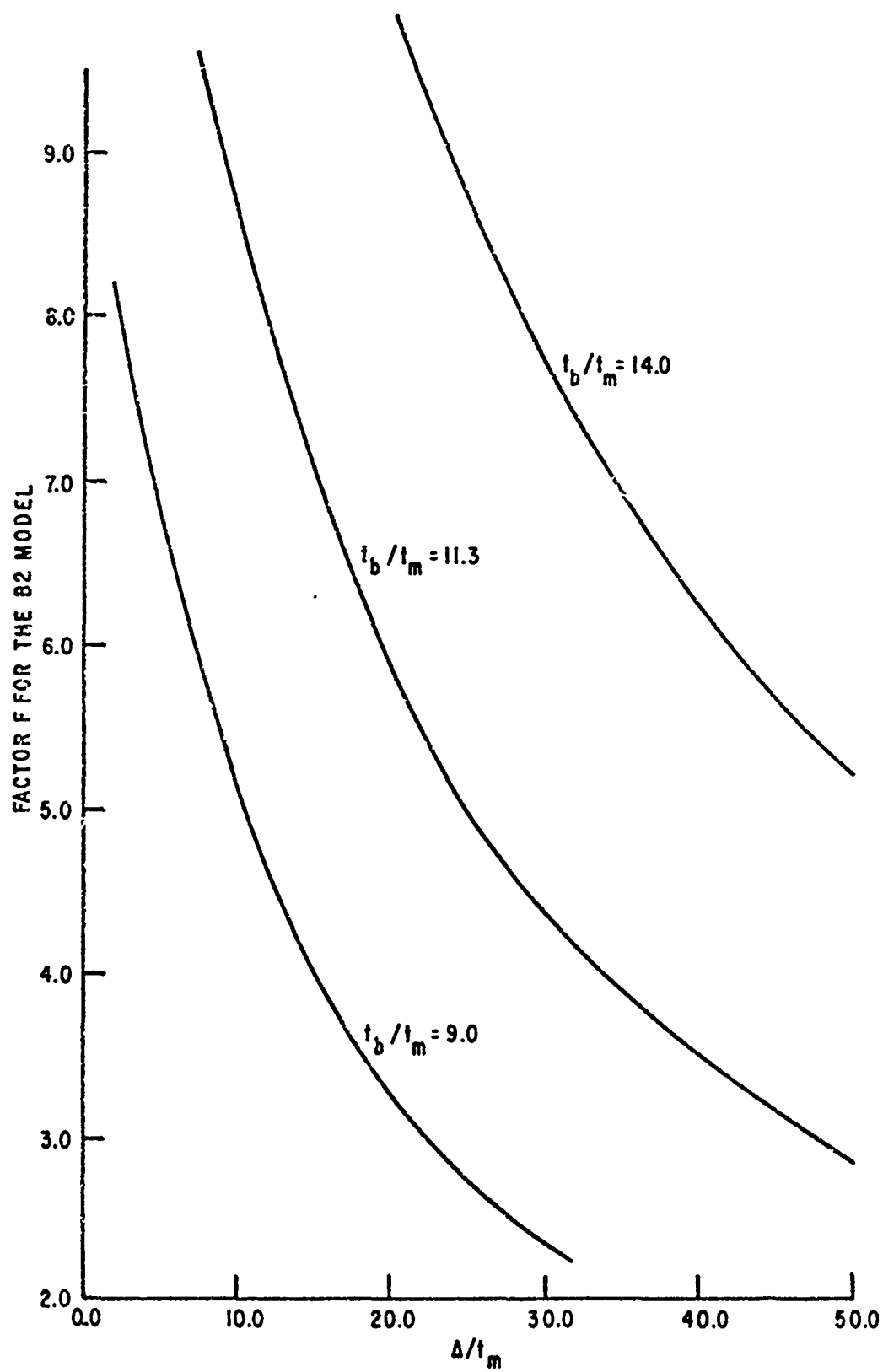


Figure 2.9 B2 Model: Equation 2.26

of the buckling load to live load deflections and to variations in the shell stiffness properties. Therefore, to determine the buckling load an estimate of the maximum live load deflection was required. Three possibilities for this estimate were immediately obvious. The first was to use the value for maximum combined bending and membrane deflections given by the split rigidity approach (Equation 2.16). By iterating between Equations 2.16 and 2.26, a value of  $P_{cr}$  equal to 11.3 was found. Note that linear elastic material behavior was assumed in both the deflection and the buckling equations above. A second approach was to use the maximum deflection predicted from a standard space frame analysis approach like NASTRAN. This method also assumed linear elastic material behavior but had the advantage of accounting for geometric imperfections in the shell. Since the B2 shell model was tested experimentally, the third alternative was to use the maximum deflection measured during the test. Results of the latter two approaches are presented later in Chapter 4.

As applied to the prediction of general buckling of the B2 model, the Von Karman approach (Equation 2.20) gave  $P_{cr} = 8.2$  psi. Linear elastic material behavior was assumed here also.

For protection against local snap-through buckling, Equation 2.21 by Buchert required that  $rgR/L^2$  be greater than .10 for the B2 model. For this model the quantity was .185, thus satisfying the criteria.

Finally, the Euler column buckling formula gave  $P_{cr} = 50.4$  psi. This was considerably higher than the other predicted critical loads, so column buckling was not expected for the B2 model.

The B1 Model. Buchert's general buckling formula is plotted in Figure 2.10. For this model  $t_b/t_m = .0560/.00785 = 7.13$  and  $R = 16.40$  inches. When the split rigidity equations were used to estimate the maximum deflection  $\Delta$  for the shell, the predicted buckling load was 22.1 psi. Results of this method using the measured experimental deflection from the B1 model test appear later.

The Von Karman approach as applied to the B1 model gave  $P_{cr} = 15.9$  psi.

For protection against local snap buckling, the B1 model provided a value of  $r_g R/L^2 = .75$  which exceeded the required .10.

For column buckling the critical Euler external pressure load for the B1 model was 199 psi, which was definitely on the safe side.

The PRET Model. Figure 2.11 represents the Buchert formula for general buckling of the PRET model. In this case,  $t_b/t_m = .1307/.0534 = 2.45$ ,  $E = 187,000$  psi, and  $R = 15.60$  inches. Using the split rigidity approach to predict the maximum deflection  $\Delta$ , the critical buckling pressure was predicted to be 4.0 psi. This and other techniques to predict the maximum deflection  $\Delta$  for use in buckling predictions are considered in Chapter 4.

An estimate of the critical buckling pressure by the Von Karman method gave a value of 3.4 psi.

For snap buckling, the PRET model had a value of  $r_g R/L^2$  of .24 which exceeded the required .10.

The Euler column buckling pressure was estimated at 24.0 psi.

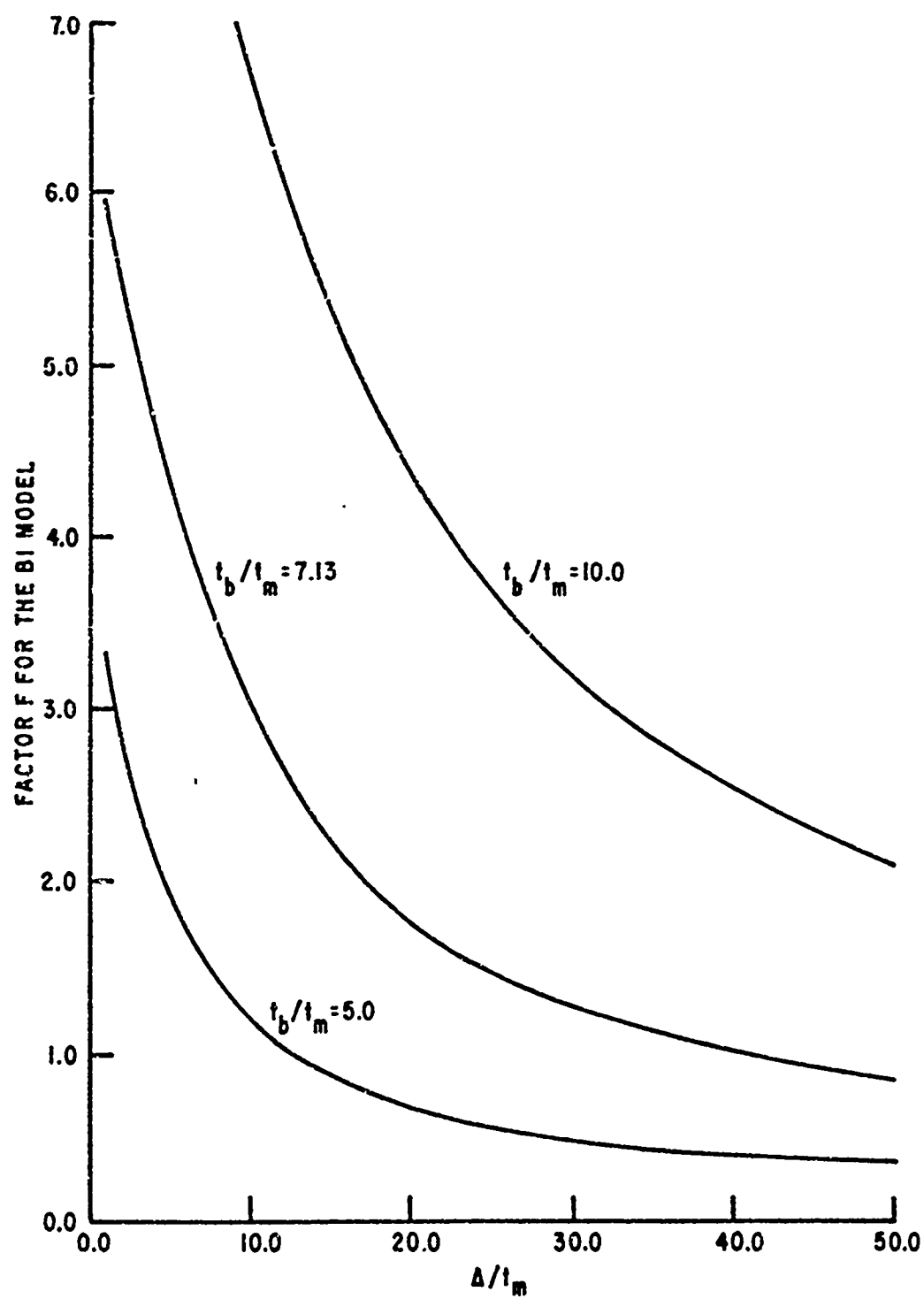


Figure 2.10 BI Model: Equation 2.26

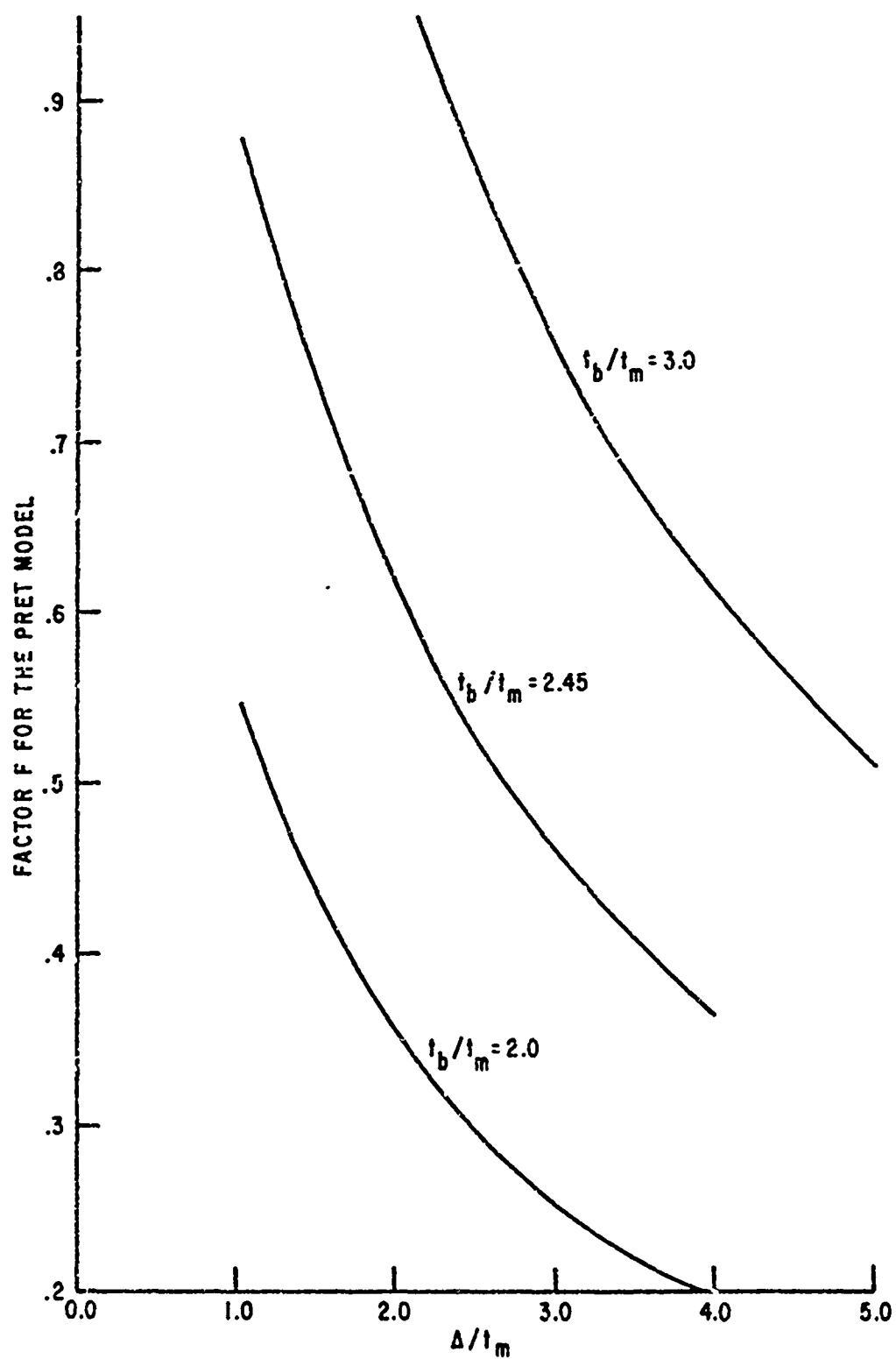


Figure 2.11 PRET Model: Equation 2.26

## CHAPTER III

### EXPERIMENTAL PROCEDURES

#### 3.1 GENERAL

In order to meet the stated objectives of part 1.3 an experimental program was developed. The procedure consisted of fabricating three spherical shell models, two of brass and one of plastic. These models were loaded with a uniform hydrostatic water pressure in a series of static pressure increments. At each pressure the radial displacement at points of instrumentation was measured and recorded. Loading continued until buckling occurred.

The types of models and the materials used in their fabrication were based on the following criteria. A spherical shape was selected and a square grid approximation was employed to enhance ease of fabrication. Member spacing was determined by placing the first circumferential member above the edge ring near the point of inflection of the theoretical bending deflection curve. This criteria applied to the two models having a two-inch grid spacing. One of the brass models was fabricated on a one-inch grid spacing to attempt to identify differences in the behavior of a coarse versus a fine mesh.

The brass material was chosen because of its ready availability in common shapes in the desired size. Brass also provided relatively well-defined elastic properties. The plastic material was chosen for its extreme ease of fabrication. This material was on hand at the Shell Structures Laboratory at the University of Missouri, as was the vacuum-forming apparatus necessary to give the model its initial

spherical shape. The effects of creep in the plastic material were recognized. It was felt, however, that the objectives of the study could be met in spite of the creep phenomena.

### 3.2 FABRICATION OF THE MODELS

3.2.1 Brass. Considering the above criteria, computations indicated that a brass H-section having the dimensions shown previously in Figure 2.4 would meet the desired design requirements. To begin fabrication of the first brass model a pattern mold was selected and the desired two-inch square grid was scribed thereon (see Figure 3.1). A mechanical guide was then assembled to conform the sections to the spherical shape of the mold as shown in Figure 3.2. The principal axes of the member were oriented parallel and normal to radial lines at each point on the sphere.

Continuous circumferential rings were assembled first, and meridional members were then added. Flanges at the ends of each member were trimmed (see Figure 3.3) to provide a tongue-in-groove joint at member intersections. Joints were initially connected using a soft-solder technique as in Figure 3.4. A high-quality silver solder was then applied to provide a secure connection at each joint. Addition of the edge ring (Figure 3.5) completed the model, several views of which appear in Figure 3.6. This first brass model, designed to simulate a two-inch square grid spacing, is hereafter referred to as the B2 test model.



Figure 3.1 Scribing the Pattern Mold



Figure 3.2 Bending the Brass Members



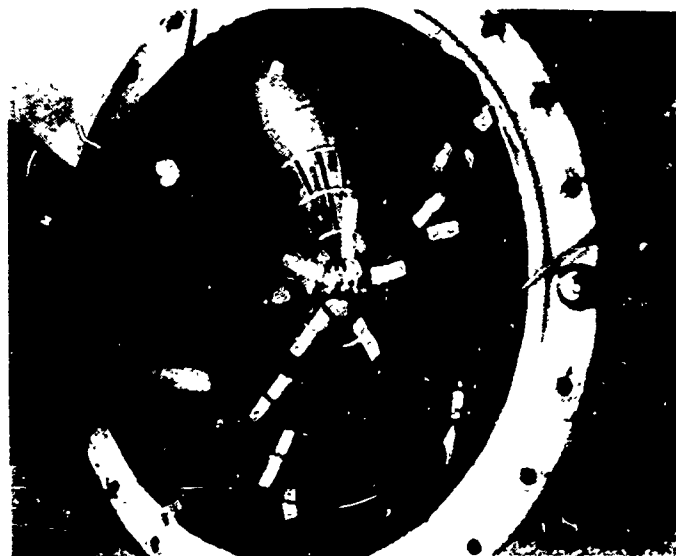


Figure 3.4 Soft-Solder Technique



Figure 3.3 Flange Trimming

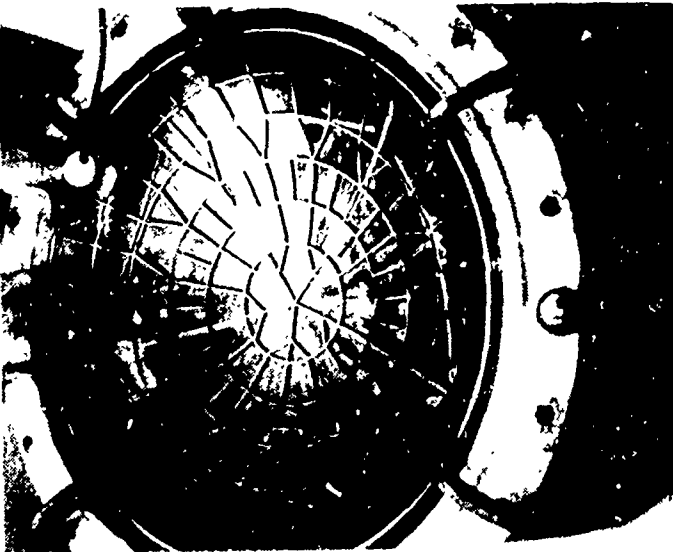


Figure 3.5 Adding the Edge Ring



Figure 3.6 Completed B2 Test Model

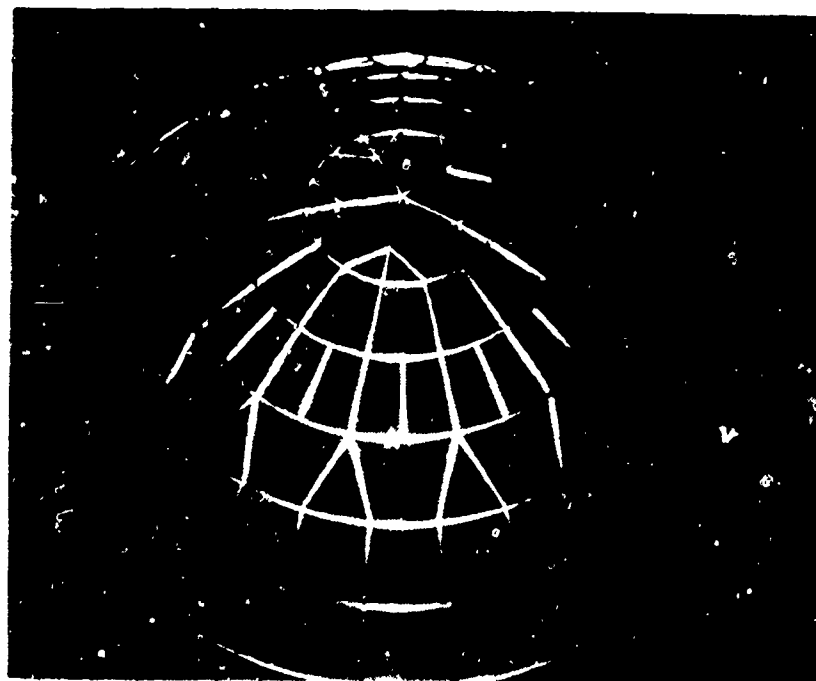
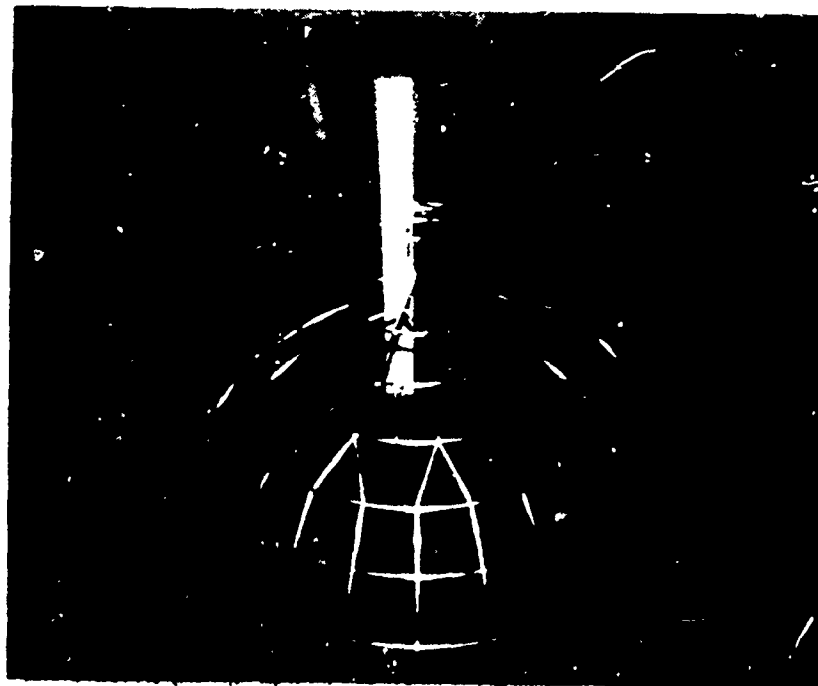


Figure 3.6 (cont.) Completed B2 Test Model

Following completion of the B2 model, it was instrumented for testing. Instrumentation consisted of soft-soldering spherical gage points (steel balls  $1/32$  inches in diameter) at locations around the shell where it was desired to know the deflections. Typical locations of gage points were at member intersections, and at half-inch intervals along meridional lines near the edge ring to monitor anticipated bending behavior. Data was not taken on the movement of the brass model edge ring due to its recessed position in the test device described later in part 3.3.1. For the brass models a total of 251 locations on the shell were instrumented.

After testing the B2 model to its buckling load, it was straightened and members were added to it to provide a subsequent test model. This second brass model, designated B1, was designed to simulate a one-inch square grid spacing of members. Fabrication procedures duplicated those of the B2 model. The B1 model is shown in Figure 3.7.

The difficulties encountered in cutting, milling, and soldering the brass models were considerable. Tolerances were very close due simply to the small size of the members. The silver-soldering technique was particularly difficult. Temperatures near  $1100^{\circ}$  F were required to flow the solder and bond the joints properly. Temperatures of this magnitude were sufficient to alter the physical properties of the material as evidenced by a lower yield stress in the tensile test results of part 4.1.1. These temperatures naturally caused significant expansion and contraction during fabrication, resulting in severe difficulties in holding tolerances and likely

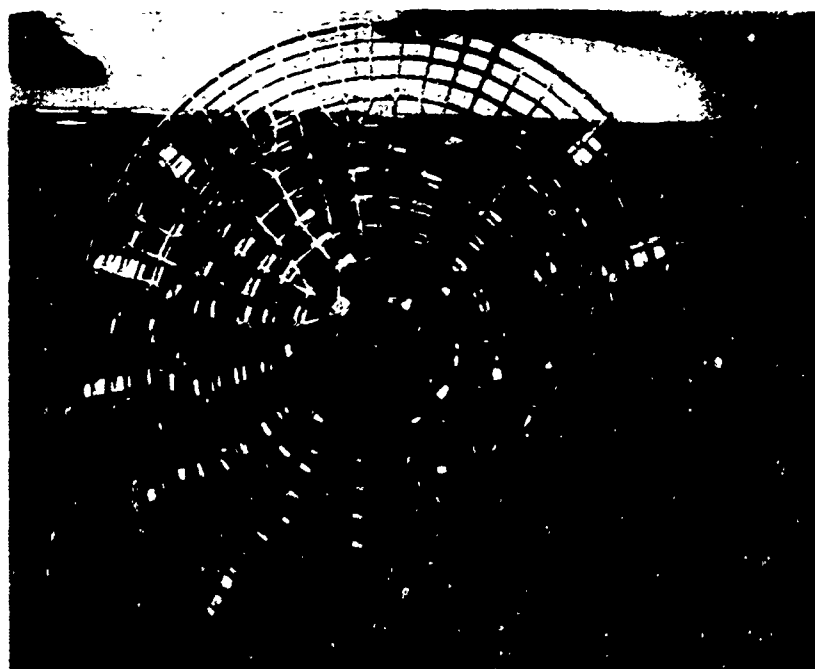
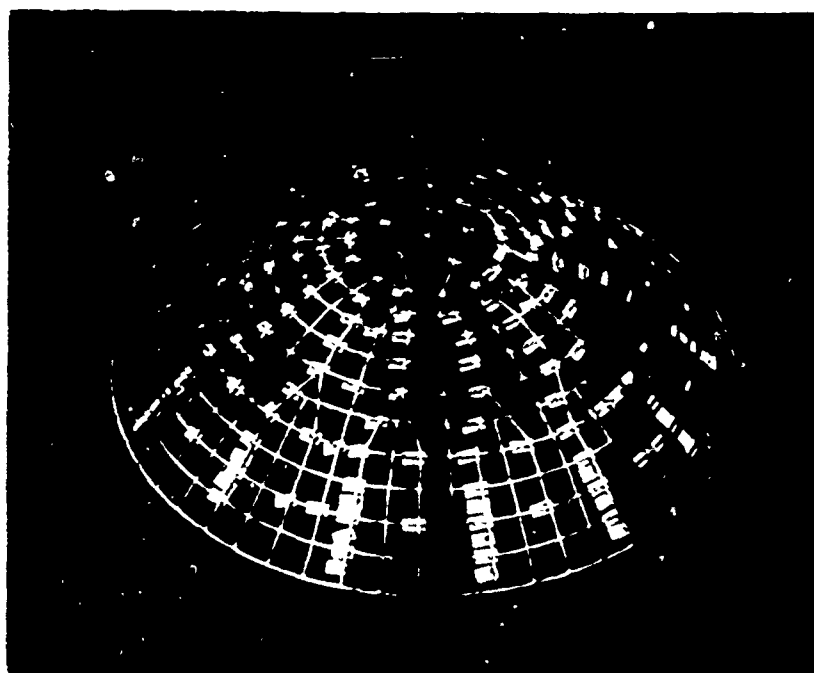


Figure 3.7 Completed B1 Test Model

producing a highly variable residual stress pattern throughout the model. The initial imperfection patterns presented in part 4.1 reflect these difficulties.

3.2.2 Plastic. A plastic test model was fabricated as part of the experimental program and is referred to as the PRET model. A two-inch square grid was to be simulated. Member size was chosen to be one-quarter inch in depth with a one-half inch width.

To fabricate the PRET model, a quarter-inch thick rectangular sheet of Boltaran 6100 was used. This plastic sheet was vacuum-formed to the desired spherical shape using the apparatus shown in Figure 3.8. This apparatus utilized an overhead heating device to soften the material, which was then lowered over a spherical mold and a vacuum applied to draw the plastic downward into the mold (see Figure 3.9). The resulting continuous plastic shell was scribed and the desired grid pattern cut out using an electric jigsaw as shown in Figure 3.10. The edge ring area was then trimmed to permit clamping into the test pressure vessel described in part 3.3.1. Thickness measurements were taken of each member at this time for use in theoretical calculations.

The completed PRET model is shown in Figure 3.11. Fabrication in this manner was significantly easier and faster than the meticulous procedures required for the brass models.

The spherical gage points for PRET were mounted using a quick-dry hobby cement. A total of 233 locations were instrumented.

### 3.3 TESTING APPARATUS AND TEST SETUP

3.3.1 Pressure Vessel. Following the fabrication of each

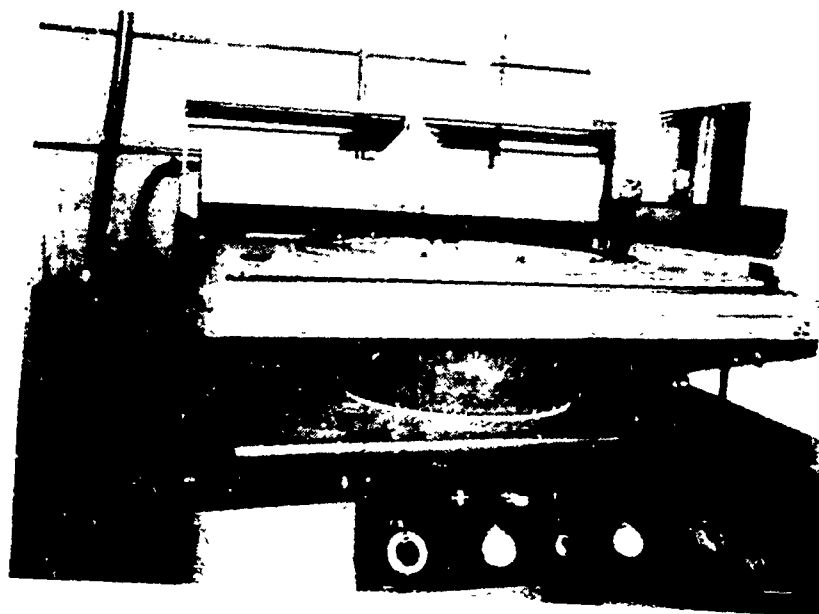


Figure 3.8 Vacuum-Forming Device

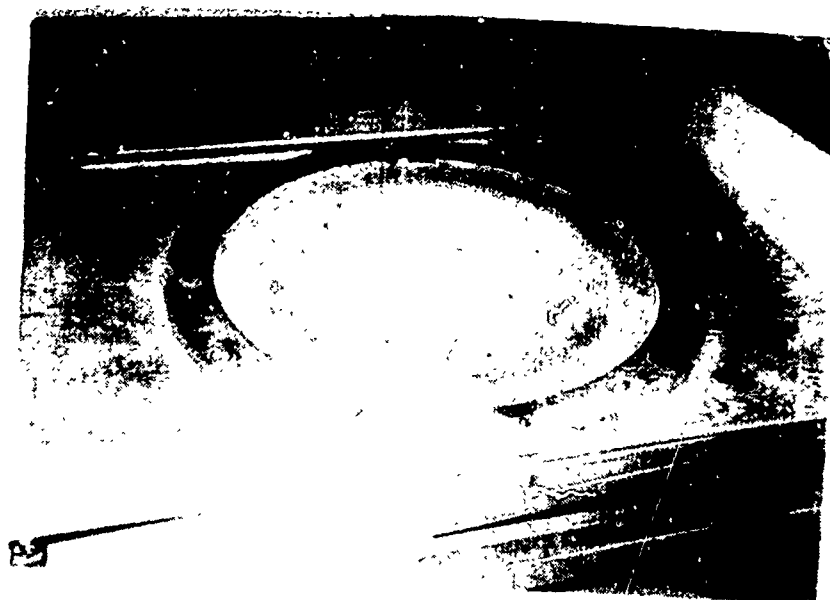


Figure 3.9 Molded PRET Model



Figure 3.10 Cutting the PRET Model



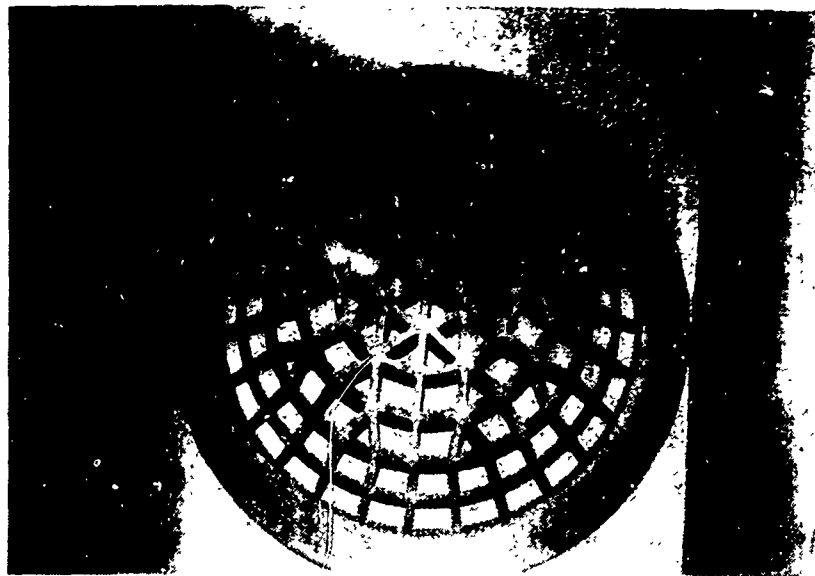
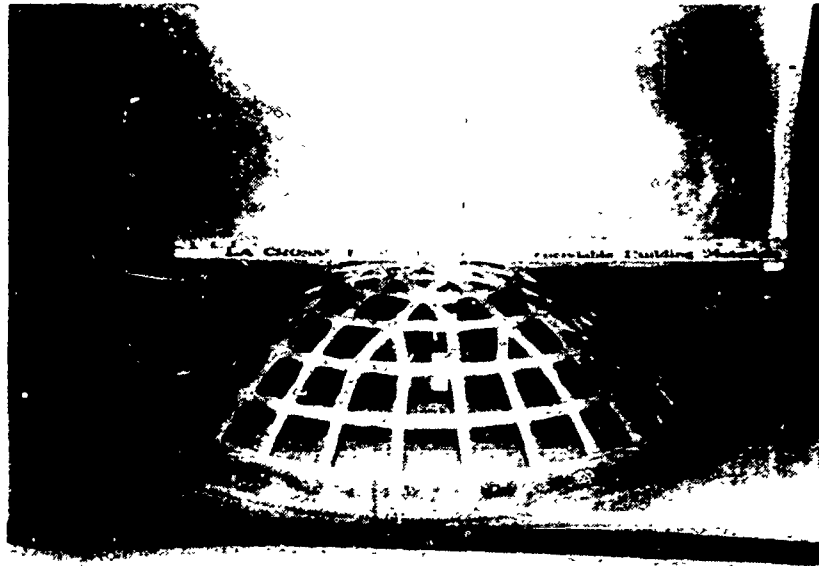


Figure 3.11 Completed PRET Test Model

model it was tested by application of incremental static loads. The loading device utilized is shown in Figure 3.12 and was simply a pressure vessel capable of applying hydrostatic water pressure loads to a test model mounted on its upper edge ring support. The water pressure source was the local water supply system.

In order to apply a pressure to a reticulated test model, it was necessary to seal the surface of the structure. This was done by forming a plastic membrane to the desired spherical shape as illustrated in Figure 3.13. The membrane-stretching device shown in the figure was developed as part of a test program on epoxy-resin shell construction at the University of Missouri Shell Structures Laboratory. For this study a double thickness of four-millimeter clear plastic membrane was placed across the supporting table and a steel ring with an appropriate seal was clamped atop the membrane. Air pressure was applied beneath the double membrane and an alternating procedure of pressurization and self-relaxation of the membrane was continued until the membrane held its desired shape without internal pressure. Shaping of the membrane was required to avoid wrinkling and subsequent uneven application of the pressure vessel load.

After shaping the membrane, it was inverted and placed in the pressure vessel with a silicone rubber seal beneath its outer edge. As observed in Figure 3.14 an inverted test model was then placed in the test apparatus and an edge ring support for the model was bolted to the upper surface of the pressure vessel. The pressure vessel bowl was then filled with water, and the trapped air beneath

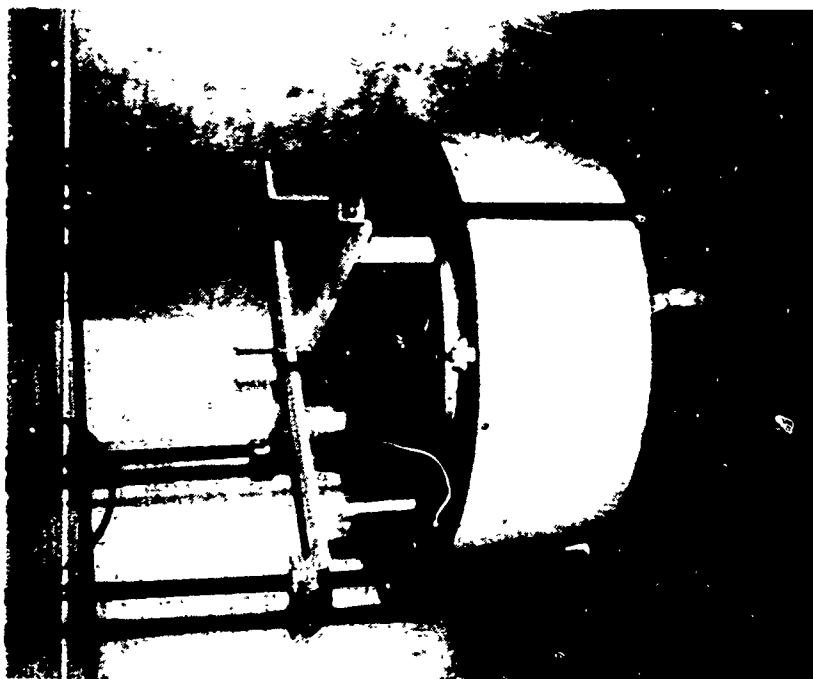


Figure 3.13 Membrane-Stretching Device



Figure 3.12 Test Pressure Vessel



Figure 3.14 Mounting a Test Model

the membrane was vented through the rubber seal.

A double valve assembly controlled water flow into the pressure vessel. The upstream valve damped any line surge and the downstream valve stabilized the water pressure at the desired level.

3.3.2 Easterby Apparatus. The objectives of this study required a highly accurate determination of the position and the movement of each experimental gage point on the test models. A test device for this purpose had been developed and utilized by Mr. Stewart Easterby, previously a graduate student at the University of Missouri at Columbia. The original device was modified slightly for the current study and is shown in Figure 3.15. It consisted basically of a tripod support bolted atop the pressure vessel with a sensing radial arm to measure gage point position.

The radial arm assembly appearing in Figure 3.16 was composed of two basic parts. The upper part of the arm was fastened to a spherical pivot at the top of the tripod support. This pivot permitted 360-degree rotation of the arm in a horizontal plane with a near 50-degree arc in a vertical plane. The center portion of the arm consisted of a mounting tube containing a linear differential transformer. This transformer was powered by direct current, and for brevity will be referred to hereafter as a DCDT (Direct Current Digital Transformer) device.

3.3.3 DCDT Device. The DCDT device was capable of a one-half inch core travel and could sense a movement as small as .0001 inches. At the lower end of the radial arm was a spherical seat fastened to the DCDT core. A spring-loaded trigger was attached thereon to permit



Figure 3.16 Radial Arm Assembly

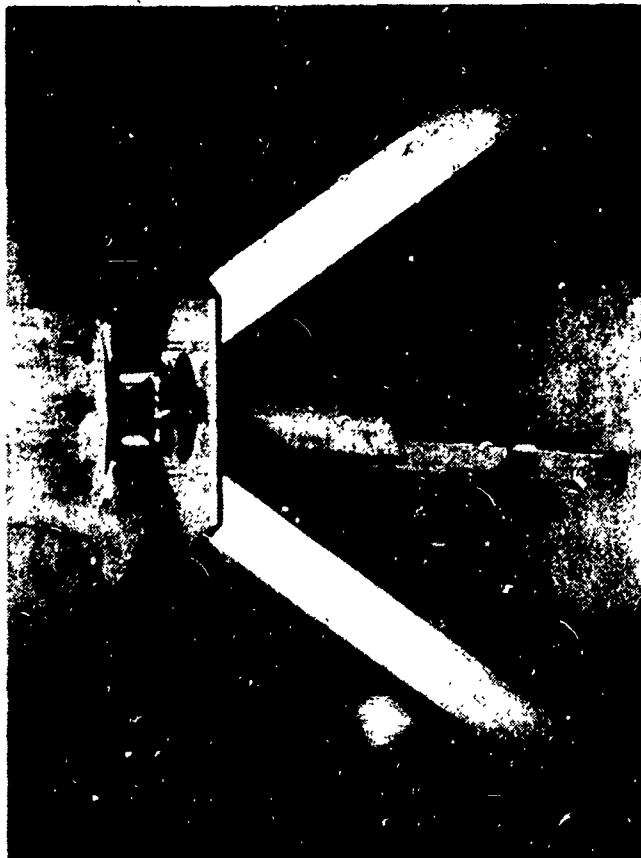


Figure 3.15 The Original Easterby Apparatus

lifting the seating tip while moving the device from one gage point to another. This latter assembly appears in Figure 3.17.

After attaching the radial arm to the tripod support, the assembled Easterby apparatus was bolted to the pressure vessel as shown in Figure 3.18. Independent measurement of potential movement of the top ring of the pressure vessel and the mounting for the radial arm pivot demonstrated that the spherical pivot behaved as a fixed reference point for gage point measurements.

3.3.4 Pressure Measurement. Two independent measurements of the applied pressure were taken during test loadings. These devices appear in Figure 3.19. An approximate pressure read-out was obtained from the standard pressure gage mounted on the side of the pressure vessel. A more accurate reading was taken using a mercury-filled manometer inclined at an angle and calibrated to provide an easily and accurately read meniscus.

It is noted from the pressure vessel setup that a differential pressure existed between the top and the bottom of the shell test specimen, which was due simply to the weight of the water. The reference level on the test specimen was taken at its mid-height, and the pressure readings were corrected accordingly. Due to the volume of water displaced by the test model itself, an equivalent initial radial pressure of .15 psi was deemed acting on the model. This small initial load is included in all pressure readings cited in this study.

#### 3.4 TEST PROCEDURE

The test apparatus was prepared for testing by first filling the pressure vessel completely with water and venting the trapped air.



Figure 3.18 Attaching the Easterby Apparatus



Figure 3.17 Spring-loaded Tip Assembly





Figure 3.19 Pressure-measuring Devices

The plastic loading membrane was then sealed and the shell was thus under its initial equivalent preload of .15 psi, as read from the pressure manometer.

An initial set of radial measurements was then taken. Data was recorded semi-automatically using the test set-up shown in Figure 3.20. The signal from the DCDT device was passed directly to a digital voltmeter. After digitizing, the signal was transferred to a modified key punch and recorded on cards. An interface device on the key punch permitted the voltmeter signal to be recorded directly by the key punch by simply pressing a recording button. Data on a typical card included the test model designation, pressure level, gage point number, and three samplings of DCDT data from each gage point. The DCDT device was re-seated on the gage point for each sampling. A reference rigidly attached to the pressure vessel was also sampled to permit later correction of the data for drift of the electronic apparatus. This point was called the GLO point (gage length zero) and was sampled intermittently from nine to fifteen times at each pressure level for each model. Total elapsed time to take all gage and reference point readings at one pressure level ranged from 45 to 75 minutes.

Upon completion of the initial data recordings, the pressure level was incremented. A 15 to 30 minute pause was made to allow the loading membrane to stretch to its new position and to permit the pressure to stabilize at the desired level. In the PRET model tests, the new pressure level was maintained slightly longer to allow creep activity to diminish.



Figure 3.20 Data Recording Devices

Another set of radial measurements was then taken. This cyclic procedure of loading and data recording was continued until buckling of the test model occurred. The deformed position of the buckled model was then photographed and the test was complete.

### 3.5 DATA REDUCTION

Due to the spherical nature of the experimental data obtained during the test procedure just described, several unique problems arose upon attempting to reduce the data to a meaningful form. First, although the test models were nominally spherical in shape, the fabrication procedures produced an imperfect surface. In order to describe this surface a method was required to define a theoretical spherical shape having a determinable radius and center location which best represented the experimental data. Deviations on the test model surface from this perfect spherical shape were called initial imperfections. In addition to the problem of defining this sphere initially, its radius  $r_0$ , the location of its center  $(X_0, Y_0, Z_0)$ , and the initial imperfections all changed as subsequent loadings were applied.

To resolve these difficulties a method of data reduction was chosen which consisted of performing a least-squares fit of a spherical surface to all data points on a test model at a given pressure. The three coordinates  $(X_0, Y_0, Z_0)$  of the center of this theoretical "best-fit" sphere were then used as a reference point to compute the radius  $r_i'$  to each gage point, where the subscript refers to gage point  $i$ . Initial imperfections  $d_i$  were computed by subtracting the radius  $r_0$  of the perfect sphere from the radius  $r_i'$  to each gage

$$d_i = r_i' - r_o \quad 3.1$$

Deflections due to an increment in the external pressure load on the test model were determined from the following expression:

$$w_i = (r_i')_2 - (r_i')_1 + [(Z_o)_2 - (Z_o)_1] \cos \phi_i \quad 3.2$$

where the numbered subscripts represent successive pressure levels. The quantity in brackets in Equation 3.2 represents a correction to account for the vertical movement of the respective best-fit sphere centers. This was necessary since it was known that the spherical pivot on the Easterby apparatus did not move vertically relative to the test model edge ring. No corrections were necessary for horizontal changes  $\Delta X_o$  and  $\Delta Y_o$  since they represented rigid body translations of the test model.

A computer program to perform the data reduction operations just described was developed and is described in Appendix C. An initial step in the program was to adjust the experimentally measured radii values  $R_i$  for any error caused by drift in the electronic apparatus. This was accomplished by adding any change in the GLO reading to all radii values measured after each GLO point sampling. Additionally, the smallest of the three readings at each gage point was discarded since the farthest projection of the tip of the DCDT device indicated the best seating of the device on a gage point. The remaining two readings were averaged and a warning was given if the

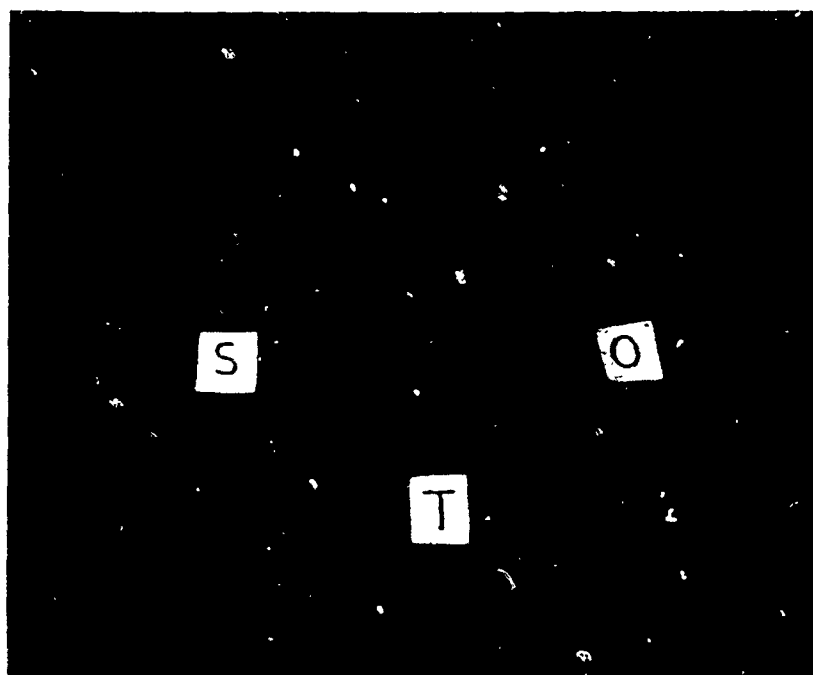
readings deviated more than  $\pm .0001$  inches from their average. This check prevented using an erroneously large data value from being inadvertently included in the data base. The computer program then performed a least-squares fit of a spherical surface to the adjusted radii,  $R_i$ . With the radius and the center of this best-fit sphere thus determined, all the required quantities were available to compute the initial imperfections  $d_i$  and the deflections  $w_i$  due to external pressure load, according to Equations 3.1 and 3.2.

### 3.6 MATERIALS TESTING

3.6.1 Brass. Three types of tensile specimens were prepared from the stock material of the brass shell models. A type S specimen was simply an eight-inch length of the H-section. Type T specimens were representative of the B2 (two-inch grid) model and had intersecting members soldered at a two-inch spacing along its length. The type O specimens were designed to represent the one-inch grid model and had the intersecting members soldered at one-inch intervals throughout. All three specimen types are shown in Figure 3.21.

All brass specimens were tested at a strain rate of approximately forty-five micro-inches per inch per second as compared to the near-static loading rate during the shell model tests. An extensometer having a two-inch gage length was used for the test, which conformed geometrically to the one- and two-inch grids of the test models.

Values of Young's modulus and the yield stress (defined at 0.2% offset) of each specimen type were determined from standard tensile tests. Since the stress-strain curve for brass was somewhat



Reproduced from  
best available copy.

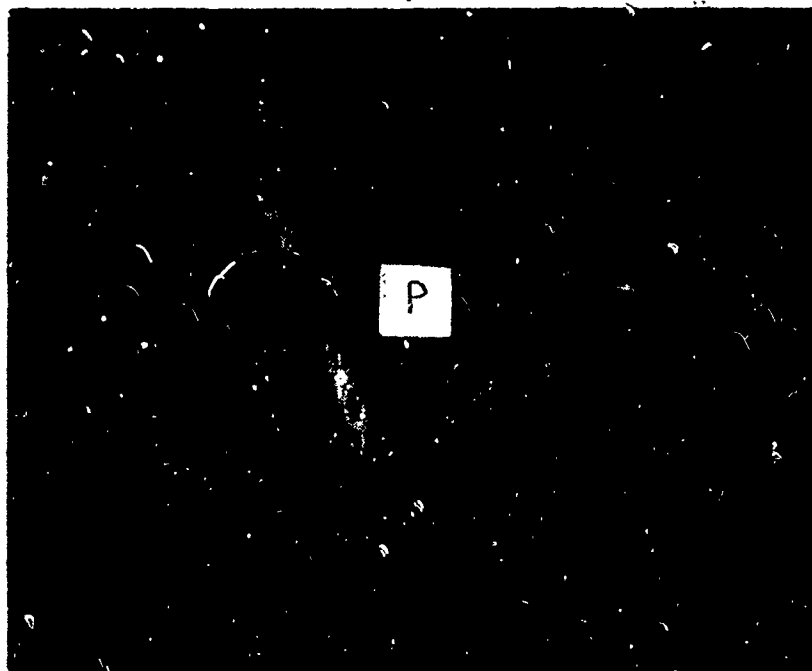


Figure 3.21 Tensile Test Specimens

nonlinear, a chord modulus was determined between 9 ksi and 54 ksi for the S-type specimens. ASTM Standard No. E8 was followed in the performance of these tests. In accordance with these specifications, a least-squares linear fit was performed in order to establish the elastic modulus of the brass.

3.6.2 Plastic. Tensile specimens (designated P-type specimens) conforming to ASTM D638-61T, "Tentative Method of Test for Tensile Properties of Plastics," were fabricated and constructed in order to determine the Modulus of Elasticity of the plastic material. Tensile specimens of this type are shown in Figure 3.21 also. The loading rate for the specimens was approximately eighty-five micro-inches per inch per second.

The tendency of the plastic material to exhibit creep was recognized at the outset of this study. To approximate the creep effects, a tension test at a constant stress of 500 psi was conducted over a four-hour time period. The results of all tension tests for both the brass and plastic specimens can be found in part 4.1.1 of this paper. Typical stress-strain curves are also presented.



## CHAPTER IV

### RESULTS AND COMPARISONS

#### 4.1 EXPERIMENTAL RESULTS

This chapter presents the results of all theoretical and experimental investigations of the three reticulated shell models. First a summary of the brass and plastic material tensile tests is given. Deflection contour plots are then presented which demonstrate the deflection patterns and magnitudes resulting from static pressure increments applied to the models. Initial imperfections in the geometries of the as-built models are also shown. A corresponding group of deflection contour plots reflect the NASTRAN code theoretical predictions for each of the models so analyzed. Comparisons and a discussion of these deflection results are given. Deflections along selected reference lines are plotted to illustrate differences in the predicted and experimental results. The application of general buckling theories to the experimentally observed buckling loads is described in a final section.

4.1.1 Materials Testing. The results of the material tests described in Chapter 3 are presented in Figures 4.1 through 4.4. Figure 4.1 represents the typical stress vs strain response of a brass H-section with no soldered joints (referred to here as an S-type specimen). Figure 4.2 shows the tensile test results for a brass H-section having soldered joints at two-inch intervals along its length (designated as a T-type specimen). The stress-strain curve for a brass

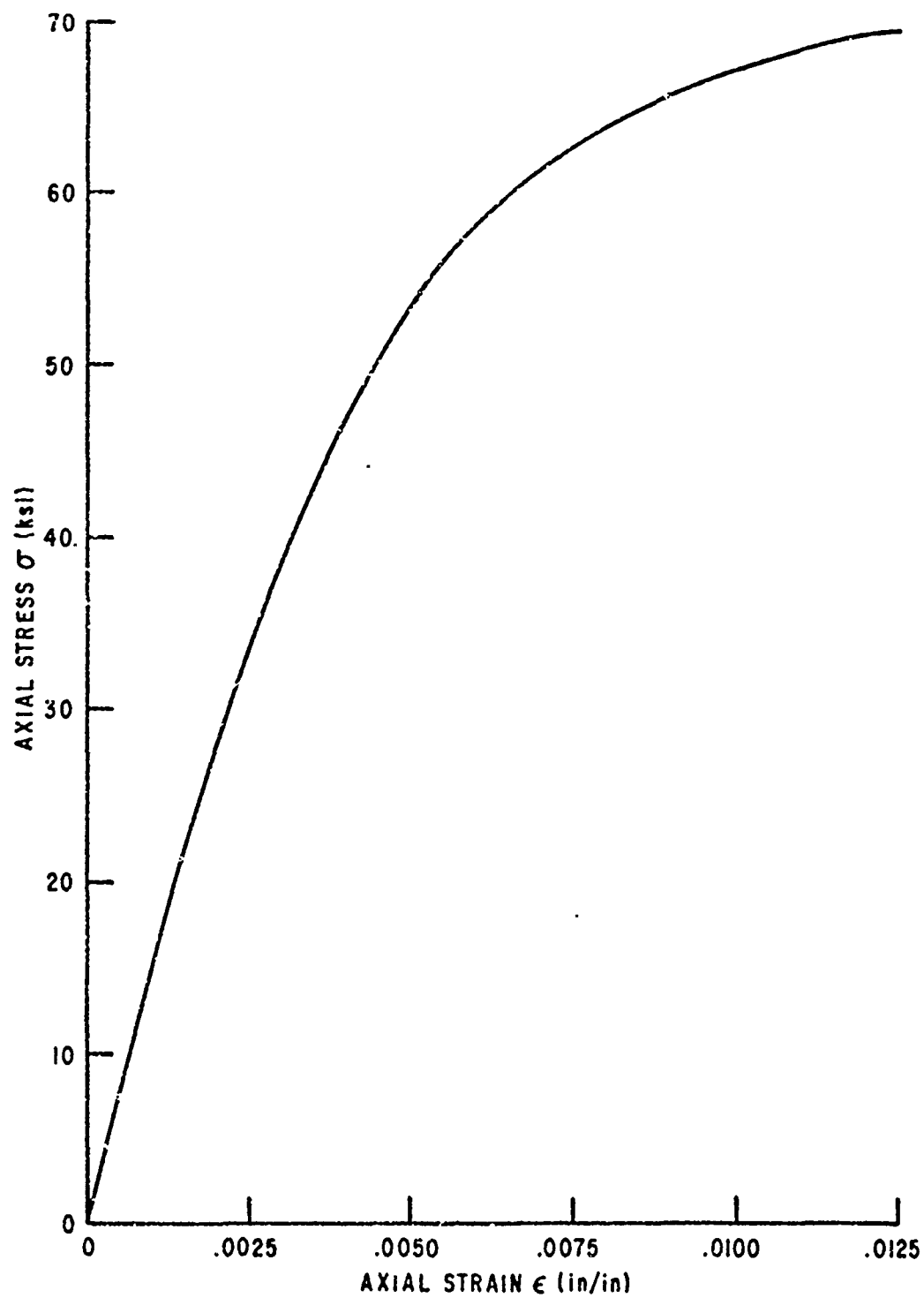


Figure 4.1 Stress vs Strain for S-Type Brass Specimen

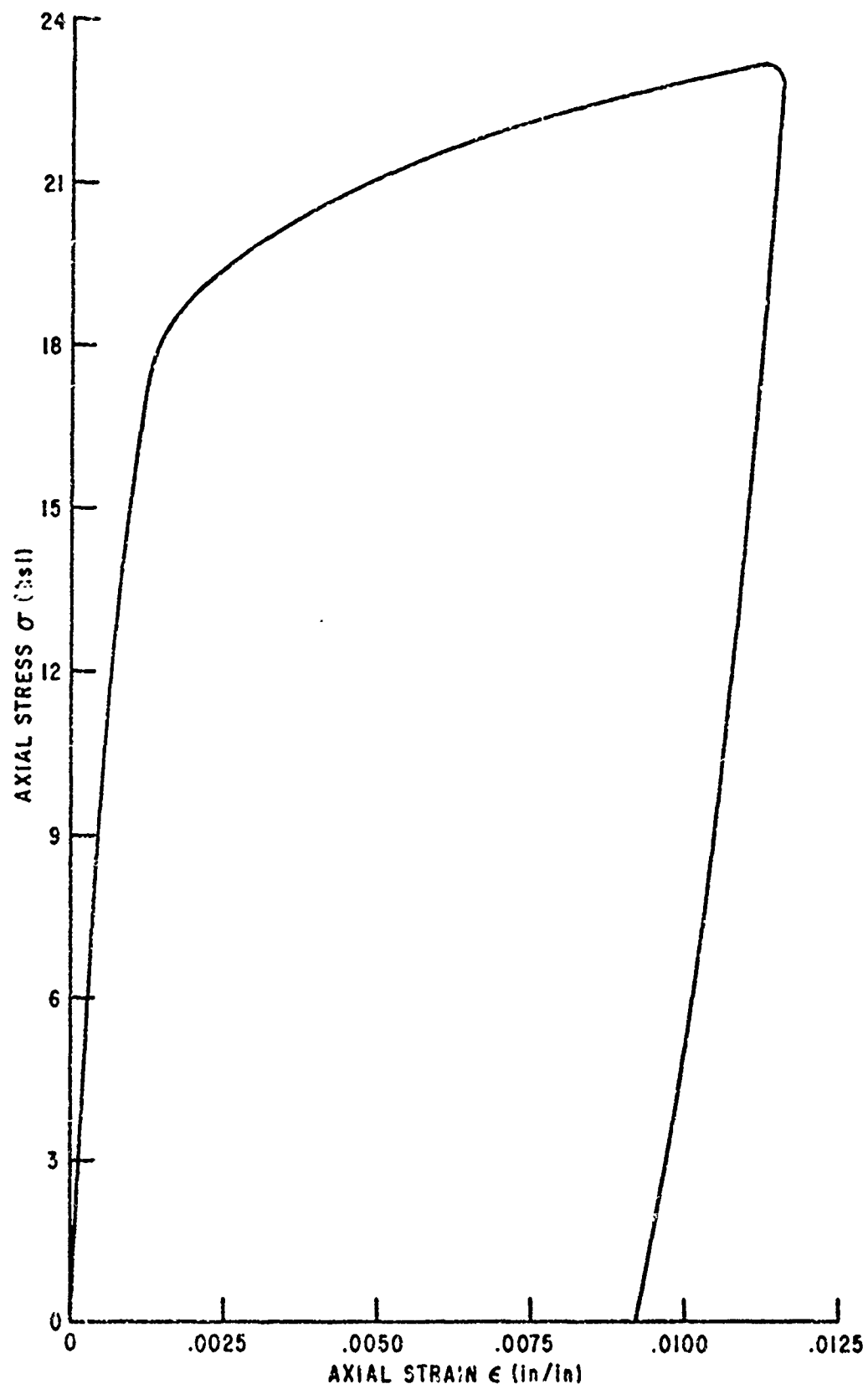


Figure 4.2 Stress vs Strain for T-Type Brass Specimen

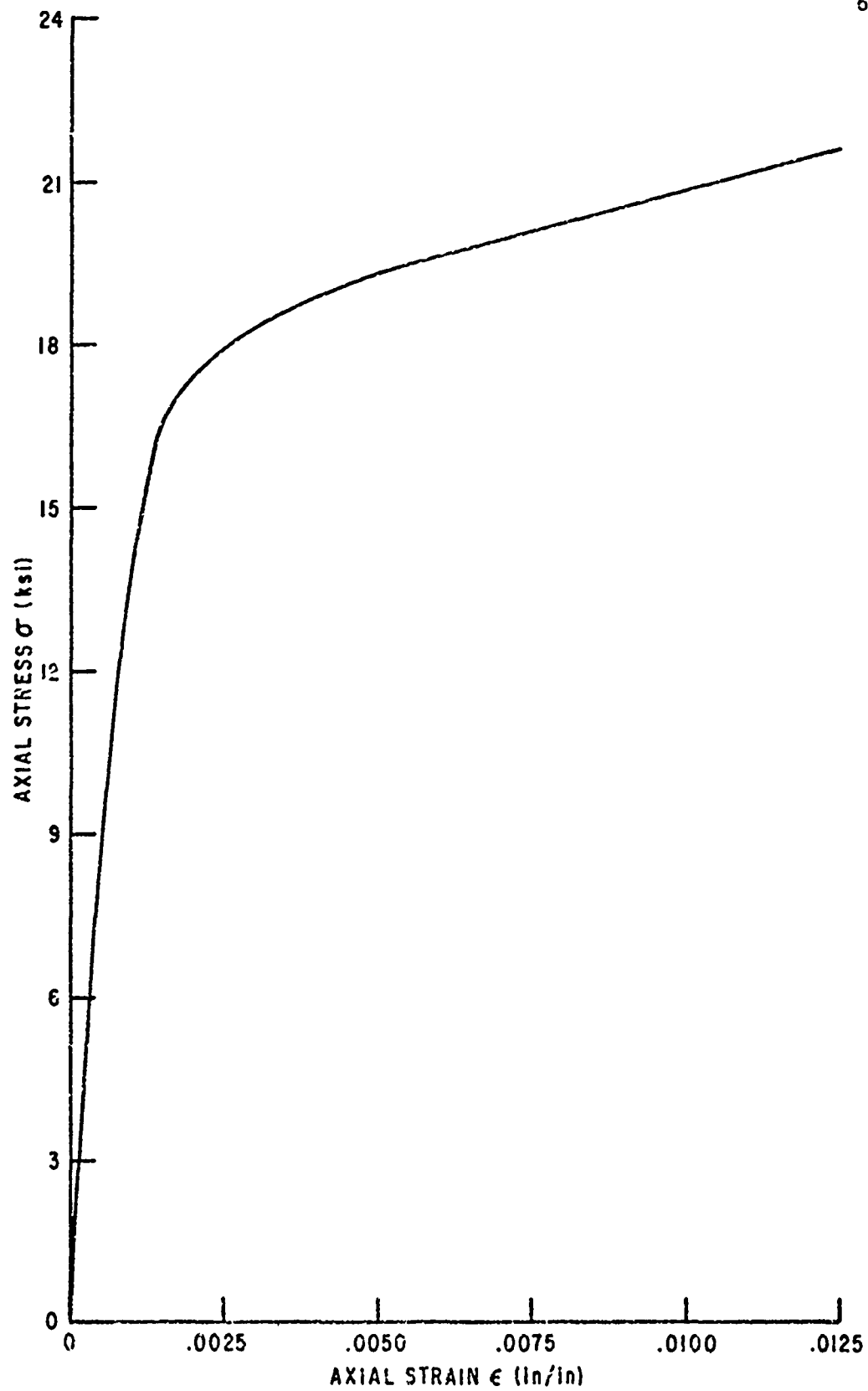


Figure 4.3 Stress vs Strain for O-Type Brass Specimen

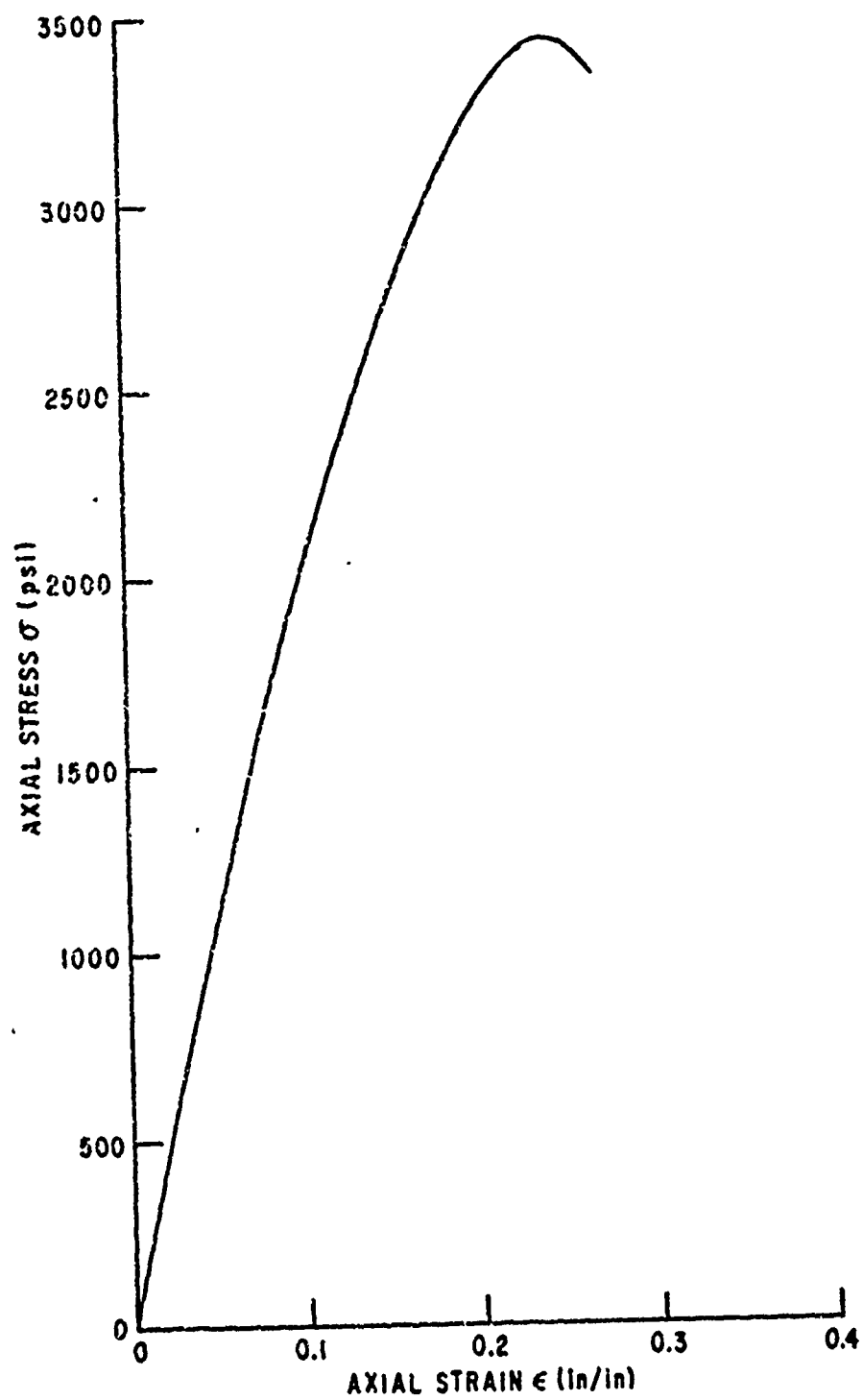


Figure 4.4 Stress vs Strain for Plastic Material

H-section with soldered joints at one-inch spacings (called an O-type specimen) appears in Figure 4.3.

In determining the tensile modulus of elasticity it was observed that the initial modulus value varied little among the three brass specimen geometries. The tensile modulus as determined from these tests was taken as  $10 \times 10^6$  psi. However, a significant reduction in the yield stress (defined at 0.2% offset) resulted from the soldering procedure. The yield stress was reduced from approximately 65 to 70 ksi for the S-type specimens to about 17 to 19 ksi for the T- and O-type specimens.

Stress vs strain response curves for the quarter-inch thick plastic tensile specimens (P-type specimens) appear in Figure 4.4. The tensile modulus thus determined was 187 ksi. This differed slightly from the manufacturer's recommended value of 200 ksi in tension and 240 ksi in flexure for the Boltaron 6100 material. The difference was possibly due to heat effects induced by the vacuum forming technique during manufacture of the plastic model. The tensile test specimens were taken from a previously heated sheet of the plastic material.

The single tension test performed to obtain a rough approximation of the effect of creep on the plastic shell produced the results in Figure 4.5. This figure shows the specimen strain in inches per inch versus the time in minutes. This was a constant stress test at a stress level of 500 psi. A maximum strain of approximately .0003 occurred near an elapsed time of three hours.

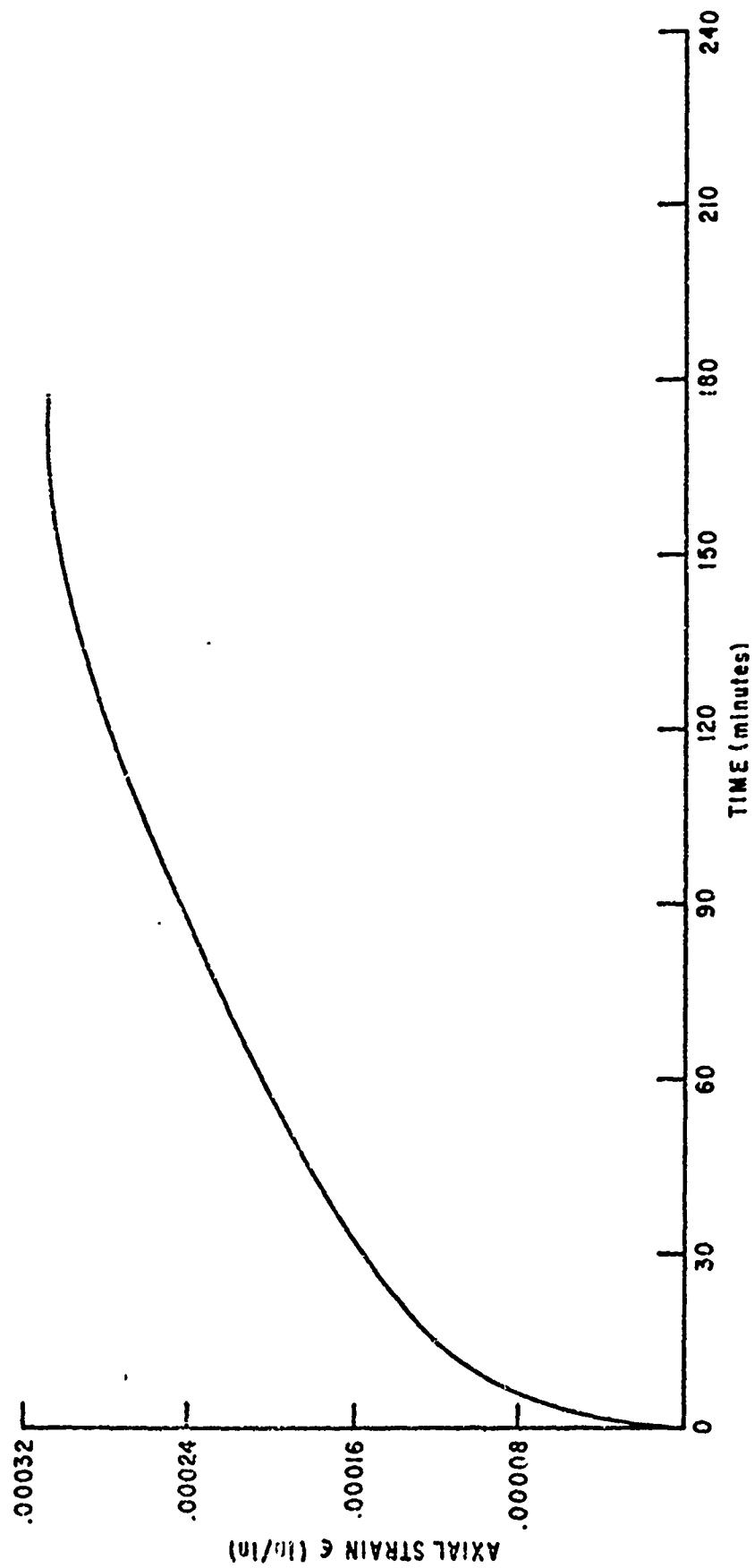


Figure 4.5 Creep Test on Plastic Material

A summary of the preceding results and of the test model geometries is given in Table 4.1.

TABLE 4.1  
MODEL SUMMARY

Model	B2	B1	PRET
Grid Spacing	2-inch	1-inch	2-inch
Material	Brass	Brass	Plastic
Cross-Section	H	H	Rectangular
Young's Modulus	$10 \times 10^6$ psi	$10 \times 10^6$ psi	187,000 psi
Yield Stress	17-19 ksi	17-19 ksi	3000 psi

4.1.2 B2 Model Deflections. Contour plots of initial imperfection data and of deflections resulting from the static incremental pressure loads applied to the B2 model are presented in subsequent figures. A schematic of the B2 member grid is given in Figure 4.6. This plot shows the grid as if viewed from the center of the spherical shell. Thus a point in the plane of the figure was located by the horizontal distance  $R_i \cdot \phi_i \cos \theta_i$ , and by the vertical distance  $R_i \cdot \phi_i \cdot \sin \theta_i$ . Also shown in the figure is the location of the final buckle. A reference line was drawn from the edge ring to the crown and back to the edge ring, and through the subsequent buckle and other large distortion regions of the model. The reference line deflections and the final buckle are discussed later in part 4.3 in which comparisons of predicted and experimental results are made. The large dots in Figure 4.6 show experimental gage point locations.



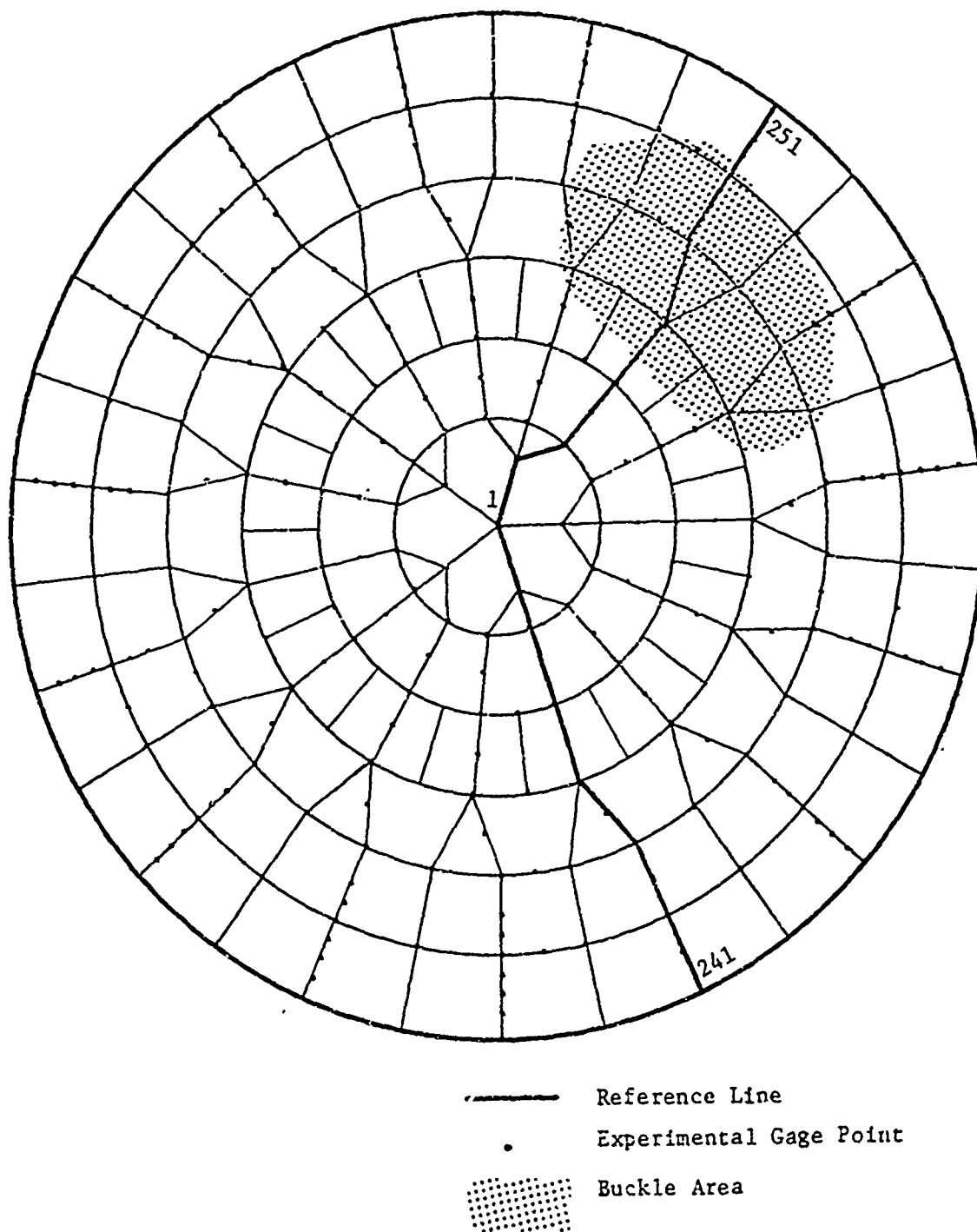


Figure 4.6 B2 Model Experimental Grid

The contour plot of Figure 4.7 represents the initial imperfections resulting from the manufacture of the B2 model. These deflections reflect the deviation of individual joints or member intersection points from a "best-fit" of a perfect spherical surface to the experimental data. The contour lines were spaced at intervals of .0200 inches. Negative values of deflections are in a direction toward the center of the shell, and shaded areas indicate regions of positive deflection. Initial imperfection data was taken with the pressure vessel filled. Considering the volume of the shell the equivalent radial pressure applied initially to the models was .15 psi, and all values of pressure loadings cited include this initial pressure.

Figure 4.8a shows the deflection contours resulting from the loading increment from a .15 psi hydrostatic pressure to a pressure of 1.0 psi. The contour interval was .0020 inches. It was observed during the test that the edge ring was not completely seated on the pressure vessel supporting lip at the .15 psi pressure level. This was reflected by the deflection pattern near the edge ring in Figure 4.8a. Consequently a reference pressure of 1.0 psi was selected for the B2 test shell from which to compare deflection patterns.

The next four plots of Figure 4.8 show deflection contour patterns in the B2 shell for 0.5 psi loading increments from 1.0 to 3.0 psi. Plots 4.8f through 4.8h represent contours for the loading ranges 1.0  $\rightarrow$  2.0 psi, 1.0  $\rightarrow$  2.5 psi, and 1.0  $\rightarrow$  3.0 psi, respectively. The contour interval was .0020 inches.

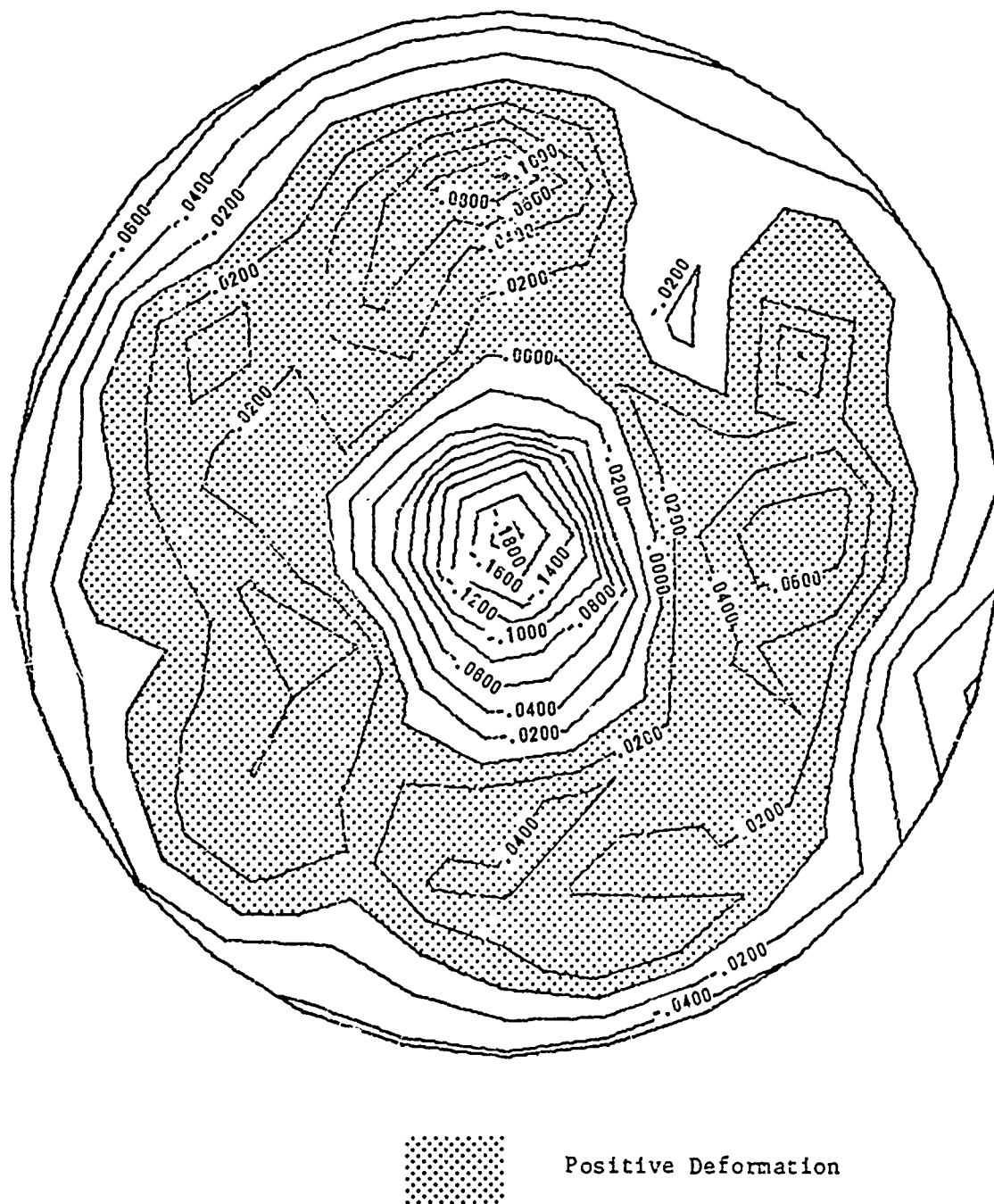


Figure 4.7 B2 Model Initial Imperfections

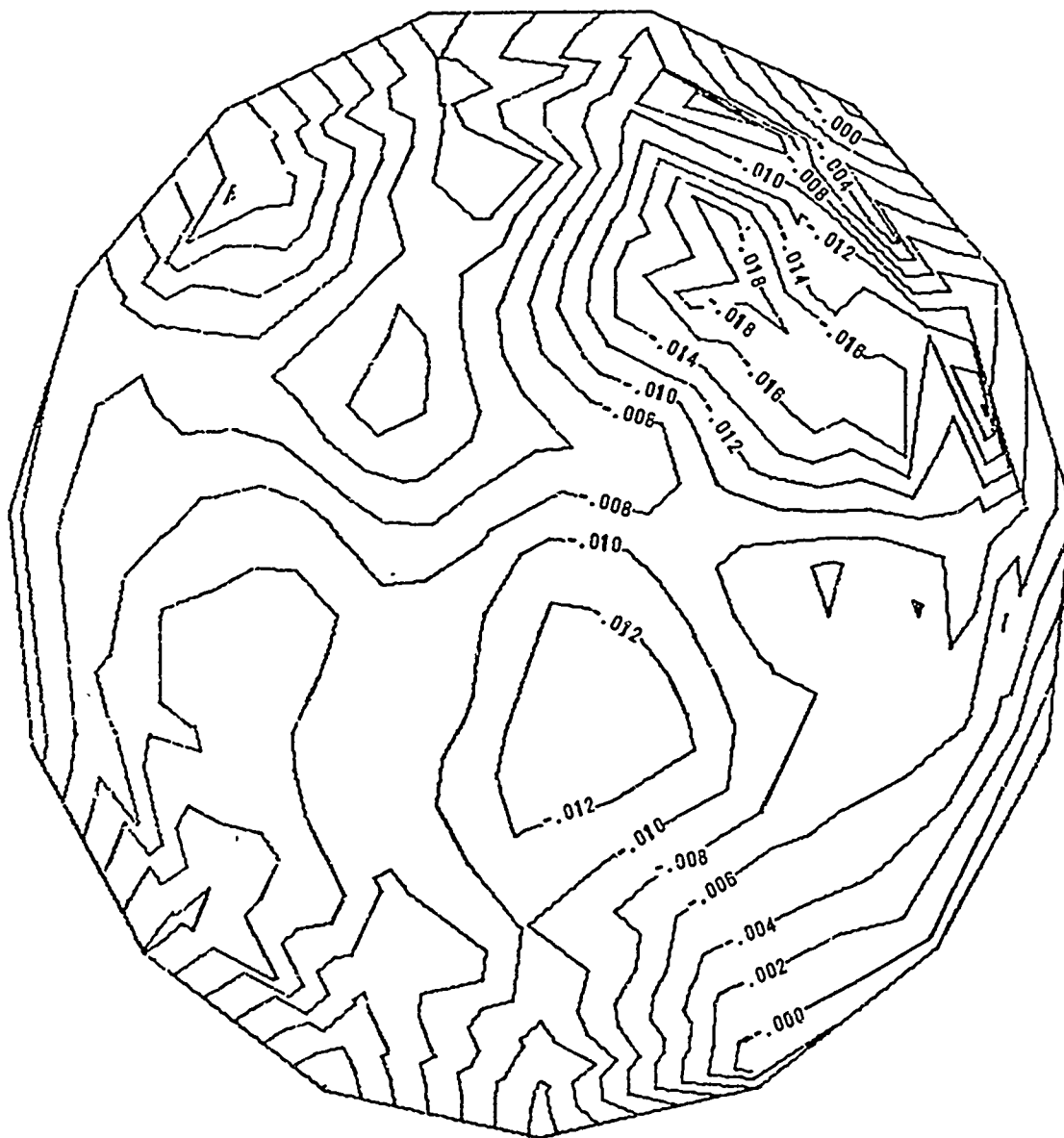


Figure 4.8a B2 Model: .15 to 1.0 psi

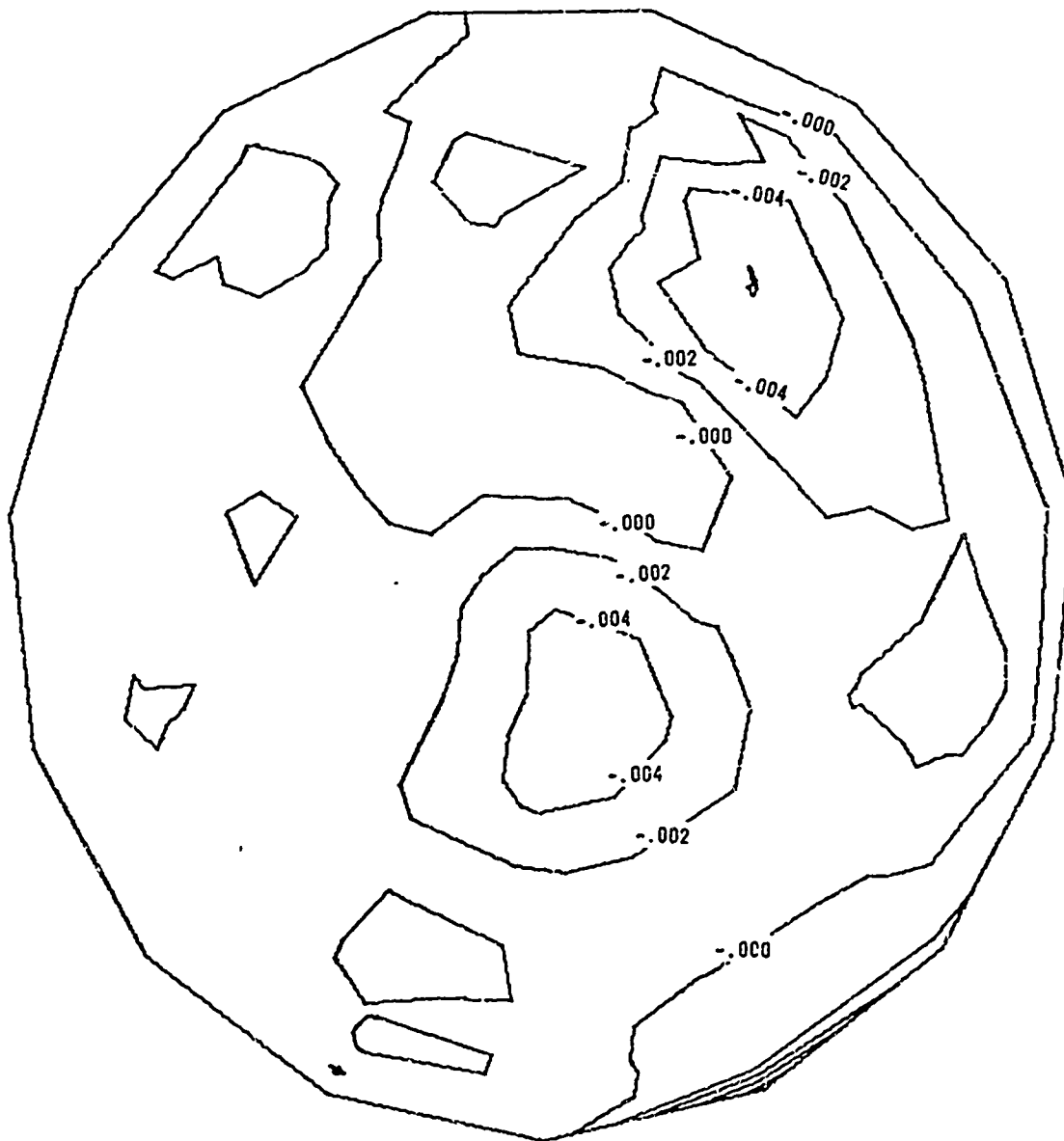


Figure 4.8b B2 Model: 1.0 to 1.5 psi

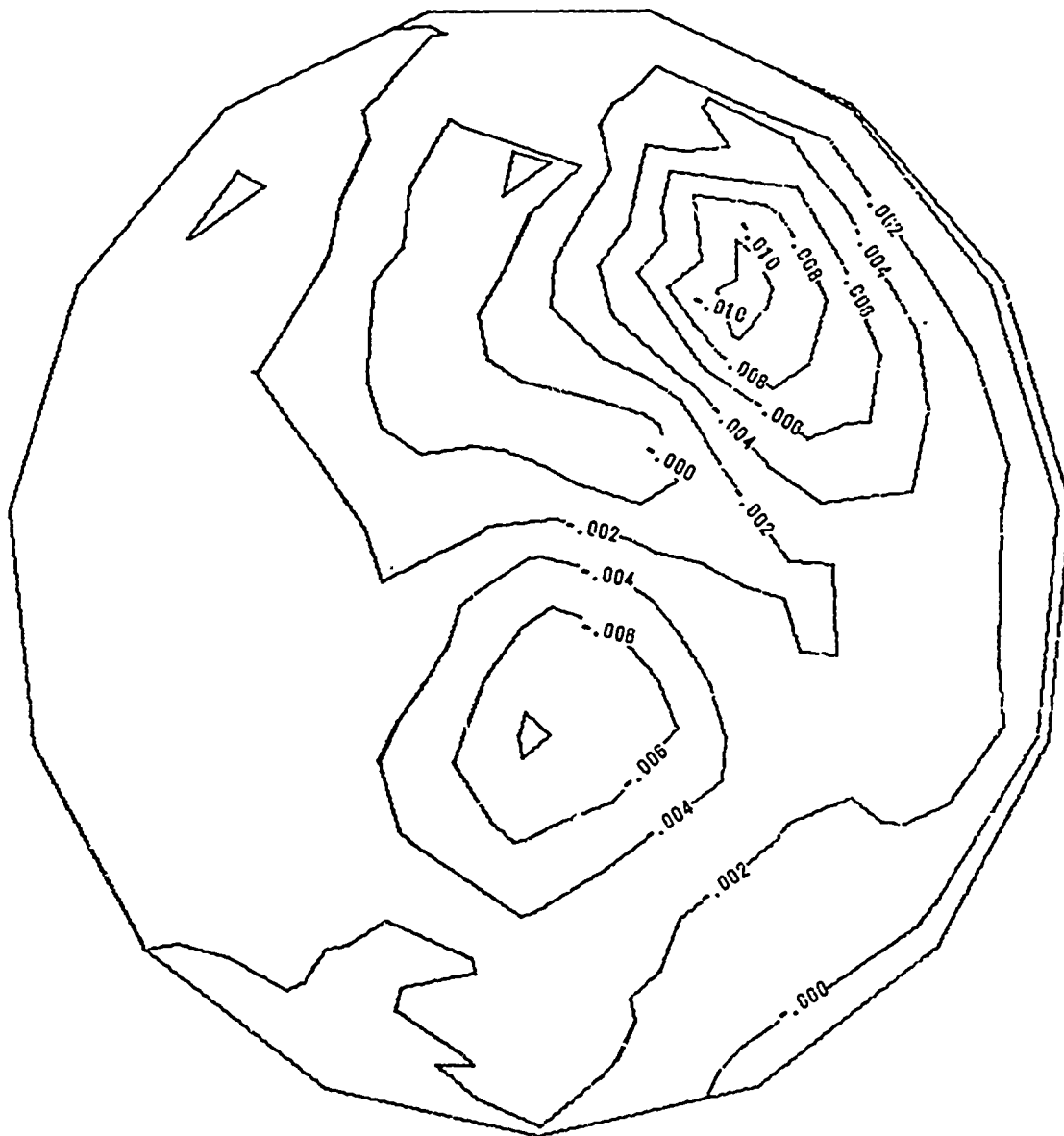


Figure 4.8c B2 Model: 1.5 to 2.0 psi

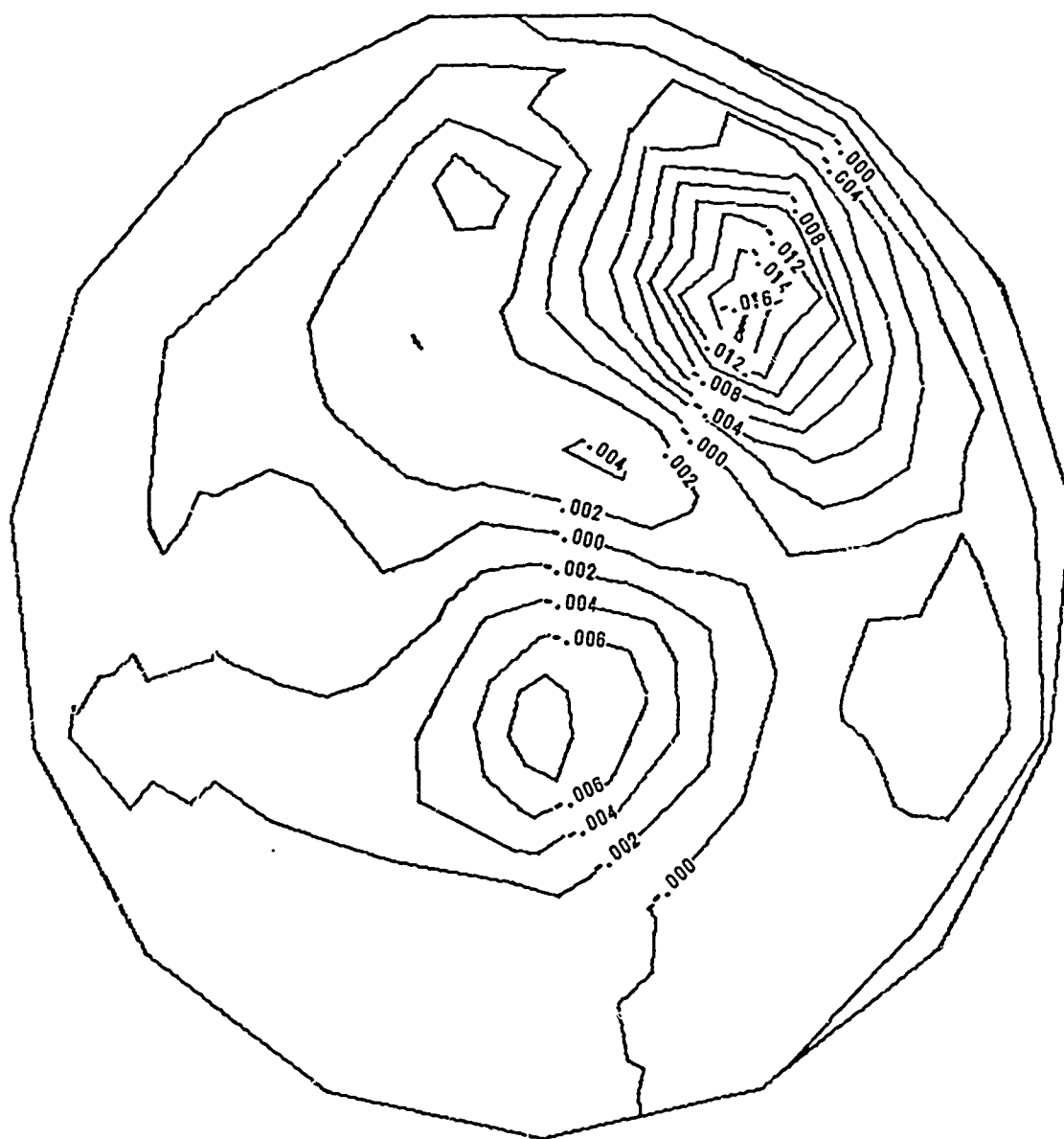


Figure 4.8d B2 Model: 2.0 to 2.5 psi

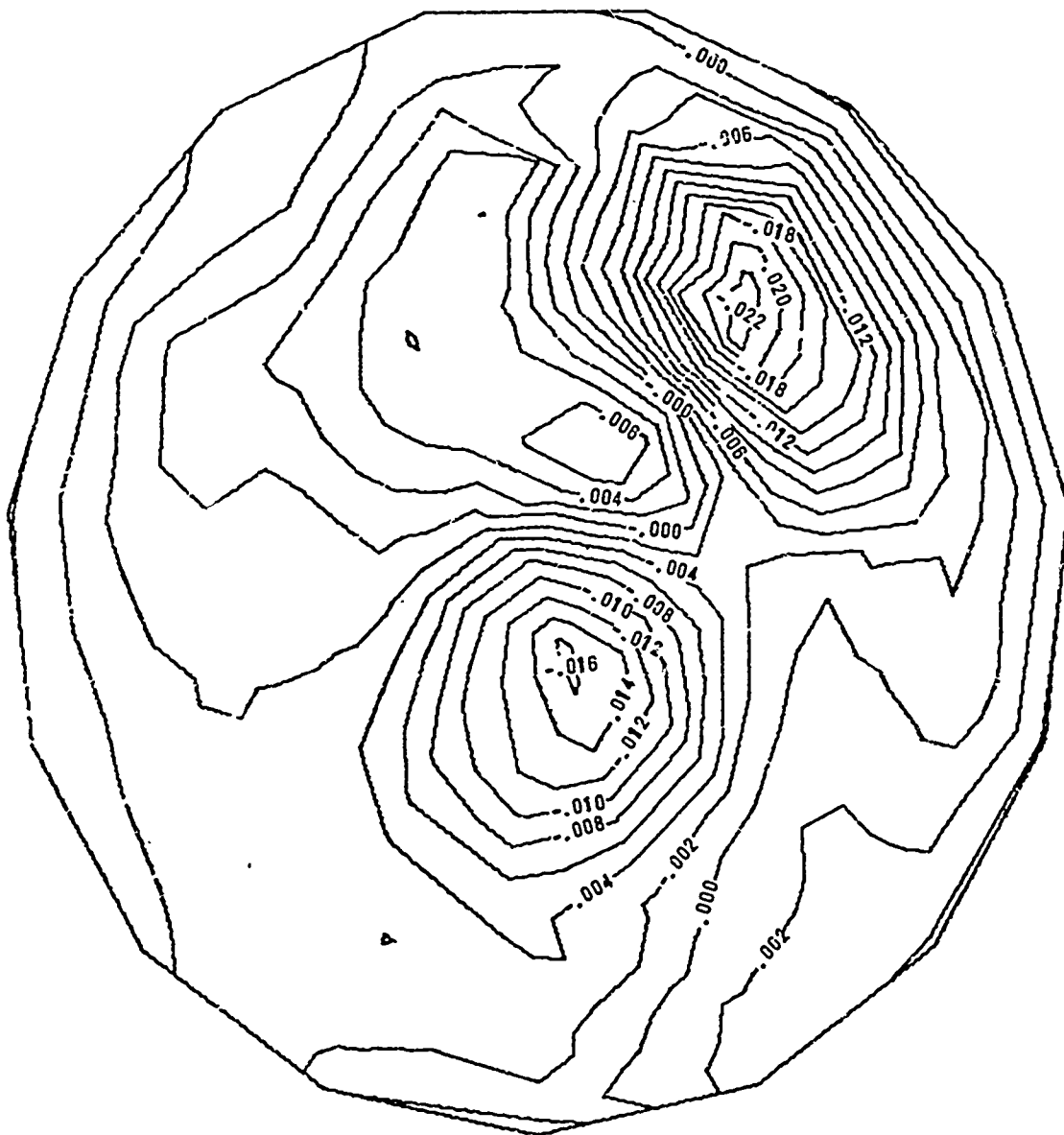


Figure 4.8e B2 Model. 2.5 to 3.0 psi



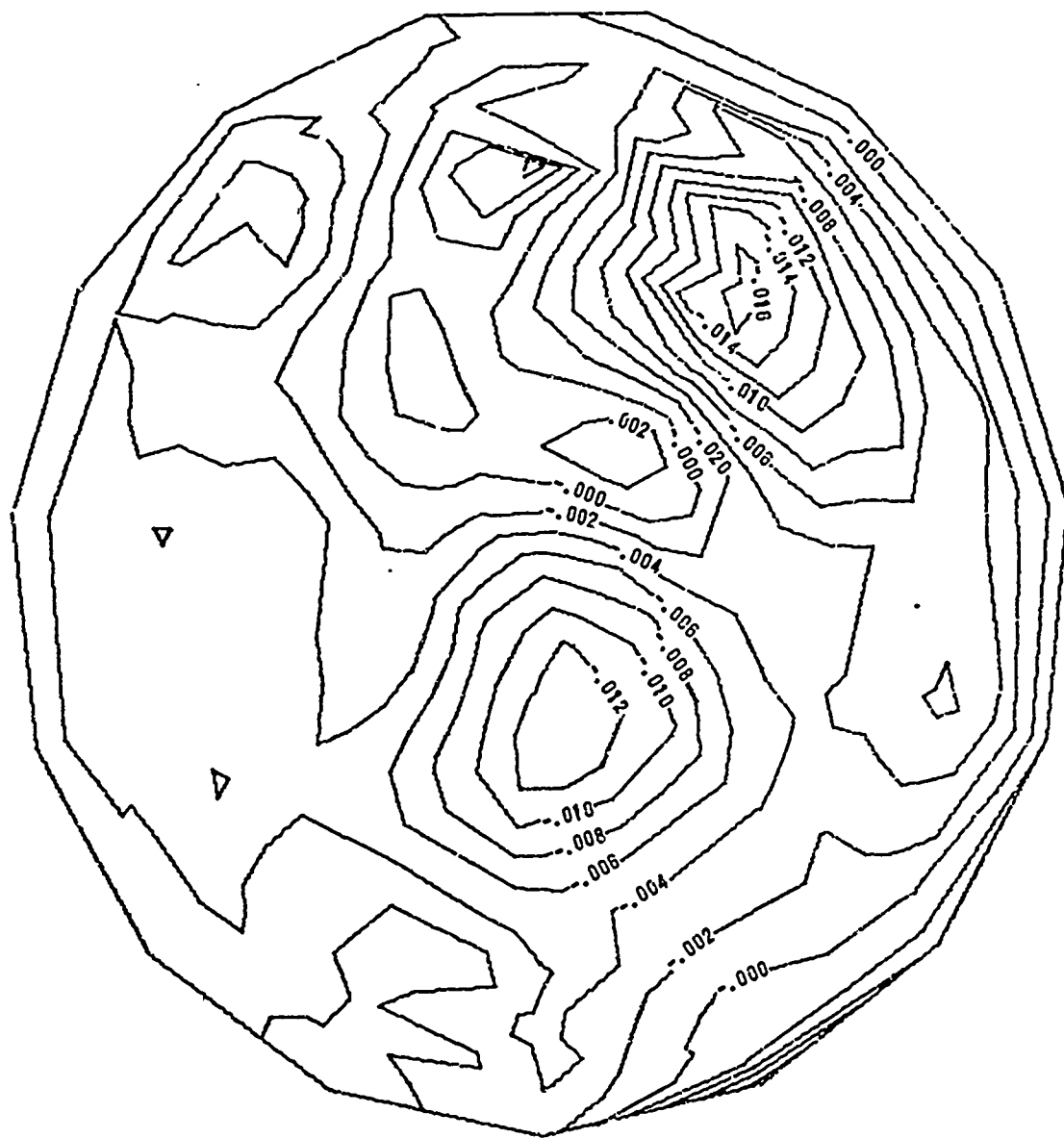


Figure 4.8f B2 Model: 1.0 to 2.0 psi

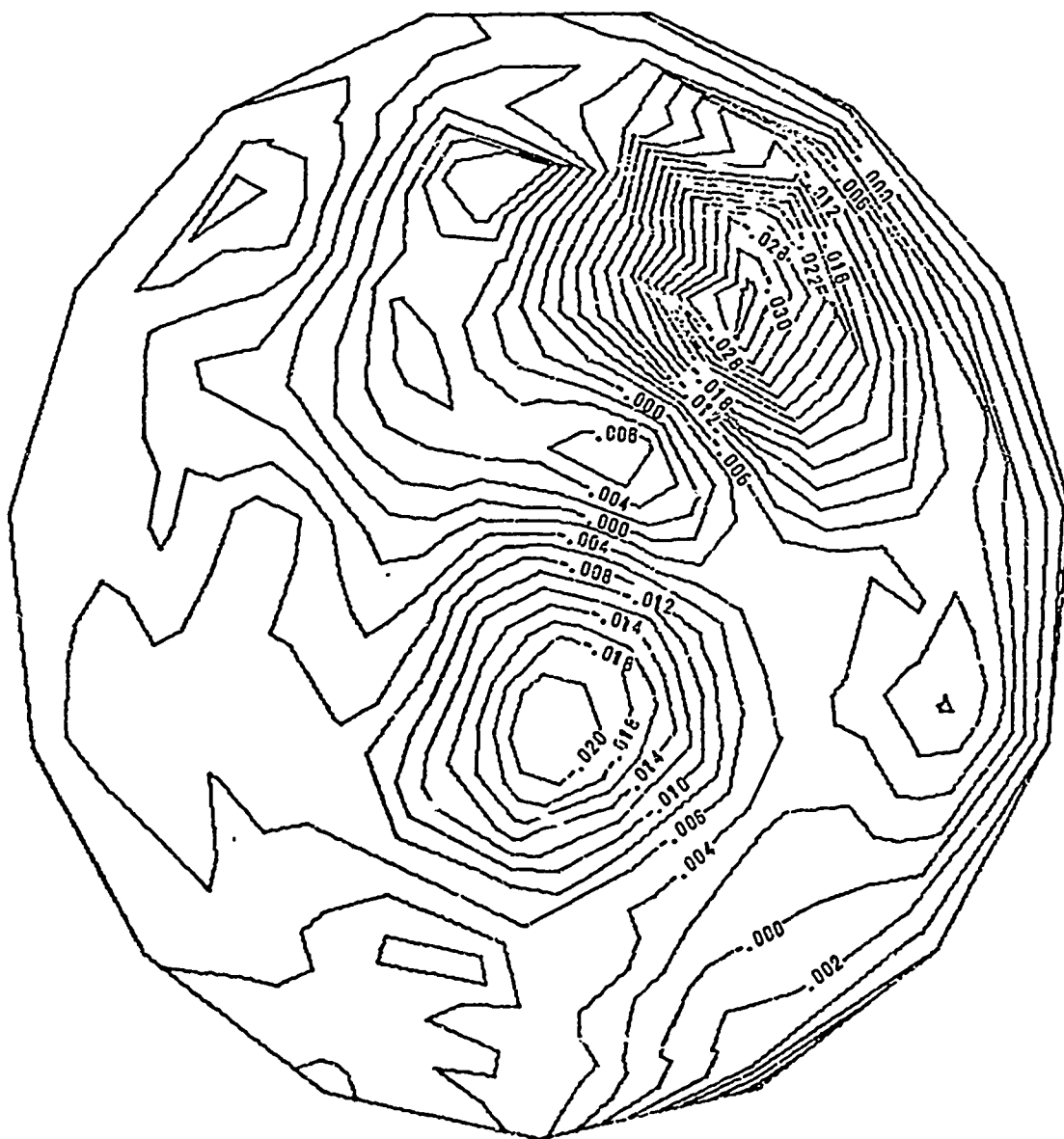


Figure 4.8g B2 Model: 1.0 to 2.5 psi

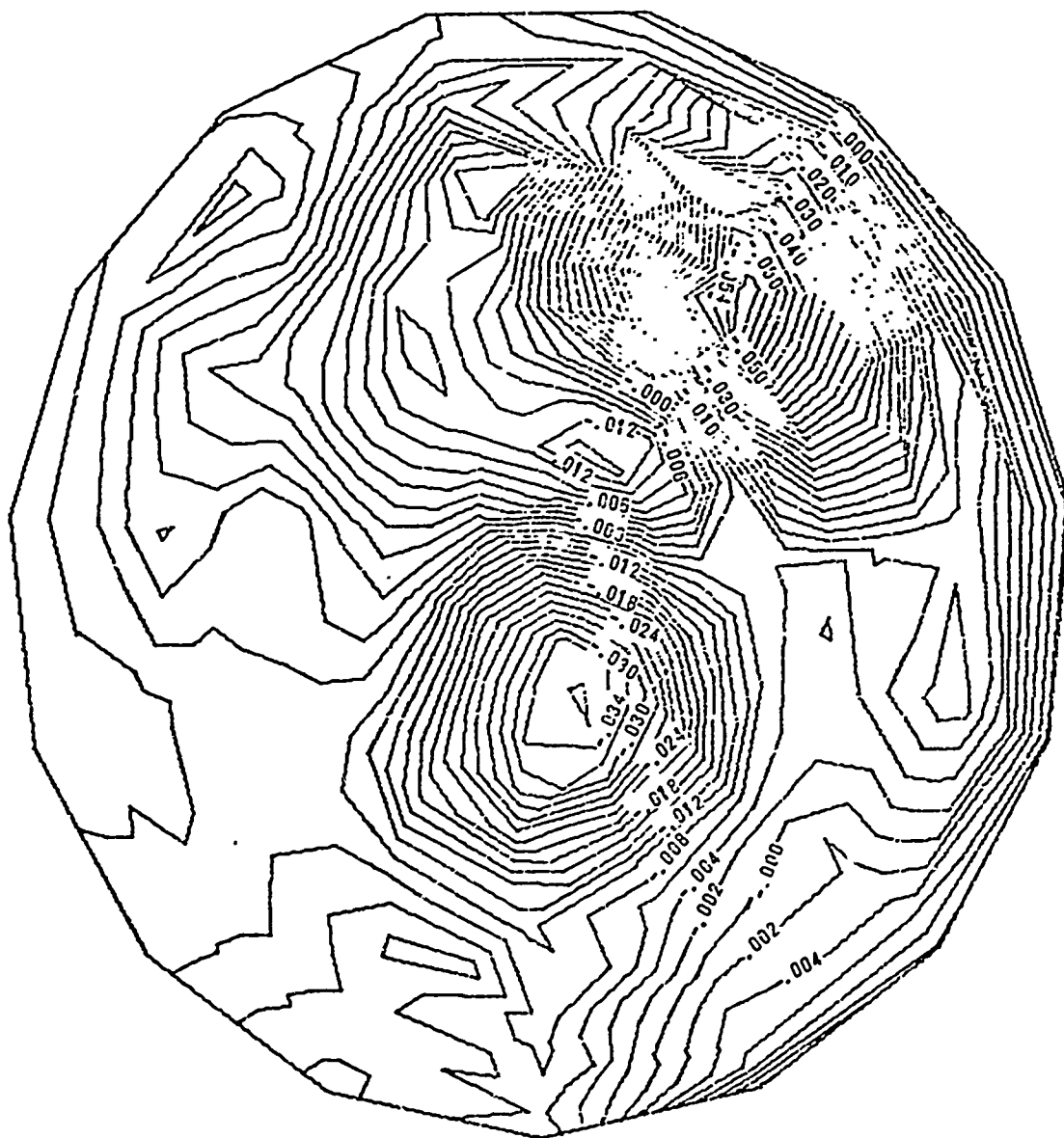


Figure 4.8h E2 Model: 1.0 to 3.0 psi

The combination of initial imperfections and live load deflections at the maximum pressure of 3.0 psi is shown in Figure 4.8i. To observe the change in the total deflection pattern, this figure can be compared with the initial imperfection plot of Figure 4.7.

4.1.3 B1 Model Deflections. Experimental results for the B1 test model are shown in Figures 4.9 through 4.11. The model grid work appears in Figure 4.9, together with the location of the final buckle. Initial imperfections for the B1 model are reflected in Figure 4.10 with a contour interval of .0200 inches.

Figure 4.11a gives results of the pressure increment from .15 psi to 1.0 psi which shows an edge ring seating problem for the B1 model also. The reference pressure for B1 experimental data was therefore chosen at the 1.0 psi level. Figures 4.11b through 4.11f represent contour plots for 1.0 psi loading increments from 1.0 to 6.0 psi pressures. Pressure increments of 1.0 to 3.0 psi, 1.0 to 4.0 psi, 1.0 to 5.0 psi and 1.0 to 6.0 psi produced the results shown respectively in Figures 4.11g through 4.11j. The contour interval for all plots in Figure 4.11 was .0040 inches.

The sum of initial imperfections and the live load deflections under the maximum external pressure load of 6.0 psi is represented by the contour plot in Figure 4.11k. A comparison of this plot with that of Figure 4.10 shows the changes in the total deflection pattern of the B1 model.

4.1.4 PRET Model Deflections. Experimental results for the plastic shell model (PRET) appear in Figures 4.12 through 4.14.

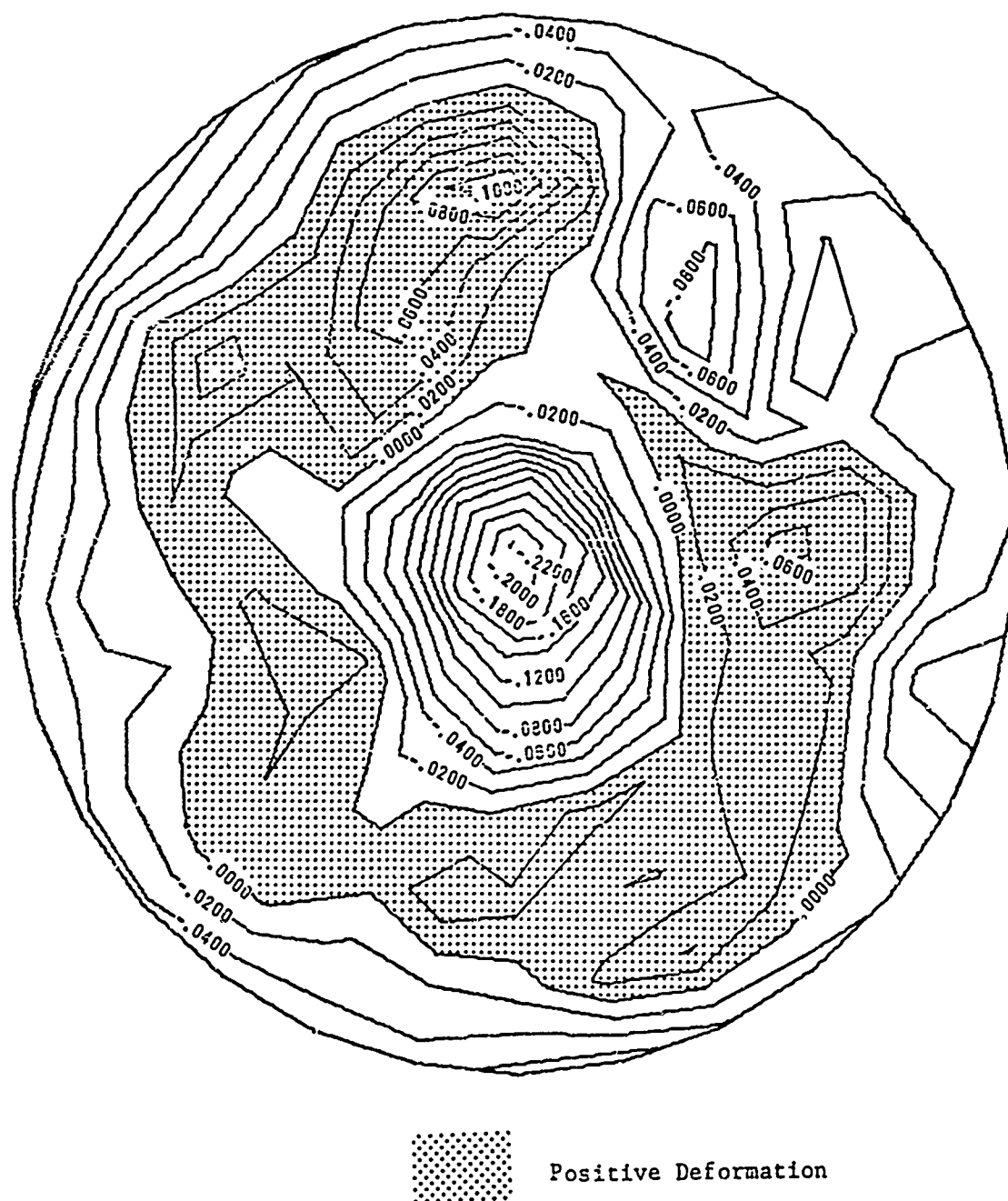


Figure 4.8i B2 Model: Imperfections  
Plus Deflections at 3.0 psi

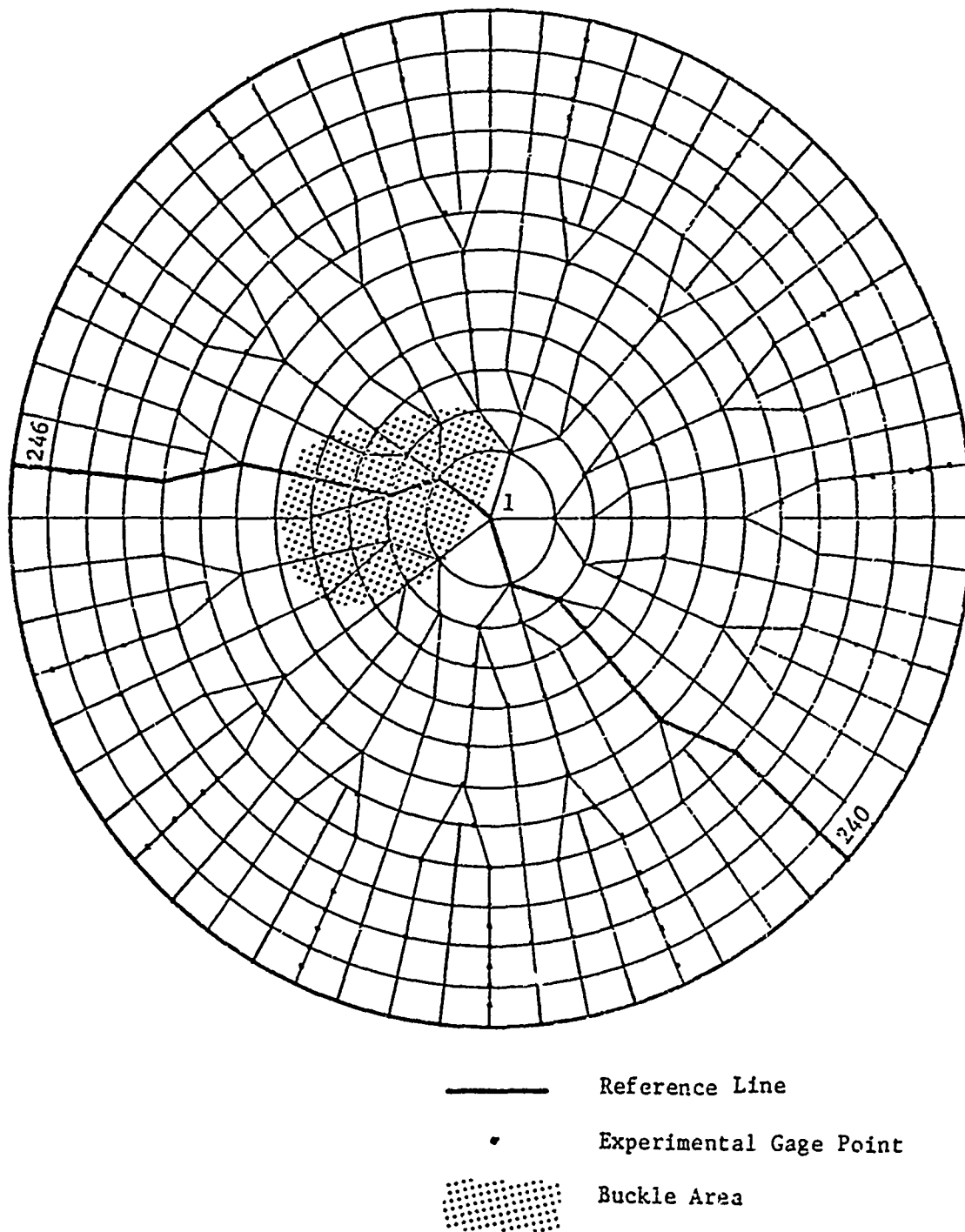


Figure 4.9 B1 Model Experimental Grid

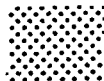


Figure 4.10 B1 Model Initial Imperfections

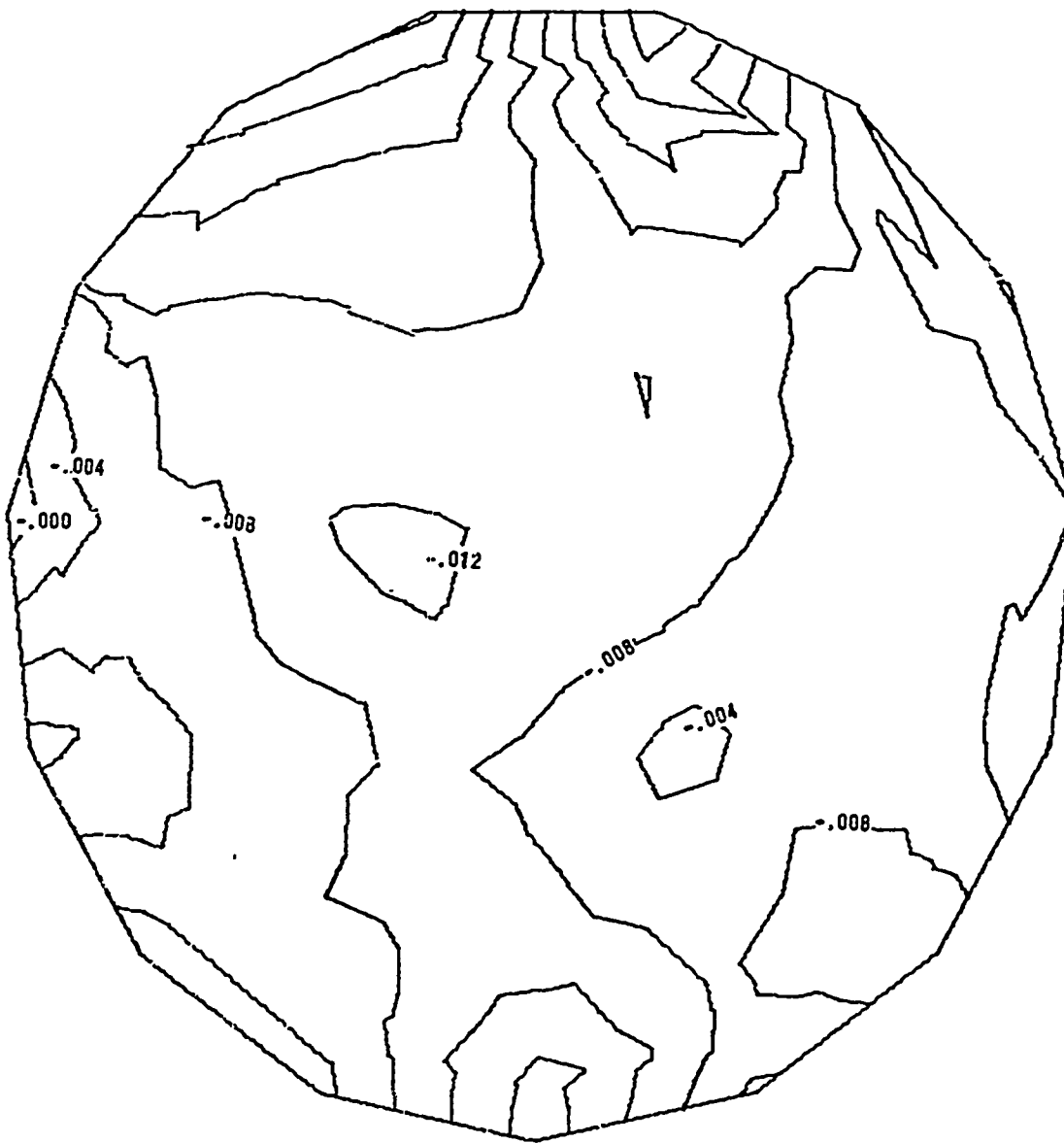


Figure 4.11a B1 Model: .15 to 1.0 psi



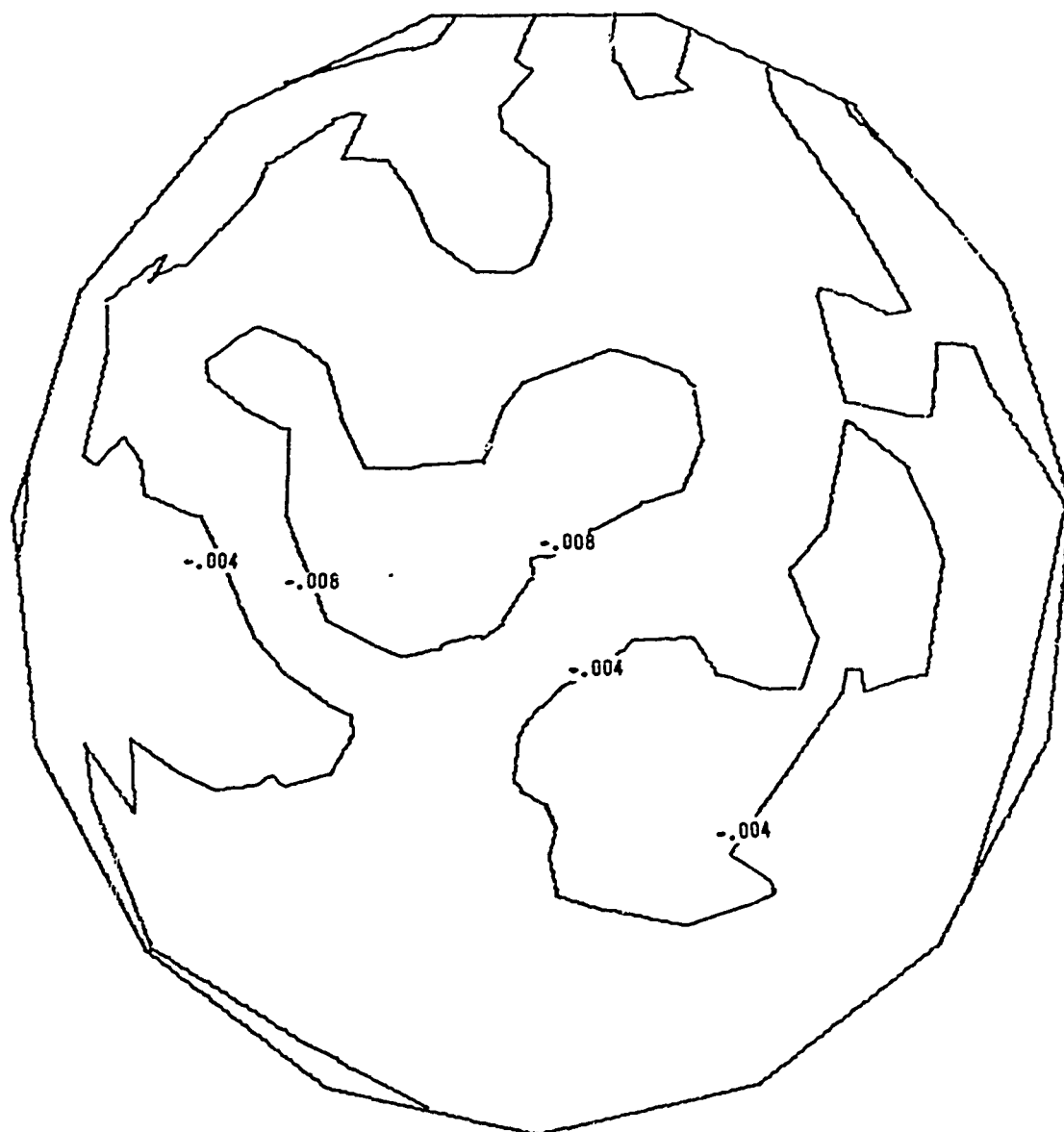


Figure 4.11b B1 Model: 1.0 to 2.0 psi

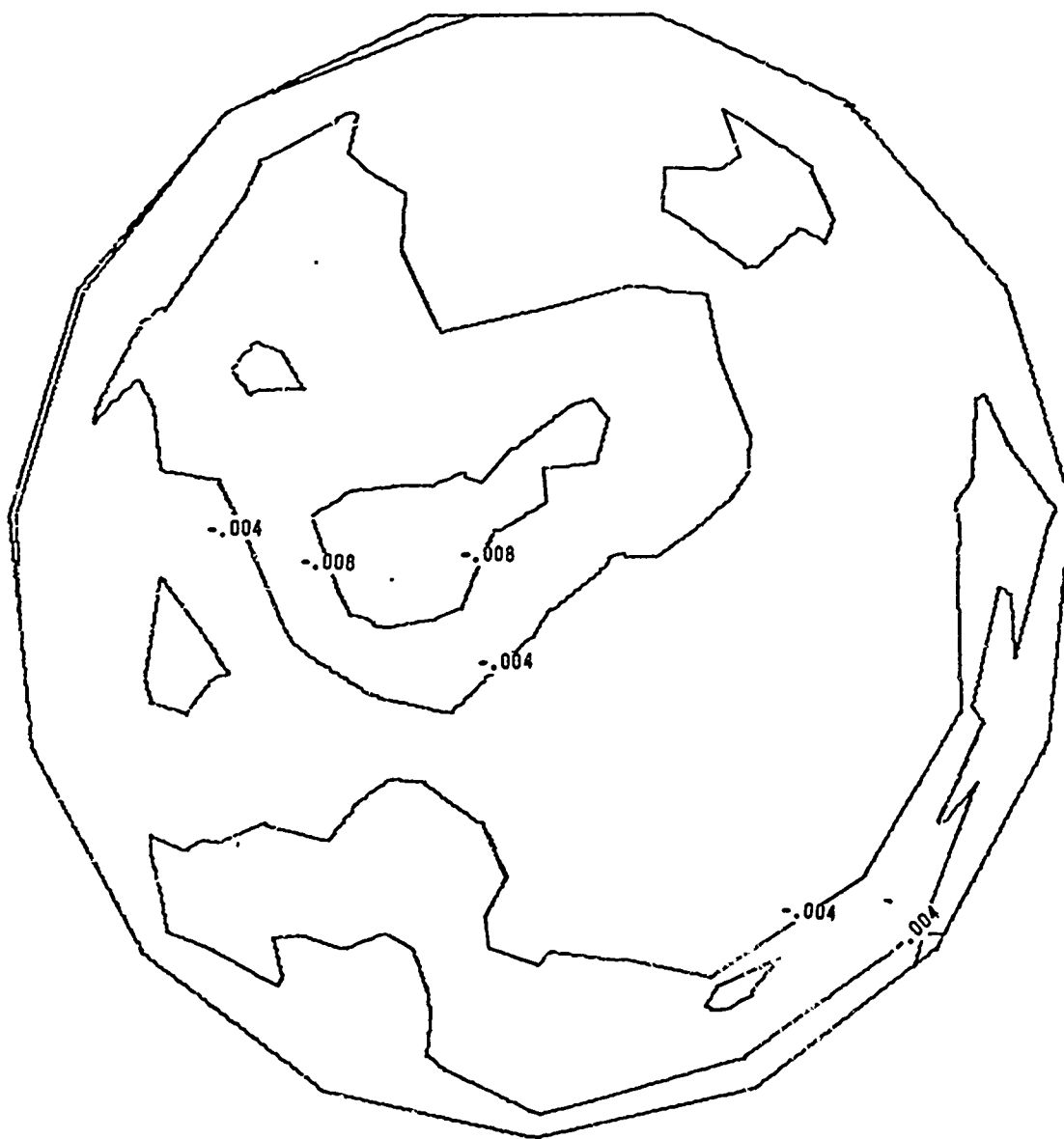


Figure 4.11c B1 Model: 2.0 to 3.0 psi



Figure 4.11d Bi Model: 3.0 to 4.0 psi

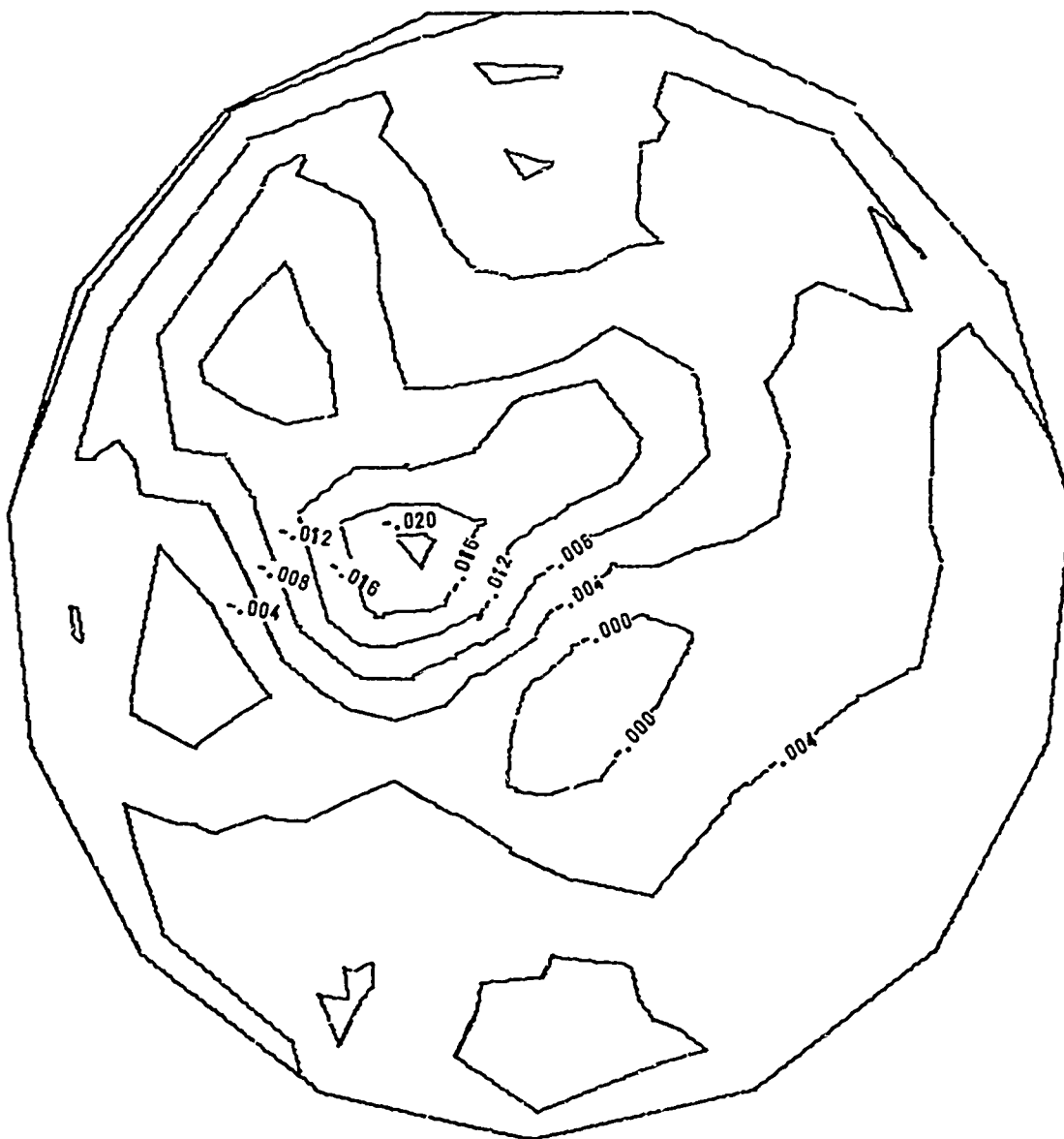


Figure 4.11e B1 Model: 4.0 to 5.0 psi

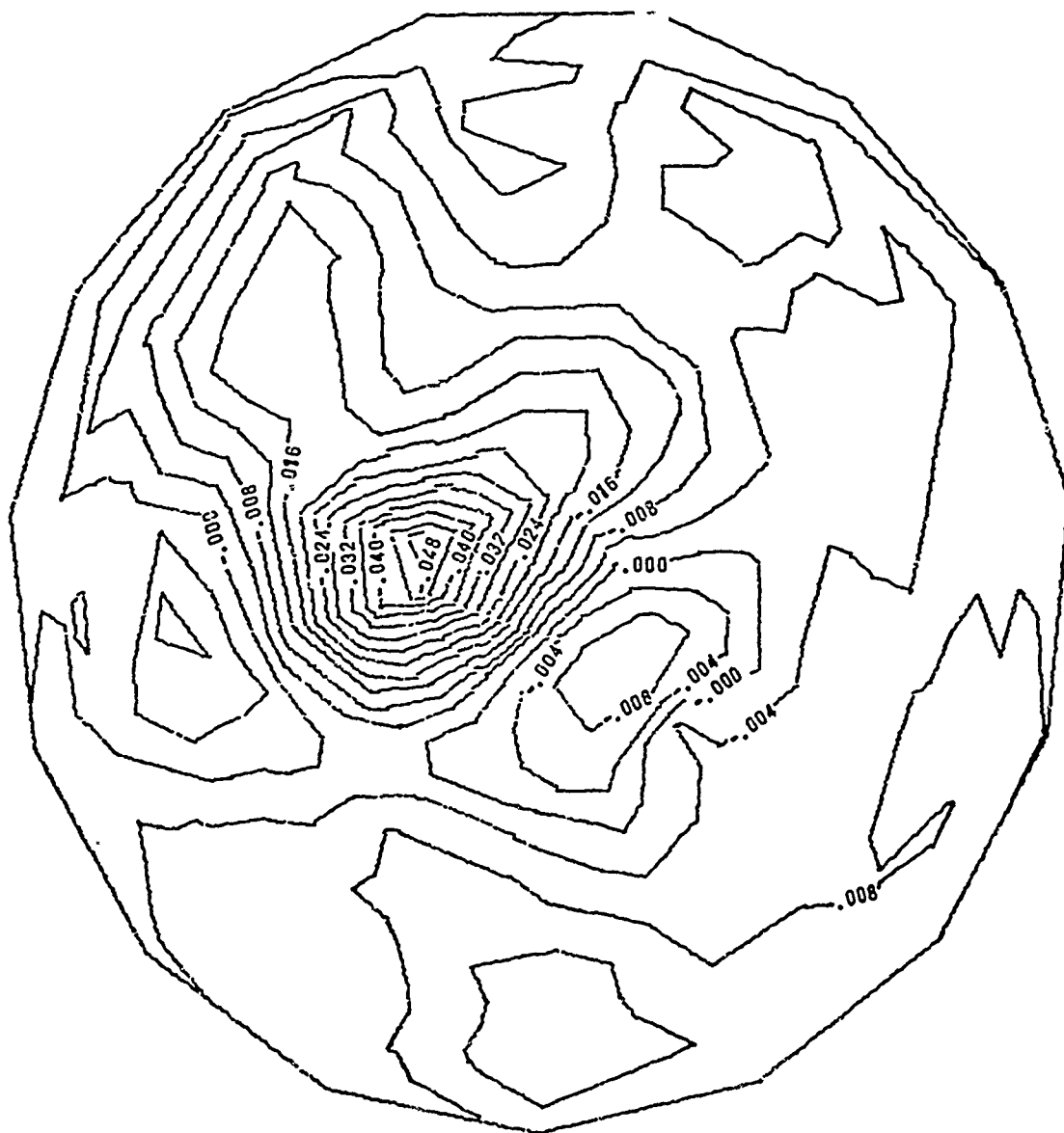


Figure 4.11f B1 Model: 5.0 to 6.0 psi

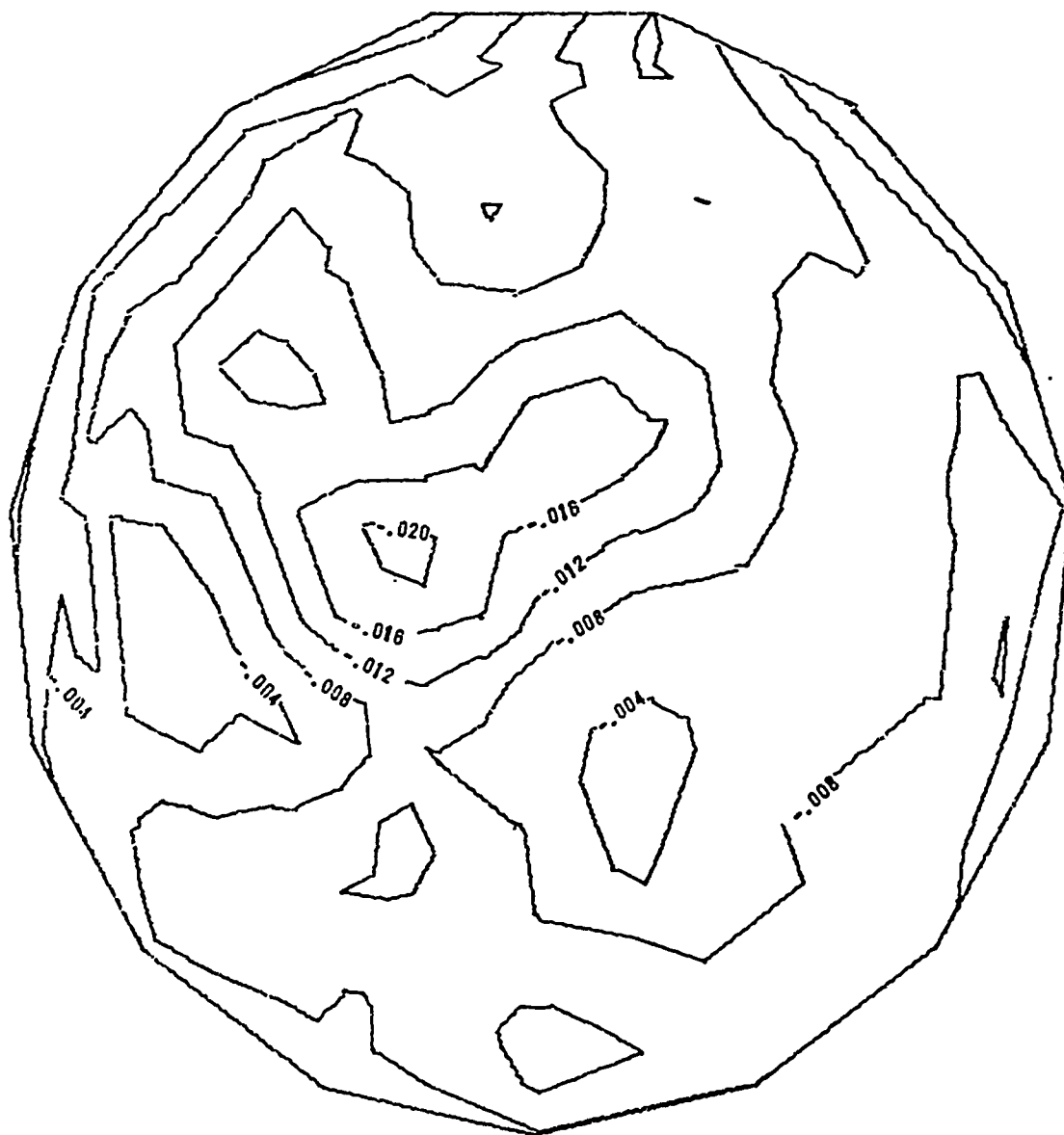


Figure 4.11g B1 Model: 1.0 to 3.0 psi

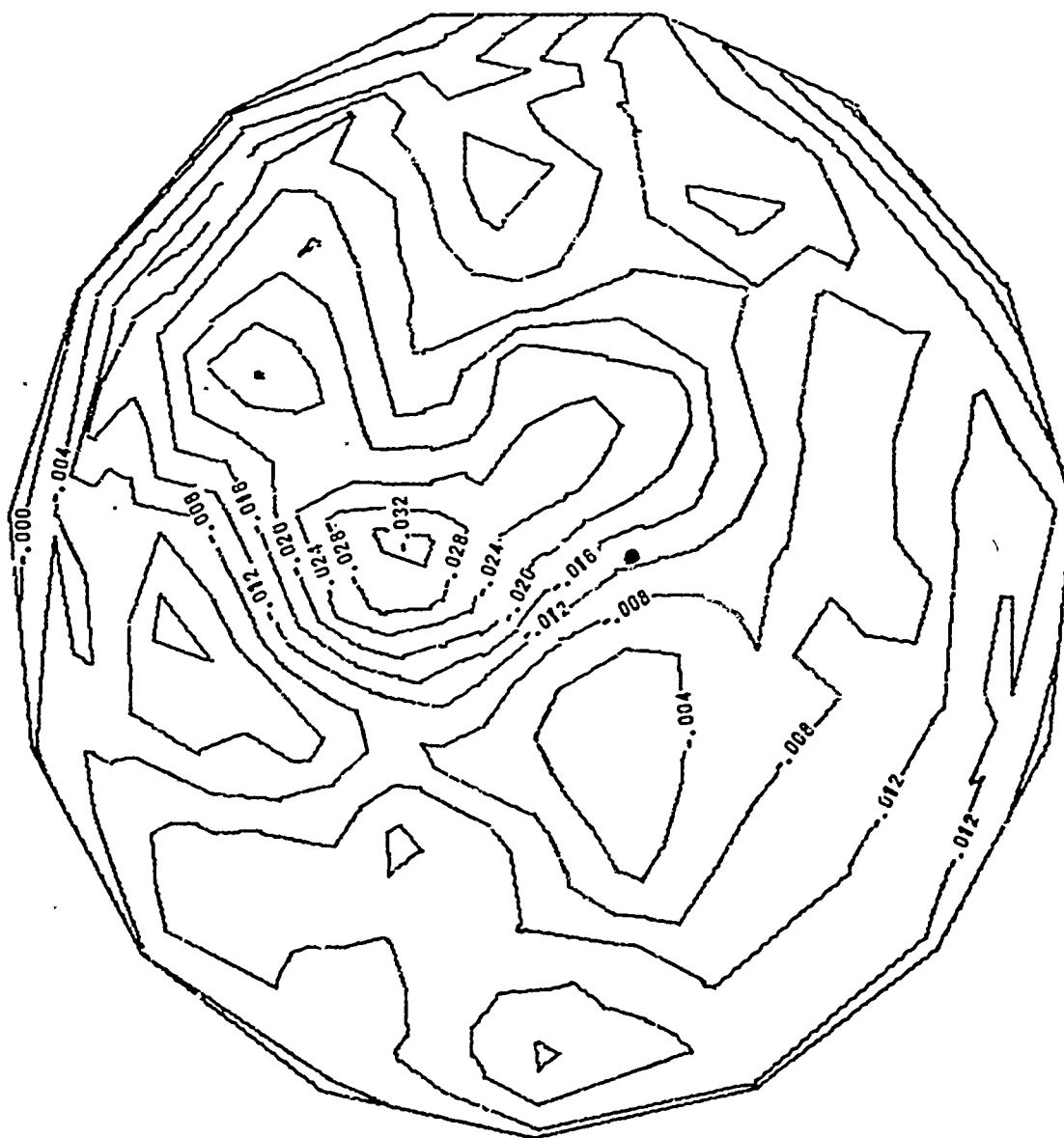


Figure 4.11h B1 Model: 1.0 to 4.0 psi.

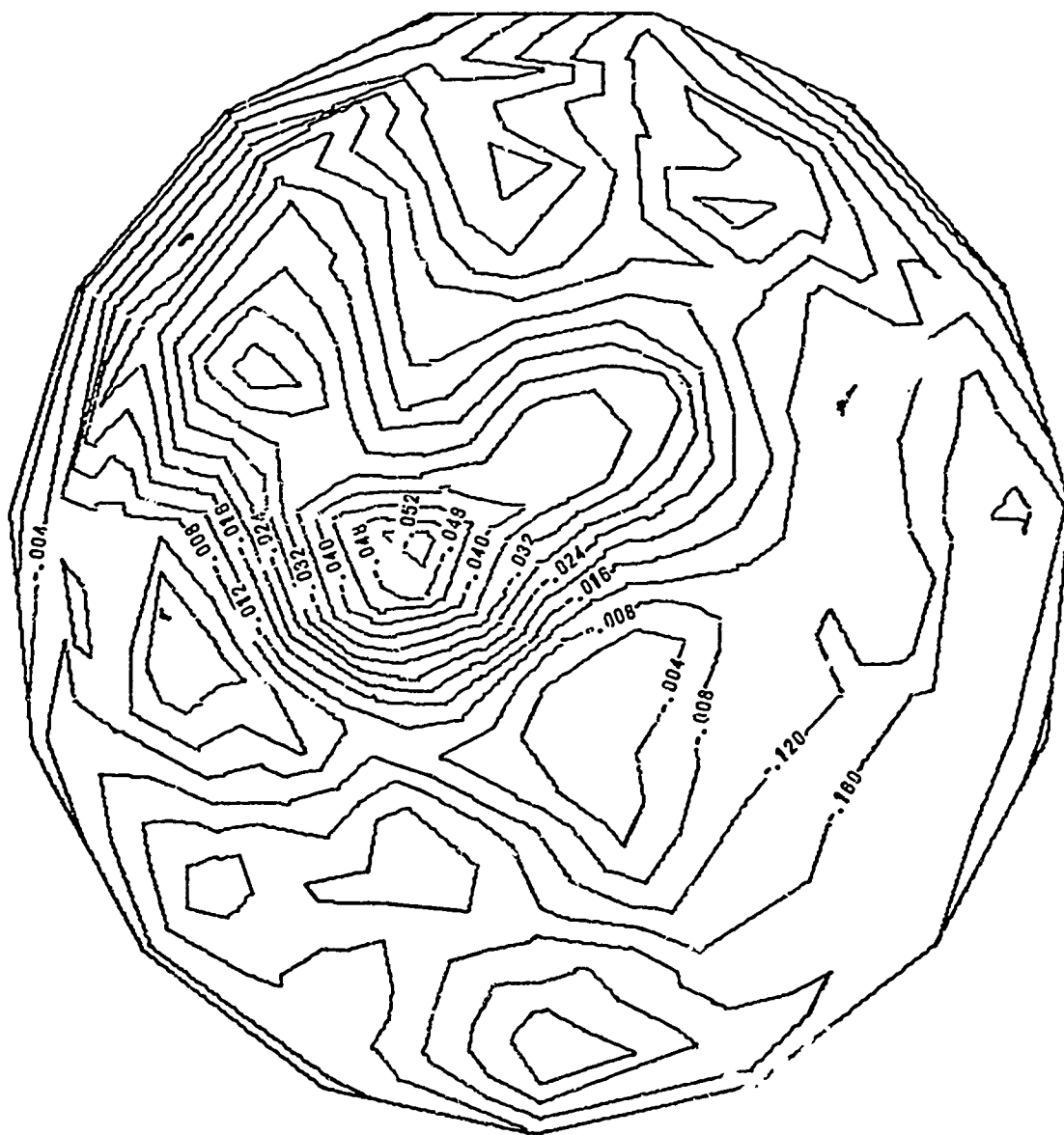


Figure 4.111 B1 Model: 1.0 to 5.0 psi





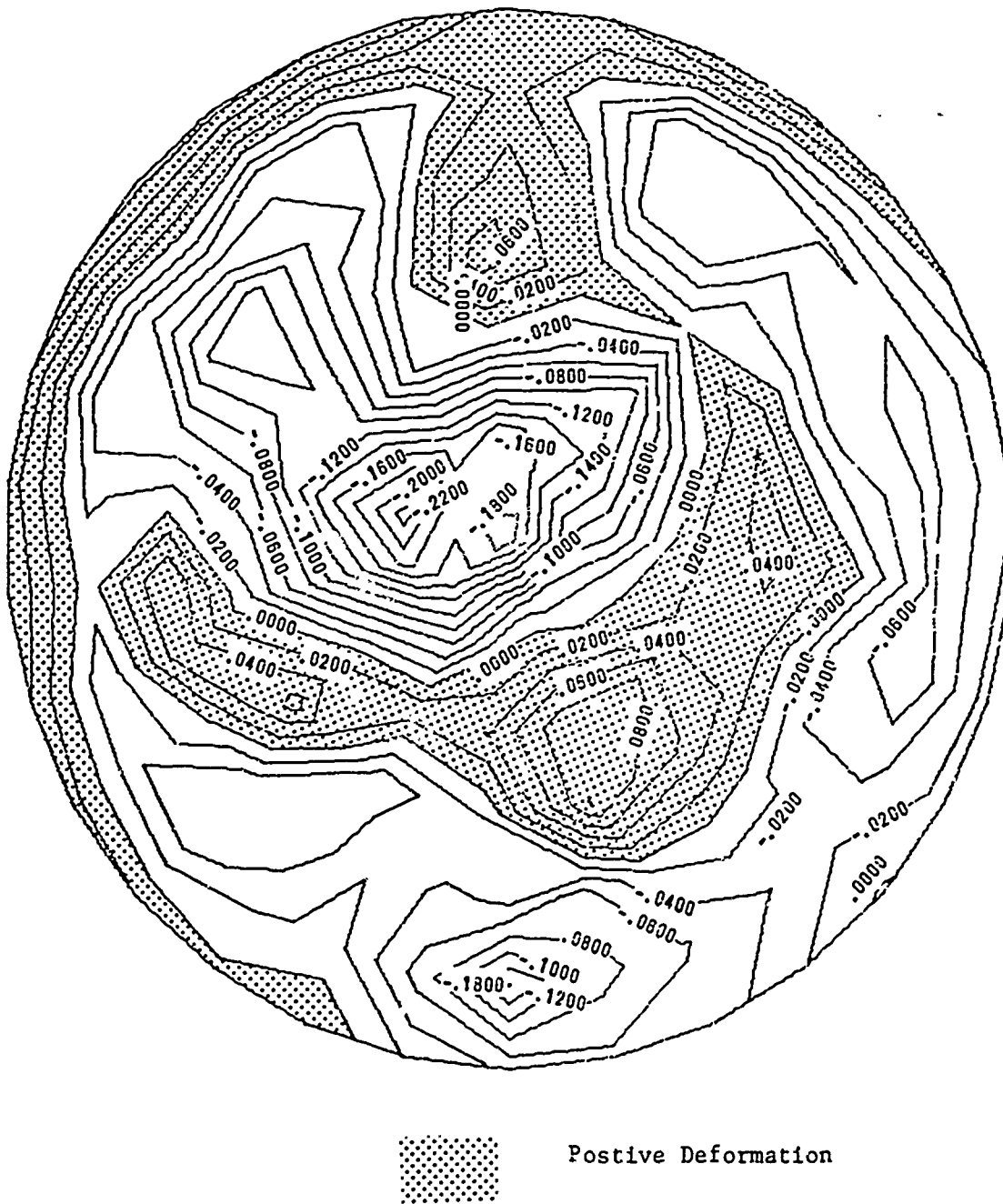


Figure 4.11k B1 Model: Imperfections Plus Deflections at 6.0 psi

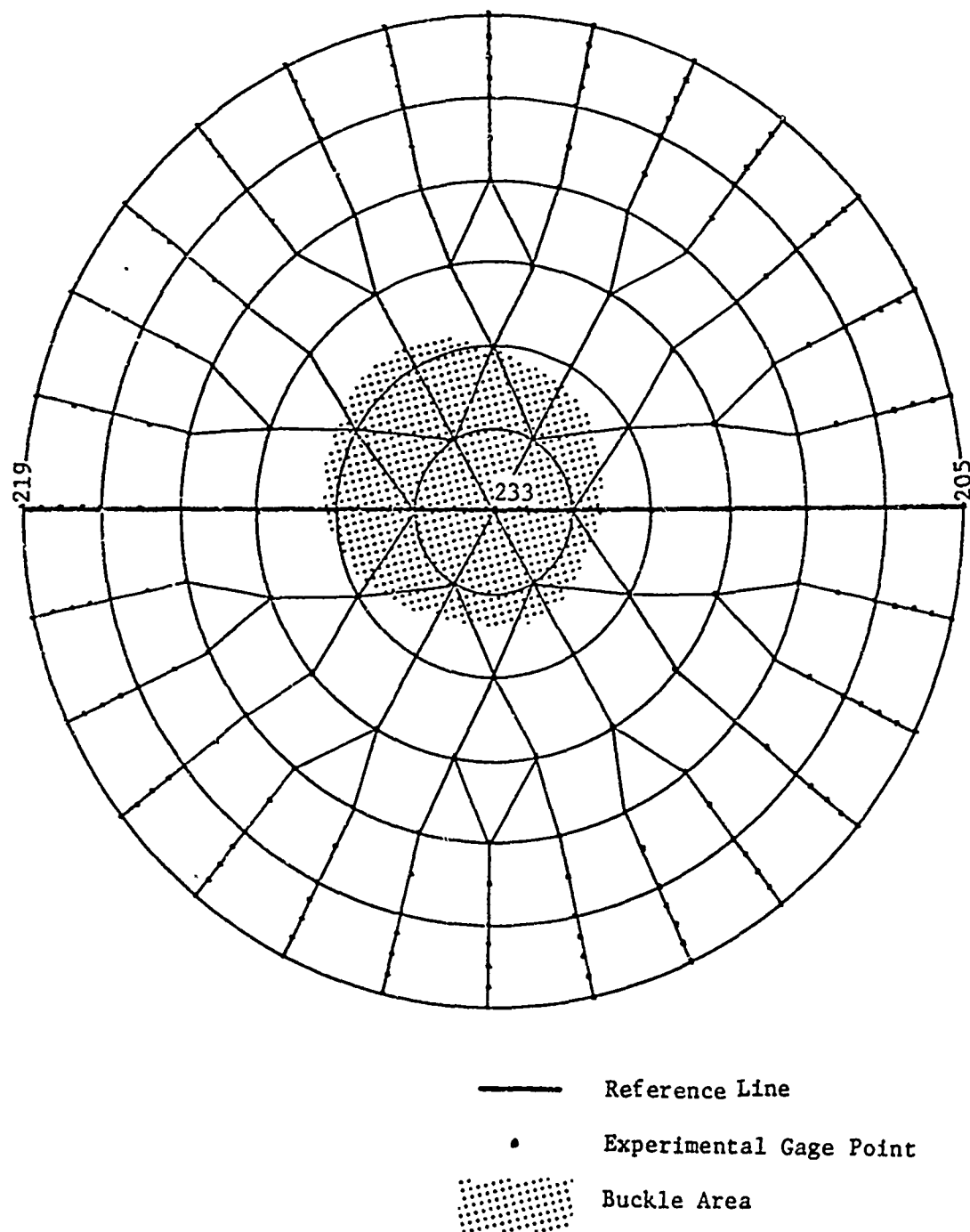
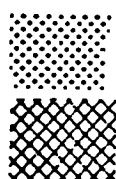
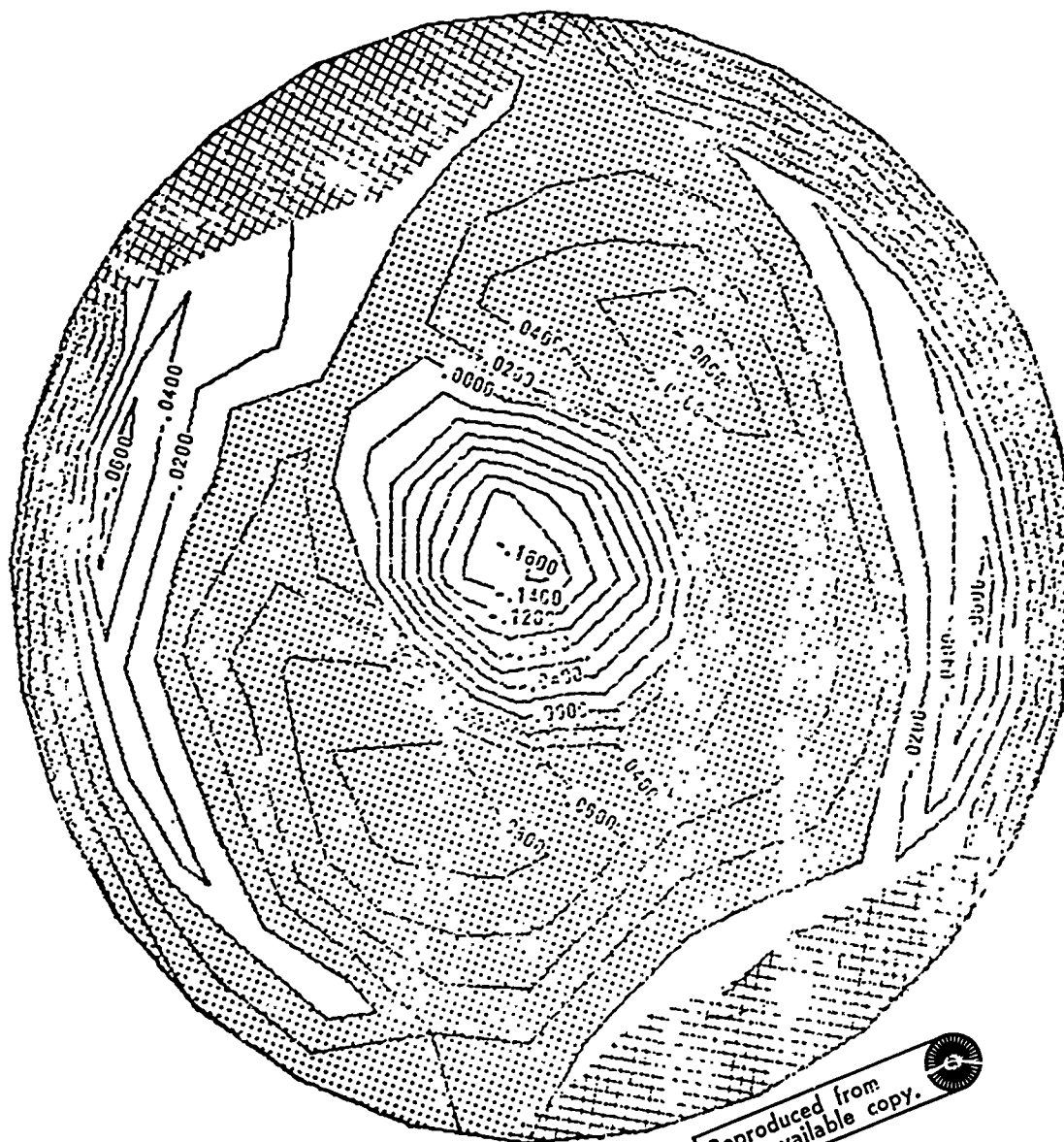


Figure 4.12 Pret Model Experimental Grid



Positive Deformation

No Data

Figure 4.13 PRET Model Initial Imperfections

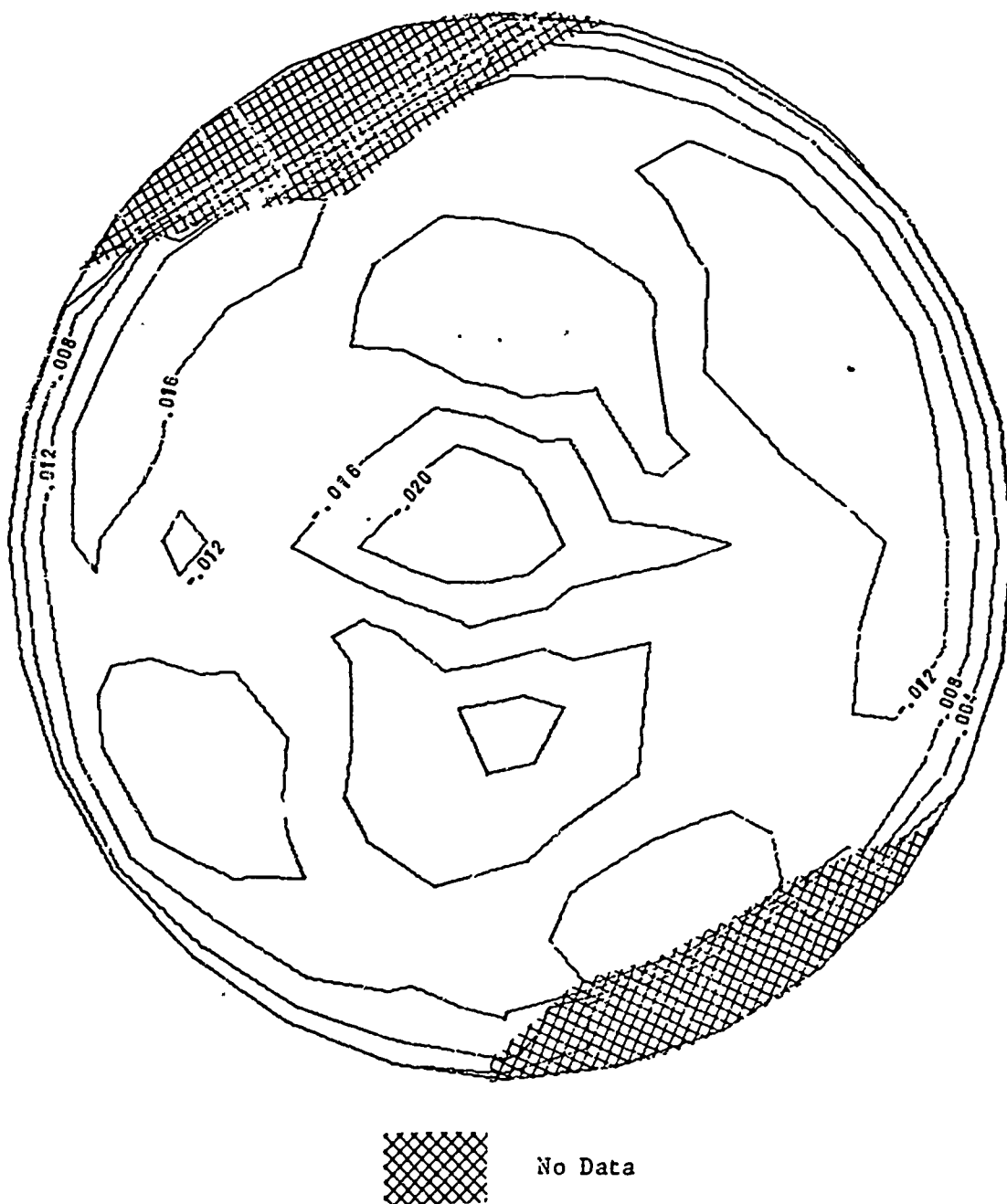


Figure 4.14a PRET Model: .15 to 1.0 psi

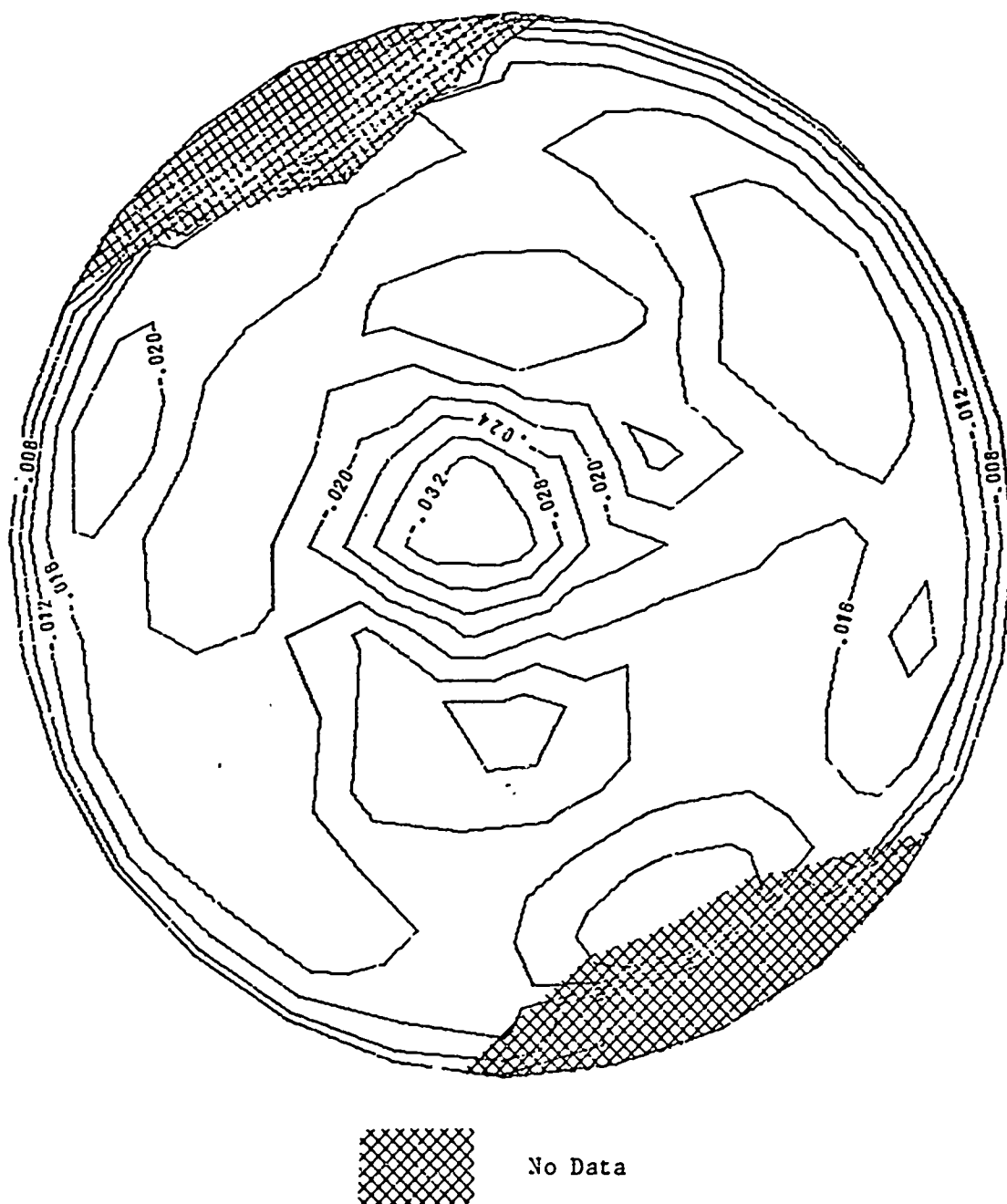


Figure 4.14b PRET Model: 1.0 to 2.0 psi

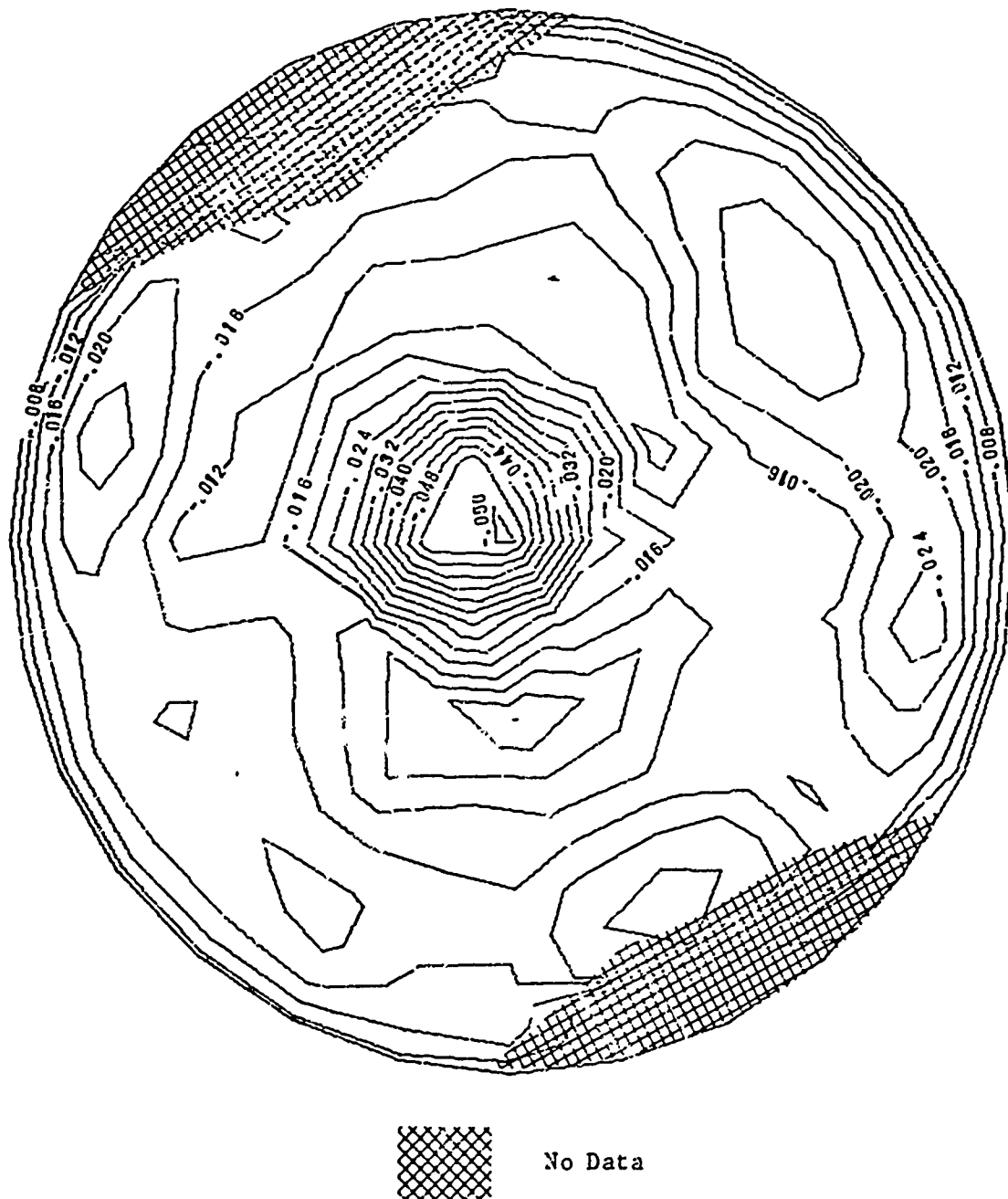


Figure 4.14c PRET Model: 2.0 to 3.0 psi

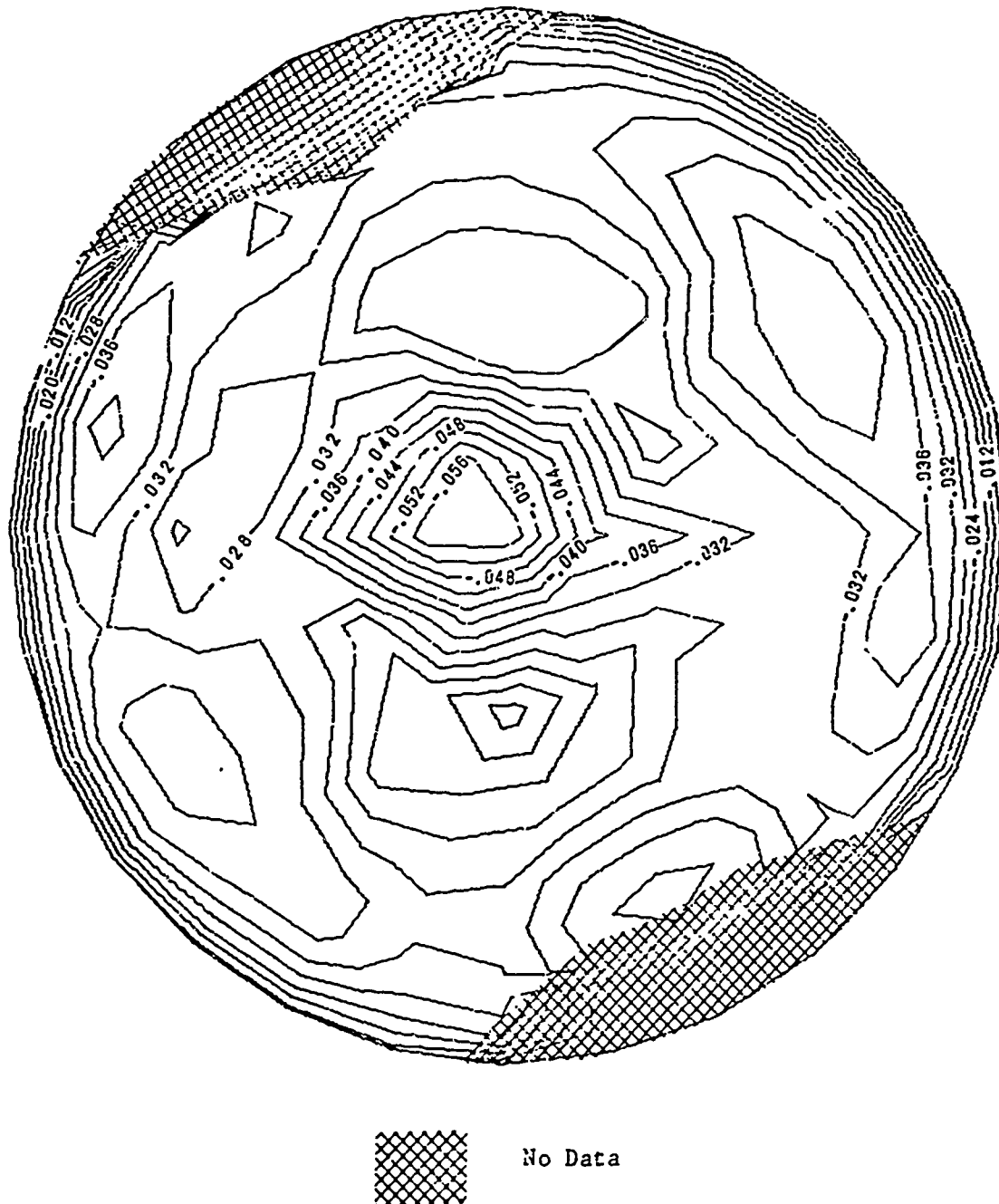


Figure 4.14d PRET Model: .15 to 2.0 psi



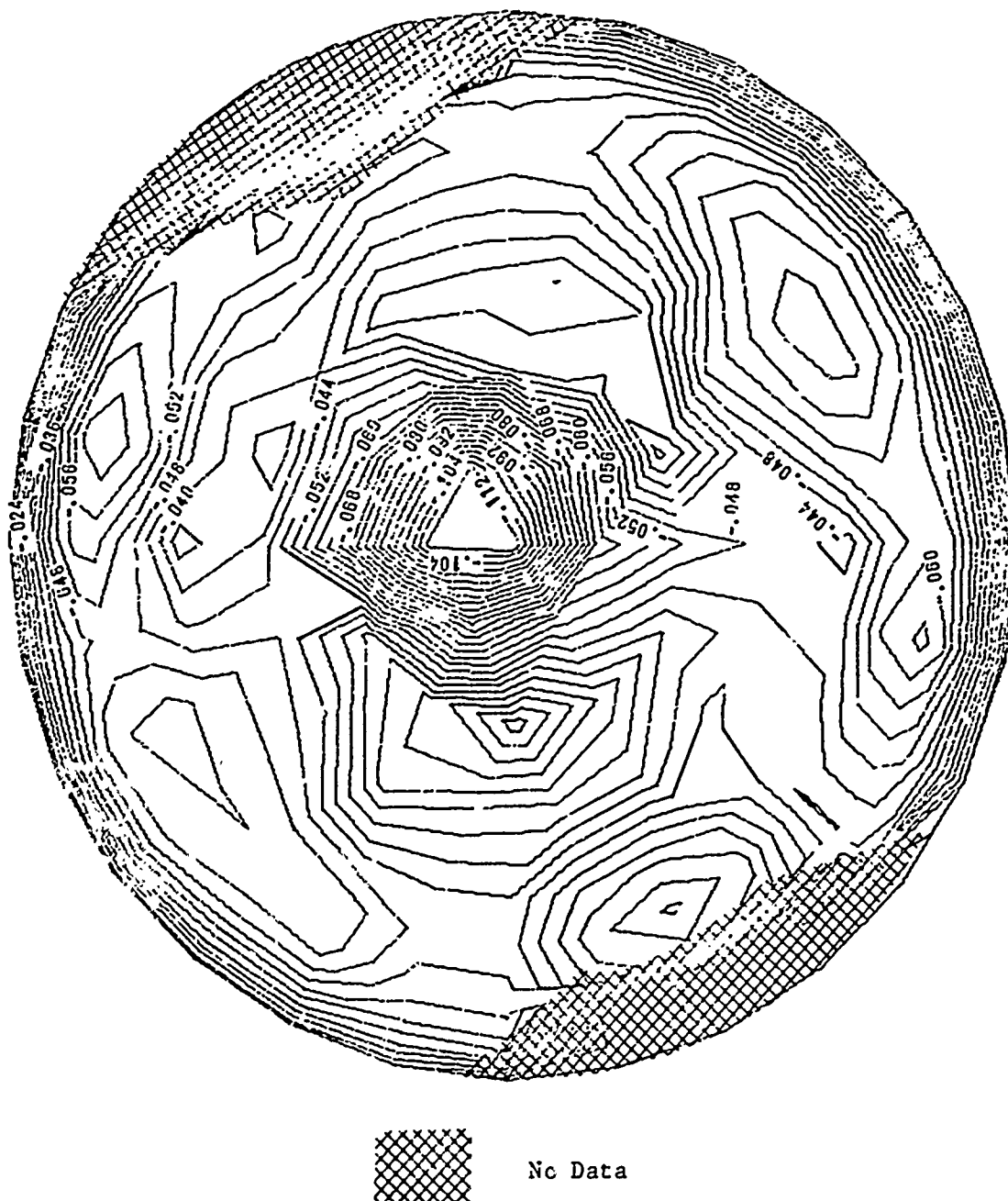


Figure 4.14e PRET Model: .15 to 3.0 psi

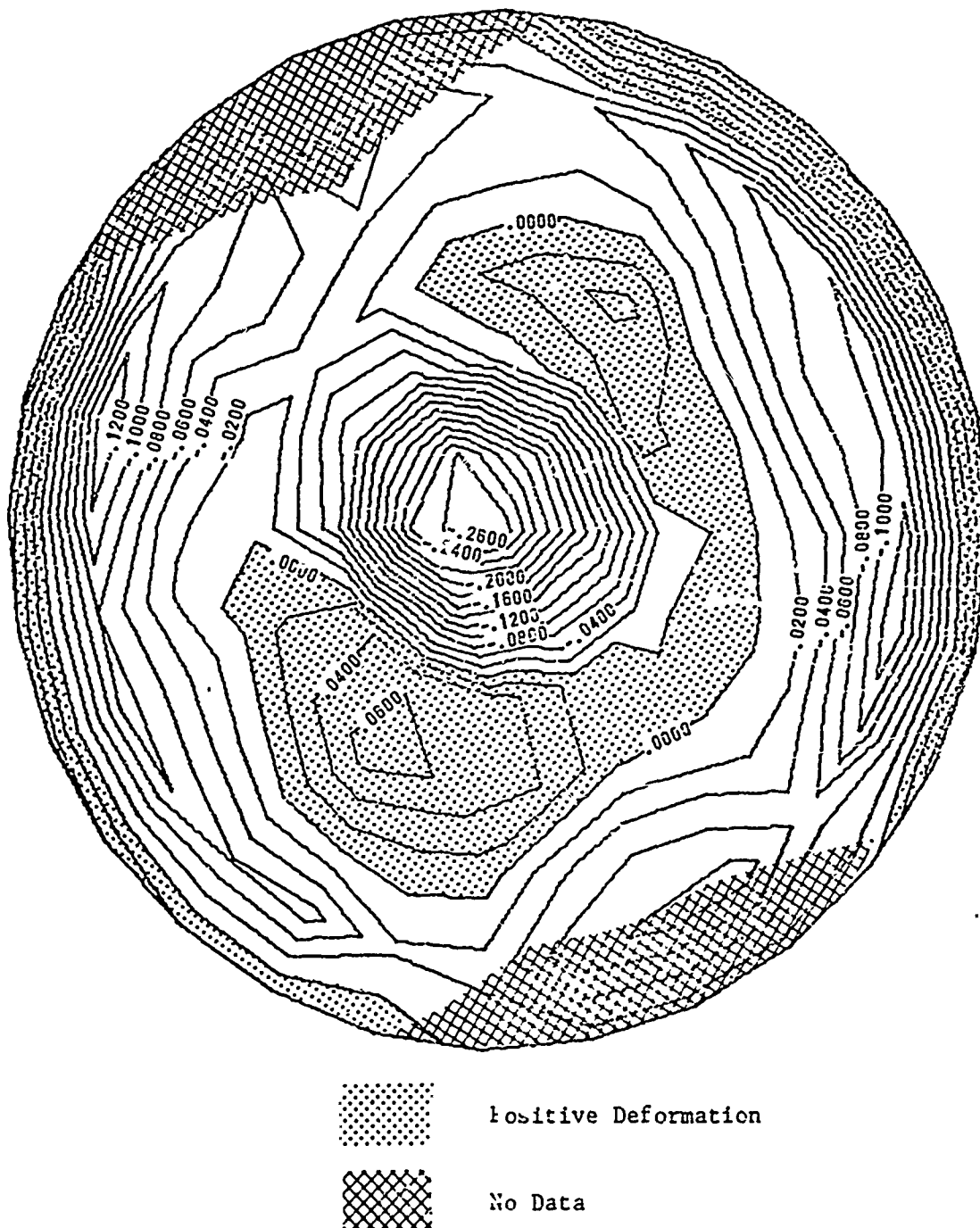


Figure 4.14f PRET Model: Imperfections Plus Deflections at 3.0 psi

The experimental grid is given in Figure 4.12, again with a reference line and the final buckle position. Figure 4.13 represents the initial imperfections for the PRET model with a contour interval of .0200 inches. Since the edge of the PRET model was clamped to the pressure vessel support lip no edge ring seating problem existed, and the reference pressure level for this model was therefore .15 psi. Deflection patterns for the experimental data from the .15 to 1.0 psi, 1.0 to 2.0 psi, 2.0 to 3.0 psi, .15 to 2.0 psi and .15 to 3.0 psi pressure increments are given respectively in Figures 4.14a through 4.14e. Figure 4.14f shows the total deflection pattern due to initial imperfections plus the live load deflections under an external load of 3.0 psi. This plot is best contrasted with the initial imperfection only plot of Figure 4.13.

The hatched areas in these figures represent experimental gage points which were inaccessible to the radial arm of the Easterby apparatus. No experimental data was therefore available at these locations.

## 4.2 THEORETICAL PREDICTIONS

4.2.1 B2 Model Predictions. Results of the NASTRAN computer code runs are presented in the following figures. Figures 4.15a through 4.15d represent deflection contours for 0.5 psi pressure increments from 1.0 to 3.0 psi. The next set of plots, Figures 4.15e through 4.15g, show predicted results for the 1.0 to 2.0 psi, 1.0 to 2.5 psi, and 1.0 to 3.0 psi pressure increments respectively. All of the above plots used contour intervals of .0020 inches. Figure 4.15h shows the sum of the initial imperfections and the predicted live load deflections at 3.0 psi pressure.

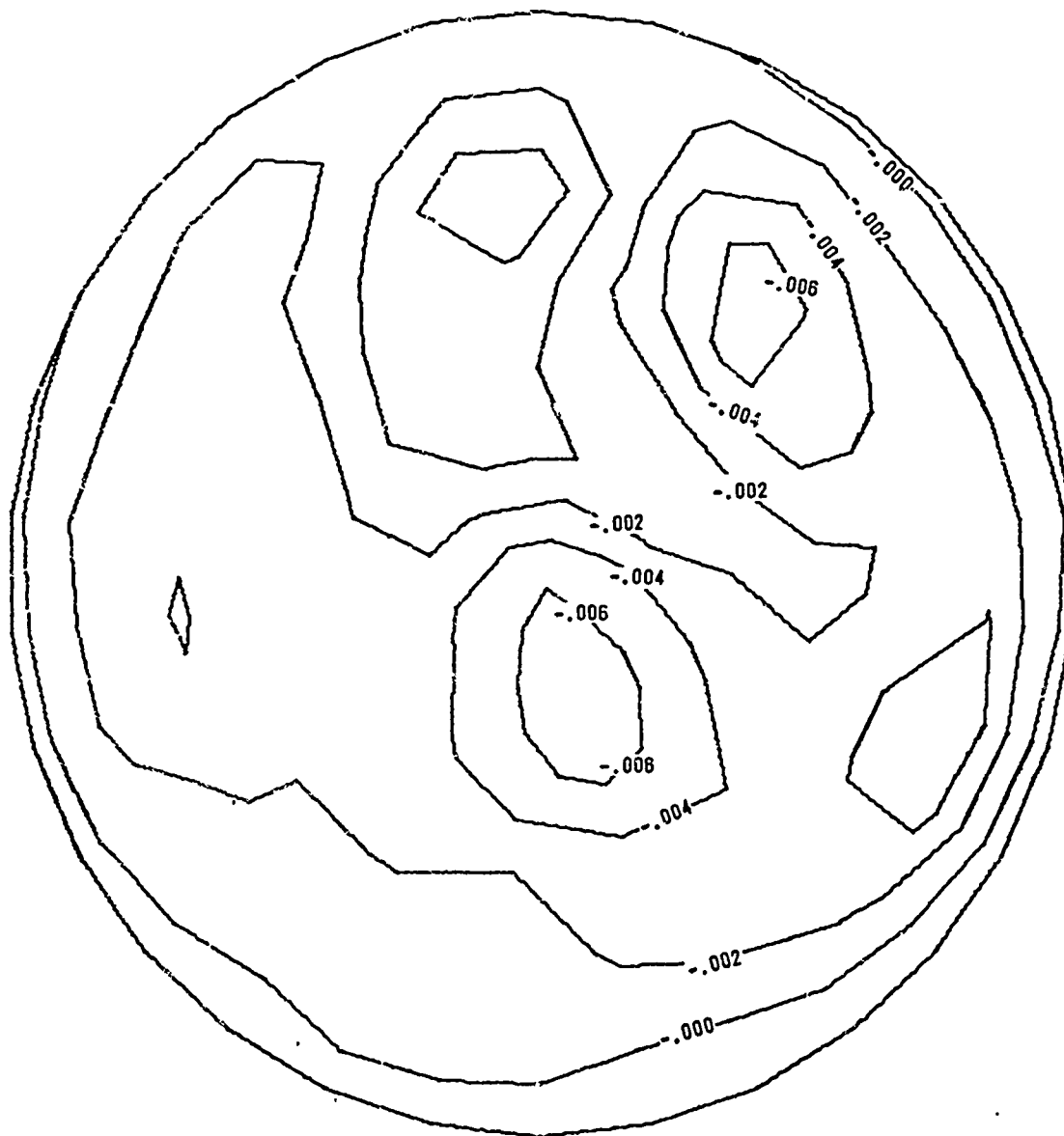


Figure 4.15a B? model: 1.0 to 1.5 psi

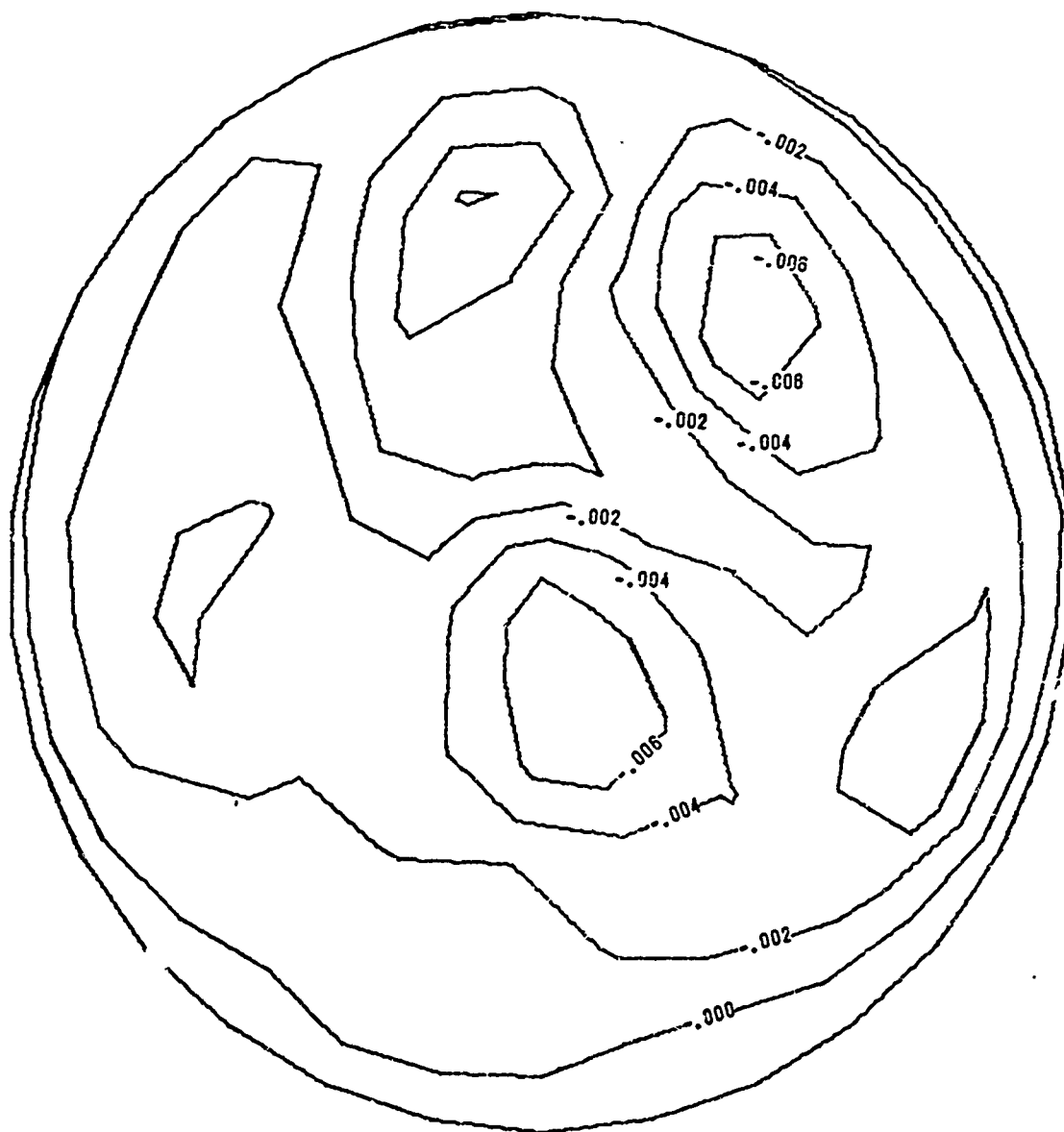


Figure 4.15b B2 Model: 1.5 to 2.0 psi

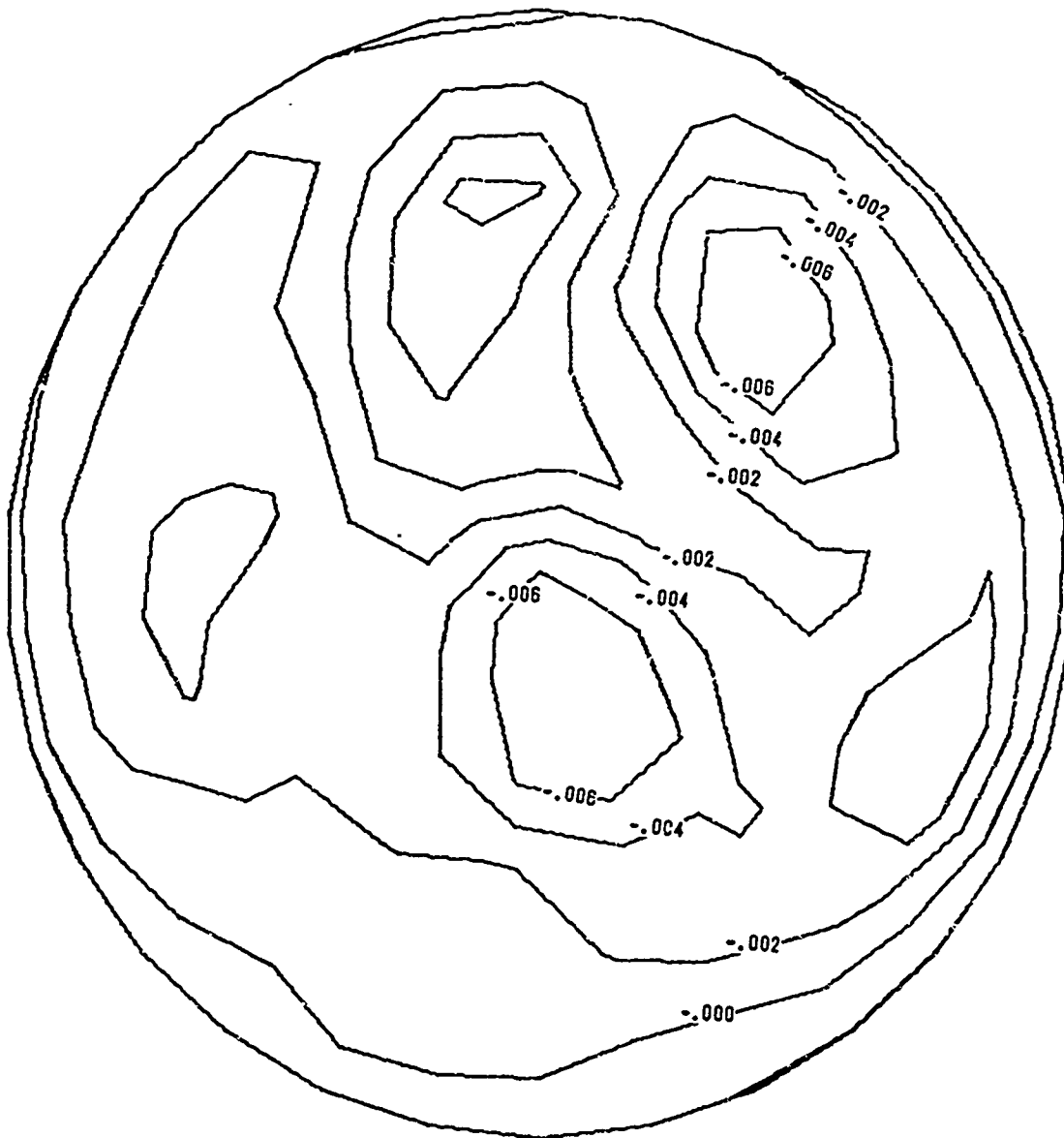


Figure 4.15c B2 Model: 2.0 to 2.5 psi

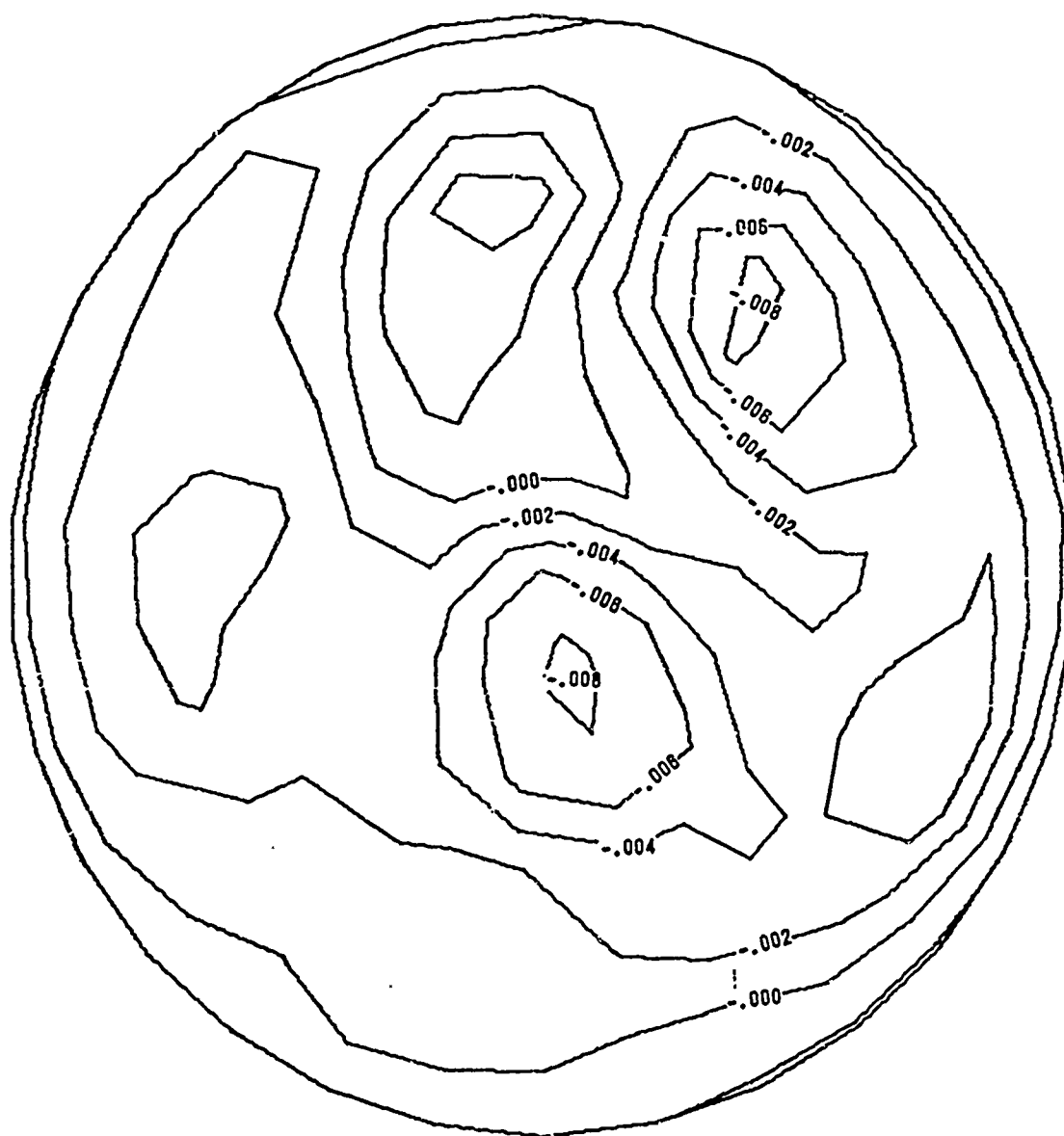


Figure 4.15d B2 Model: 2.5 to 3.0 psi

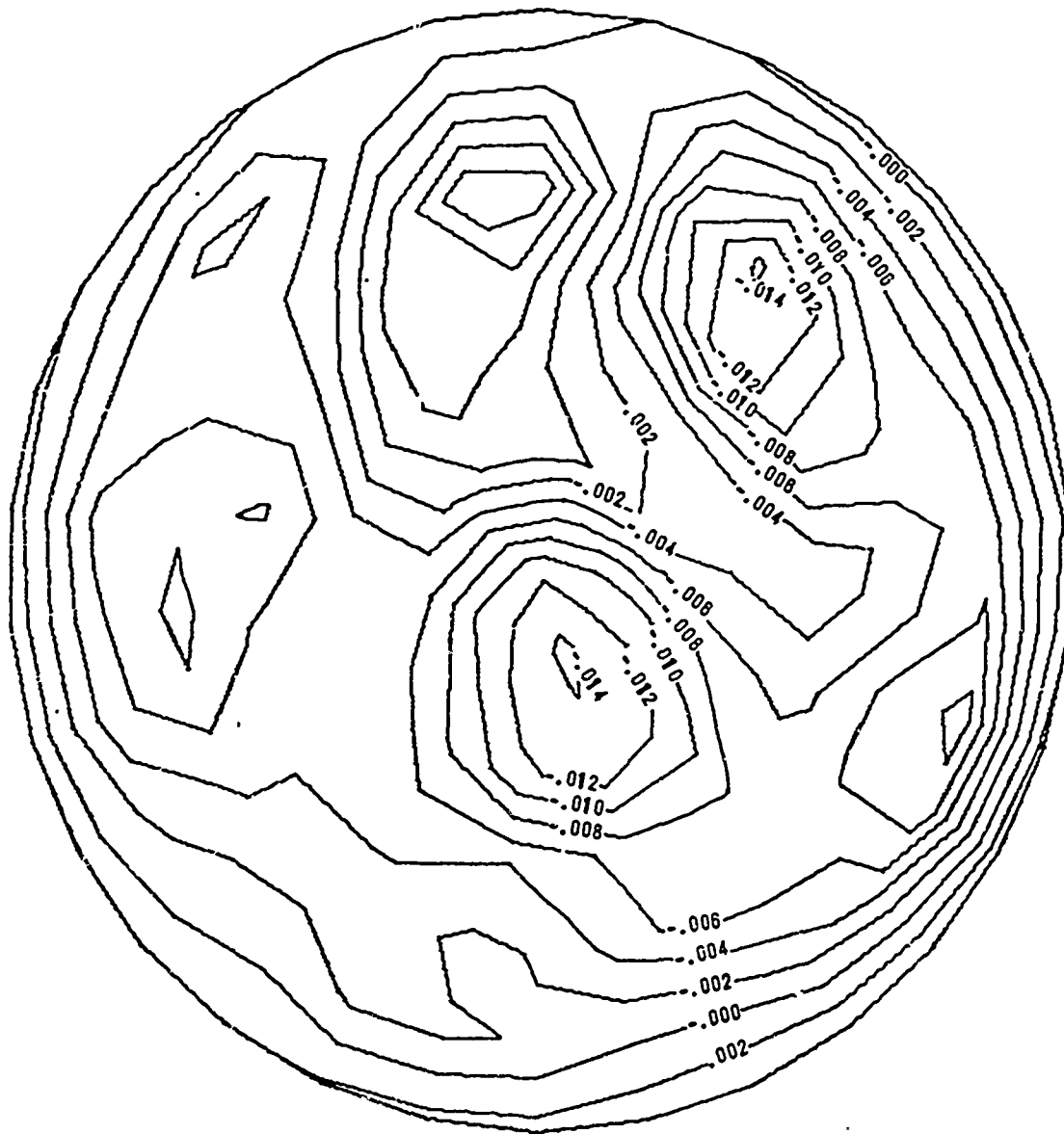


Figure 4.15e B2 Model: 1.0 to 2.0 psi



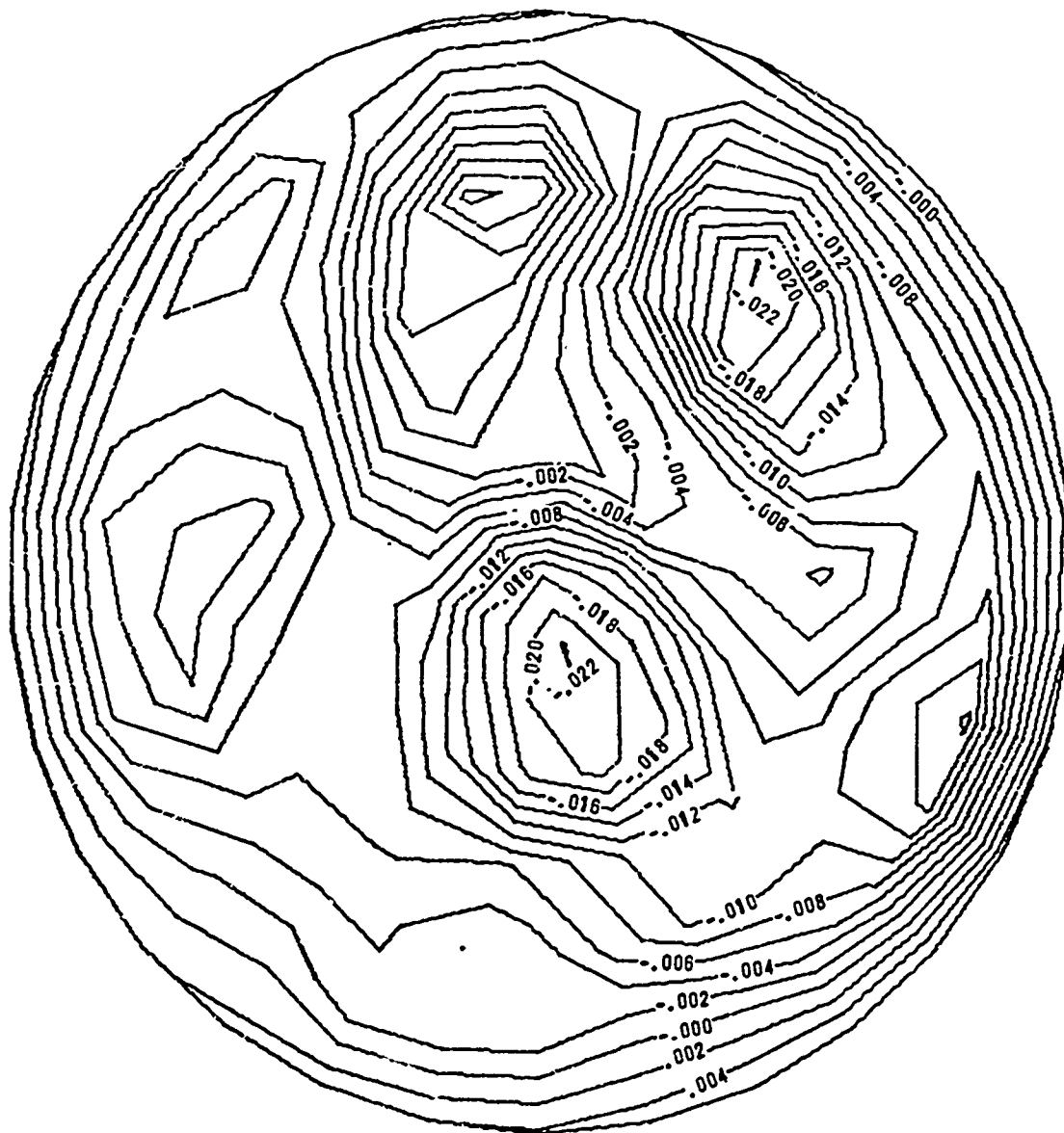


Figure 4.15f B2 Model: 1.0 to 2.5 psi



Figure 4.15g B2 Model: 1.0 to 3.0 psi

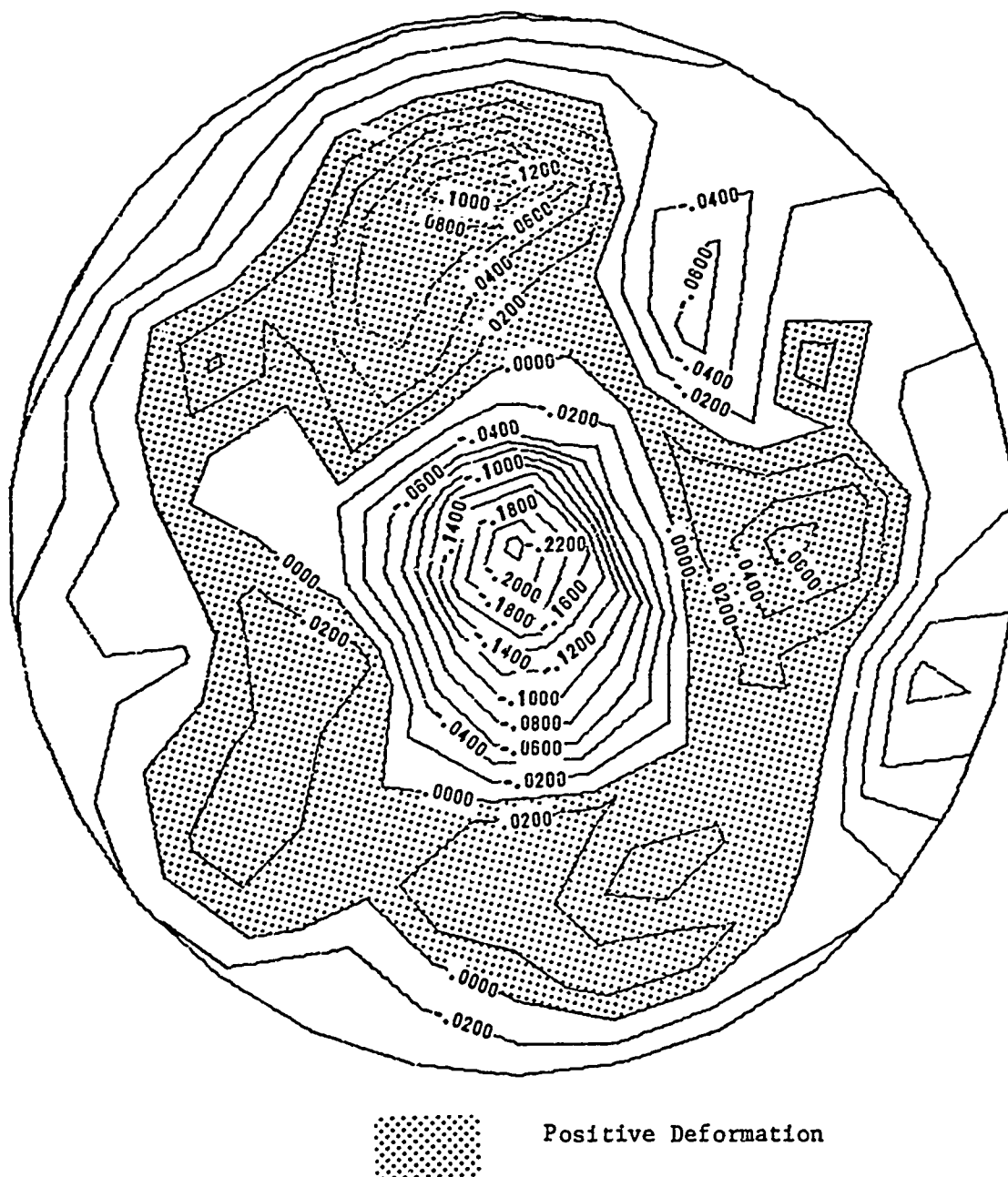


Figure 4.15h B2 Model: Imperfections Plus  
Deflections at 3.0 psi

As noted in Chapter 2, no theoretical predictions for the B1 test model were made. Since the joints of all members were not instrumented, the joint locations were unavailable.

4.2.2 PRET Model Predictions. Predictions of deflection contours for the PRET test model are given in Figure 4.16. The following pressure increments are represented in order: .15 to 1.0 psi, 1.0 to 2.0 psi, 2.0 to 3.0 psi, .15 to 2.0 psi, and .15 to 3.0 psi. A contour interval of .0040 inches was used. Figure 4.16f shows the combination of initial imperfections and the predicted live load deflections at an external pressure of 3.0 psi.

#### 4.3 COMPARISON OF PREDICTED AND EXPERIMENTAL RESULTS

4.3.1 B2 Model Deflections. Comparisons of experimental and theoretical deflections for the B2 model were made from Figures 4.8 and 4.15. Upon doing so, it was immediately obvious that the correct deflection patterns were well predicted but their magnitudes at locations of large deflections were less accurate. In order to better illustrate these differences the deflections along a reference line were plotted in Figure 4.17 for the same pressure increments as in the previous contour plots. This reference line (shown in Figure 4.6) was selected so as to trace through areas on the shell experiencing the largest displacements and thus representing potential areas of buckle formation.

Three types of predictions are shown by lines representing radial deflection in inches versus the meridional position of various experimental points. Predictions using the split rigidity approach

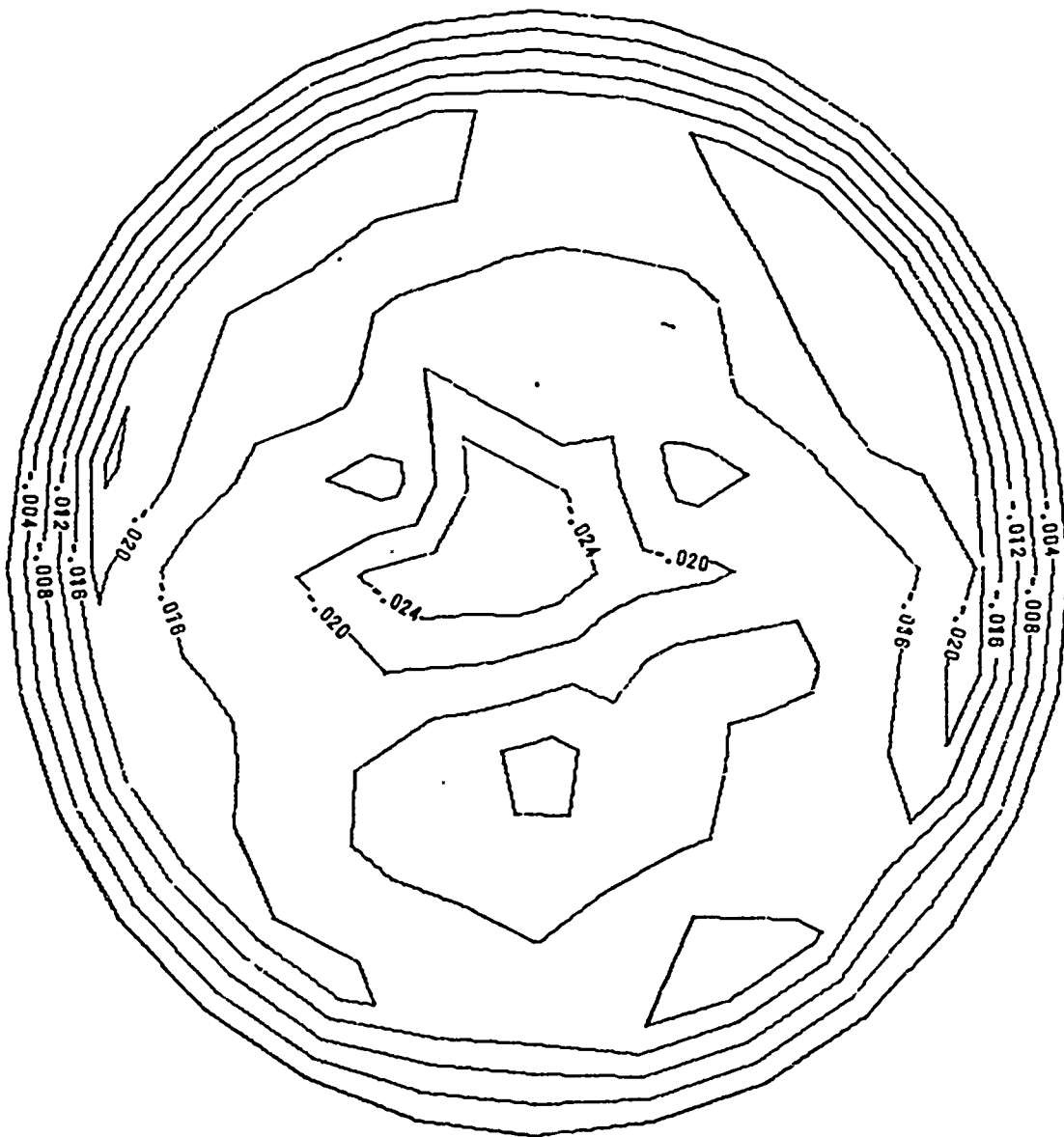


Figure 4.16a PRET Model: .15 to 1.0 psi

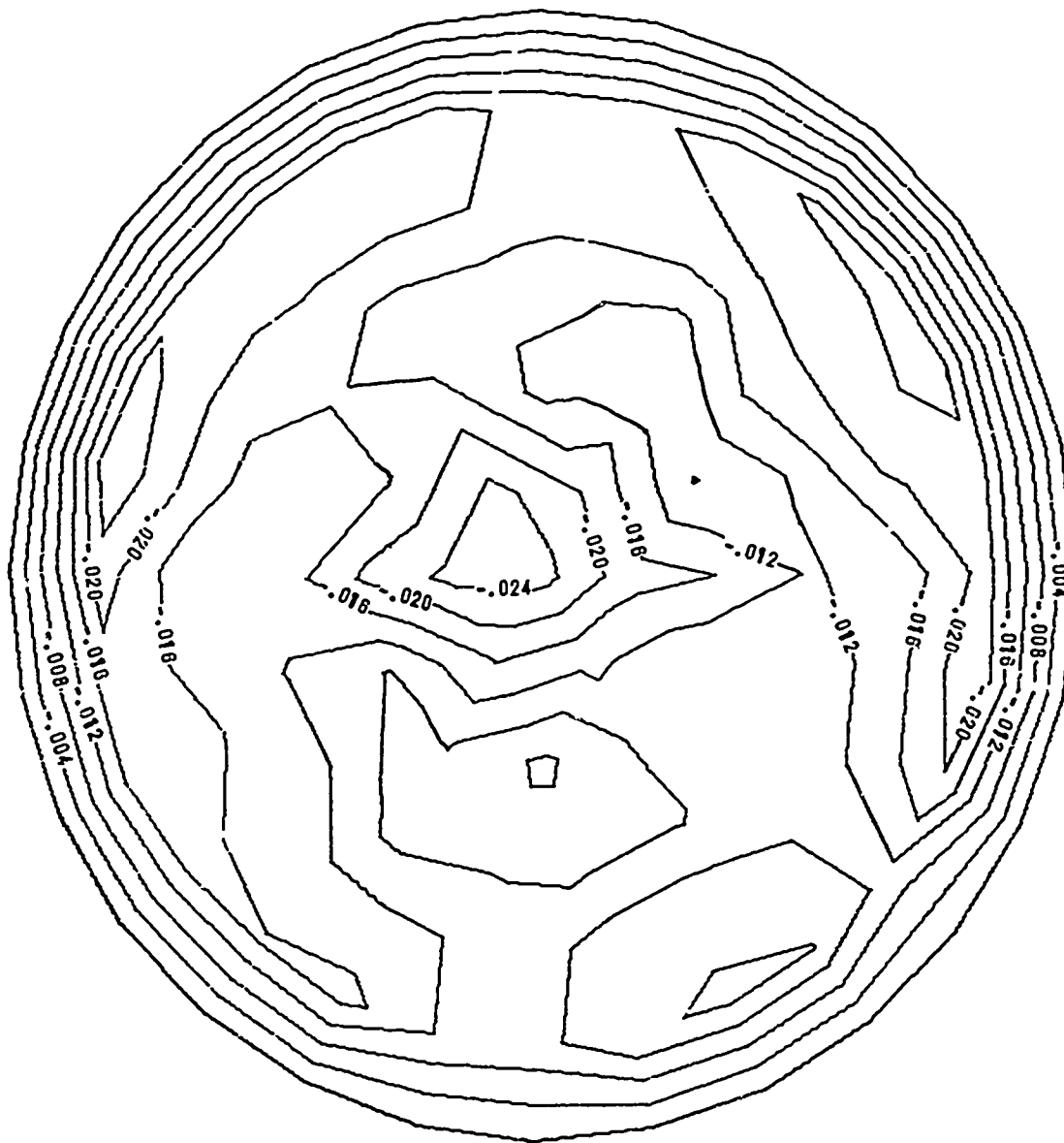


Figure 4.16b PRET Model: 1.0 to 2.0 psi

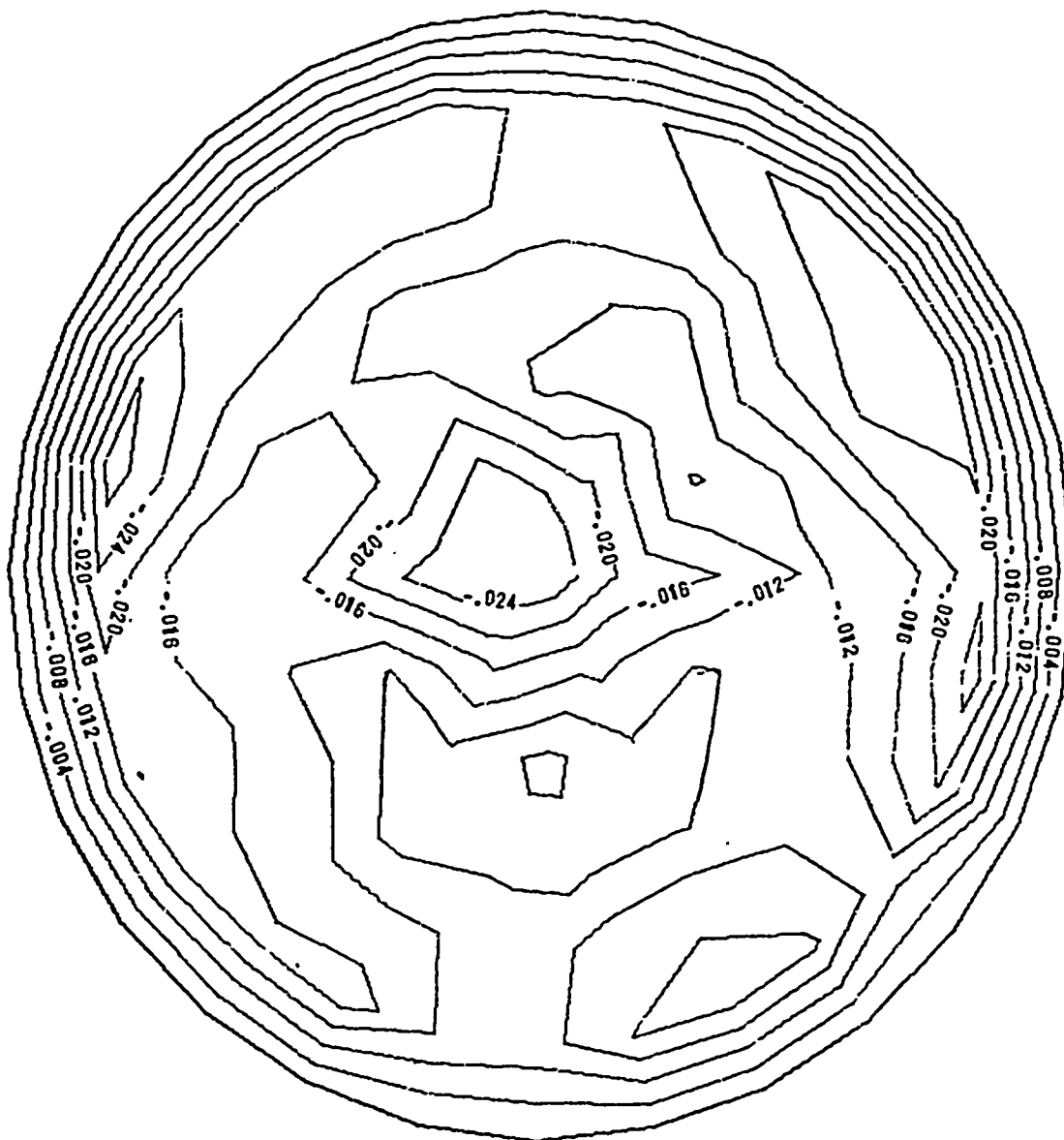


Figure 4.16c PRET Model: 2.0 to 3.0 psi

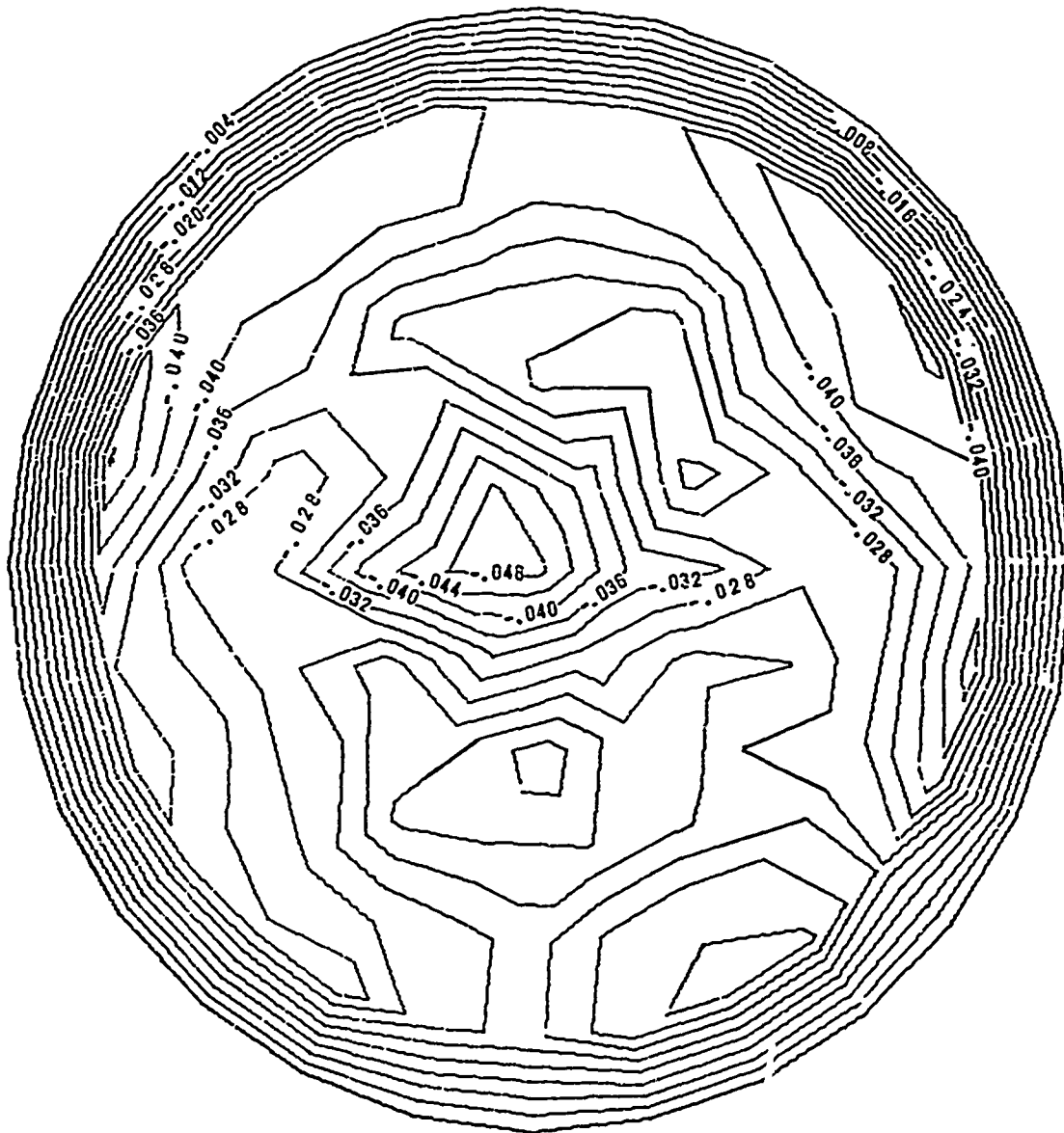


Figure 4.16d PRET Model: .15 to 2.0 psi



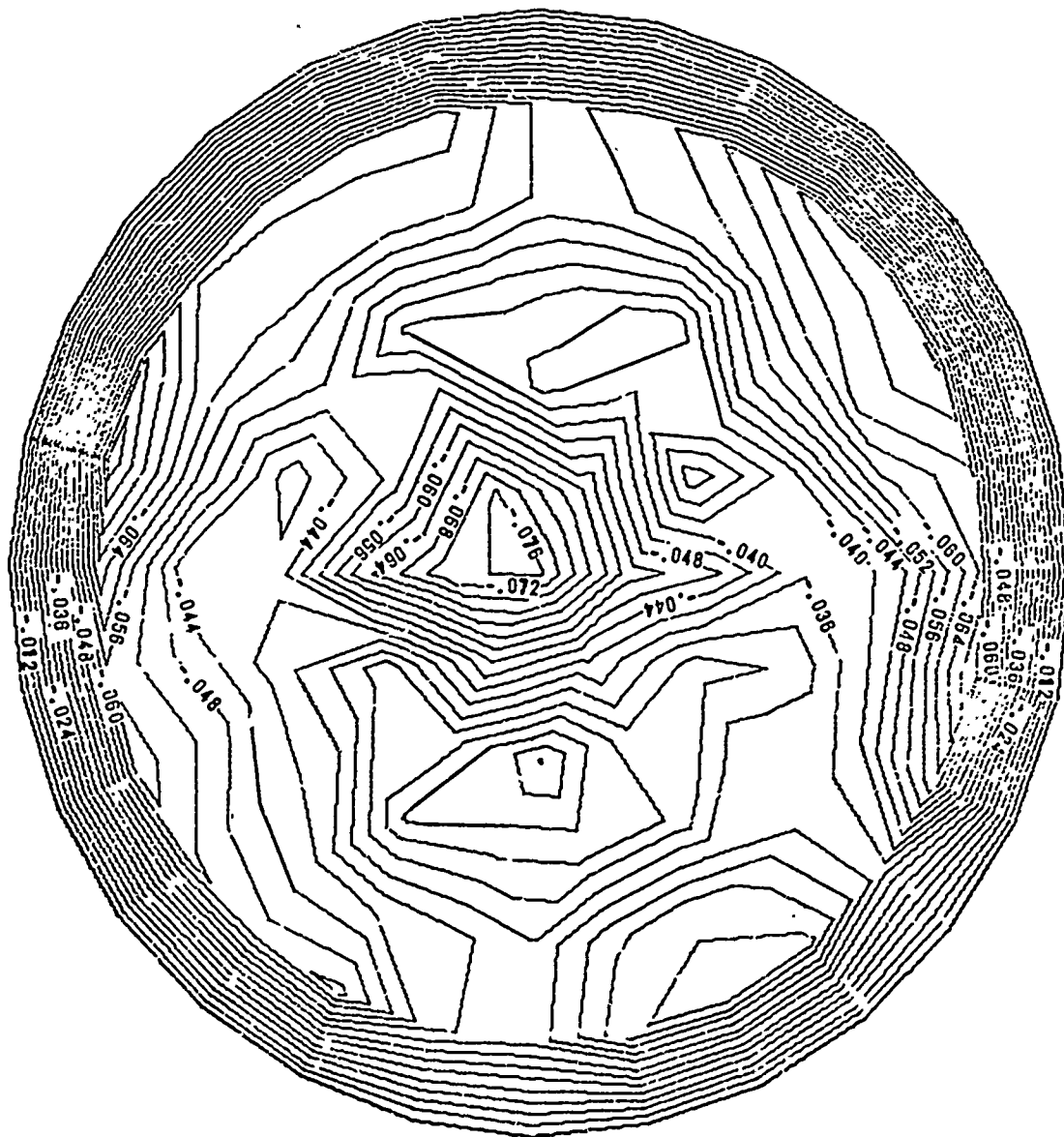


Figure 4.16e PRET Model: .15 to 3.0 psi

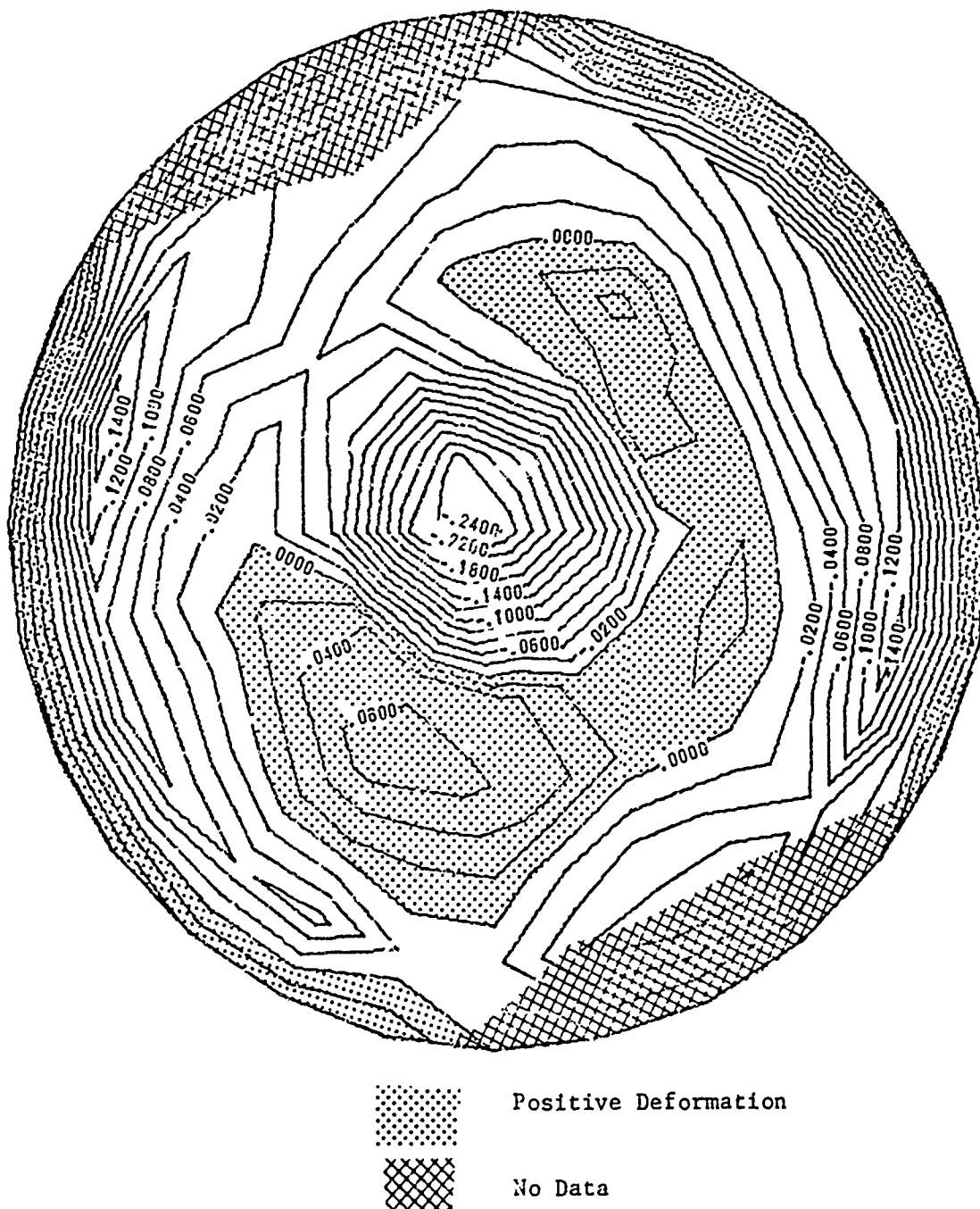


Figure 4.16f PRET Model: Imperfections Plus Deflections at 3.0 psi

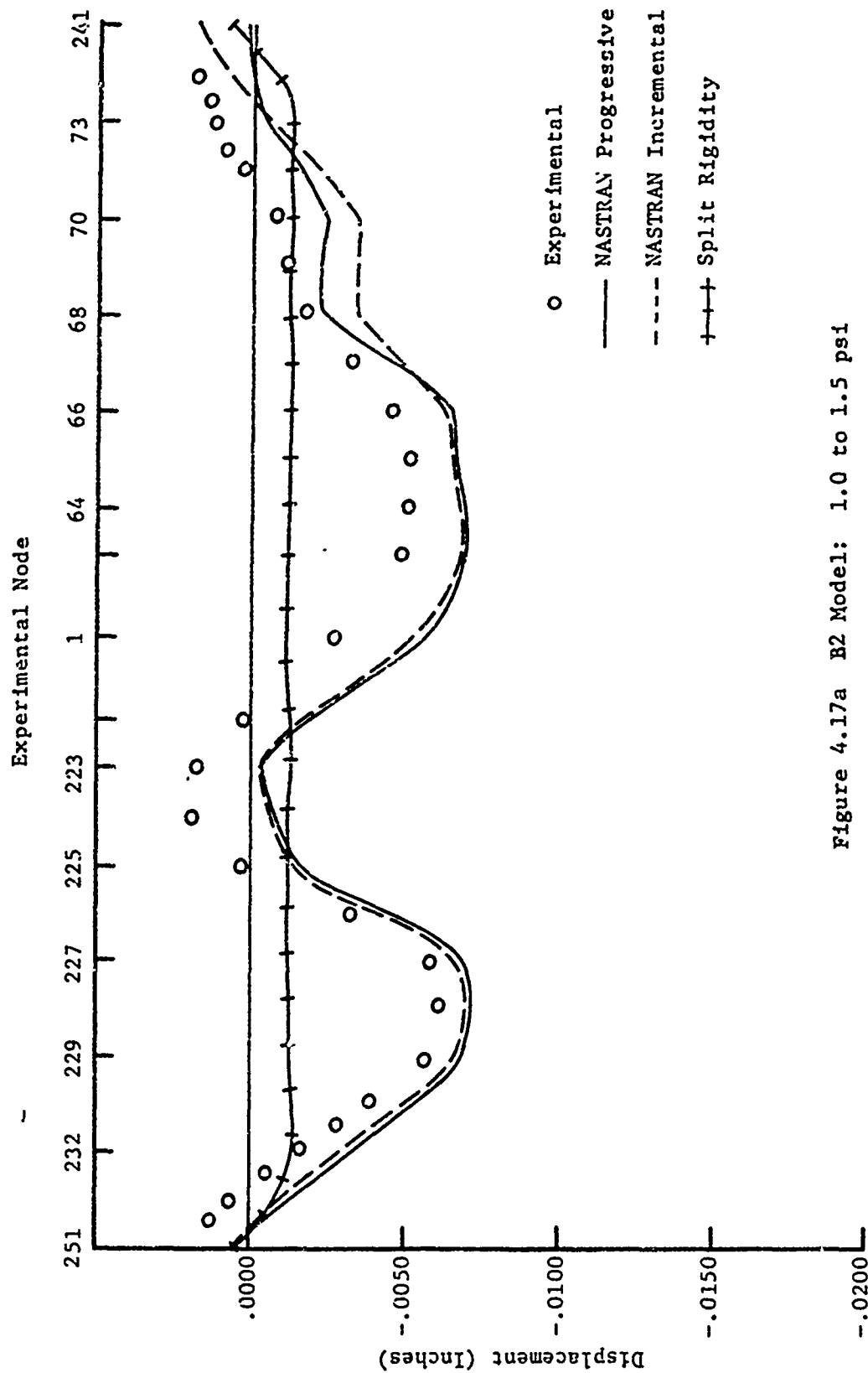


Figure 4.17a B2 Model: 1.0 to 1.5 psi

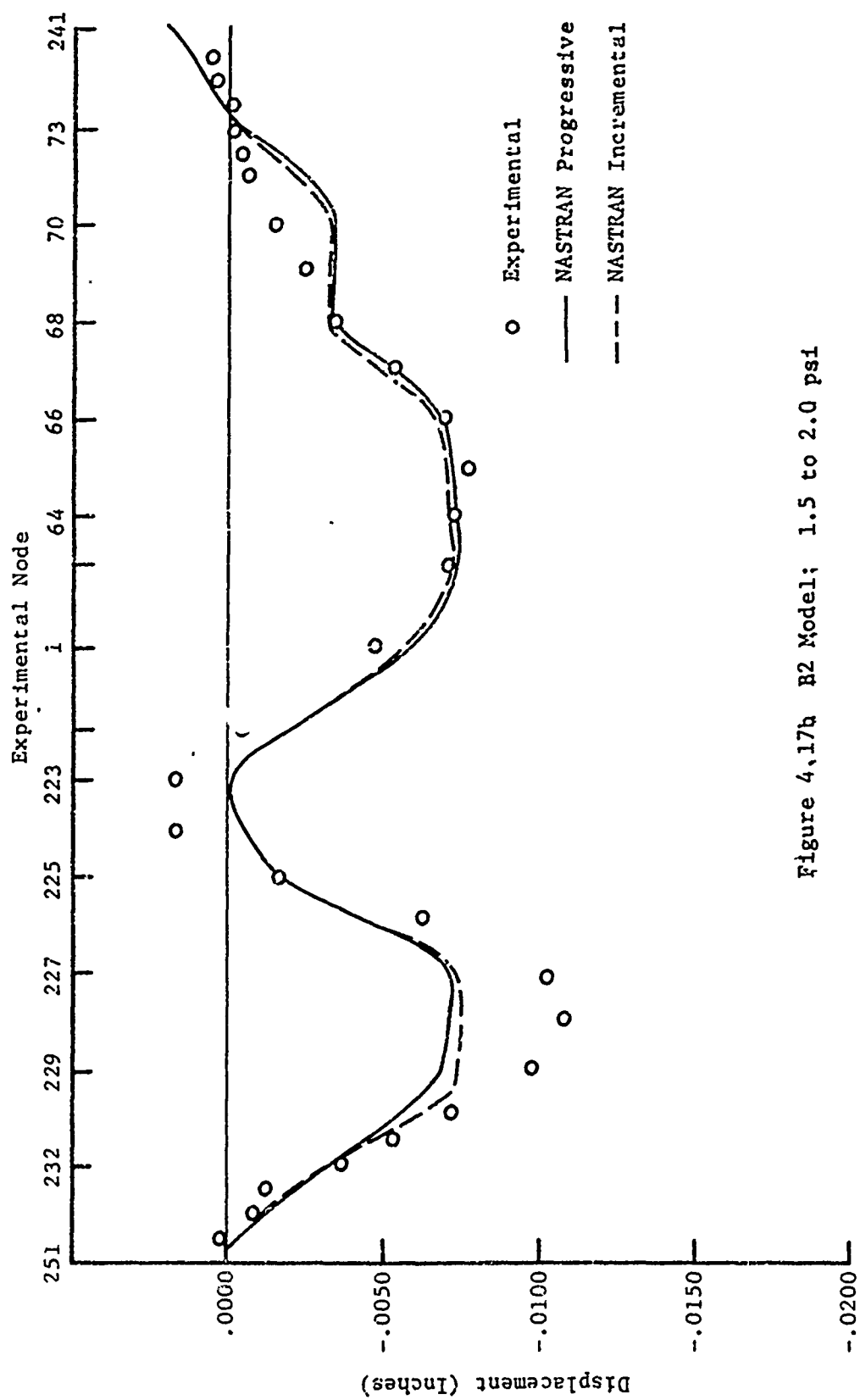


Figure 4.17b B2 Model; 1.5 to 2.0 psi

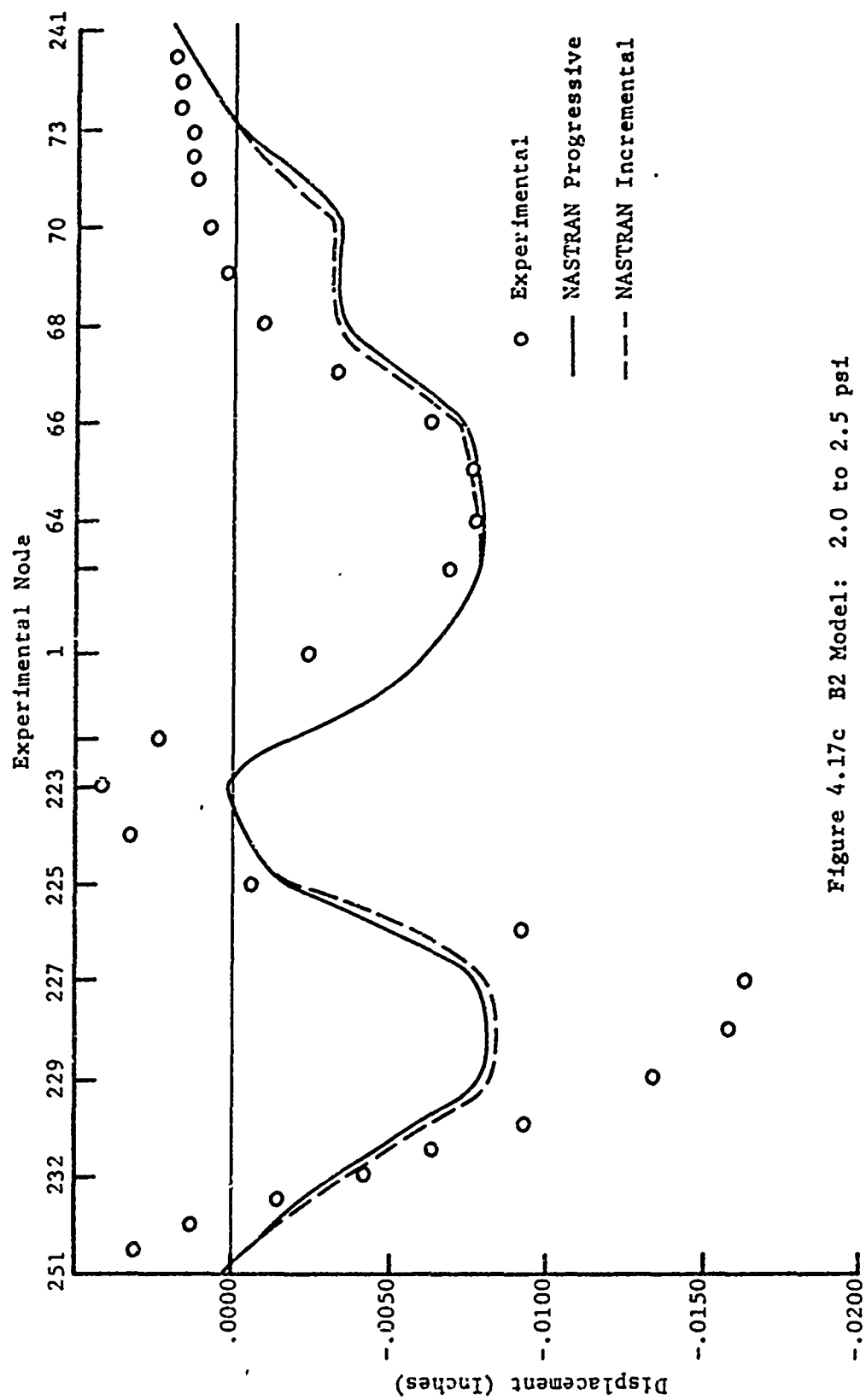


Figure 4.17c B2 Model: 2.0 to 2.5 psi

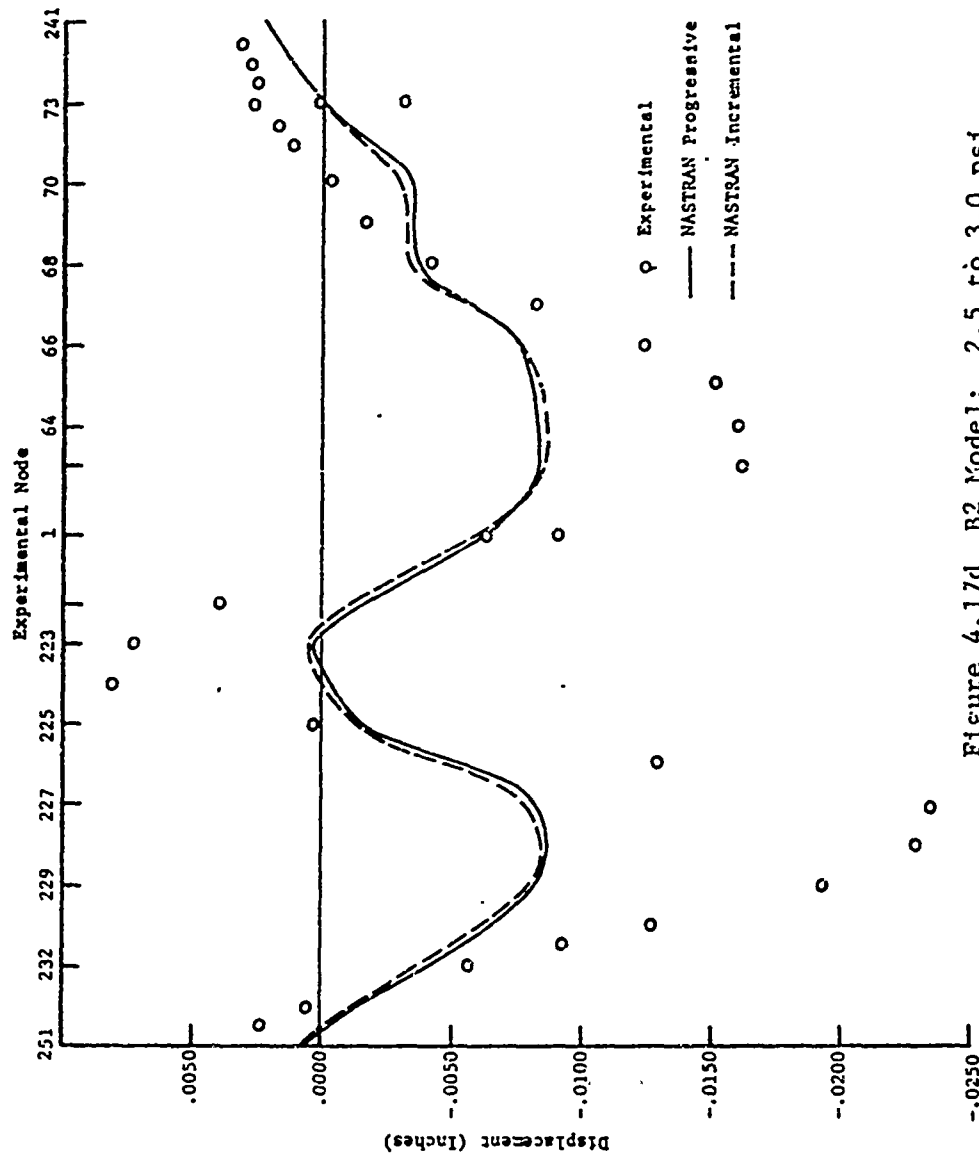


Figure 4.17d B2 Model: 2.5 to 3.0 psi

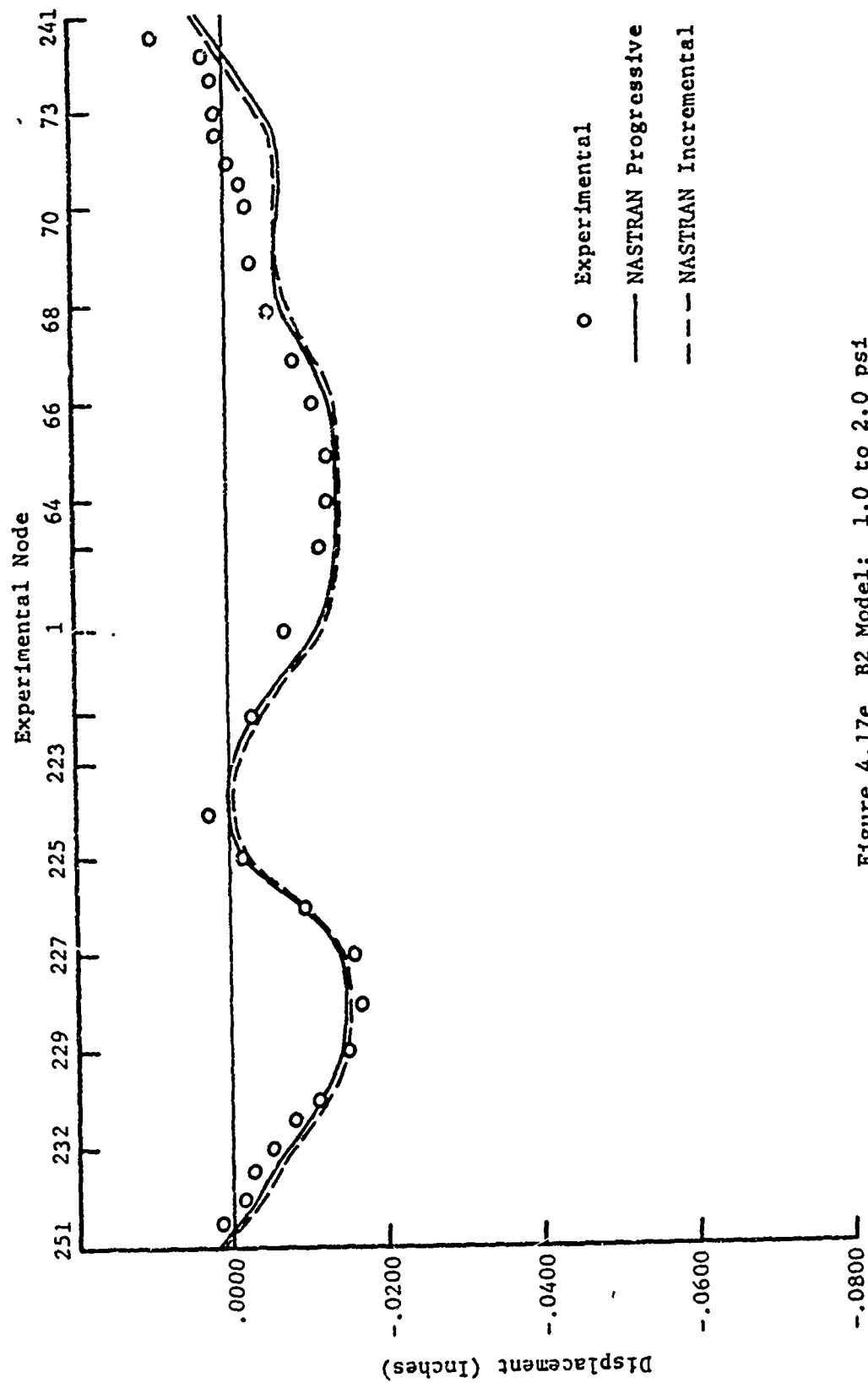


Figure 4.17e B2 Model: 1.0 to 2.0 psi

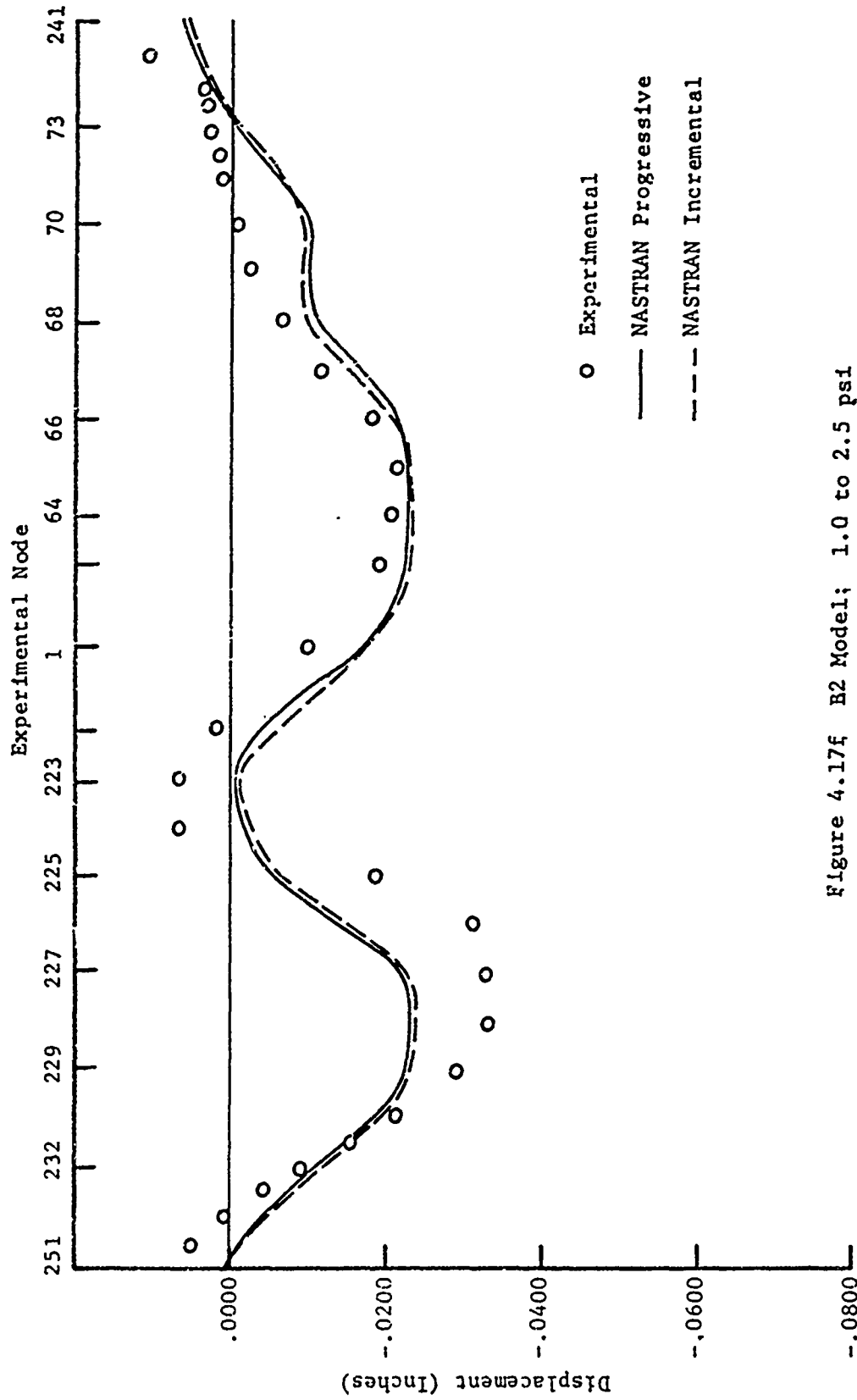


Figure 4.17f B2 Model; 1.0 to 2.5 psi



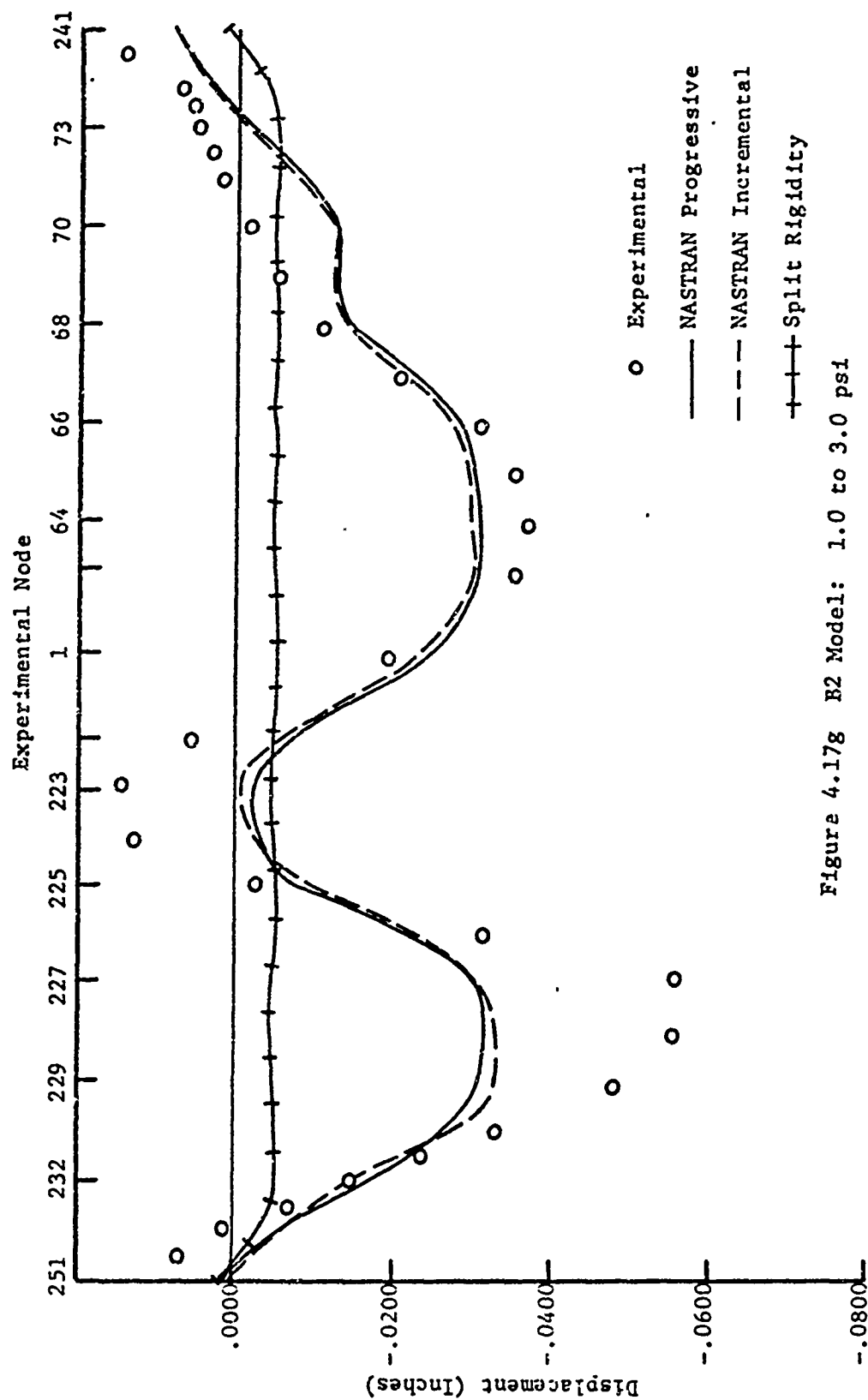


Figure 4.17g B2 Model: 1.0 to 3.0 psi

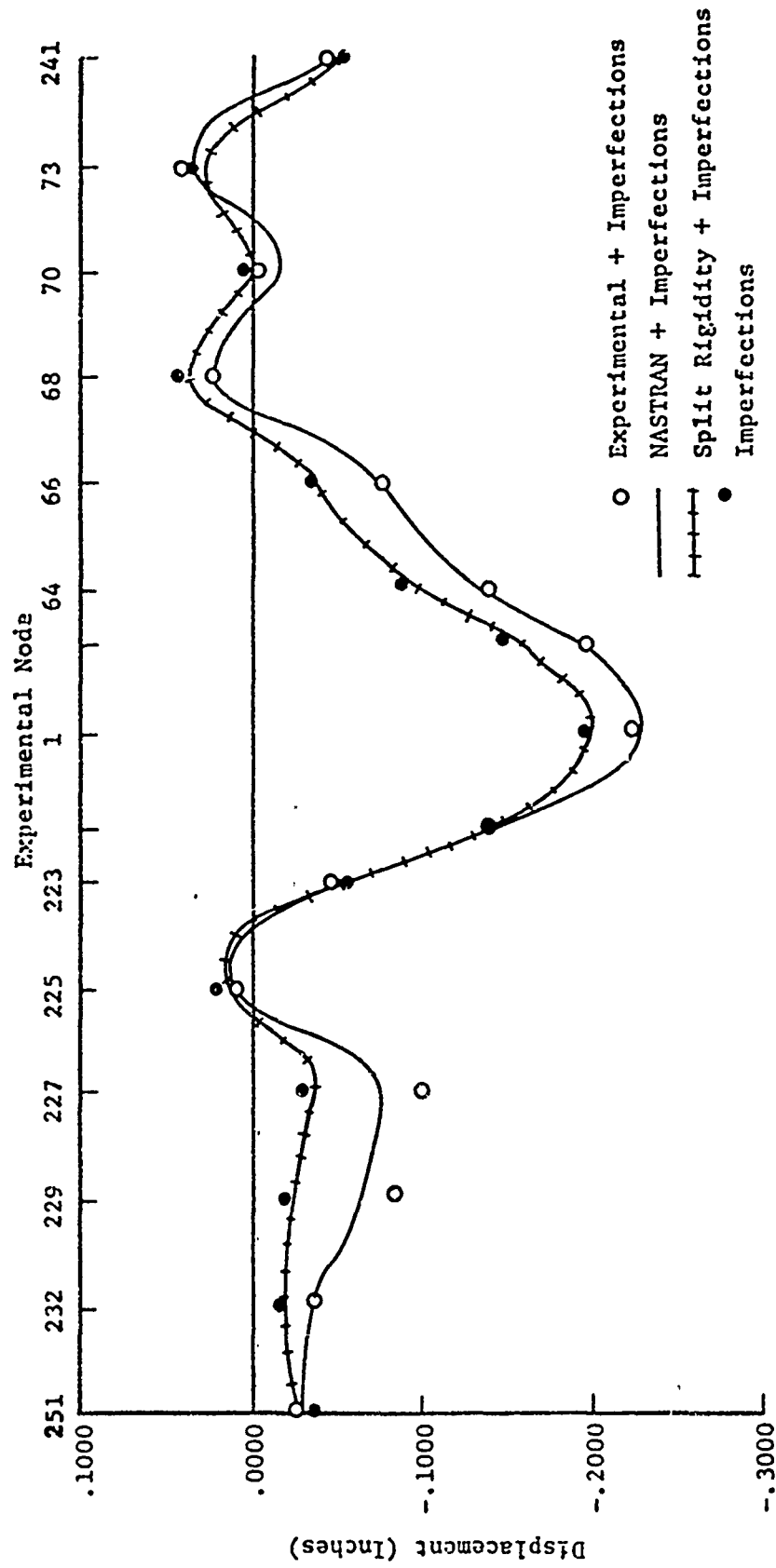


Figure 4.17h B2 Model: Imperfections Plus Deflections

as expressed by Equation 2.10 are shown as the hatched line in these figures. NASTRAN predictions appear as the dashed and solid lines. For the B2 model, the solid lines were calculated by adding the displacements predicted from a previous load increment to the grid positions at the start of that increment to get a new set of grid point locations for subsequent loading. This prediction method was called the "progressive" method. A second set of NASTRAN predictions appears as the dashed lines in the figures. For these calculations, the grid positions at the start of each load increment were taken as those measured experimentally. These predictions were called the "incremental" calculations. The remaining data on these figures are the experimental deflection values at each point along the reference line and are represented by the circles.

These figures also showed good deflection pattern agreement between NASTRAN calculations and the experimental results, with magnitudes in potential buckle regions being underpredicted. This agreement demonstrated that the original imperfections determined the future deflection distribution and the location of the potential and final buckles. Comparison of the progressive and incremental NASTRAN calculations showed that the nonlinear growth of the imperfections in potential buckle areas was not caused by geometry changes alone. A calculation of stresses in these distressed areas indicated that material nonlinearities occurred in the members. For example, at joint 227 the maximum combined axial and bending stress as predicted by the NASTRAN incremental method at 2.0 psi external pressure load was 12.6 ksi, and was 16.2 ksi at 2.5 ksi external load. Note that

stress results were conservative since they ignored the potentially severe residual stresses initially present in the shell due to the soldering procedure, and neglected as well the underprediction of deflection at node 227 above the 2.0 psi load level. Figure 4.2 showed that significant nonlinear material behavior was expected above the 16 ksi stress level. It can safely be assumed therefore, that the underprediction in the growth of the deflection pattern in distressed areas was due to material nonlinearities in the brass.

It was also clear that for live load deflection predictions, the split rigidity method was inadequate to predict either the deflection pattern or its magnitudes. This method ignored initial residual stresses and material nonlinearities. Due to the magnitude of the initial imperfections, the combination of split rigidity predictions and imperfections shows reasonable agreement as observed from Figure 4.17h. This combination of imperfections and live load deflections is common practice, particularly for computing buckling loads as will be shown later in part 4.4.

Since no NASTRAN predictions could be made and since the split rigidity theory was inapplicable due to violation of its basic assumptions, no reference line deflection plots were made for the B1 model.

4.3.2 PRET Model Deflections. Comparisons of NASTRAN predicted and experimental deflection patterns for the PRET model were made by observing corresponding plots of Figures 4.14 and 4.16. Excellent agreement between theory and experiment was observed except at locations near the edge ring. These discrepancies were due in

part to the difference in the pinned edge assumed in NASTRAN and the actual edge support in the test.

Deflections along the reference line of Figure 4.12 appear for the PRET model in Figure 4.18. NASTRAN predictions for the "progressive" type analysis appear as the solid lines, and dashed lines represent the "incremental" type approach. Split rigidity theory predictions appear as hatched lines and experimental values are shown by circles. Deflection magnitudes were well predicted throughout except, as expected, in the potential buckle areas (areas showing the largest inward deflections).

Close agreement of incremental and progressive type analyses again suggested that nonlinear growth of the initial imperfection pattern was due to more than an imperfect shell geometry. Material nonlinearity, although likely a factor near the time of buckle formation, did not appear to initiate the nonlinear deflections near the crown. For example, calculation of combined axial and bending stresses in this area reflected typical values around 1000 psi at an external pressure of 3.0 psi. Figure 4.4 indicated an approximate yield stress of 3000 psi. Even if the experimentally measured deflections were predicted (they were up to 50 percent low), the resulting member stresses would still not indicate member yielding. Although the basic assumptions of the NASTRAN analyses did not duplicate the actual test conditions, the deflections over the majority of the shell indicated the assumptions were satisfactory. The most likely reason for not predicting the correct crown deflections was therefore creep in the plastic material. The single approximate creep test cited in Figure 4.5

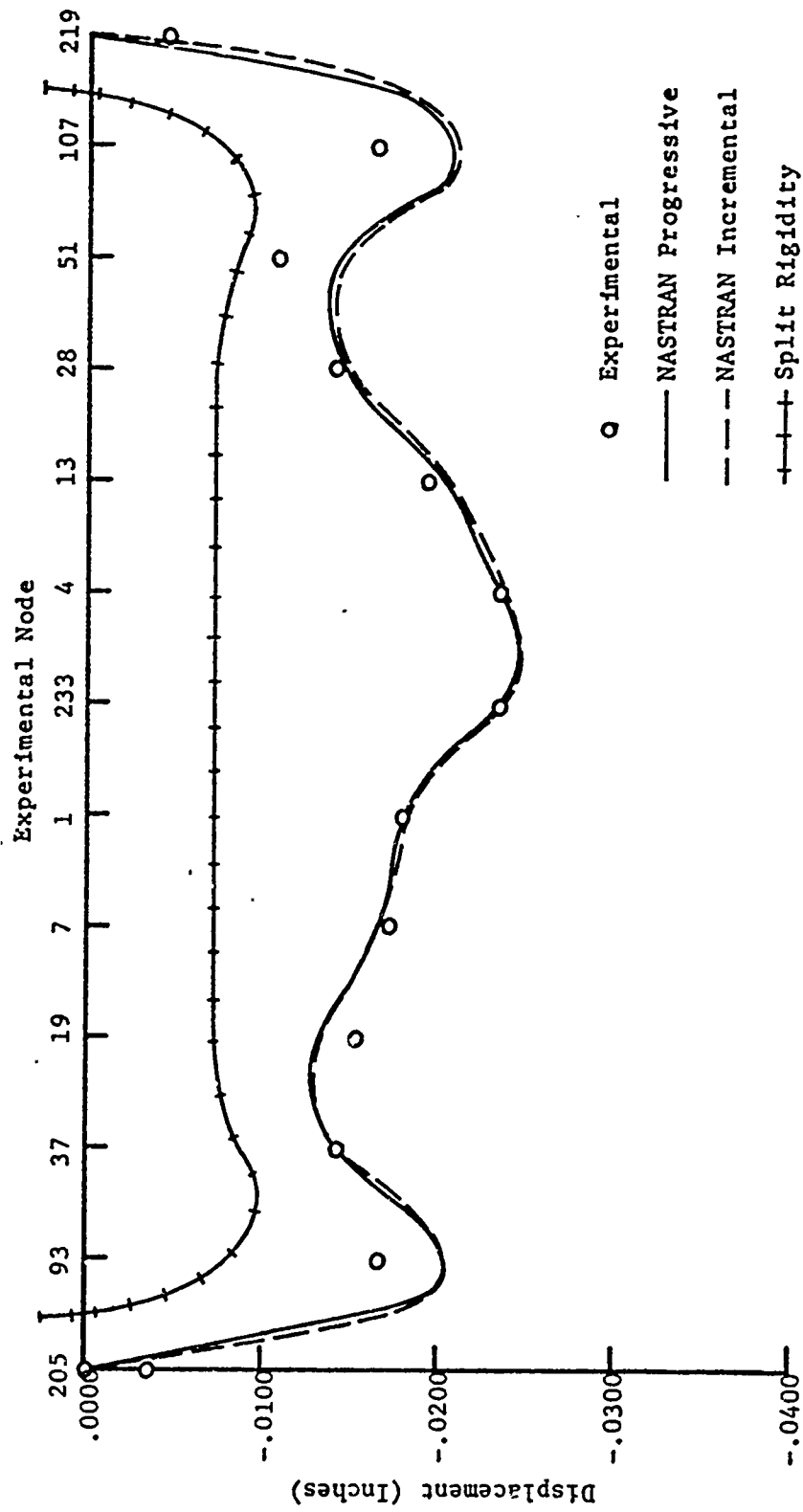


Figure 4.18a PRET Model: .15 to 1.0 psi

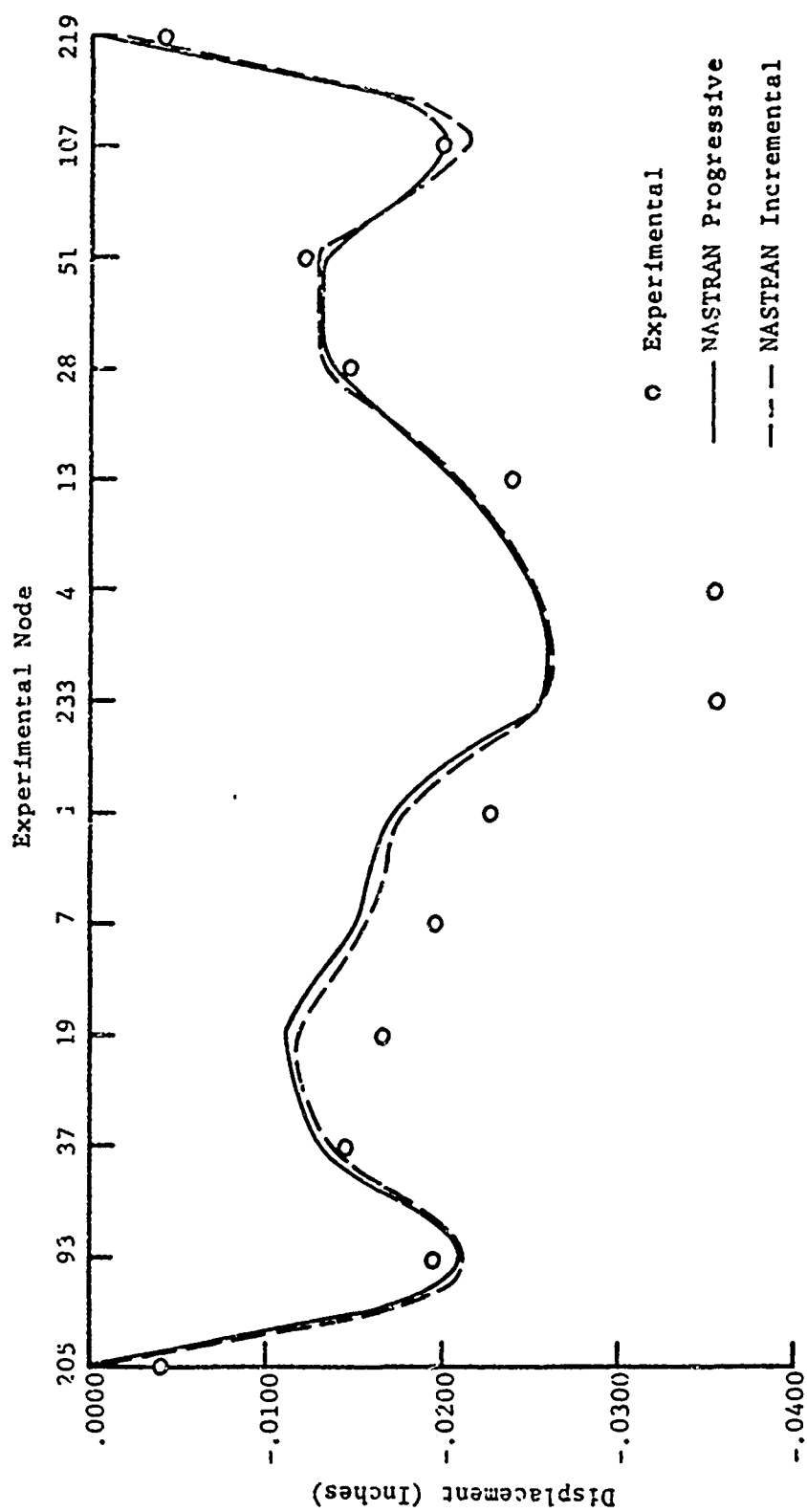


Figure 4.18b PRET Model: 1.0 to 2.0 psi

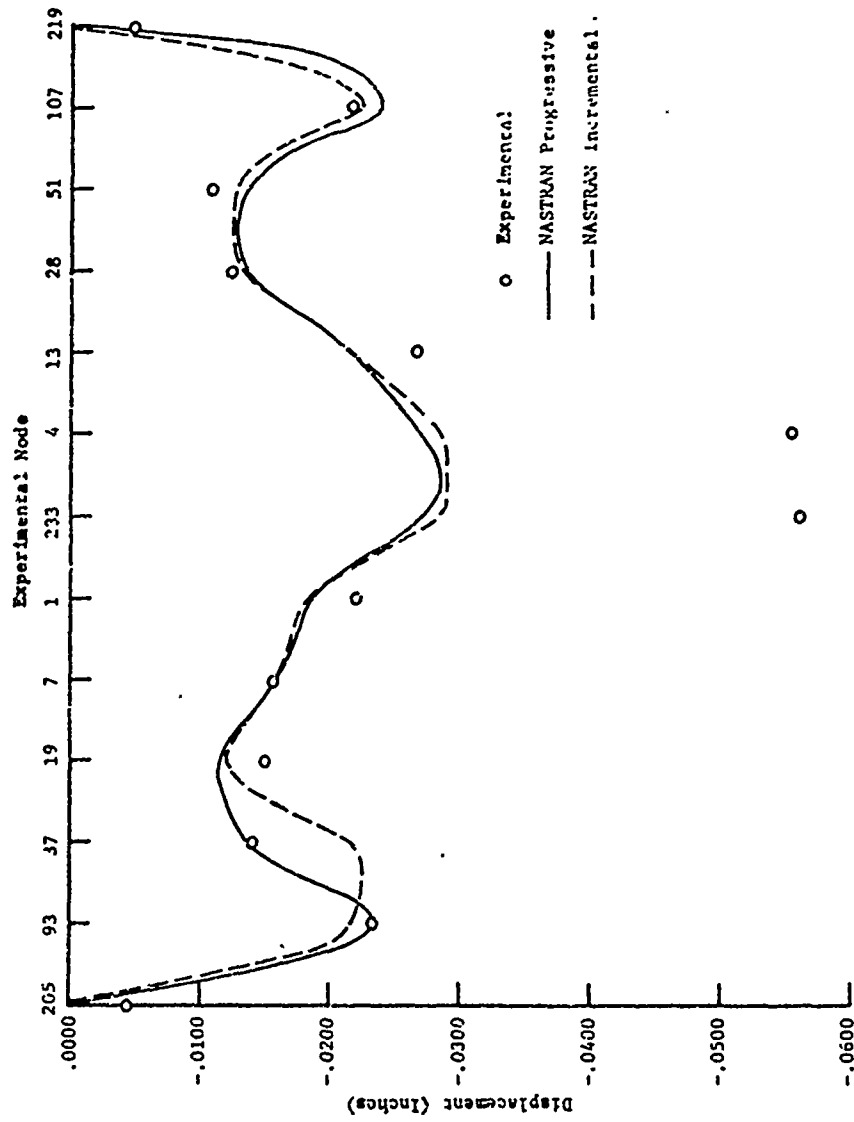


Figure 4.18c PRET Model: 2.0 to 3.0 psi



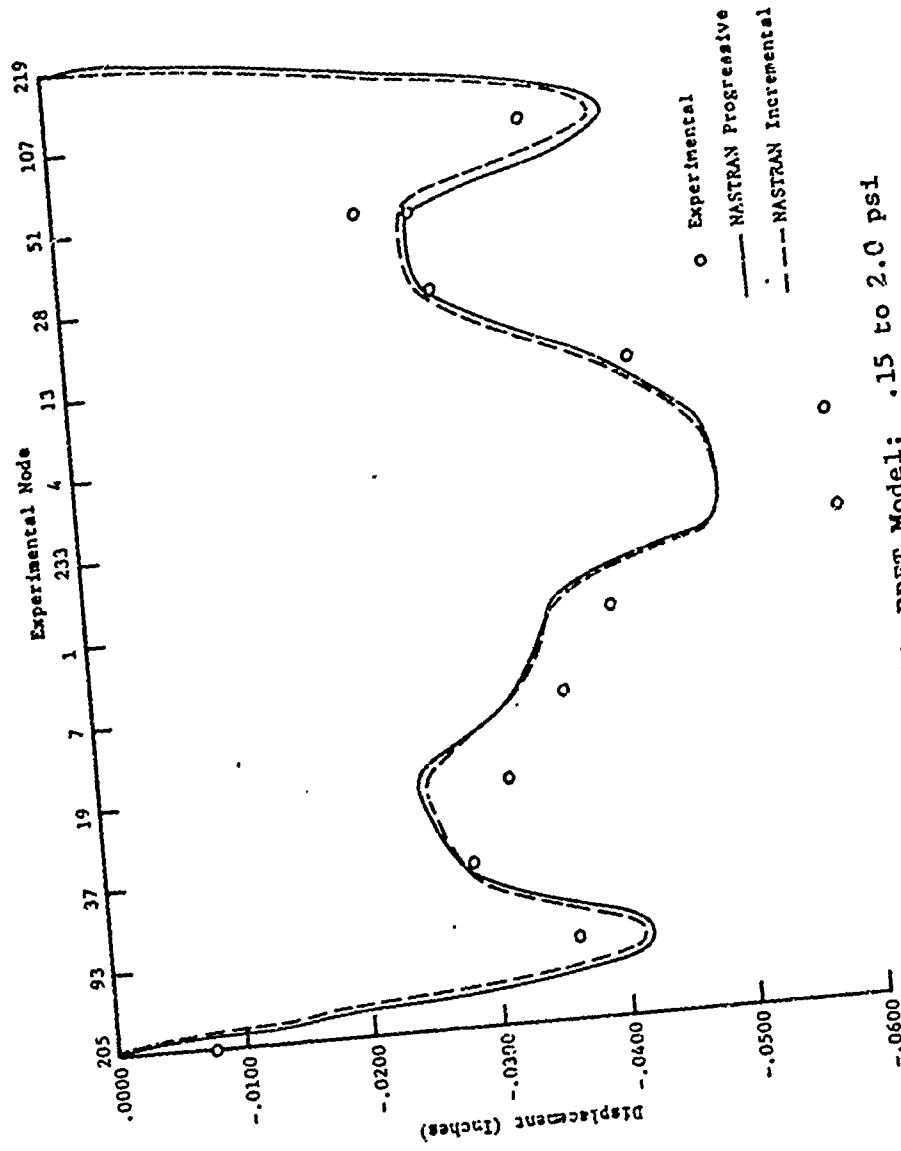


Figure 4.18d PRET Model: .15 to 2.0 psi

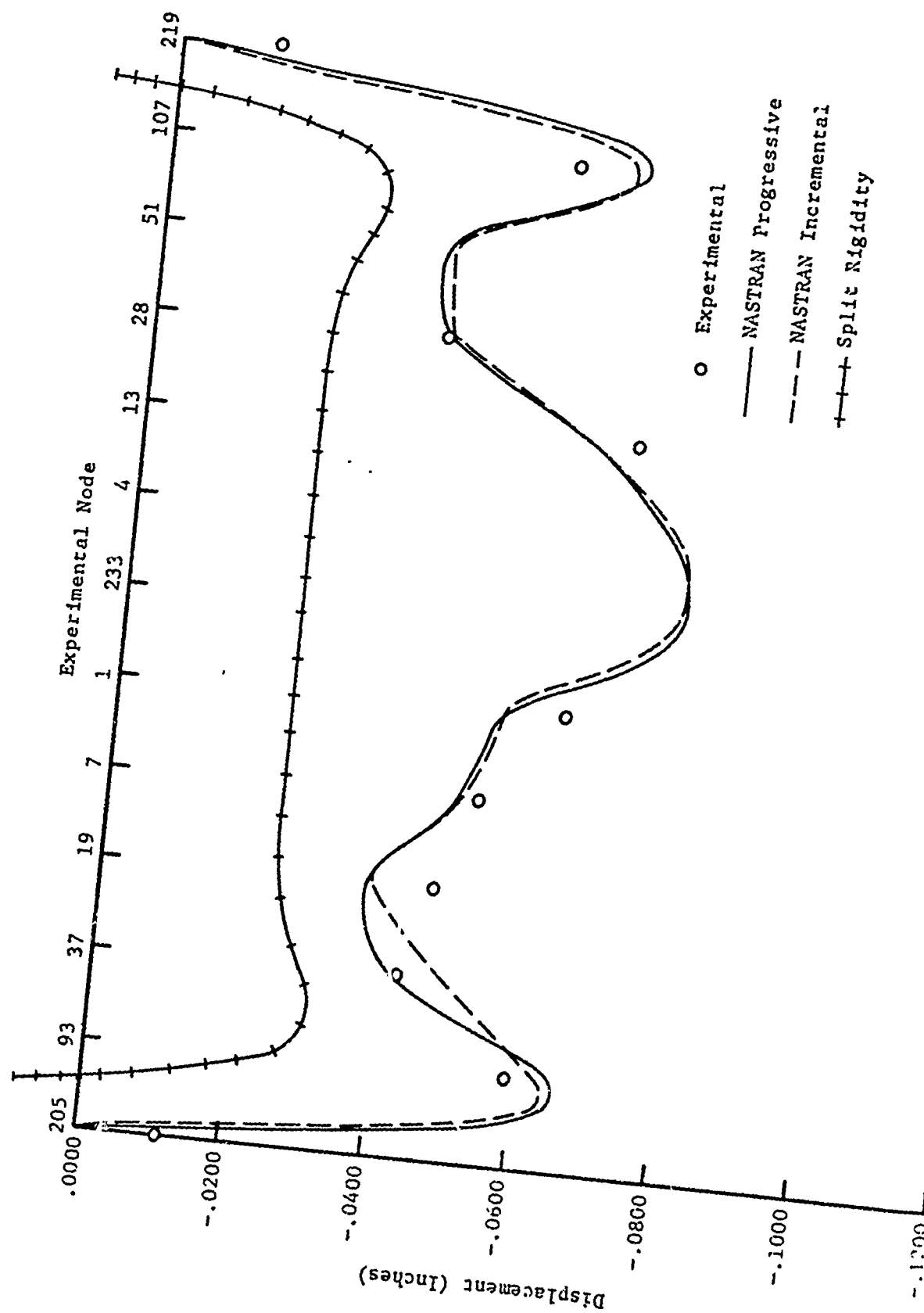


Figure 4.18e PRET Model: .15 to 3.0 psi

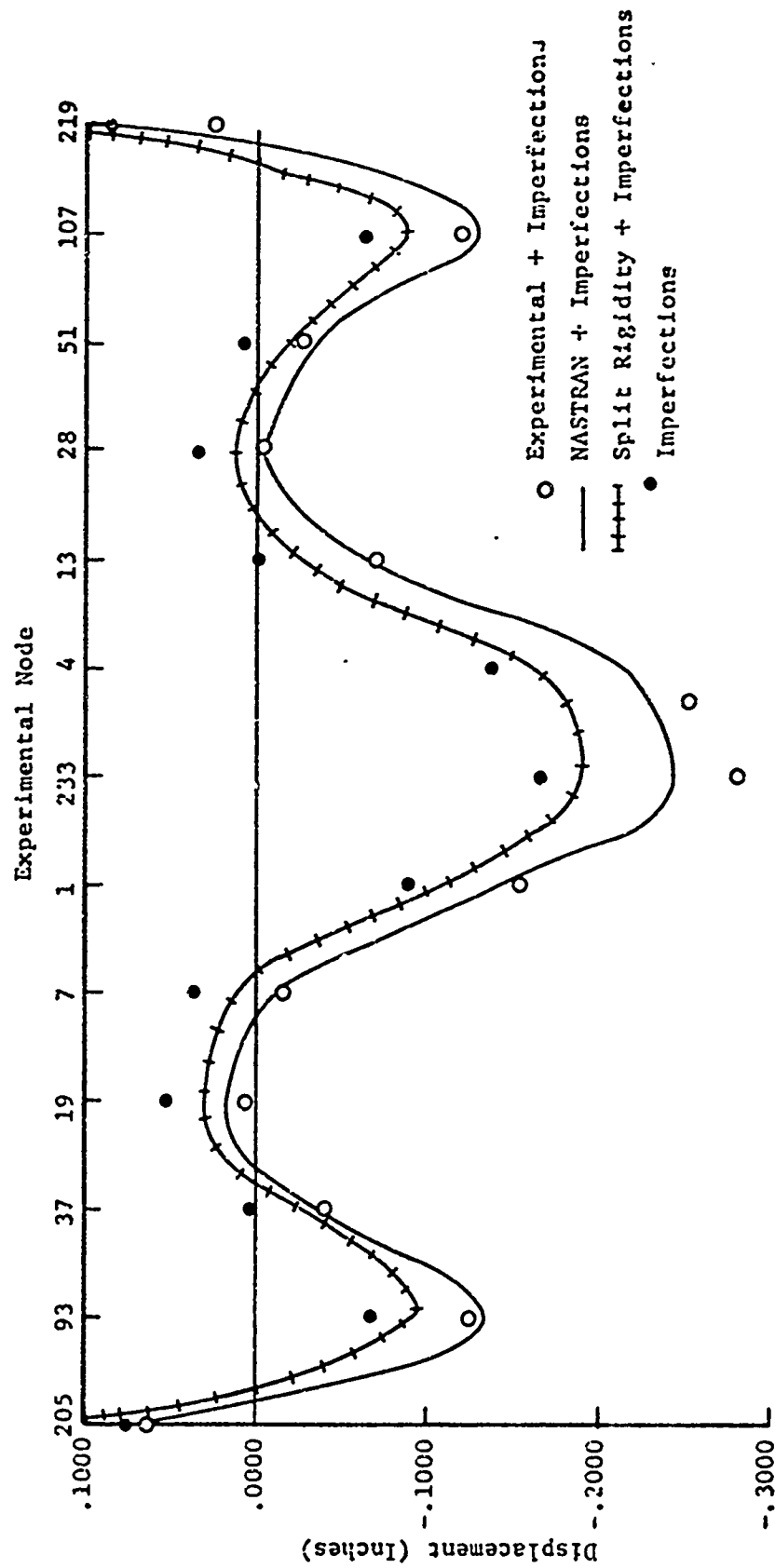


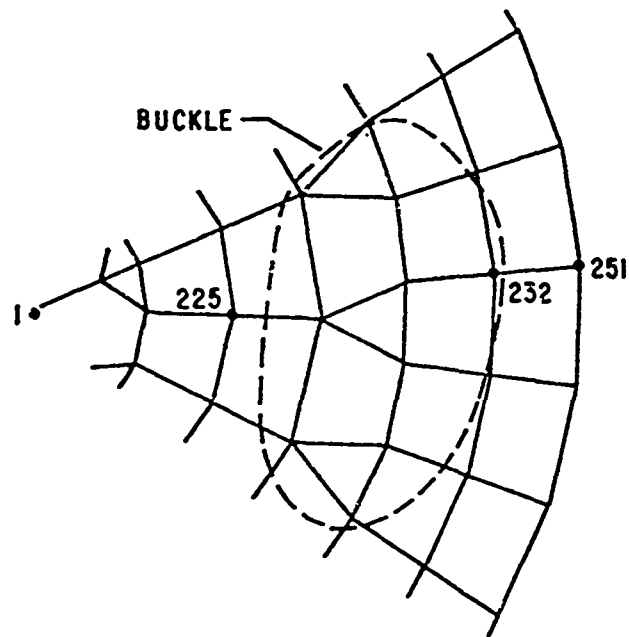
Figure 4.18f PRET Model: Imperfections Plus Deflections

was conducted at 500 psi axial stress. One can safely assume that peak shell stresses reached 1500 to 2000 psi at the 3.0 psi pressure level. The effects of creep typically increase at higher stresses. It was therefore speculated that creep, and finally the combined effects of creep and material yielding, led to the significant nonlinear deflections and later to buckling of the PRET test model.

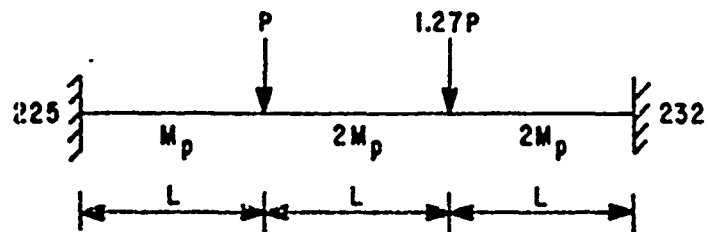
The split rigidity concept again failed to predict the live load deflection patterns and magnitudes, although the total deflection results including imperfections were again reasonable as shown in Figure 4.18f. The basic assumptions in this analysis of 1) linear material behavior and 2) a uniform grid pattern which produced uniform equivalent membrane and bending thicknesses, were not adequately satisfied by the test conditions.

4.3.3 Discussion of Deflection Results. Since the appreciable under-prediction of maximum deflections in the B2 model was due to material yielding, a simple plastic analysis of a portion of the buckled area was made. This analysis had two objectives: 1) to determine if plastic behavior was to be expected, and 2) to approximate the magnitude of the deflections if plastic behavior occurred.

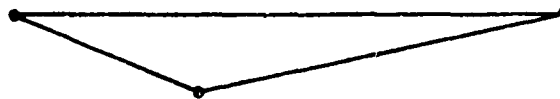
The area of the shell analyzed is shown in Figure 4.19a. This area experienced large plastic deformations not predicted by the elastic analyses. The actual geometry of this area was assumed equivalent to the planar case of Figure 4.19b. This assumption ignored potential shell action resulting from the approximately 1 : 20 rise to span ratio of the section analyzed. The opening angle of the section was  $22.2^\circ$ . Nodal loads were applied in proportion to those



(b) THE PLANAR CASE



(c) THE MECHANISM



(d) BENDING MOMENT DIAGRAM

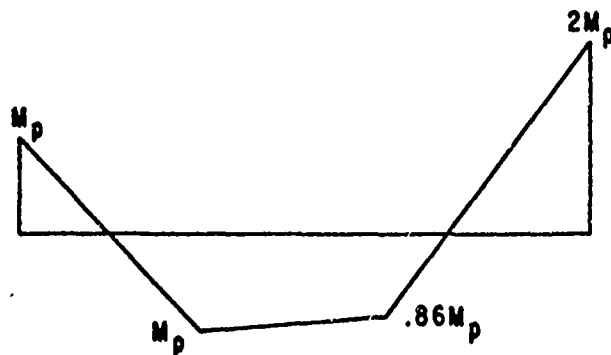


Figure 4.19 Plastic Analysis of B2 Buckled Area

used in the NASTRAN analyses. Continuous joints were assumed, and the supporting joints were taken as fixed.

Results of the analysis showed the correct mechanism to be that shown in Figure 4.19c, with the resulting moment diagram of Figure 4.19d. The ultimate load (assuming a yield stress of 18 ksi for the brass material) was  $P_u = 6.52$  lb. Since the equivalent concentrated load  $P$  for a one psi external pressure increment was 6.05 lb, plastic behavior was definitely to be expected for the maximum B2 loading which exceeded 3.0 psi.

The analysis also showed the last hinge would form at node 227. The deflection thus computed was approximately .0500 inches at node 227. To get an estimate of how well this analysis predicted the excess deflections not predicted by NASTRAN, the following procedure was used. The NASTRAN-predicted displacements at nodes 225 and 232 were added as rigid body motion to those calculated by the plastic analysis. The total deflection at node 227 was thus computed to be .0640 inches, or about 90 percent of the experimentally measured value at the 3.0 psi external pressure load.

This analysis, although rather crude, indicated plastic behavior was to be expected in the B2 model test and provided a rough estimate of the deflection to be anticipated at ultimate load. The combined results of the deflection studies also demonstrated the current critical need for relatively quick and accurate analysis techniques for predicting inelastic load-deformation behavior in space frames and reticulated shells. This point will become more obvious in the next

section, where buckling theories incorporating deflection criteria are examined.

#### 4.4 BUCKLING RESULTS

4.4.1 Parameter Variations. Several types of buckling were previously investigated in part 2.3. Experimental buckling results showed that general buckling occurred in all three models. Therefore, two general buckling theories will be compared with test results in this section. These theoretical buckling equations are repeated as follows:

Buchert:

$$p_{cr_E} = \frac{2Et_m^2}{R^2} \left\{ -0.54 \frac{\Delta}{t_m} - 0.145 \sqrt{9.9 \left(\frac{\Delta}{t_m}\right)^2 + 3.08 \left(\frac{t_b}{t_m}\right)^3} \right. \\ \left. + \sqrt{1.09 \left(\frac{\Delta}{t_m}\right)^2 - 0.03 \frac{\Delta}{t_m} \sqrt{9.9 \left(\frac{\Delta}{t_m}\right)^2 + 3.08 \left(\frac{t_b}{t_m}\right)^3} + 0.359 \left(\frac{t_b}{t_m}\right)^3} \right\} \quad 2.18$$

Von Karman: (adapted to the split rigidity concept)

$$p_{cr_E} = .365E \left(\frac{t_m}{R}\right)^2 \left(\frac{t_b}{t_m}\right)^{3/2} \quad 2.20$$

Linear elastic material behavior was assumed in these equations and they were therefore adjusted for anticipated plastic behavior as follows:

$$p_{cr_p} = \eta p_{cr_E} \quad 2.19$$

where  $\eta$  was termed a "plasticity reduction factor."

Application of the above equations to the three test models required interpretation of the following key parameters:

$E$  = Young's modulus

$t_m, t_b$  = equivalent membrane and bending thicknesses of the reticulated shell models

$R$  = shell radius

$\Delta$  = maximum radial deflection of the shell

$\eta$  = plasticity reduction factor

Each of these parameters required that certain estimates and/or assumptions be made. A brief discussion of each parameter and its effect on the buckling equations follows.

Young's modulus  $E$  for the brass and plastic materials was determined from standard tensile tests and interpreted as discussed in part 4.1.1.

The equivalent thicknesses of the test models required an estimate of an "average" member spacing and member pattern since these quantities varied along the shell meridians. Since the model designs were based on approximating a square grid pattern, the grid spacings of 2.0 inches for the B2 and PRET models and 1.0 inches for the B1 model were used in the buckling equations.

It was observed during the tests that the local radius of curvature of the potential buckle areas changed rapidly during the loading sequence. Table 4.2 shows this effect. Beside each pressure noted in the table are two values of radius  $R$ . The first was computed by fitting a spherical surface to the experimental results for the gage points within a region surrounding and including the final buckle



TABLE 4.2

## CHANGE IN RADIUS OF BUCKLE AREA WITH INCREASE IN PRESSURE

B2 MODEL (.0040 contour, 27 pts., Fig. 4.8e)			B1 MODEL (.0160 contour, 27 pts., Fig. 4.11f)			PRET MODEL (.0120 contour, 18 pts., Fig. 4.14c)		
PRESSURE (psi)	BUCKLE RADIUS (in)	SHELL RADIUS (in)	PRESSURE (psi)	BUCKLE RADIUS (in)	SHELL RADIUS (in)	PRESSURE (psi)	BUCKLE RADIUS (in)	SHELL RADIUS (in)
0.15	17.50	16.17	0.15	18.56	16.39	0.15	18.76	15.59
1.00	17.59	16.17	1.00	18.58	16.39	1.00	18.92	15.59
1.50	17.74	16.17	2.00	18.61	16.40	2.00	19.31	15.59
2.00	17.95	16.18	3.00	18.68	16.40	3.00	20.25	15.60
2.50	18.38	16.18	4.00	18.78	16.40	(Buckle)		
3.00	18.94	16.18	5.00	18.94	16.41	Multiplying factor=.60		
(Buckle)			6.00	19.57	16.42			
Multiplying factor=.73			(Buckle)					

Multiplying factor=.71

area. The region was chosen as the area for which deflections were significantly in excess of those predicted by NASTRAN during the highest load increment. The area was taken within the noted contour of the figure indicated in the table. For example, the fit for the buckle area of the B2 model was computed using the 27 experimental points located within the .0040 contour of Figure 4.8c. The second radius value noted in the table was that for the entire shell and was computed using all experimental data points. The buckle radius changed rapidly, while the shell radius was affected little during the buckle formation. If the largest buckle radii thus determined were substituted into the buckling equations 2.18 and 2.20, the predicted buckling loads would be reduced (at a minimum) by the multiplying factors noted in the table. These factors were computed from the ratio of the shell radius to the buckle radius at the maximum pressure noted in Table 4.2.

The effect of deflections on the buckling pressure predicted by Equation 2.18 was shown previously in Figures 2.9, 2.10, and 2.11. As stated in part 2.3.2, the maximum deflection  $\Delta$  could be chosen as the deflection 1) predicted using the split-rigidity method, 2) predicted by NASTRAN, or 3) measured experimentally. Current practice<sup>(37)</sup> is to add the initial imperfections to the live load deflections determined from the preceding three techniques. Other estimates were also possible and are summarized in the following section.

To show the effect of the plasticity reduction factor  $\eta$ , the B2 model was studied as an example. Computation of the factor from Equation 2.19 required an estimate of the shell member axial stress. The factor  $\eta$  is therefore plotted versus the axial stress  $\sigma_A$  for the

tensile test of Figure 4.3, and the results are shown in Figure 4.20.

To account for nonlinear behavior below the yield stress of the material the initial tangent modulus was used for  $E$  in Equation 2.9.

4.4.2 Buckling of the B2 Model. Photographs of the B2 test model after it had buckled are shown in Figure 4.21. The buckling pressure was between 3.0 and 3.5 psi.

A complete summary of the load-deformation relationships and the applicable general buckling theories is represented in Figure 4.22a, b, and c, and in Table 4.3. The results of two deflection prediction techniques are shown in the figures. The hatched line represents the split rigidity theory prediction of the maximum deflection due to combined membrane and bending effects. The solid line represents the NASTRAN prediction of the maximum deflection in the B2 model. This maximum occurred at node 227, which was the central point of the final buckle. The experimentally measured deflections at the same location are shown by the circles in the figure.

Two general buckling theories assuming elastic material behavior also appear in Figure 4.22. Buchert's formula (Equation 2.18) showed the effect of deflections on the predicted critical buckling load and is represented by the dashed line. The Von Karman theory (Equation 2.20) as adapted to the split rigidity concept predicted a constant buckling load independent of shell deflections and is noted at the 8.2 psi level.

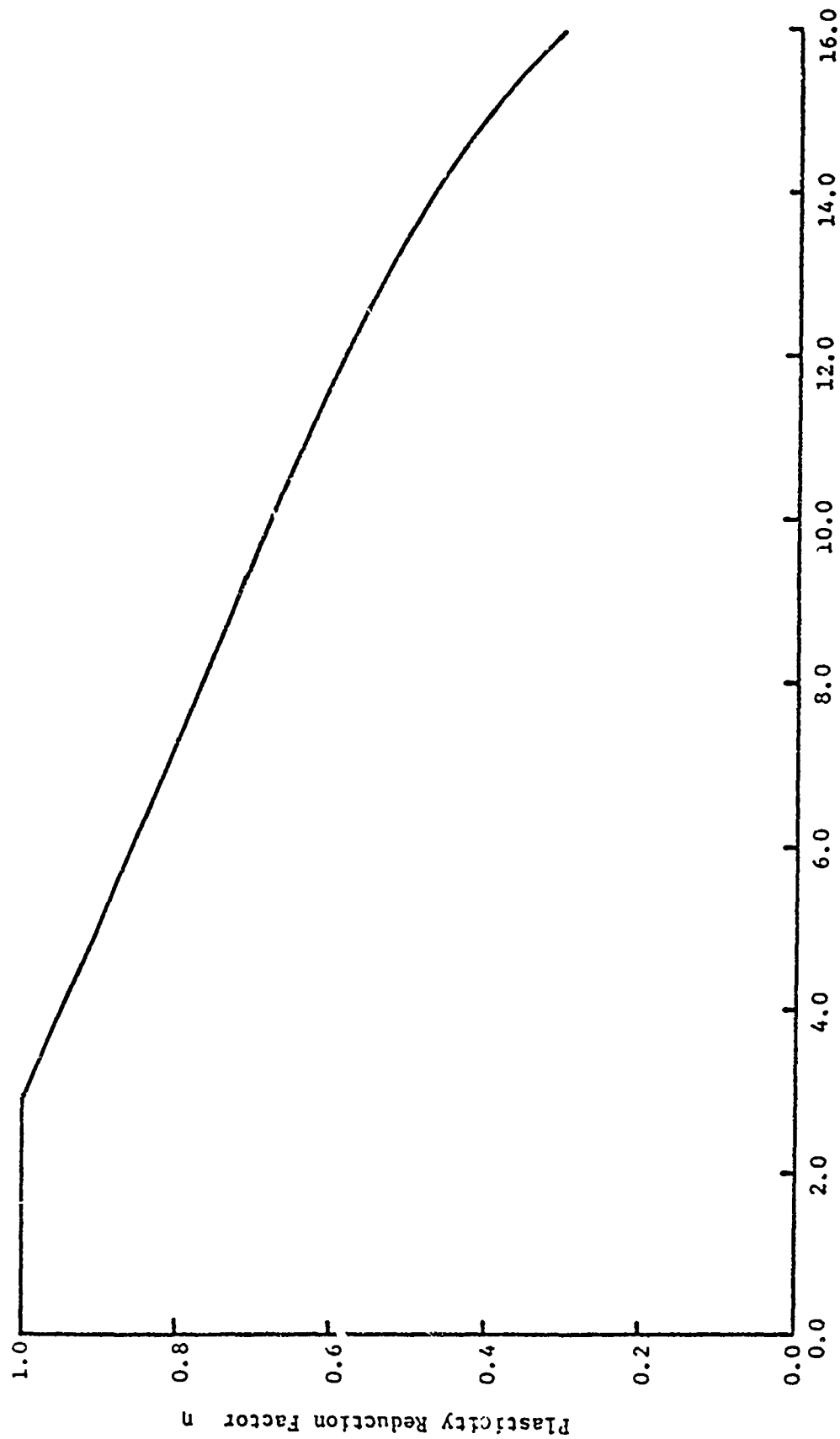


Figure 4.20 Effect of the Plasticity Reduction Factor



Reproduced from  
best available copy.



Figure 4.21 Buckled B2 Test Model

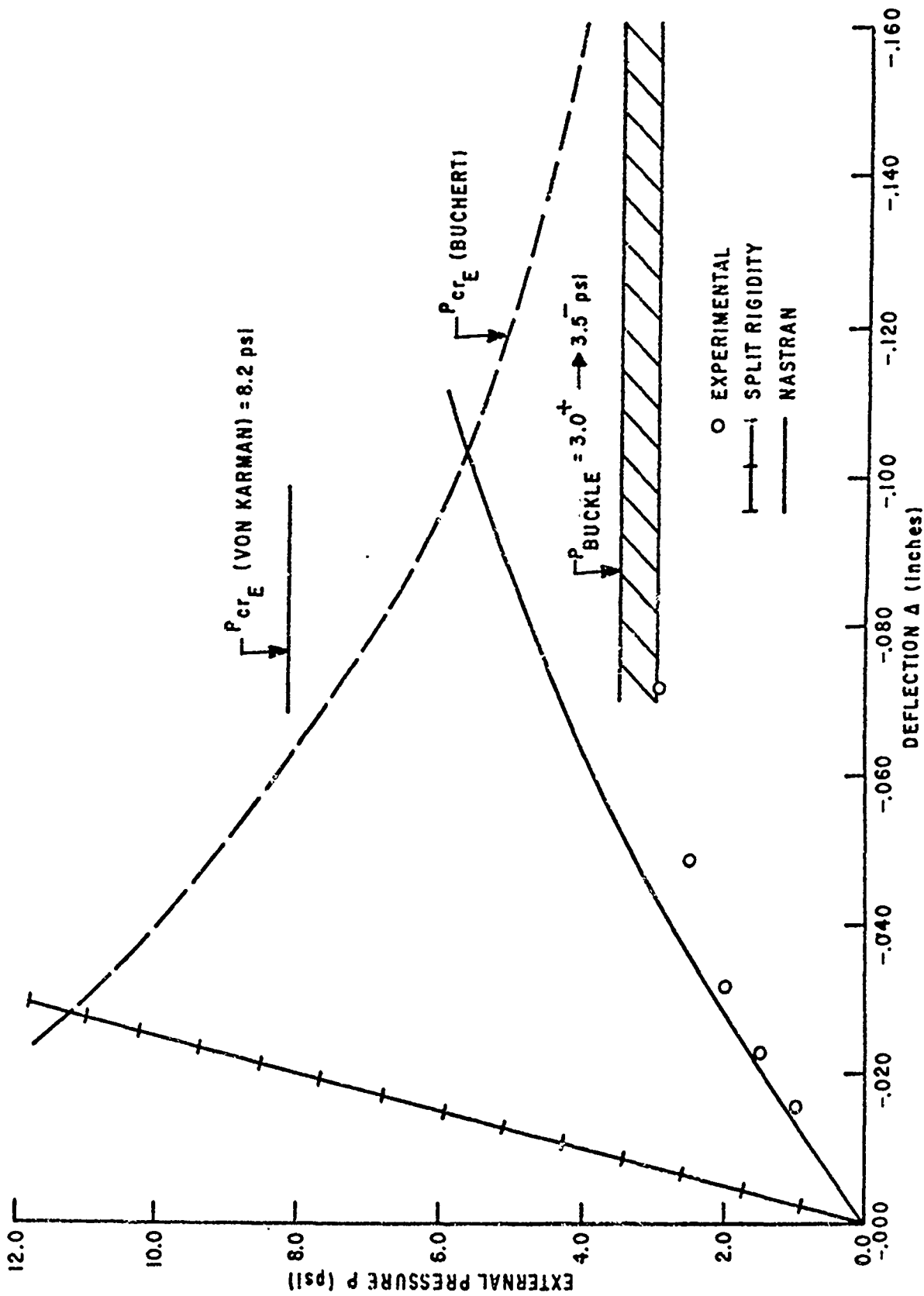


Figure 4.22a B2 Model: Load-Deflection Without Imperfections

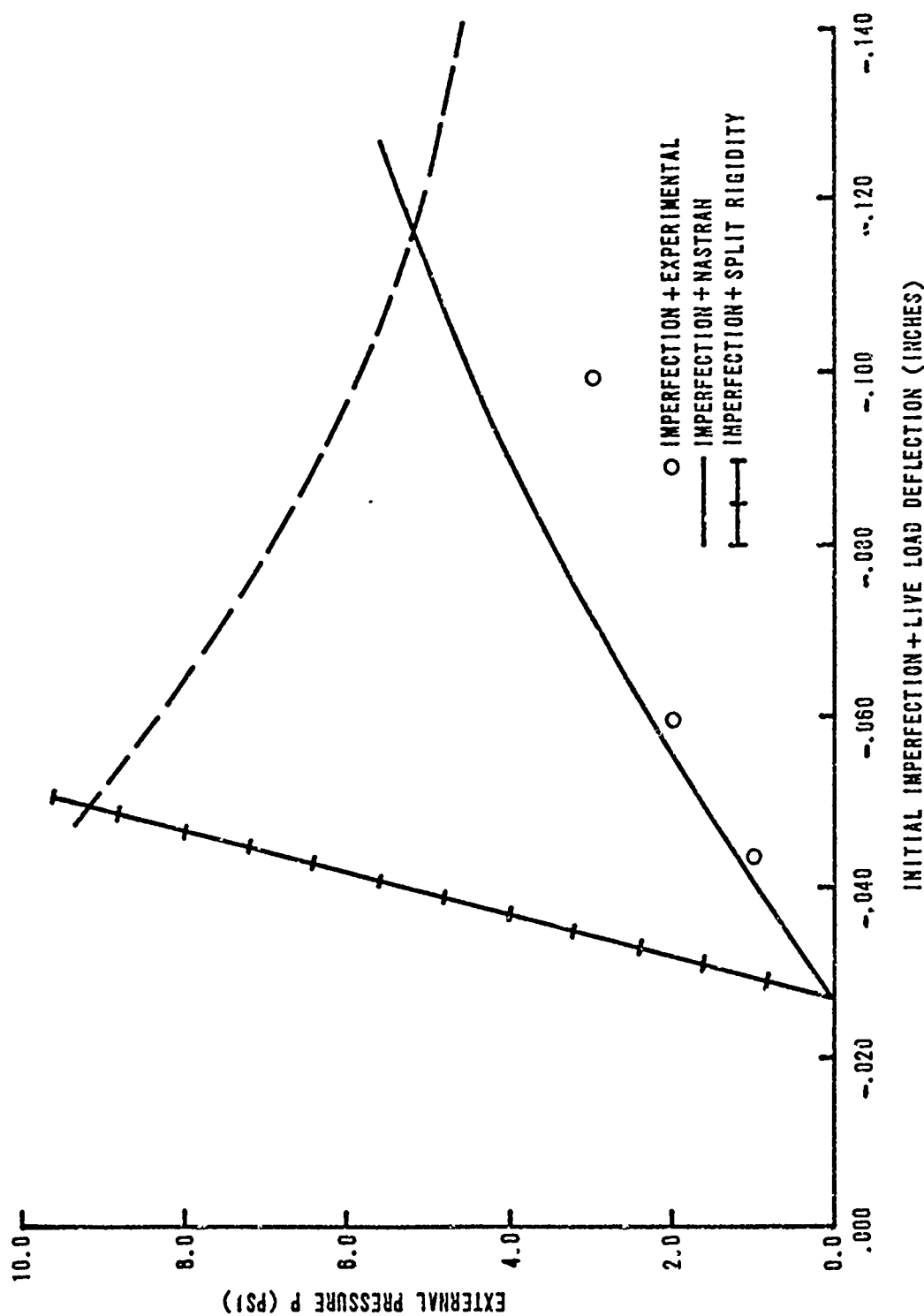


Figure 4.22b B2 Model: Load-Deflection with Global Imperfections

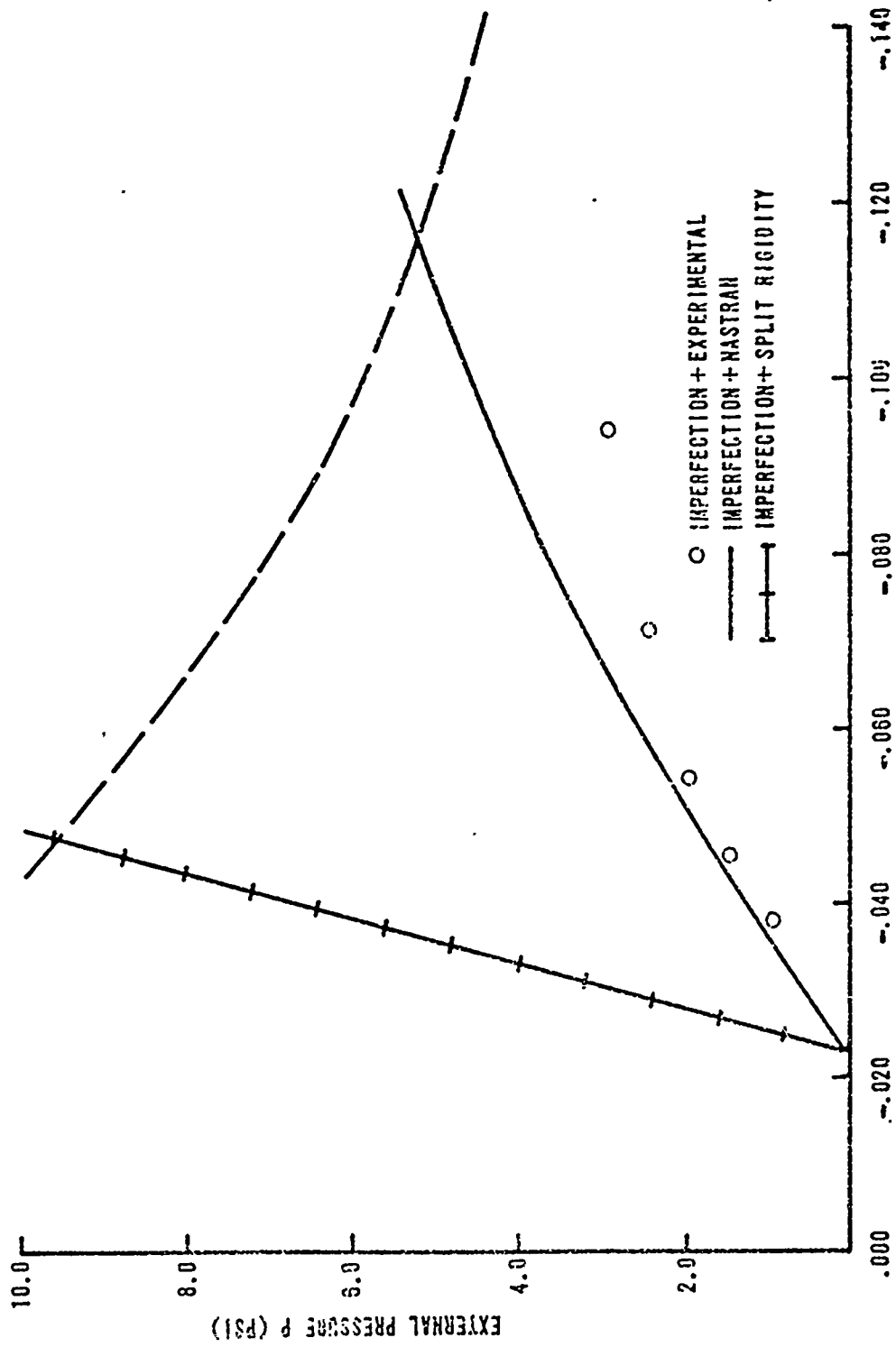


Figure 4.22c B2 Model: Load-Deflection with Local Imperfections



As previously mentioned, the initial imperfections are usually added to the live load deflections, and the combined total deflection used for the quantity  $\Delta$  in Equation 2.18. Figure 4.22a shows load vs live load deflections only. Figure 4.22b represents the same type of relationships, however the deflections shown are the combination of live load deflections and "global" initial imperfections. Global imperfections were those computed by performing a least-squares fit of a sphere to all the data points and applying Equation 3.1. The abscissa of Figure 4.22c represents the sum of the "local" initial imperfections and the live load deflections. Local initial imperfections were computed by performing a least-squares fit of a sphere to only those data points within the area of the final buckle, and then applying Equation 3.1. Recall that Table 4.2 was compiled using this approach in order to trace the change in the local radius of the buckle area.

A summary of all buckling load predictions is presented in Table 4.3. General buckling predictions are given for both Buchert and Von Karman theories, and the Euler column buckling load is shown. These results permit a quick comparison of the various theories and the assumptions which were made.

Since the live load deflection predictions were based on linear elastic analyses and it was known that nonlinear behavior occurred, it was necessary to apply a plasticity reduction factor to the results. For the B2 Model at the buckling load the member axial stress was estimated to be 7 ksi. From Figure 4.20, the corresponding reduction factor was 0.8. The predicted results of

TABLE 4.3

## SUMMARY OF PREDICTED BUCKLING LOADS

Test Model	B2			B1			PRET	
	3.0→3.5 psi			6.0→6.5 psi			3.15 psi	
Observed Buckling Load								
Type of Imperfection	None	Global	Local	None	Global	Local	None	Global Local
Imperfection Magnitude	-	-.0269	-.0225	-	-.1105	-.0273	-	-.1644 -.0523
Von Karman		8.2			15.9			3.4
Euler		50.4			199			24.0
Eq. 2.18: Δ Source								
Experimental	3.25	3.25	3.25	6.2	6.2	6.2	2.7	1.55 2.3
Predicted (NASTRAN)	5.7	5.2	5.3	-	-	-	3.1	1.6 2.45
Predicted (Split Rigidity)	11.3	9.2	9.6	22.1	10.0	17.6	4.0	1.75 3.0

Table 4.3 for the B2 model would therefore be modified by this factor. As an example, using the NASTRAN predictions (which were considered more credible than the split rigidity technique for predicting live load deflections) the predicted buckling load using Equation 2.18 was 5.7, 5.2, or 5.3 psi depending on the choice of the initial imperfection value. Current practice is to use the local imperfection in combination with the live load deflection. Thus the predicted buckling load for the B2 model by using the preceding reasoning (see Figure 4.22c) was 4.2 psi, a value within approximately 30 per cent of the observed buckling pressure.

From the parameter variations discussed in the previous section, another correction factor related to Equation 2.18 was considered. From Table 4.2, the local radius of the buckled area was shown to increase rapidly as the buckling load was approached. Extrapolating the experimental deflection curve of Figure 4.22c to its horizontal asymptote, the deflection at incipient buckling was .133 inches. A local radius of 19.5 inches was required in Equation 2.18 to predict the correct buckling load. Projecting the B2 model results in Table 4.1 above the 3.0 psi level, it is entirely reasonable to assume that this critical radius value was achieved near the critical buckling load.

4.4.3 Buckling of the B1 Model. The buckled configuration of the B1 test model is shown photographically in Figure 4.23. The buckling pressure was between 6.0 and 6.5 psi.

Load-deformation relationships and general buckling criteria for the B1 model are summarized in Figure 4.24a, b, and c, and in



Reproduced from  
best available copy.



Figure 4.23 Buckled B1 Test Model

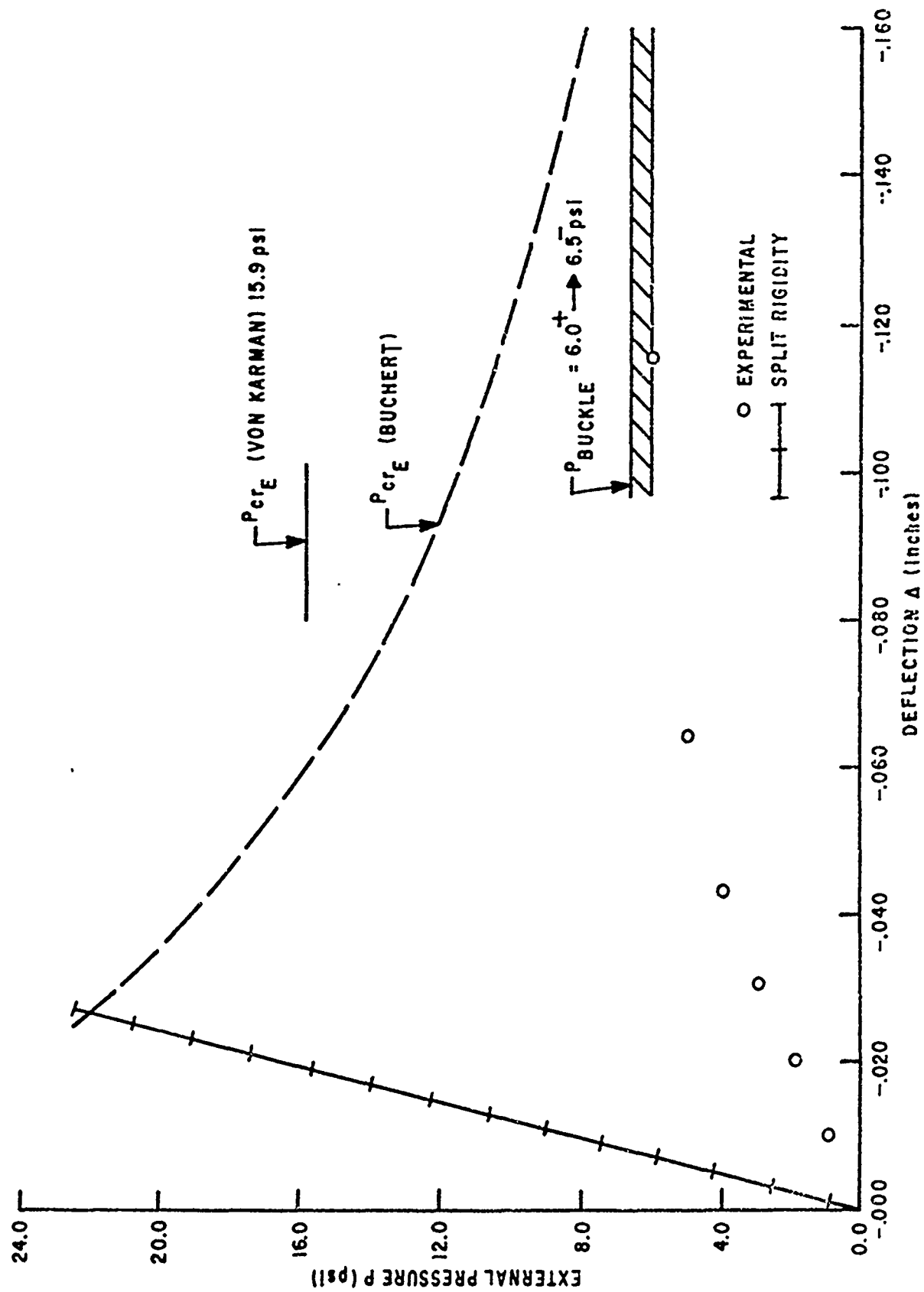
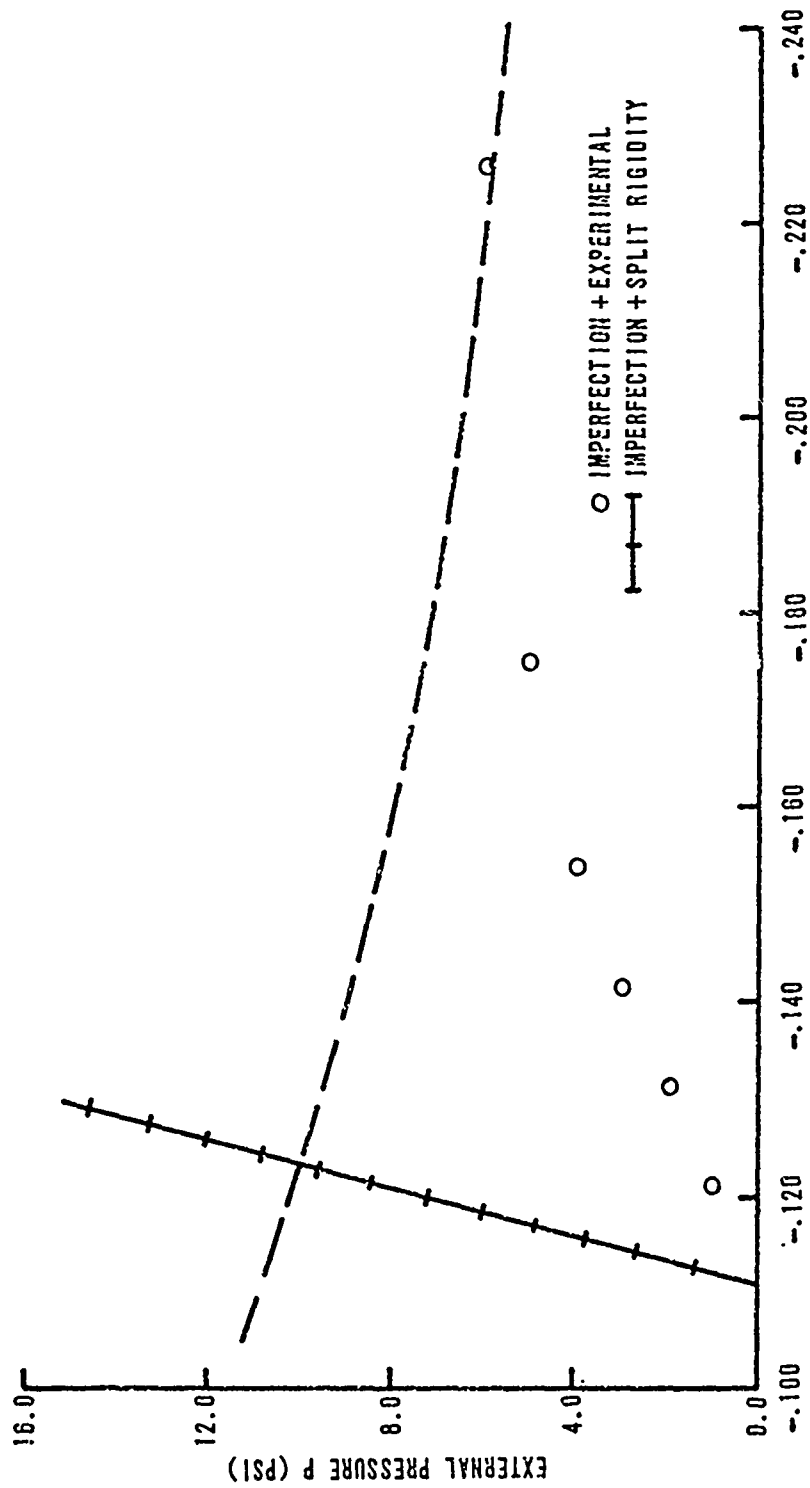


Figure 4.24a B1 Model: Load-Deflection without Imperfections



INITIAL IMPERFECTION + LIVE LOAD DEFLECTION (INCHES)

Figure 4.24b B1 Model: Load-Deflection with Global Imperfections

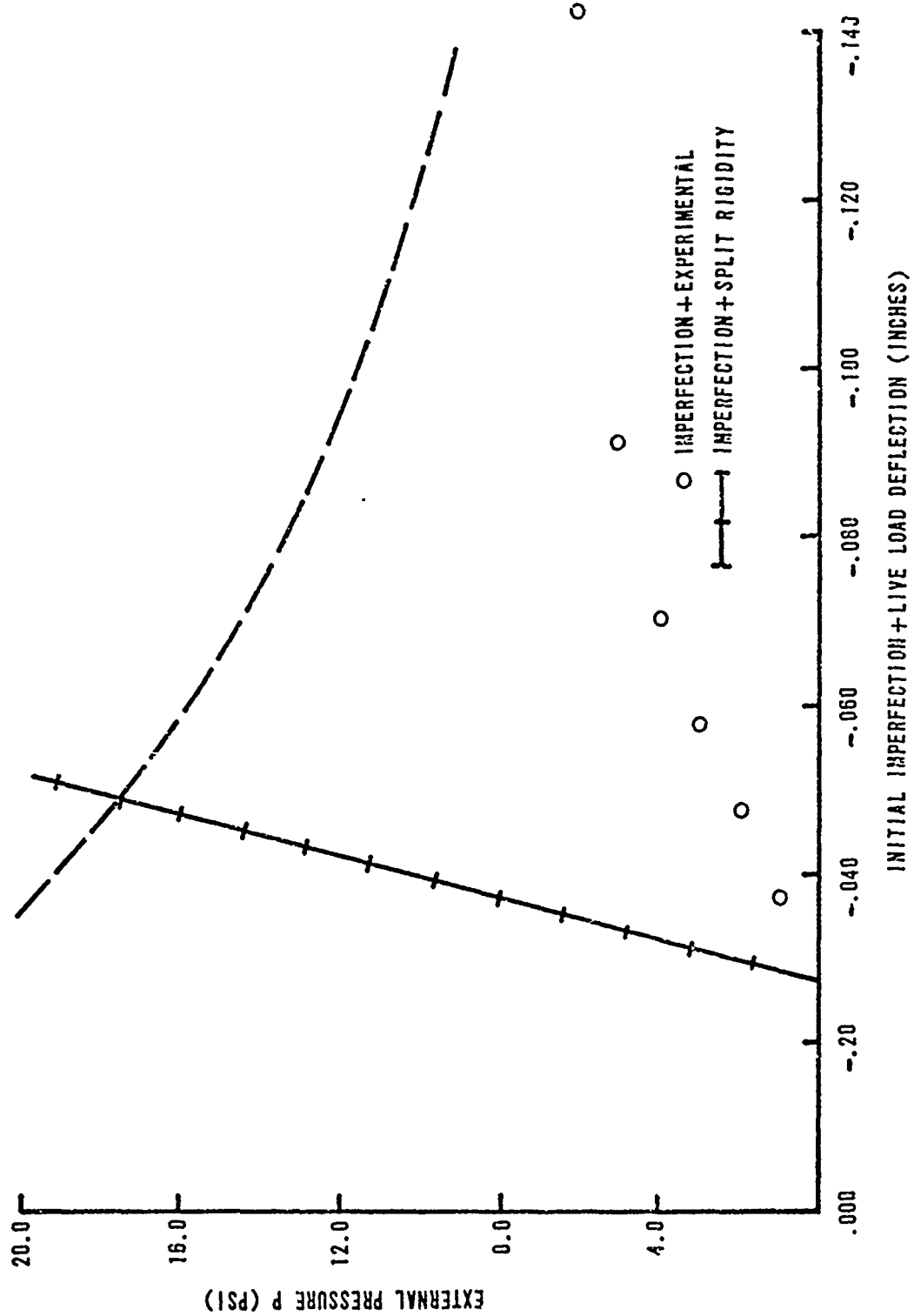


Figure 4.24c B1 Model: Load-Deflection with Local Imperfections

Table 4.3. Only the split rigidity prediction of deflection is shown in the figures since NASTRAN calculations were not made for the B1 model. Both the Buchert general buckling equation (dashed line) and the Von Karman criteria appear in the figure.

A maximum deflection at incipient buckling of .157 inches was estimated for the B1 model. Considering geometry changes only, the required buckle area radius to correctly predict the actual buckling pressure using Equation 2.18 and Figure 2.24c was 19.0 inches. The results of the radius change study (see Table 4.2) showed that this radius value was likely achieved at a pressure slightly below the 6.0 psi level.

4.4.4 Buckling of the PRET Model. Figure 4.25 shows the PRET model after it buckled at an external pressure of 3.15 psi.

The PRET model buckling criteria and load-deformation behavior are shown in Figure 4.26a, b, and c, and Table 4.3. Both NASTRAN (solid line) and split rigidity (hatched line) deflection predictions are shown along with the Buchert (dashed line) and Von Karman buckling predictions.

As Figure 4.26c shows, when the NASTRAN prediction of maximum live load deflection plus the local initial imperfection was used in Equation 2.18 a buckling load of 2.45 psi was predicted. This predicted critical pressure was 78 per cent of the actual value, which represents an under-prediction. The results of Table 4.2 indicate that a significant local radius change occurred in the buckle area. This evidence also substantiates the under-prediction of the critical pressure for the PRET model. This under-prediction of buckling behavior was not totally unexpected, and has been observed by numerous other investigators.





Figure 4.25 Buckled PRET Test Model

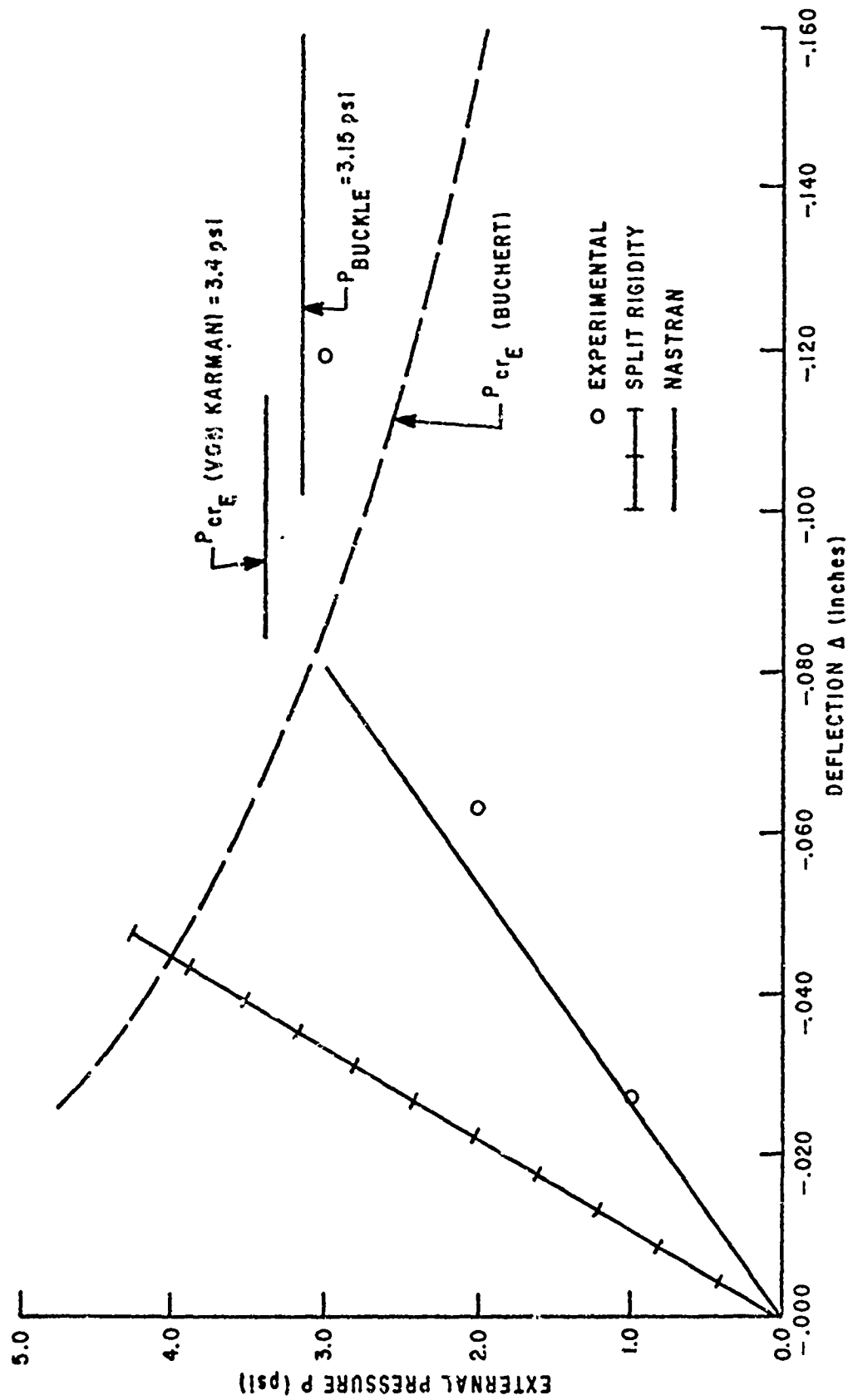


Figure 4.26a PRET Model: Load-Deflection without Imperfections

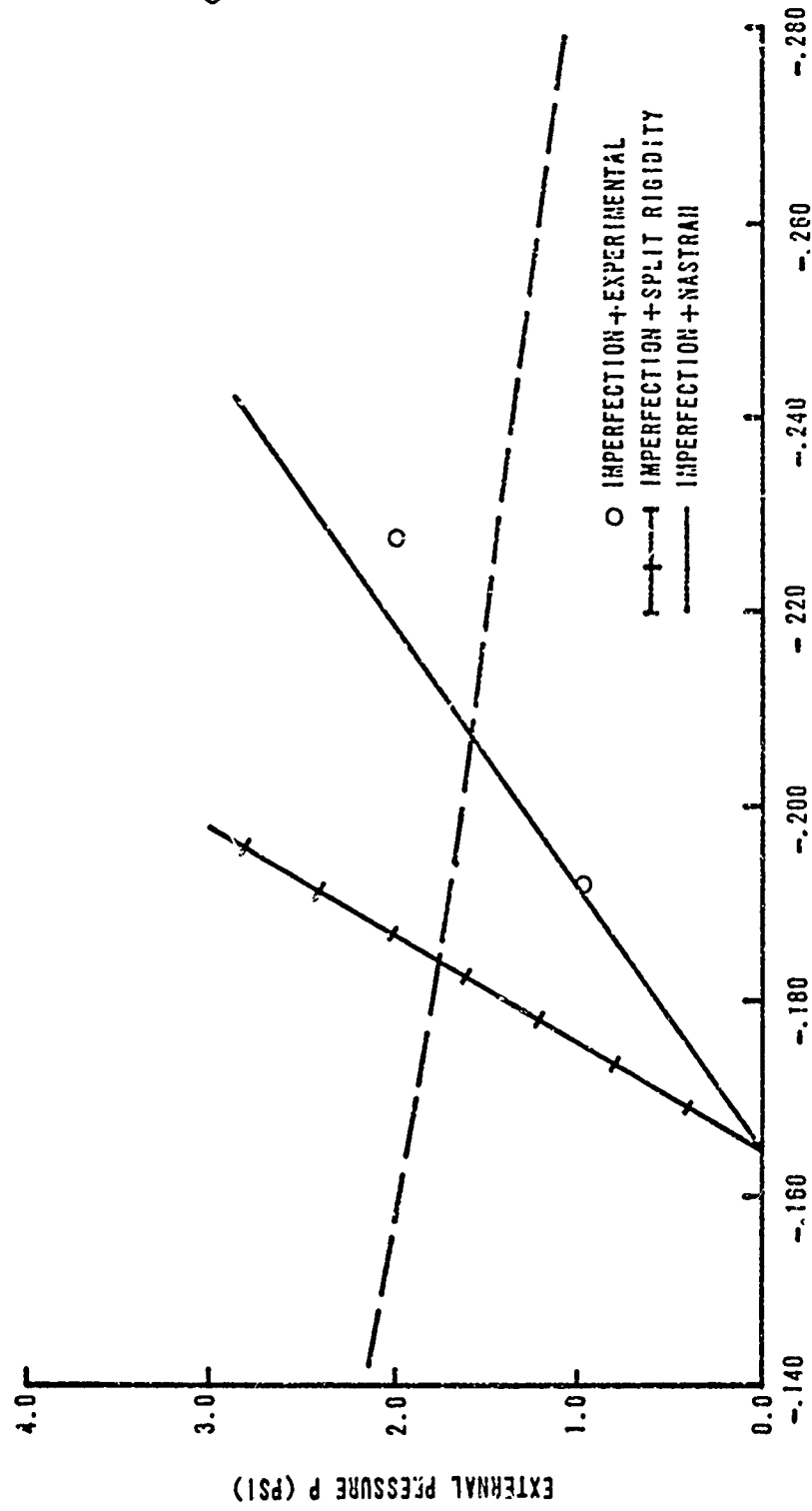
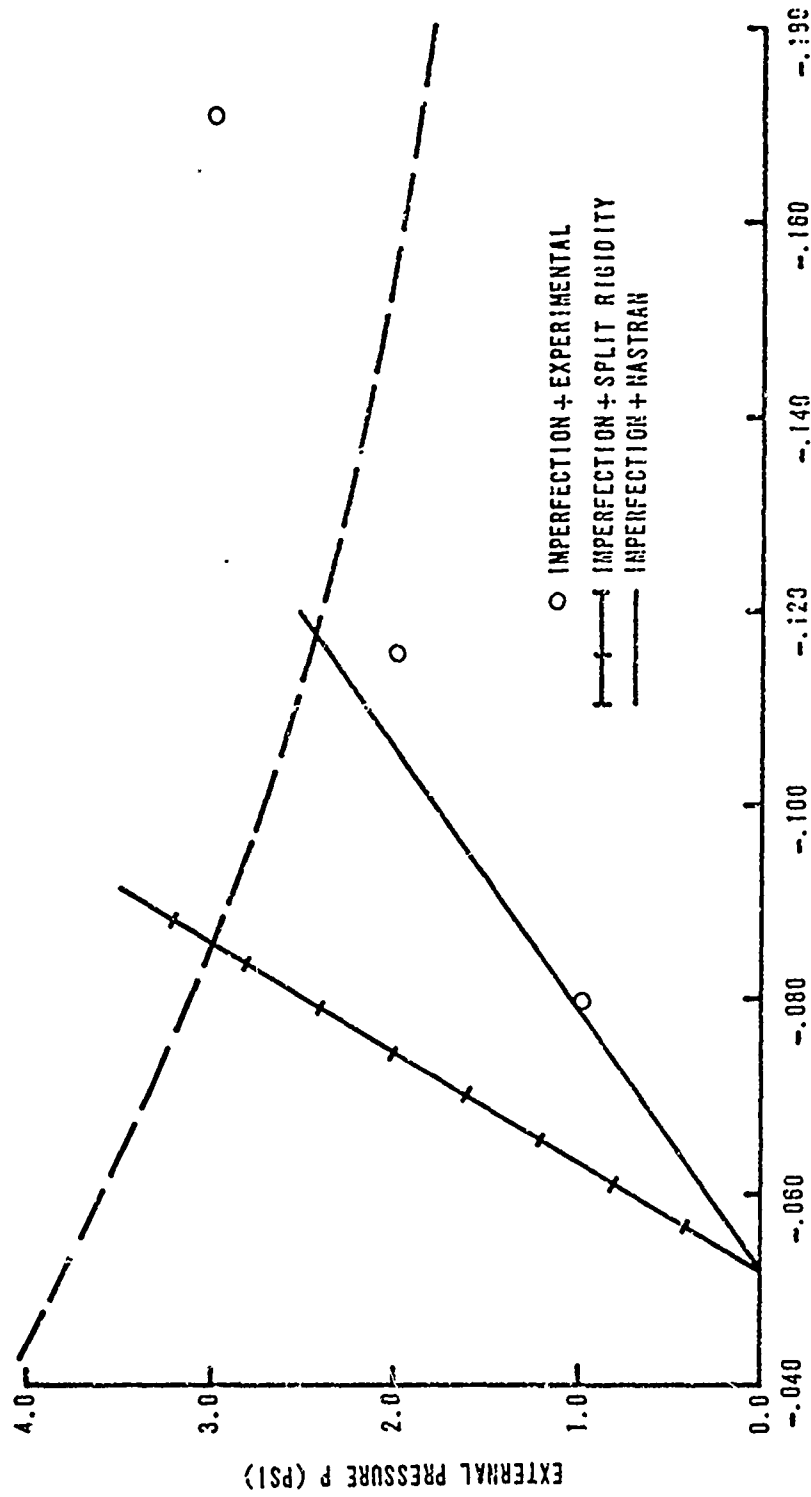


Figure 4.26b PRET Model: Load-Deflection with Global Imperfections



INITIAL IMPERFECTION + LIVE LOAD DEFLECTION (INCHES)

Figure 4.26c PRET Model: Load-Deflection with Local Imperfections

## CHAPTER V

## SUMMARY AND CONCLUSIONS

5.1 SUMMARY

The objectives of this research were to 1) determine if reticulated domes could be analyzed and would behave as continuous domes, 2) to determine their load-deformation response up to the point of buckling, and 3) to study the growth of imperfections in model reticulated domes. A fourth objective was to check the validity of several current buckling theories as applied to reticulated domes.

A theoretical analysis was developed to predict the load-deformation relationships of spherical reticulated domes subjected to a uniform static radial pressure load. A "split rigidity" concept was described in which the shell was given an equivalent membrane and an equivalent bending thickness. Equivalent, in this case, meant a thickness equal to that of a continuous shell responding similarly in membrane and bending action. The theory was based on elastic material behavior.

A second analysis approach was employed in the study, namely a space frame analysis using the NASTRAN finite element computer code. The measured geometry of the test models was used as input to the analysis. The results of the application of a series of incremental static loads were studied, with the deflected position of the joints added to the original geometry to provide initial conditions for a subsequent load increment.

An experimental program to check the validity of the above theories was then conducted. Three reticulated shell models were fabricated to simulate the following grid patterns: 1) a brass model with a two-inch square grid; 2) a brass model with a one-inch square grid; 3) a plastic model with a two-inch square grid. The brass models were constructed of 1/8-inch H-sections. The plastic model was vacuum-formed to a spherical shape and the desired reticulated member grid pattern was then cut from the molded shell. Tensile specimens of each material type were fabricated and were tested to determine the appropriate material properties.

The test models were loaded hydrostatically with water pressure in a test pressure vessel. The radial deflections at approximately 250 locations on each model were measured at increasing increments of load. Measurements were made using a unique pivoted radial arm fabricated specifically for spherical shell testing, and measuring to an accuracy of .0001 inches displacement.

The deflection data taken at each load for the models was reduced by fitting a spherical surface through the data using a least-squares technique. Comparisons of theoretical predictions and experimental data were then made by plotting deflections along specified reference lines, and by making contour plots of the deflection patterns throughout the model shell. The growth of initial imperfections was then studied by comparing the initial imperfection pattern with the deflection behavior under load.

Loading of each model continued until buckling occurred in some portion of the shell. The buckling loads were then compared

with several existing buckling theories. These theories included general buckling theories by Buchert and Von Karman, local snap buckling by Wright, and Euler column buckling.

## 5.2 CONCLUSIONS

Fabrication of the brass reticulated domes was quite difficult. The silver-soldering technique required considerable heat, with the resulting temperature differentials in the model causing severe problems in maintaining design tolerances. Inward radial imperfections ranged from 1/120th to 1/80th of the shell radii. In addition to the imperfection problem, the high heat levels applied to the brass caused material property changes. Examination of the results of the brass material property tests indicated a significant reduction in the material yield stress near the structural joints by nearly a factor of four. The speculation of considerable inelastic material behavior in regions of high deflections and stresses was verified. The large nonlinear growth of the initial imperfection pattern was primarily due to inelastic material response, and led directly to the buckling failure of the brass models. Significant residual stress patterns from the soldering technique apparently influenced the inelastic material response also. Yielding of the material was not as significant a factor in the plastic model. Rather, accelerated creep at high stress levels was considered the primary influence on the nonlinear growth of the initial imperfection pattern. Both materials, as expected, exhibited a somewhat nonlinear stress-strain behavior at low stress levels during tensile material property tests.

The spherical shell test technique using the modified Easterby apparatus proved to be fast, reliable, and accurate. The device produced repeatable results with the desired sensitivity. Data sampling with the semi-automatic key punch interface speeded the process significantly. The data reduction program developed in the course of this study provided a greatly simplified, rapid, and straightforward procedure for handling the voluminous data produced during the experimental program.

After development of the split rigidity approach for predicting deflections and comparison of its predictions with the experimental results, it was apparent that this approach did not adequately predict live load deflections for the test models in the study. This was not unexpected when the basic assumptions made in the split rigidity theory were examined. First, designing a reticulated spherical shell with uniform equivalent membrane and bending thicknesses was not totally achieved in the models employed. Second, the brass material used was not a linear elastic material as assumed, and the plastic material experienced creep phenomena not accounted for in the theory. Finally, a test model with initially stress-free members was not achieved. The split rigidity concept produced considerably better results for the plastic model than for those constructed of brass and when live load deflections were added to the initial imperfections the results were reasonable. The validity of the split rigidity approach for predicting live load deflections was not clearly established by this study since its basic assumptions were not adequately satisfied.



The analysis approach using the NASTRAN code, however, proved to be more reliable and to shed considerable light on the source of the nonlinear growth of deflection patterns in reticulated shells. When compared with experimental results the NASTRAN predictions exhibited good accuracy as to the shape of the deflected model. The actual magnitude of the predicted deflections was less accurate due to material nonlinearity and early yielding in the brass models, and to creep in the plastic shells. These factors were not accounted for in the NASTRAN approach.

The experimental results also demonstrated that the deflection pattern growth was primarily dictated by the initial imperfection pattern following model fabrication. Without exception, the three models tested showed that the deflection patterns continued to grow as during the first load increment (although not linearly), and that the point of maximum deflection during the first load increment (ignoring edge ring seating) became the location of the final buckle at the buckling load.

The results of the check of current general buckling theories for reticulated shells indicated satisfactory results for Buchert's theory. Buckling of the models was predicted within thirty percent. The plastic material behavior of the brass models was accounted for through the use of plasticity reduction factors. The predicted buckling load was below the experimental results for the plastic model and was above the results for the brass models.

The practical implications of this study are two-fold. First, the split rigidity concept should not be considered invalidated by the results of this research effort. In fact, the buckling load for all three models was satisfactorily predicted using Buchert's equation (based on split rigidity theory) and considering the total deflection to be the sum of the live load deflection as predicted by NASTRAN plus the local imperfection. The imperfections in the test models obviously dominated their buckling behavior. For the case of actual reticulated shells which would be built to closer tolerances, the split rigidity theory would be expected to predict live load deflections more accurately. Thus, this approach remains an extremely useful, quick, and economical tool for the preliminary design of reticulated domes. Initial estimates of member sizing can be greatly facilitated by this method prior to a necessarily more costly and rigorous conventional space frame analysis.

Secondly, the design and more particularly the construction of a reticulated dome could realistically be checked by first performing a post-construction survey of the shape of the shell. Using the as-built geometry of the shell, a final computer analysis could be made to determine points of maximum predicted deflection in the constructed dome. These locations could then be checked using the appropriate buckling equations such as those examined in this study. Although not recommended for all domes, a post-construction analysis of this type could be potentially helpful in making decisions on the adequacy of construction projects which are questionable or in dispute.

It is clear that an exact technique for the prediction of load-deformation behavior of reticulated shells up to the point of buckling is not currently available. However, an existing technique for the prediction of buckling loads in reticulated domes has produced satisfactory results for the experimental verifications in this study. The results of this effort have been presented in the hope that added insight has been gained into the problem and that others may be guided and encouraged by these results to conduct further research in the area.

## APPENDIX A

## THE SPLIT RIGIDITY ANALYSIS METHOD

The theory and analysis presented in this section were utilized<sup>(20)</sup> in the prediction of bending and membrane deflections of reticulated spherical shells under uniform radial load. The principle of the split rigidity concept is introduced here. Basic assumptions of the method are presented, expressions for forces and moments are developed, and boundary conditions for various degrees of edge fixity are examined.

A.1 ASSUMPTIONS

The following assumptions formed the basis of the split rigidity deflection prediction concept:

- 1) The shell material behaved in a linear elastic manner.
- 2) A reticulated spherical shell was to be examined.
- 3) The shell was loaded by a uniform radial pressure.

4) A constant equivalent thickness was assumed to replace the shell-like structure for membrane action, and another constant equivalent thickness replaced the reticulated structure for bending behavior.

A.2 BENDING DEFLECTION THEORY

A.2.1 General. The problem was to investigate the bending effect on a reticulated spherical shell by forces and moments uniformly distributed along its lower edge or springing. By treating the shell as having constant "equivalent" membrane and bending thicknesses a modified closed form analysis as applied to

thin shells was performed. An equivalent membrane thickness was obtained by considering only the membrane behavior of the shell, and an equivalent bending thickness was determined by studying the effects of bending action on the shell. This concept was called the split-rigidity concept.

A.2.2 Equilibrium. The basic shell theory referenced herein was given by Timoshenko<sup>(11)</sup>. Its extension to include the split rigidity concept follows. The theory development began by considering the equilibrium of a shell element bounded by two meridians and two parallel circles as shown in Figure A.1. The angle  $\theta$  defined the position of a meridian. The angle  $\phi$  defined the position of a parallel circle, formed by a normal to the surface and the axis of rotation. A meridian plane and a plane perpendicular to a meridian at a point on the surface were principal planes of curvature, and the principal radii of curvature were of magnitude  $R$  for the spherical case. From the figure,  $r_o = R \sin \phi$ . Based on the assumption of a symmetrically applied load, the circumferential force  $N_\theta$  and  $M_\theta$  (per unit length of shell) were constant along a given circumferential line. The meridional normal force  $N_\phi$ , shear force  $Q_\phi$ , and bending moment  $M_\phi$  (per unit length) changed along a meridian as noted in the figure. The external load  $Z$  (force per square unit of shell) normal to the shell was the only load applied. Changes in curvature were neglected in deriving the three basic equations of equilibrium.

By taking the summation of forces tangent to a meridian, the following differential equation resulted.

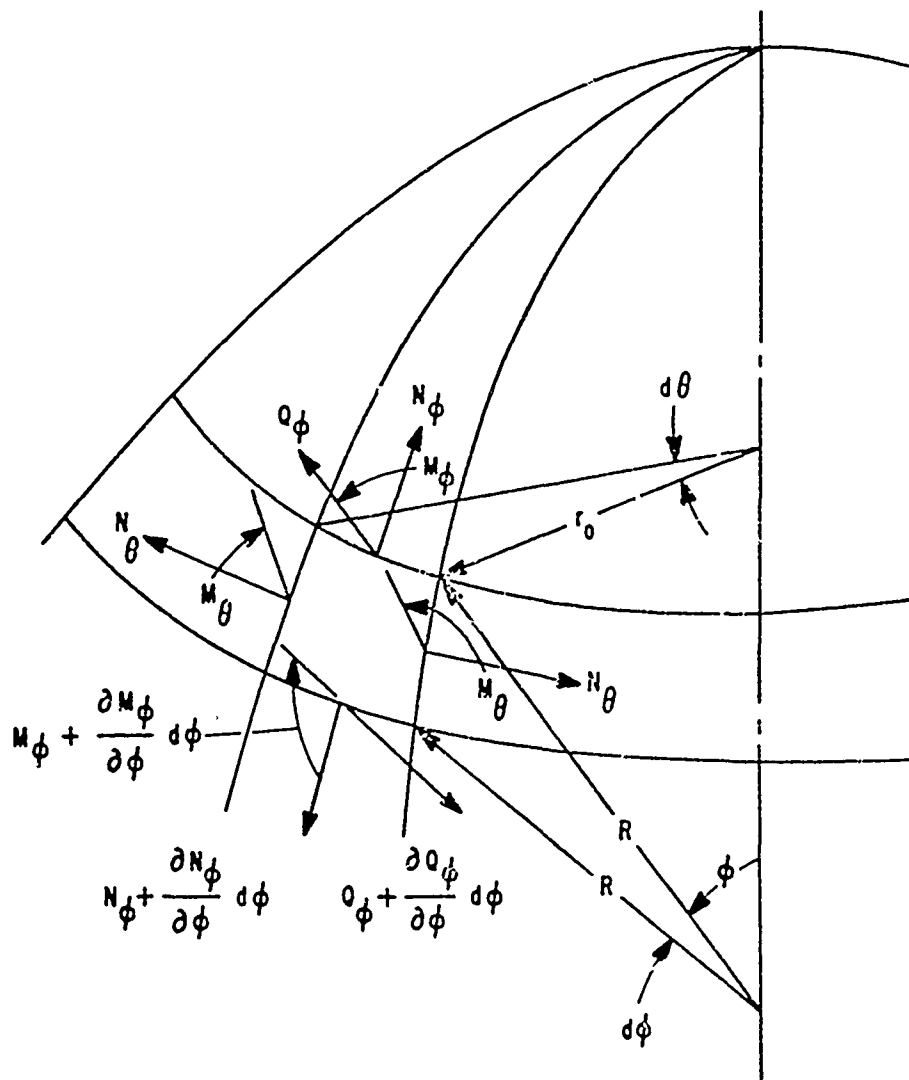


Figure A.1 Free-Body Diagram of a Shell Element

$$\frac{d}{d\phi} (N_{\phi}'' r_o) - N_{\theta}'' \cos\phi + Q_{\phi} r_o = 0 \quad A.1$$

The summation of forces perpendicular to a meridian gave

$$N_{\phi}'' r_o + N_{\theta}'' R \sin\phi - \frac{d}{d\phi} (Q_{\phi} r_o) + Z r_o R = 0 \quad A.2$$

The final equilibrium equation evolved from taking the summation of moments with respect to a tangent to the parallel circle. This gave

$$\frac{d}{d\phi} (M_{\phi} r_o) - M_{\theta} R \cos\phi + Q_{\phi} r_o R = 0 \quad A.3$$

A.2.3 Strains and Curvature Changes. For a symmetrical deformation of the shell, the displacement of a point on the shell was described by the displacement  $w$  normal to the middle surface and the displacement  $v$  tangent to a meridian as shown in Figure A.2. Due to these displacements, an element of a meridian changed in length by the amount

$$\frac{dv}{d\phi} - w \quad A.4$$

Since the original length of the element was  $R \cdot d\phi$ , the strain in the meridional direction,  $\epsilon_{\phi}$ , was

$$\epsilon_{\phi} = \frac{1}{R} \left( \frac{dv}{d\phi} - w \right) \quad A.5$$

An element of the parallel circle underwent a strain  $\epsilon_{\theta}$  due to the given displacements which was equal to

$$\epsilon_{\theta} = \frac{1}{R} (v \cot\phi - w) \quad A.6$$

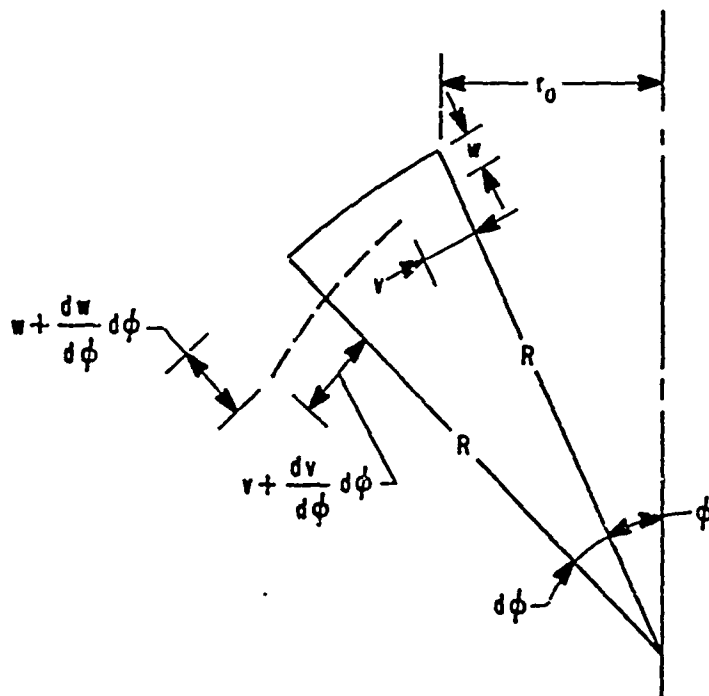


Figure A.2 Shell Displacements

In order to obtain expressions for bending moments, the changes in curvature were required. In terms of the given displacements the change in curvature of a meridian was

$$\chi_{\phi} = \frac{1}{R^2} \frac{d}{d\phi} \left( v + \frac{dw}{d\phi} \right) \quad \text{A.7}$$

Similarly, in the plane perpendicular to a meridian the change in curvature was given by

$$\chi_{\theta} = \frac{\cot \phi}{R^2} \left( v + \frac{dw}{d\phi} \right) \quad \text{A.8}$$



A.2.4 Forces and Bending Moments. By the use of Hooke's law the membrane forces and strains were related. Thus,

$$N_{\phi}'' = \frac{Et_m}{R(1-\nu^2)} \left[ \left( \frac{dv}{d\phi} - w \right) + \nu(\nu \cot \phi - w) \right] \quad A.9$$

$$N_{\theta}'' = \frac{Et_m}{R(1-\nu^2)} \left[ (\nu \cot \phi - w) + \nu \left( \frac{dv}{d\phi} - w \right) \right] \quad A.10$$

In the above expressions  $E$  was the modulus of elasticity and  $\nu$  was Poisson's ratio for the shell material. Since these equations were obtained by considering membrane stresses and strains only,  $t_m$  was used to designate the membrane thickness of the shell.

By relating bending moments and changes in curvature in a like manner, the following results were obtained

$$M_{\phi} = \frac{-Et_b^3}{12R^2(1-\nu^2)} \left[ \frac{d}{d\phi} \left( \nu + \frac{dw}{d\phi} \right) + \nu \cot \phi \left( \nu + \frac{dw}{d\phi} \right) \right] \quad A.11$$

$$M_{\theta} = \frac{-Et_b^3}{12R^2(1-\nu^2)} \left[ \cot \phi \left( \nu + \frac{dw}{d\phi} \right) + \nu \frac{d}{d\phi} \left( \nu + \frac{dw}{d\phi} \right) \right] \quad A.12$$

In these equations  $t_b$  was designated as the bending thickness of the shell, since the expressions evolved from bending considerations only. The practice of assuming  $t_m$  and  $t_b$  to be different quantities was, as mentioned before, called the split-rigidity concept.

A.2.5 Differential Equation Solution. The equilibrium equations, Equations 1 to 3, contained five unknowns. They were the forces  $N_{\phi}''$ ,  $N_{\theta}''$ , and  $Q_{\phi}$ , and the bending moments  $M_{\phi}$  and  $M_{\theta}$ . By substituting Equations A.9 to A.12 into the equilibrium equations, the number of unknowns was reduced to three:  $\nu$ ,  $w$ , and  $Q_{\phi}$ .

Geckeler<sup>(31)</sup>, however, suggested an alternate method of solution by introducing two new variables. The first,  $V$ , was the angle of rotation of a tangent to a meridian.

$$V = \frac{1}{R} \left( v + \frac{dw}{d\phi} \right) \quad A.13$$

The second variable,  $U$ , was defined as

$$U = RQ_{\phi} \quad A.14$$

For simplicity, Equation A.1 was replaced by considering equilibrium of the shell above a parallel circle (see Figure A.3). Since the objective was to determine the secondary bending effects at the edge, no external load was assumed acting on the shell.

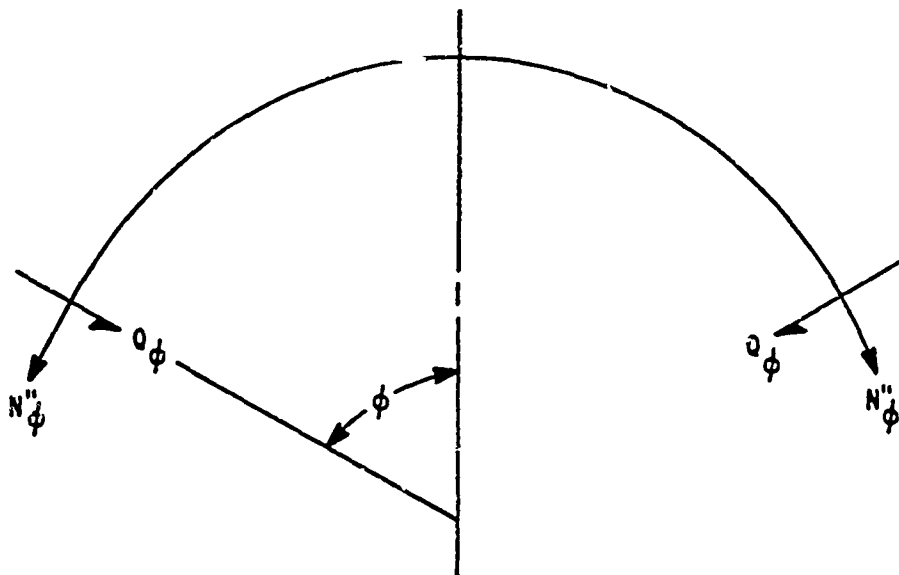


Figure A.3 Shell Edge Forces

$$N_{\phi}'' = Q_{\phi} \cot \phi = \frac{U}{R} \cot \phi \quad A.15$$

Substituting this expression into Equation A.2 and simplifying  
(note  $Z = 0$ ) gave

$$N_{\theta}'' = \frac{dQ_{\phi}}{d\phi} = \frac{1}{R} \frac{dU}{d\phi} \quad A.16$$

To relate  $U$  and  $V$ , Equations A.9 and A.16 were solved for the  
displacements  $v$  and  $w$  in terms of  $N_{\phi}''$  and  $N_{\theta}''$ , giving

$$\frac{dv}{d\phi} - w = \frac{R}{Et_m} [N_{\phi}'' - vN_{\theta}''] \quad A.17$$

$$v \cot \phi - w = \frac{R}{Et_m} [N_{\theta}'' - vN_{\phi}''] \quad A.18$$

Eliminating  $w$  from Equations A.17 and A.18 gave

$$\frac{dv}{d\phi} - v \cot \phi = \frac{R(1+v)}{Et_m} [N_{\phi}'' - N_{\theta}''] \quad A.19$$

Differentiating Equation A.18 yielded

$$\frac{dv}{d\phi} \cot \phi - \frac{v}{\sin^2 \phi} - \frac{dw}{d\phi} = \frac{R}{Et_m} \frac{d}{d\phi} [N_{\theta}'' - vN_{\phi}''] \quad A.20$$

By eliminating the derivative  $dv/d\phi$  from Equations A.19 and A.20, the  
following resulted:

$$v + \frac{dw}{d\phi} = RV = \frac{R(1+v) \cot \phi}{Et_m} [N_{\phi}'' - N_{\theta}''] - \frac{R}{Et_m} \frac{d}{d\phi} [N_{\theta}'' - vN_{\phi}''] \quad A.21$$

Substituting Equations A.15 and A.16 for  $N_\phi''$  and  $N_\theta''$ , the first of two equations relating  $U$  and  $V$  was obtained.

$$Et_m V = \frac{1}{R} \frac{d^2 U}{d\phi^2} - \frac{\cot\phi}{R} \frac{dU}{d\phi} + \frac{1}{R} (-\nu + \cot^2\phi) U \quad A.22$$

A second equation relating  $U$  and  $V$  was obtained by substituting Equations A.11 and A.12 for  $M_\phi$  and  $M_\theta$  into the third equilibrium equation, Equation A.3. Using the new variables  $U$  and  $V$  and introducing the flexural rigidity quantity  $D_b = Et_b^3/12(1-\nu^2)$ , the desired equation was

$$-\frac{U}{D_b} = -\frac{1}{R} \frac{d^2 V}{d\phi^2} - \frac{\cot\phi}{R} \frac{dV}{d\phi} + \frac{1}{R} (\nu + \cot^2\phi) V \quad A.23$$

Thus the problem of edge bending of a spherical shell required integration of the two second order differential equations A.22 and A.23. Note that constant equivalent thicknesses were assumed throughout. In terms of  $Q_\phi$  and  $V$ , the above equations were

$$\frac{d^2 Q_\phi}{d\phi^2} + \cot\phi \frac{dQ_\phi}{d\phi} - (-\nu + \cot^2\phi) Q_\phi = -Et_m V \quad A.24$$

$$\frac{d^2 V}{d\phi^2} + \cot\phi \frac{dV}{d\phi} - (\nu + \cot^2\phi) V = \frac{R^2 Q_\phi}{D_b} \quad A.25$$

Rather than solving the preceding two equations completely, an approximation was introduced and justified as follows. For thin shells, the quantities  $Q_\phi$  and  $V$  damp out rapidly with increasing distance from the edge. Figure A.4<sup>(9)</sup> shows this damping effect for several quantities of interest. It was assumed that  $Q_\phi$  and  $V$  were much smaller than their first derivatives, and that their first derivatives were in turn much smaller than their second derivatives.

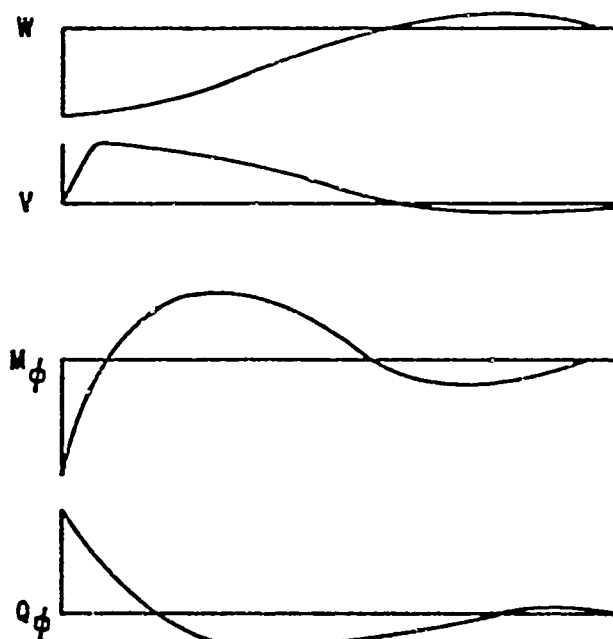


Figure A.4 Damping of the Edge Effects

This assumption was verified as shown later. Equations A.24 and A.25 thus reduced to

$$\frac{d^2 Q_\phi}{d\phi^2} = -Et_m V \quad \text{A.26}$$

$$\frac{d^2 V}{d\phi^2} = \frac{R^2 Q_\phi}{D_b} \quad \text{A.27}$$

These equations differed from the approach reported by Timoshenko<sup>(11)</sup> in that the membrane and bending effects were separated. This separation (the basis of the split rigidity concept) is reflected in the use of the membrane thickness  $t_m$  and the bending rigidity term  $D_b$ . By eliminating  $Q_\phi$  from the above, the following fourth order differential equation<sup>(9)</sup> was obtained:

$$\frac{d^4 V}{d\phi^4} + 4\kappa^4 V = 0 \quad \text{A.28}$$

where

$$\kappa^4 = 3R^2 (1-\nu^2) \frac{t_m}{r_b^3} \quad \text{A.29}$$

Equation A.28 is generally known as the Geckeler<sup>(31)</sup> Equation.

Its general solution was represented as

$$V = C_1 e^{-\kappa\phi} \sin(\kappa\phi + \gamma_1) + C_2 e^{\kappa\phi} \sin(\kappa\phi + \gamma_2) \quad \text{A.30}$$

where  $\gamma$  represented phase angles to be determined from the edge boundary conditions. Knowing that the edge disturbance damped out when moving away from the edge, the first term in Equation A.30 was disregarded. A new variable  $\alpha$ , the angular distance from the lower edge or springing of the shell, was introduced. By denoting  $\phi_s$  as the opening angle of the shell from the apex to the springing as shown in Figure A.5, the following relationship was observed:

$$\alpha = \phi_s - \phi \quad \text{A.31}$$

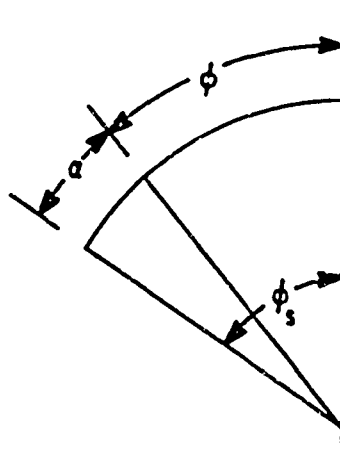


Figure A.5 Angular Variables

Thus the solution of the differential equation was written as

$$V = Ce^{-\kappa\alpha} \sin (\kappa\alpha + \gamma) \quad A.32$$

Note at this point the previous argument that the lower order terms for  $Q_\phi$  and  $V$  in Equations A.24 and A.25 were ignored. The first derivative effectively multiplied Equation A.32 for  $V$  (similarly for  $Q_\phi$ ) by  $\kappa$ , and the second derivative multiplied it by  $\kappa^2$ . Haas<sup>(9)</sup> stated that for thin shells (shells having a minimum radius to thickness ratio of at least 50), the value of  $\kappa$  is approximately 10. (For reticulated shells, the thin shell criteria becomes  $R/t_m$ , where  $R$  is the radius and  $t_m$  is the membrane thickness.) Since the second and third terms in Equations A.24 and A.25 were approximately one-tenth and one-hundredth the value of the respective terms used in the solution, it was felt that this approximation was justified.

A.2.6 Final Expressions. The expression for the slope of a tangent to a meridian,  $V$ , was given by Equation A.32.

The shear force  $Q_\phi$ , due to edge bending, was obtained from Equation A.27. Differentiating  $V$  the first time gave

$$\frac{dV}{d\phi} = \kappa Ce^{-\kappa\alpha} [\sin (\kappa\alpha + \gamma) - \cos (\kappa\alpha + \gamma)] \quad A.33$$

Using the trigonometric identity for the difference of two angles, the following was observed:

$$\sin [(\kappa\alpha + \gamma) - \frac{\pi}{4}] = \frac{1}{\sqrt{2}} [\sin (\kappa\alpha + \gamma) - \cos (\kappa\alpha + \gamma)] \quad A.34$$

Thus

$$\frac{dV}{d\phi} = \sqrt{2} \kappa C e^{-\kappa\alpha} \sin \left( \kappa\alpha + \gamma - \frac{\pi}{4} \right) \quad A.35$$

Therefore, differentiating  $V$  resulted in multiplying the basic quantity by  $\sqrt{2} \kappa$  and employing a phase shift of  $-\pi/4$ . The final expression for the shear force  $Q_\phi$  thus became

$$Q_\phi = \frac{2D_b \kappa^2}{R^2} C e^{-\kappa\alpha} \sin \left( \kappa\alpha + \gamma - \frac{\pi}{2} \right) \quad A.36$$

The meridional force  $N_\phi''$ , due to edge bending, was given by Equation A.15

$$N_\phi'' = Q_\phi \cot \phi \quad A.37$$

The circumferential force  $N_\theta''$  was obtained from Equation A.16

$$N_\theta'' = \frac{dQ_\phi}{d\phi} = \frac{2\sqrt{2} D_b \kappa^3}{R^2} C e^{-\kappa\alpha} \sin \left( \kappa\alpha + \gamma - \frac{3\pi}{4} \right) \quad A.38$$

The deflection  $w$ , normal to the shell, was of primary interest in this study. In Figure A.6, note that the increase  $\delta$  in the radius of a parallel circle was given by

$$\delta = r_o \epsilon_\theta = (R \sin \phi) \epsilon_\theta \quad A.39$$

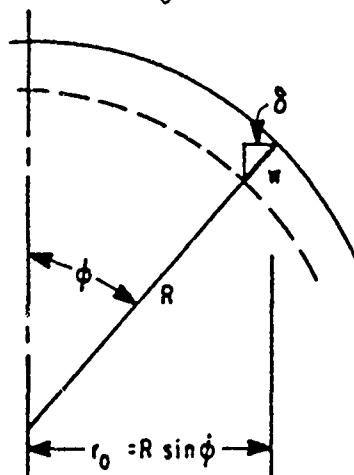


Figure A.6 Displacement of a Point



Thus the desired deflection  $w$  due to bending was

$$w = \frac{-\delta}{\sin\phi} = -R\epsilon_{\theta} = -\frac{R}{Et_m} (N_{\theta}'' - \nu N_{\phi}'') \quad A.40$$

From Equations A.37 and A.38, note that  $N_{\theta}''$  was of the order  $\sqrt{2}\kappa$  greater than  $N_{\phi}''$ , so the second term in Equation A.40 was dropped.

The final expression for  $w$  then became

$$w = -\frac{RC}{\sqrt{2}\kappa} e^{-\kappa\alpha} \sin\left(\kappa\alpha + \gamma - \frac{3\pi}{4}\right) \quad A.41$$

Finally, the expression for the meridional bending moment  $M_{\phi}$  was obtained from the combination of Equations A.11 and A.13.

Dropping the lower-ordered term  $V$  for the reason given previously,

$$M_{\phi} = -\frac{D_b \sqrt{2}\kappa}{R} C e^{-\kappa\alpha} \sin\left(\kappa\alpha + \gamma - \frac{\pi}{4}\right) \quad A.42$$

### A.3 BOUNDARY CONDITIONS

A.3.1 Deflection Compatibility. Figure A.7 illustrates the primary force reactions and the compatibility restoring forces and moments (9) between a shell and its edge beam support. The first requirement to satisfy compatibility between the shell and the edge

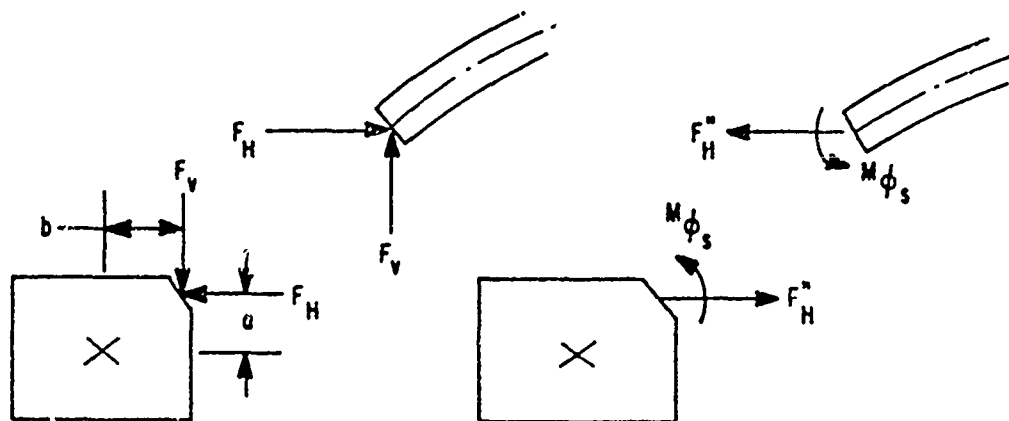


Figure A.7 Compatibility Restoring Forces

beam was for deflections. Therefore the following was necessary:

$$w_s + w_s'' = w_b + w_b'' \quad A.43$$

In the above equation as in those following, non-primed quantities represented primary or membrane ef. cts, and double-primed quantities reflected the effects of bending. The subscript "s" denoted properties of the shell, and "b" denoted properties of the edge beam.

The deflections in Equation A.43 were given as follows:

$$w_s = -\frac{r_o \epsilon_\theta}{\sin \phi_s} = -\frac{R}{Et_m} (N_{\theta_s} - \nu N_{\phi_s}) \quad A.44$$

where the subscripted angles  $\phi_s$  and  $\theta_s$  denoted values at the shell springing, and

$$w_s'' = -\frac{R}{Et_m} (N_{\theta_s}'' - \nu N_{\phi_s}'') \quad A.45$$

where  $N_{\phi_s}''$  was neglected because it was of the order  $\sqrt{2}\kappa$  smaller than  $N_{\theta_s}''$  (see Equations A.37 and A.38). Also,

$$w_b' = -\frac{R}{E} \frac{F_{Hr_o}}{A_b} = \frac{Rr_o N_{\phi_s} \cos \phi_s}{EA_b} \quad A.46$$

where  $A_b$  was the cross-sectional area of the edge beam, and

$$w_b'' = -\frac{R}{E} \left( -\frac{F_{Hr_o}''}{A_b} \right) = \frac{Rr_o Q_{\phi_s}}{EA_b \sin \phi_s} \quad A.47$$

Substituting Equations A.44 through A.47 into Equation A.43 and evaluating the terms at the springing where  $\alpha = 0$ , the requirement for deflection compatibility was that the constant C be as follows:

$$C = \frac{-2\kappa^2 \left[ \frac{N_{\theta s}}{t_m} + N_{\phi s} \left( \frac{r_o \cos \phi_s}{A_b} - \frac{v}{t_m} \right) \right]}{E \left[ \sqrt{2}\kappa \sin \left( \gamma - \frac{3\pi}{4} \right) + \frac{r_o t_m}{A_b \sin \phi_s} \sin \left( \gamma - \frac{\pi}{2} \right) \right]} \quad A.46$$

A.3.2 Rotation Compatibility. A second requirement for compatibility was that the rotations of the shell and the edge beam match. This requirement was stated as

$$v_s'' + v_s'' = v_b'' + v_b'' \quad A.49$$

where the subscripts and primes were as defined previously. Since there was no edge rotation induced by primary stresses, the first term dropped out. The other terms were defined as follows:

$$v_s'' = C e^{-\kappa \alpha} \sin (\kappa \alpha + \gamma) \quad A.50$$

$$v_b = (F_H a - F_V b) V_T = (-a N_{\phi s} \cos \phi_s + b N_{\phi s} \sin \phi_s) V_T \quad A.51$$

where  $V_T$  was the rotational flexibility of the edge beam (or the rotation for a unit moment  $M_{\phi}$ ) and was given by Roark<sup>(32)</sup> as

$$V_T = \frac{R^2}{EI} \quad A.52$$

Next,

$$v_b'' = (M_{\phi s} + F_H a) V_T = \left( M_{\phi s} + \frac{Q_{\phi s}}{\sin \phi_s} a \right) V_T \quad A.53$$

Substituting Equations A.50 through A.53 into Equation A.49, the requirement for rotation compatibility at the springing became

$$\frac{C \sin \gamma}{V_\tau} = N_{\phi_s} (-a \cos \phi_s + b \sin \phi_s) \quad \text{A.54}$$

$$+ \frac{\sqrt{2} \kappa D_b C}{R} [-\sin(\gamma - \frac{\pi}{4})] + \frac{a\sqrt{2} \kappa}{R \sin \phi_s} \sin(\gamma - \frac{\pi}{2})$$

For any case of edge support, the simultaneous solution of Equations A.48 and A.54 for C and  $\gamma$  supplied the required data for the determination of combined membrane and bending deflections along a shell meridian by the following formula:

$$w = -\frac{R}{Et_m} [N_\theta - \nu N_\phi] - \frac{RC}{\sqrt{2}\kappa} e^{-\kappa\alpha} \sin(\kappa\alpha + \gamma - \frac{3\pi}{4}) \quad \text{A.55}$$

Two special cases of edge support were examined as follows:

A.3.3 Simply Supported Edge. The case of a very flexible edge beam was readily analyzed by noting that the edge bending moment  $M_{\phi_s}$  was zero. This effectively replaced Equation A.54 from which  $\gamma$  was otherwise determined. From Equation A.42 the phase angle was then equal to  $\pi/4$ . The constant C was found from Equation A.48, and the results substituted into Equation A.55 to give the values for combined membrane and bending deflections along a meridian.

A.3.4 Fixed Edge. Since at a fixed edge the slope V was zero, the phase angle  $\gamma$  became zero. The combined membrane and bending deflections were then found as in the previous case.

## APPENDIX B

## STATIC ANALYSIS BY THE STIFFNESS METHOD

A static analysis by the stiffness method was performed using the NASTRAN finite element computer code. The code has numerous analysis options, finite elements, and types of loadings which make it a very useful and versatile structural analysis tool. Described in this section are the options used in the analysis of the reticulated shell models, the program flow, and the solution procedure in a typical NASTRAN static analysis.

B.1 ASSUMPTIONS AND DEFINITIONS

Linear elastic material behavior was assumed in the analysis method described herein. Joints were assumed to provide full moment transfer. The location of each joint was specified to a high degree of accuracy using the measurement techniques described in Chapter 3.

The analyses of the test models utilized the advantage offered by the spherical geometry of the shells. NASTRAN provided for description of the problem geometry in either rectangular, cylindrical, or spherical displacement coordinate systems as shown in Figure B.1. Each joint, or grid point, had a unique displacement coordinate system associated with it. The so-called "global" coordinate system was the collection of all displacement component directions in their own coordinate systems. All matrices were formed and all displacements were calculated in the global coordinate system.

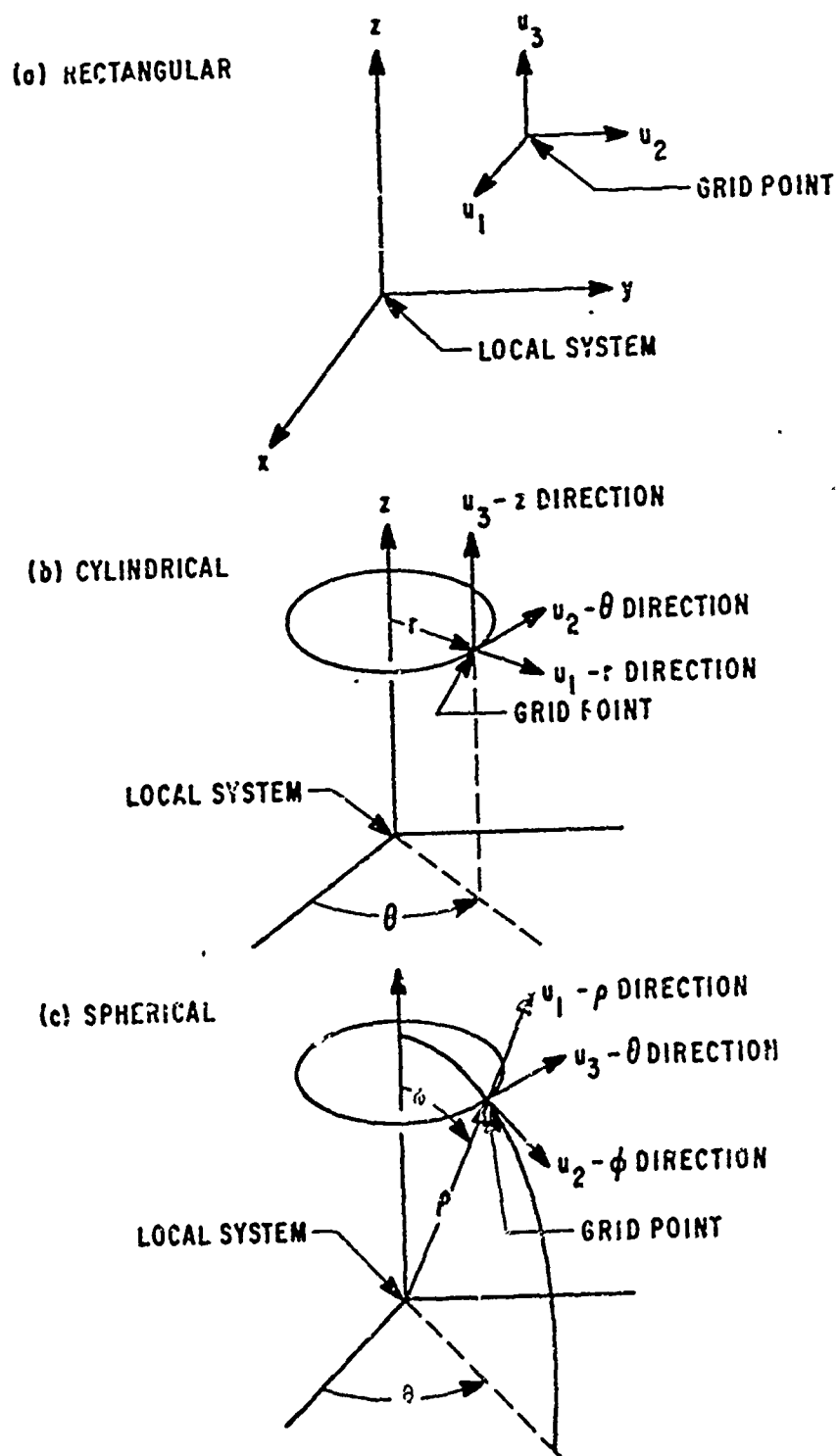


Figure B.1 NASTRAN Coordinate Systems

NASTRAN finite elements included rod, bar, plate, and shell elements, among others. Bar elements were selected for the reticulated shell analyses. The bar element included axial, bending, and torsional behavior.

Static loadings available included concentrated loads at grid points, pressures on surfaces, or equivalent loads resulting from thermal expansion, from enforced deformations of structural elements, or from enforced displacements of grid points. The first option was selected and applied here, with each concentrated load calculated as described in part 2.2.

Constraints could be applied to a structure in the form of single-point and multipoint constraints. Single-point constraints were applied by specifying the value of enforced displacements, any or all of which could be zero. Multipoint constraints were defined by an equation of the form  $\sum_j A_j u_j = 0$ , which implied a linear relationship among the specified degrees of freedom  $u_j$ . Multipoint constraints were employed to enforce a zero vertical displacement of the brass model edge ring.

## B.2 GENERAL PROBLEM FLOW

The general problem flow of a NASTRAN static analysis by the stiffness method is shown in the flow chart of Figure B.2. The application of the pattern shown is presented in the following section as the solution procedure is described.

## B.3 NASTRAN SOLUTION PROCEDURE

Having input all the required data to NASTRAN, the geometry processor performed the following tasks. All coordinate systems were

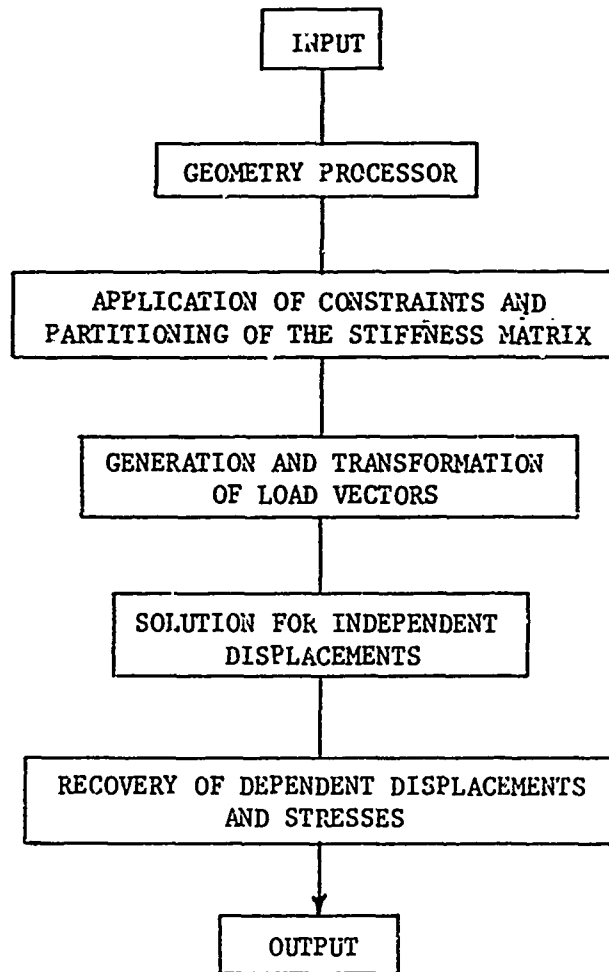


Figure B.2 General Problem Flow



transformed and the locations of all grid points were determined in the "basic" or global coordinate system (a rectangular coordinate system). Internal resequencing of grid point numbers was performed if specified. Multipoint and single-point constraint equations were then generated.

The stiffness matrices were then formed and assembled one grid point at a time, by columns, in internal sequencing order. At this point the global stiffness matrix was complete.

Before imposing constraints the structural problem was stated as

$$[K_{gg}] \{u_g\} = \{P_g\} \quad B.1$$

where  $[K_{gg}]$  = the global stiffness matrix

$\{u_g\}$  = the global displacement matrix

$\{P_g\}$  = the global load matrix

In the above equations, square brackets indicate two-dimensional arrays and twisted brackets denote column vectors.

Multipoint constraints were expressed as

$$[R_g] \{u_g\} = 0 \quad B.2$$

where  $[R_g]$  was a matrix of constraint coefficients supplied by the user. By specifying the degrees of freedom made dependent by each constraint equation, the  $\{u_g\}$  matrix was partitioned to

$$\{u_g\} = \begin{Bmatrix} u_n \\ u_m \end{Bmatrix} \quad B.3$$

where  $u_m$  was the set of dependent degrees of freedom. The constraint coefficient was similarly partitioned as

$$[R] = [R_n | R_m] \quad B.4$$

Thus Equation B.2 was

$$[R_n] \{u_n\} + [R_m] \{u_m\} = 0 \quad B.5$$

Since  $[R_m]$  was nonsingular, a multipoint constraint matrix was defined as

$$[G_m] = - [R_m]^{-1} [R_n] \quad B.6$$

so that

$$\{u_m\} = [G_m] \{u_n\} \quad B.7$$

The structural problem as stated in Equation B.1 was expressed

as

$$\begin{bmatrix} K_{nn} & K_{nm} \\ K_{nm}^T & K_{mm} \end{bmatrix} \begin{Bmatrix} u_n \\ u_m \end{Bmatrix} = \begin{Bmatrix} P_n \\ P_m \end{Bmatrix} \quad B.8$$

where the superscript T indicated a matrix transpose.

By adding the equations of constraint to the above equations of equilibrium, the result in partitioned form was

$$\begin{bmatrix} K_{nn} & K_{nm} & G_m^T \\ K_{nm}^T & K_{mm} & -I \\ G_m & -I & 0 \end{bmatrix} \begin{Bmatrix} u_n \\ u_m \\ q_m \end{Bmatrix} = \begin{Bmatrix} P_n \\ P_m \\ 0 \end{Bmatrix} \quad B.9$$

where  $\{q_m\}$  was the vector of constraint forces on  $\{u_m\}$ , and  $[I]$  denoted the identity matrix. Upon eliminating  $u_m$  and  $q_m$  the result was

$$[\bar{K}_{nn}] \{u_n\} = \{\bar{P}_n\} \quad B.10$$

where

$$\bar{K}_{nn} = K_{nn} + K_{nm} G_m + G_m^T K_{nm} + G_m^T K_{mm} G_m \quad B.11$$

and

$$\bar{P}_n = P_n + G_m^T P_m \quad B.12$$

As described earlier, single-point constraints were applied to the set of displacements  $u_s$  in the form

$$\{u_s\} = \{Y_s\} \quad B.13$$

where  $\{Y_s\}$  was the enforced displacement vector, any or all of whose members could be zero. Therefore  $\{u_n\}$  was further partitioned as

$$\{u_n\} = \begin{Bmatrix} u_f \\ u_s \end{Bmatrix} \quad B.14$$

where  $\{u_f\}$  was the free or unconstrained vector. The stiffness matrix  $[\bar{K}_{nn}]$  similarly became

$$[\bar{K}_{nn}] = \begin{bmatrix} K_{ff} & K_{fs} \\ K_{fs}^T & K_{ss} \end{bmatrix} \quad B.15$$

The complete structural equations including the single-point forces of constraint  $q_s$  became

$$\begin{bmatrix} K_{ff} & K_{fs} & 0 \\ K_{fs}^T & K_{ss} & -I \\ 0 & I & 0 \end{bmatrix} \begin{Bmatrix} u_f \\ u_s \\ q_s \end{Bmatrix} = \begin{Bmatrix} P_f \\ P_s \\ Y_s \end{Bmatrix} \quad B.16$$

A straightforward elimination gave

$$[K_{ff}] \{u_f\} = \{P_f\} - [K_{fs}] \{Y_s\} = \{\bar{P}_f\} \quad B.17$$

Solution of Equation B.16, as with all other equations of the form  $[A] \{X\} = \{B\}$ , was accomplished using triangular decomposition.

No matrix inversions were performed in NASTRAN.

The solution procedure of Figure B.2 thus progressed to the point of generating and transforming the load vectors. The global load vector  $\{P_g\}$  was partitioned according to the multipoint constrained coordinates  $u_m$  and the coordinates  $u_n$  which were not multipoint constrained, or,

$$\{P_g\} = \begin{Bmatrix} P_n \\ P_m \end{Bmatrix} \quad B.18$$

Multipoint constraints were eliminated by

$$\{\bar{P}_n\} = \{P_n\} + [G_m^T] \{P_m\} \quad B.19$$

$\{\bar{P}_n\}$  was further partitioned according to the single-point constrained set  $u_s$  and the free coordinate set  $u_f$  as

$$\{\bar{P}_n\} = \begin{Bmatrix} P_f \\ P_s \end{Bmatrix} \quad B.20$$

whereupon the single-point constraints were eliminated by

$$\{\bar{P}_n\} = \{f_n\} + [G_m^T] \{P_m\} \quad B.21$$

Solution of Equation B.17 allowed recovery of the independent displacements  $u_n$  in the following manner. The single-point constraint set  $u_s$  was evaluated as

$$\{u_s\} = \{Y_s\} \quad B.22$$

where  $Y_s$  was the enforced displacement vector. The free and constrained displacements,  $u_f$  and  $u_s$ , were then merged to form

$$\begin{array}{c} u_f \\ \{ \overline{\quad} \} \rightarrow \{u_n\} \\ u_s \end{array}$$

where the arrow designated the merging process.

The last step in the problem flow of Figure B.2 was performed by recovering the multipoint constraint set  $u_m$ ,

$$\{u_m\} = [G_m] \{u_n\} \quad B.23$$

and by merging  $u_n$  and  $u_m$  to form the global displacement matrix

$$\begin{array}{c} u_n \\ \{ \overline{\quad} \} \rightarrow \{u_g\} \\ u_m \end{array} \quad B.24$$

A simple task to recover the single-point forces of constraint was accomplished using the second row of Equation B.16, or,

$$\{q_s\} = -\{P_s\} + [K_{fs}^T] \{u_f\} + [K_{ss}] \{u_s\} \quad E.25$$

Having the  $g1 \ 1$  displacement matrix, the solution procedure was completed by calculating the internal forces and stresses in the conventional manner. This information was then output in appropriate form. For example, typical bar element output included bending moments at both ends in two planes, transverse shear forces in two planes, axial force, and torque.

## APPENDIX C

## LEAST-SQUARES SPHERICAL FIT COMPUTER PROGRAM

C.1 GENERAL

The computer program described in this section was developed to reduce the data from the test series described in Chapter 3. The function of the program was to perform a least-squares fit of a spherical surface to the test data, and it will be described in four parts. The theory of the fitting technique is developed first. Operation of the mainline program is then described, followed by that of the two program subroutines. The final portion of this appendix describes typical input and output formats and includes variable definitions and a program listing.

C.2 THEORY OF THE LEAST-SQUARES FIT

The objective of the following theoretical development was to determine a theoretical spherical surface which provided the best "least-squares" fit to a set of radial measurements on a test model of a spherical reticulated dome. The geometry of the problem is given in Figure C.1. In this figure, point J represents the origin of the coordinate system and physically was the center of the spherical pivot of the Easterby apparatus described in part 3.3.2. Experimental values of the radial measurements taken during the tests are denoted by  $R_i$ . The subscript refers to gage point  $P_i$  on the test model, which was located at  $(X_i, Y_i, Z_i)$  relative to the origin.

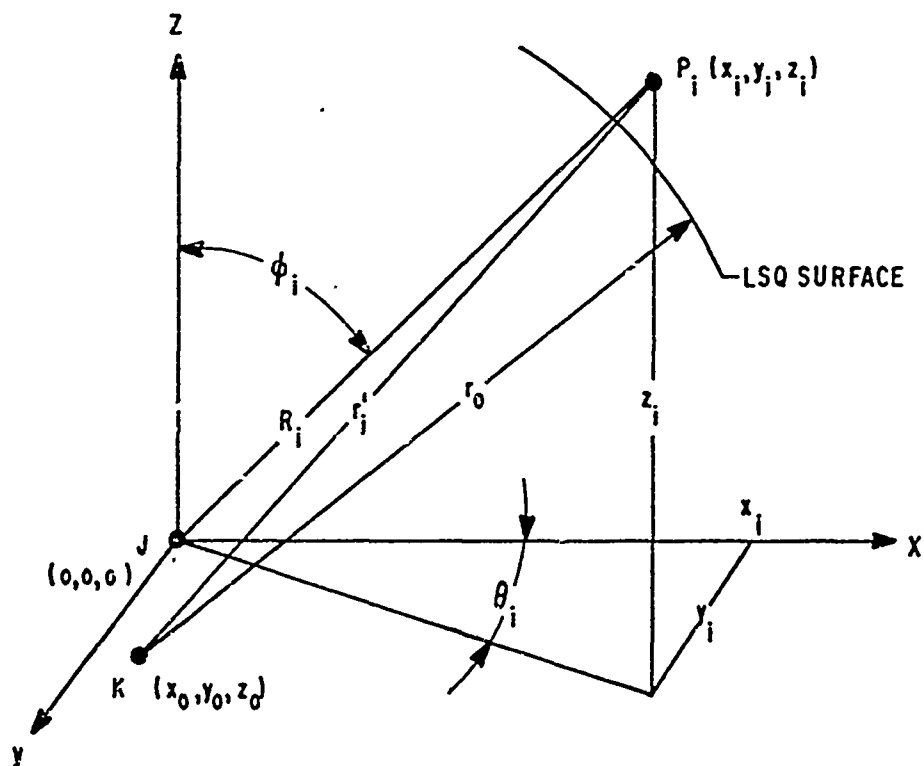


Figure C.1 Coordinate System for Spherical Fit



Point K denotes the center of the theoretical spherical surface and is located at the coordinates  $(X_0, Y_0, Z_0)$ . The radius of this surface is given by the quantity  $r_0$ . It is assumed that points J and K are sufficiently close together that the angles  $\phi_i$  and  $\theta_i$  required to locate each gage point can be satisfactorily computed from  $R_i$  and the arc distances measured on the surface of the shell. The quantity  $r_i'$  represents the distance from the theoretical sphere center at point K to gage point  $P_i$  on the test model, and can be expressed mathematically in rectangular coordinates as:

$$r_i'^2 = (X_i - X_0)^2 + (Y_i - Y_0)^2 + (Z_i - Z_0)^2 \quad C.1$$

Transforming to spherical coordinates, the following apply:

$$X_i = R_i \sin \phi_i \cos \theta_i = R_i A_i$$

$$Y_i = R_i \sin \phi_i \sin \theta_i = R_i B_i \quad C.2$$

$$Z_i = R_i \cos \phi_i = R_i C_i$$

Substituting expressions C.2 into Equation C.1 and simplifying gives

$$r_i' = [R_i^2 - 2R_i(X_0 A_i + Y_0 B_i + Z_0 C_i) + X_0^2 + Y_0^2 + Z_0^2]^{1/2} \quad C.3$$

Assume that  $N$  experimental values of  $R_i$ ,  $\phi_i$ , and  $\theta_i$  were given along with the above expression  $r_i'$  relating these values to the theoretical sphere center. It was desired to determine the radius  $r_0$  and the center coordinates  $X_0$ ,  $Y_0$ ,  $Z_0$  of a theoretical spherical surface which provided the best least-squares fit to the experimental data values,  $R_i$ . In mathematical terms, it was required to determine the minimum value of a function defined as

$$S = \sum_{i=1}^N (r_0 - r'_i)^2 \quad C.4$$

Thus  $S$  represents the sum of the squares of the differences between the radius of the best-fit sphere and the radial distances to the shell.

In order to minimize  $S$ , (a function of the four unknowns  $r_0$ ,  $X_0$ ,  $Y_0$ ,  $Z_0$ ) the first partial derivative of  $S$  with respect to each unknown was set equal to zero. Solving the first such equation for  $\partial S / \partial r_0$  gave

$$\begin{aligned} \frac{\partial S}{\partial r_0} &= \frac{\partial}{\partial r_0} \left[ \sum_{i=1}^N (r_0 - r'_i)^2 \right] = \sum_{i=1}^N \frac{\partial}{\partial r_0} \left[ (r_0 - r'_i)^2 \right] \\ &= \sum_{i=1}^N 2(r_0 - r'_i) \cdot \frac{\partial}{\partial r_0} (r_0 - r'_i) = \sum_{i=1}^N 2(r_0 - r'_i) = 0 \end{aligned}$$

Therefore,

$$r_0 = \frac{\sum_{i=1}^N r'_i}{N} \quad C.5$$

Similarly,

$$\begin{aligned} \frac{\partial S}{\partial X_0} &= \sum_{i=1}^N \frac{\partial}{\partial X_0} \left[ (r_0 - r'_i)^2 \right] = - \sum_{i=1}^N 2(r_0 - r'_i) \cdot \frac{\partial}{\partial X_0} r'_i \\ &= -2 \sum_{i=1}^N (r_0 - r'_i) \cdot \frac{1}{2} (r'_i)^{-1} (-2R_i A_i + 2X_0) = 0 \end{aligned}$$

Thus,

$$\sum_{i=1}^N \frac{(r_0 - r'_i)}{r'_i} (X_0 - R_i A_i) = 0 \quad C.6$$

The two remaining partials were similar to the preceding operation and are summarized as

$$\sum_{i=1}^N \frac{(Y_0 - r'_i)}{r'_i} (Y_0 - R_i B_i) = 0 \quad C.7$$

$$\sum_{i=1}^N \frac{(r_0 - r'_i)}{r'_i} (Z_0 - R_i C_i) = 0 \quad C.8$$

Thus the Equations C.5 through C.8 represent four simultaneous nonlinear equations in  $r_0$ ,  $X_0$ ,  $Y_0$ , and  $Z_0$ . When solved they yield the radius and center coordinates of the theoretical "best-fit" spherical surface to the experimental data points.

Solution of these equations was accomplished using an iterative linear extrapolation technique. Essentially it consisted of making a small change in each variable, computing the change in the four summations, and projecting along the slope of each variation to the desired solution. For example the solution of Equation C.6 is diagrammed in Figure C.2. The summation in C.6 was computed for two

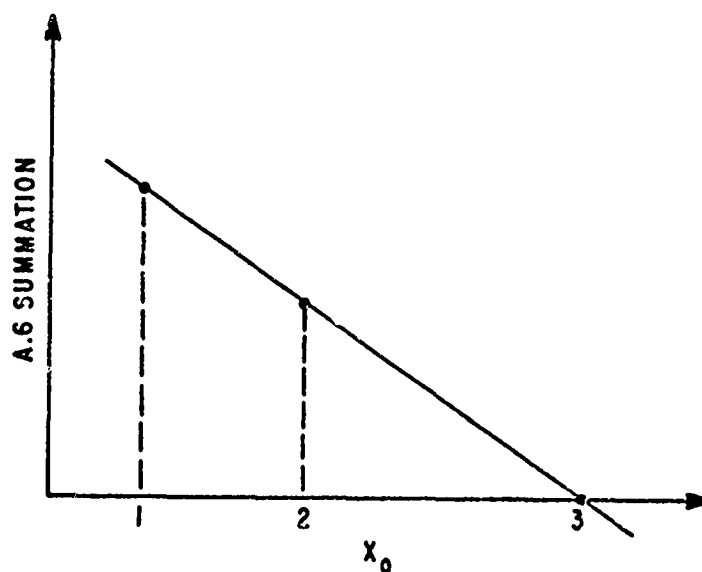


Figure C.2 Solution of Equation C.6

trial values of  $X_0$  as indicated by points 1 and 2. The slope of a line through the resulting ordinates projected through point 3, which was the desired solution for  $X_0$  if the summation varied linearly with  $X_0$ . Experience indicated that the variation of the equations was very nearly linear, which allowed setting confident convergence limits on the summations. A bound of  $\pm 0.000025$  inches was established for each of the four unknowns.

### C.3 MAINLINE PROGRAM

The mainline program is presented in the flow chart of Figure C.3. Only the main operations are included thereon with a complete print-out of the program given on pages 211 through 213.

The first step was to read loop indices and first estimates for the unknowns  $X_0$ ,  $Y_0$ ,  $Z_0$ , and for convergence limits on the summations of Equations C.5 through C.8. Angular locations  $\phi_1$  and  $\theta_1$  (the original design values were used) for each gage point were then read and the coordinate transformation constants  $A_1$ ,  $B_1$ , and  $C_1$  were computed. The gage points to be used in the spherical fit were also read.

At this point a loop began in which data for all pressure levels of interest was reduced. First a pass was made to subroutine REDUCE for calculation of the experimental radii  $R_1$ . A call was made to subroutine ITER to perform the fit of a spherical surface to the experimental data. Radial distances  $r_1'$  from the theoretical sphere center to each gage point were then calculated. Initial imperfections were determined by subtracting the radius  $r_0$  for the

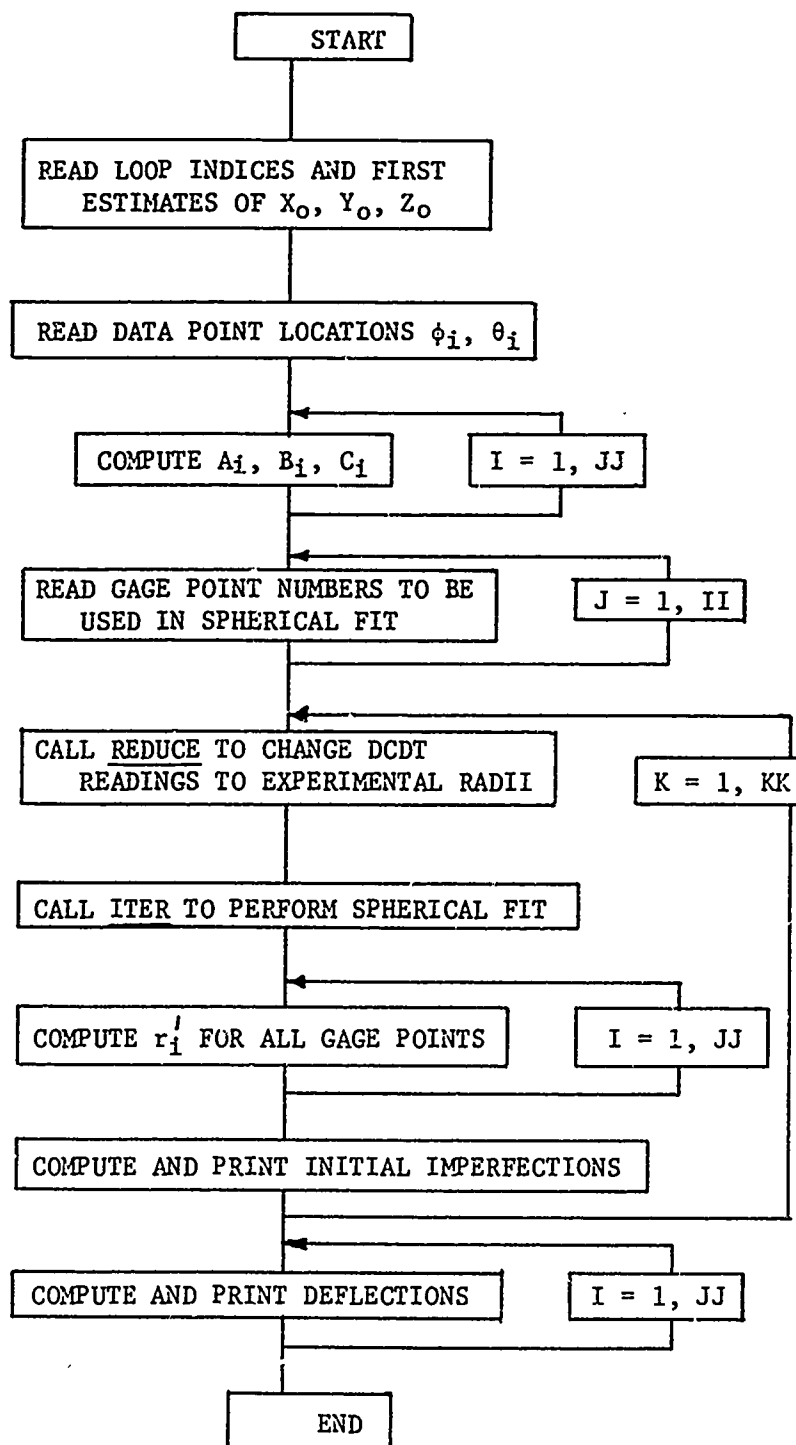


Figure C.3 Mainline Program Flow Chart

best-fit sphere from the  $r_i'$  values. The loop was completed with the storage of  $r_i'$  values in an array for later manipulation.

Deflections (due to load) at the  $i$ th gage point between any two pressure levels 1 and 2 were found using the following expression:

$$w_i = (r_i')_2 - (r_i')_1 + [(Z_o)_2 - (Z_o)_1] \cos \phi_i \quad C.9$$

#### C.4 SUBROUTINES

C.4.1 Subroutine REDUCE. The function of this subroutine was to change the voltmeter readings of the DCDT device of part 3.3.3, to values of experimental radii  $R_i$ . Its operation is diagrammed in the flow chart of Figure C.4. A print-out is given on page 214.

A description of several radial arm dimensions is made here with the aid of Figure C.5. This figure is a schematic of the radial arm assembly in which the distance  $S_1$  was the measured distance from the spherical pivot of the Easterby apparatus to the flat portion of the radial arm tip when the voltmeter reading was identically zero. The dimension  $S_2$  was the measured distance from the flat portion of the tip when this tip was properly seated, to the middle surface of the test shell model.

The subroutine commenced with the reading of the test model designation, the constants  $S_1$  and  $S_2$  and the pressure level. For each gage point the two largest voltmeter readings were selected and averaged, since the farthest travel represented proper seating of the spring-loaded DCDT tip. This average, rather than the largest measurement only, was taken to avoid a gross error in reading a single

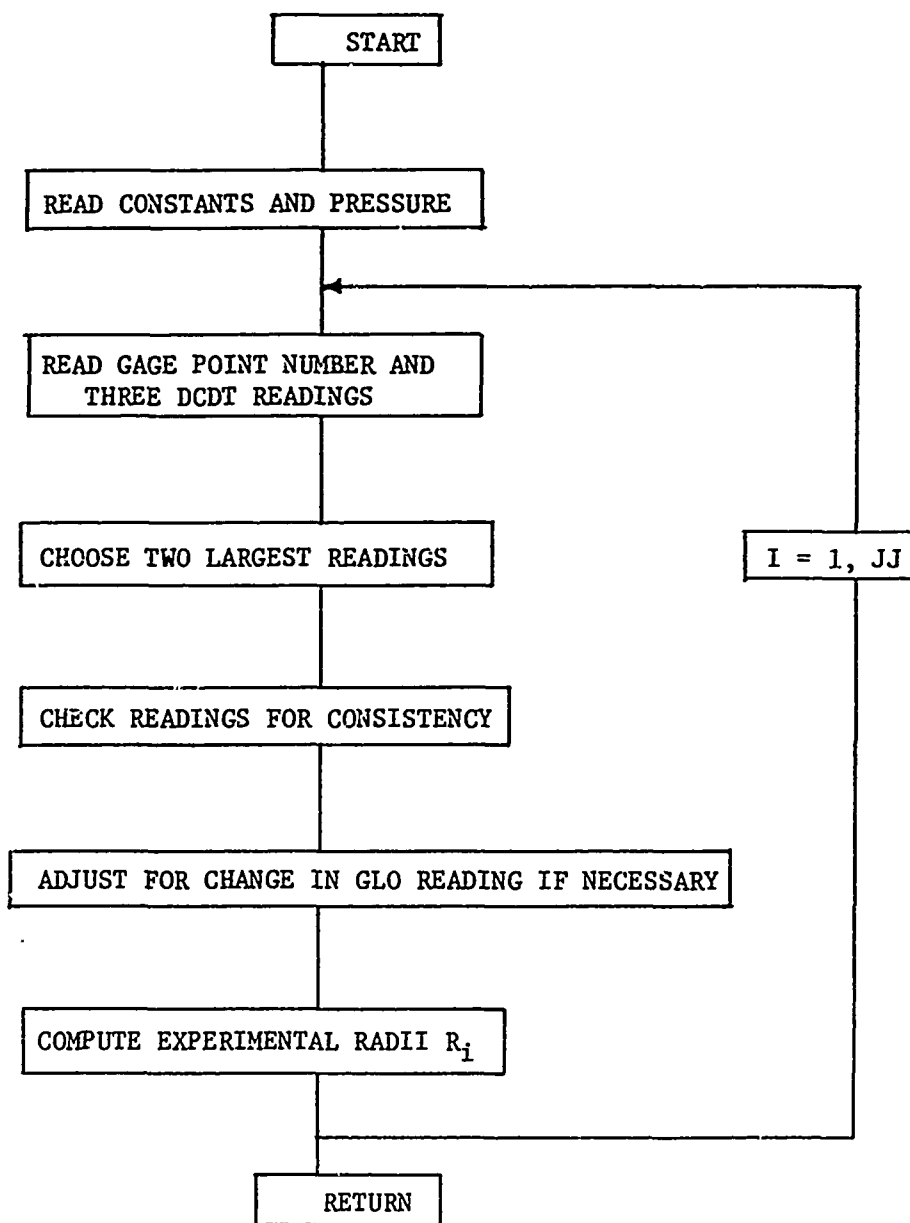


Figure C.4 Subroutine REDUCE Flow Chart

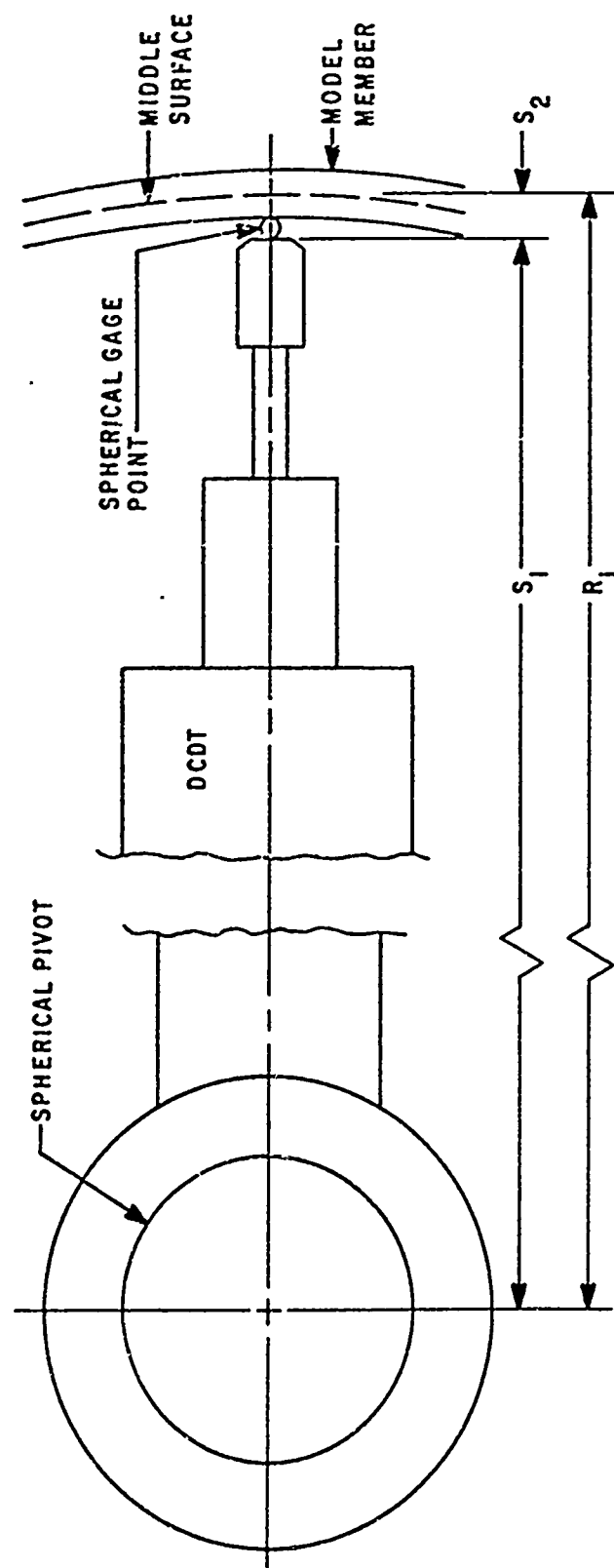


Figure C.5 Schematic of Radial Arm Assembly



large data value. Such an error would have been detected when checking the two readings against their average, and if a deviation larger than  $\pm .0001$  inches were noted a warning message was printed. The experimental radius was then computed by the following expression:

$$R_1 = S_1 + S_2 + V_R - \Delta R \quad C.10$$

In this equation,  $V_R$  is the average voltmeter reading converted to inches and  $\Delta R$  represents the drift in the recording apparatus as reflected by a change in the reading of the GLO gage point. The calibration factor for the DCDT device was 25 volts per inch.

C.4.2 Subroutine ITER. This subroutine performed a least-squares fit of a spherical surface to the experimental radii  $R_1$ . A flow chart of this routine is presented in Figure C.6 and a print-out can be found on pages 215 through 217. Note that the program version documented herein was executed on a machine having sixty-bit words. The user is cautioned that if low-bit machines are used, the following variables should be designated as double precision:  $r_1'$ ,  $r_0$ , and the summations of Equations C.5 through C.8.

Upon entry to subroutine ITER,  $r_1'$  and the summations of Equations C.6 through C.8 were computed based on initial estimates of  $X_0$ ,  $Y_0$ , and  $Z_0$ . The quantity  $r_0$  was computed directly from Equation C.5. Increments were then added to  $X_0$ ,  $Y_0$ , and  $Z_0$  prior to entering the main iteration loop of the routine. This loop established a second solution set to Equations C.5 through C.8. As illustrated in Figure C.2 for the solution for Equation C.6, the iterative solution technique extrapolated linearly a solution for  $X_0$ ,  $Y_0$ , and  $Z_0$  at the point where

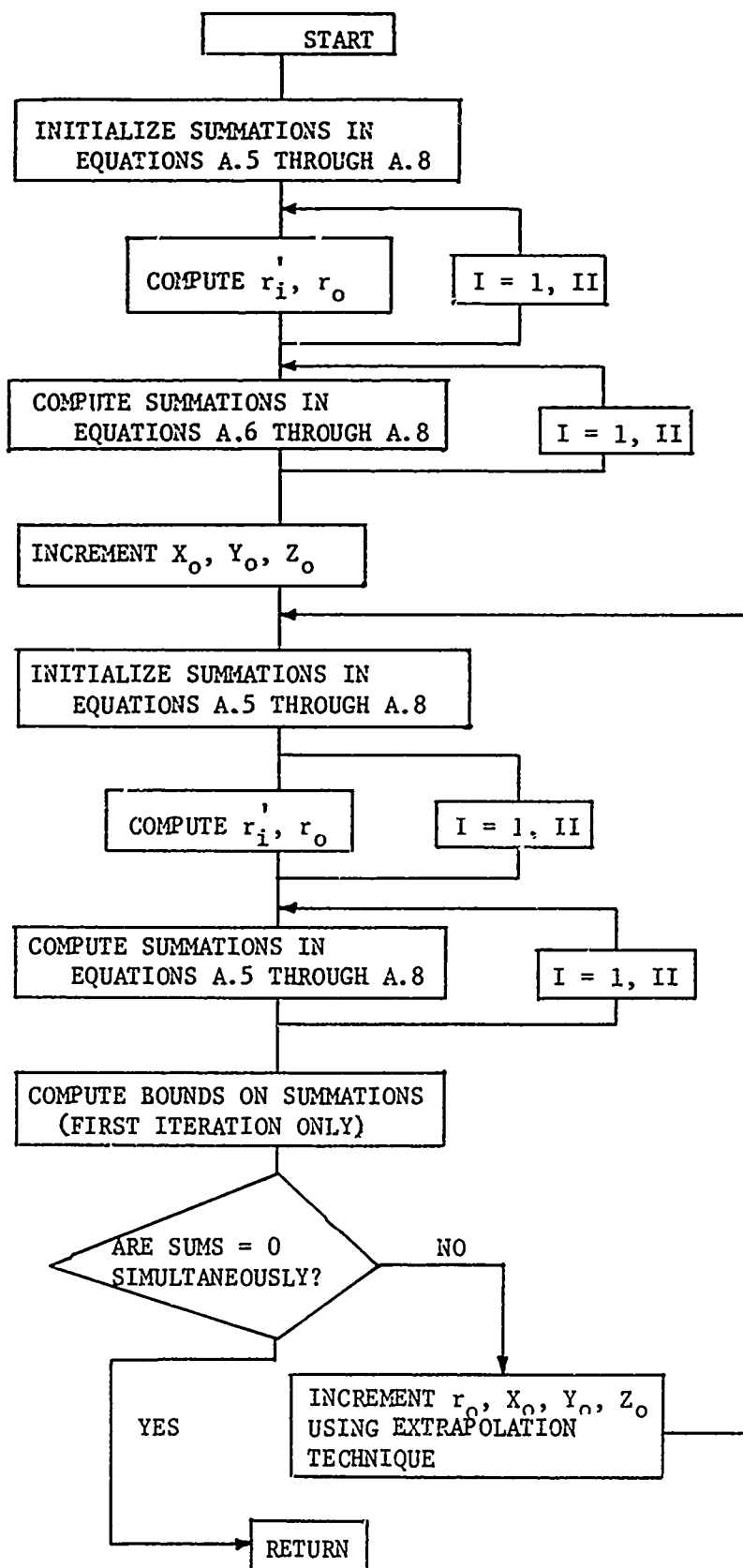


Figure C.6 Subroutine ITER Flow Chart

the respective summations were zero. During this first projection, the convergence limits for the summations were computed based on a bound of  $\pm .000025$  inches for each of the four unknowns. If the convergence criteria were not met,  $X_0$ ,  $Y_0$ , and  $Z_0$  were incremented based on the linear extrapolation and the loop was repeated until convergence occurred. Normally convergence was attained within five to seven iterations.

### C.5 PROGRAM INPUT AND OUTPUT

C.5.1 Input Data. The input data required by the program is shown on page 218. Six card types are used and are described below. The basic units used are pounds and inches.

Card type 1 contains four variables. One card is required. The variables are: KK, II, JJ and JP.

FORMAT: (20(1X,I3))

KK -- The number of data sets (one per pressure level) to be fitted.

II -- The total number of gage points on the test model.

JJ -- The number of gage points to be used in the least-squares fit.

JP -- The number of pressure pairs to be compared through deflection calculations.

Card type 2 contains 10 variables spread over two cards. They are  $X_0$ ,  $Y_0$ ,  $Z_0$ ,  $DX_0$ ,  $DY_0$ ,  $DZ_0$ ,  $ESX$ ,  $ESY$ ,  $ESZ$ , and  $ERROR$ .

FORMAT: (1X,7F10.6)

$X_0$ ,  $Y_0$ ,  $Z_0$  -- Initial guess at location of theoretical sphere center K with respect to the origin J in Figure C.1.

$DX_0$ ,  $DY_0$ ,  $DZ_0$  -- First trial increments in  $X_0$ ,  $Y_0$ , and  $Z_0$ , respectively.

ESX, ESY, ESZ -- Convergence limits on the summations of Equations

C.6 through C.8.

ERROR -- The desired accuracy on X0, Y0, and Z0.

Card type 3 contains 2\*JP variables, 20 variables per card.

They are IP1(K) and IP2(K).

FORMAT: (20(1X,I3))

IP1(K) -- Data set number (in order read in) of the lower of two pressure levels to be compared.

IP2(K) -- Data set number of the higher of two pressure levels to be compared.

Card type 4 contains 2\*JJ variables, six variables per card. They are PHD(I) and THD(I).

FORMAT: (3(4X,2F8.2,6X))

PHD(I) -- The meridional angle from the Z-axis in Figure C.1 locating each gage point (angle in degrees)

THD(I) -- The circumferential angle from the X-axis in Figure C.1 locating each gage point (angle in degrees).

Card type 5 contains II variables, twenty per card. They are IX(J).

FORMAT: (20(1X,I3))

IX(J) -- The gage points to be used in the least-squares fit.

Card type 6 contains four variables. One card is required. They are MODEL, S1, S2, and PR(N).

FORMAT: (1X,A4,7X,3(4X,F10.0))

MODEL -- An alphameric character designating the test model.

S1,S2 -- Radial arm dimensions defined in Figure C.5.

PR(N) — The pressure level to which the following data applies.

Card type 7 contains six variables, four of which are read.

A total of JJ cards are required plus one card per GLO measurement.

The four pertinent variables are K, (RD(J), J = 1,3).

FORMAT: (18X,I3,4X,F6.0,2(7X,F6.0))

K -- The gage point number.

RD(J) -- DCDT output voltage (in volts) as transcribed to cards  
through the key punch of part 3.5.

C.5.2 Typical Program Output. In addition to echo-printing the input data, the program output consisted of three general types of output. This output is shown in its printed form on pages 219 to 221.

Output type 1 was printed from subroutine ITER and monitored the least-squares iteration scheme. The quantities printed at every cycle in order from left to right were: RO,XO,YO,ZO, followed by the summations of Equations C.6 through C.8, respectively, and a cycle counter ICNT.

FORMAT: (7(2X,F13.6),I6)

Output type 2 presents the results of the data reduction for both original and final data. The quantities printed are in order: gage point number i, experimental radius  $R_i$ , theoretical radius  $r_i'$ , and the difference between the theoretical radius  $r_i'$  and the radius  $r_o$  of the theoretical best-fit sphere. The latter quantity, entitled DIFF on the printout, represented the initial imperfections in the shell.

FORMAT (3(1X,I3,2X,F8.4,2X,F8.4,2X,F7.4,7X)

Output type 3 gives values of the gage point deflections between pressure levels. The quantities printed are gage point number  $i$ , followed by its deflection  $DEF_i$ .

FORMAT: (8(4X,I4,F7.4)

## DEFINITION OF VARIABLES IN THE MAINLINE PROGRAM

A(I) =  $\sin(\text{PHI}) * \cos(\text{THE})$   
 B(I) =  $\sin(\text{PHI}) * \sin(\text{THE})$   
 C(I) =  $\cos(\text{PHI})$   
 D(I) = TEMPORARY STORAGE LOCATION FOR VARIABLE A(I)  
 DEF(I) = DEFLECTION AT GAGE POINT I BETWEEN TWO PRESSURE LEVELS  
 DIFF(I) = DIFFERENCE BETWEEN RADIUS RO OF BEST-FIT SPHERE AND  
 RADIUS RIP FROM ITS CENTER TO GAGE POINT I.  
 DXO = INCREMENT IN XO  
 DYO = INCREMENT IN YO  
 DZO = INCREMENT IN ZO  
 E(I) = TEMPORARY STORAGE LOCATION FOR VARIABLE B(I)  
 ERROR = ALLOWABLE VARIANCE IN XO, YO, AND ZO  
 ESX = ALLOWABLE VARIANCE IN EQUATION A.6 SUMMATION  
 ESY = ALLOWABLE VARIANCE IN EQUATION A.7 SUMMATION  
 ESZ = ALLOWABLE VARIATION IN EQUATION A.8 SUMMATION  
 F(I) = TEMPORARY STORAGE LOCATION FOR VARIABLE C(I)  
 I = LOOP INDEX  
 IP1(K) = LOWER OF TWO SETS OF PRESSURE LEVEL DATA BEING  
 COMPARED  
 IP2(K) = UPPER OF TWO SETS OF PRESSURE LEVEL DATA BEING  
 COMPARED  
 IX(J) = GAGE POINT NUMBERS TO BE USED IN LEAST-SQUARES FIT.  
 J = LOOP INDEX  
 JJ = TOTAL NUMBER OF GAGE POINTS ON A TEST MODEL  
 JP = NUMBER OF PRESSURE LEVEL COMPARISONS TO BE MADE  
 K = LOOP INDEX  
 KK = NUMBER OF PRESSURE LEVEL DATA SETS TO BE REDUCED  
 L = TEMPORARY STORAGE LOCATION FOR VARIABLE IP1(K)  
 M = TEMPORARY STORAGE LOCATION FOR VARIABLE IP2(K)  
 MODEL = ALPHAMERIC DESIGNATION OF TEST MODEL  
 N = LOOP INDEX  
 PHD(I) = MERIDIONAL LOCATION OF GAGE POINT I IN DEGREES  
 PHI(I) = PHD CONVERTED TO RADIAN  
 PI = 3.14159265  
 PR(N) = PRESSURE LEVEL BEING ANALYZED  
 R(I) = EXPERIMENTAL RADIUS TO GAGE POINT I MEASURED FROM  
 SPHERICAL PIVOT CENTER ON EASTERBY APPARATUS  
 RF(M,I) = TEMPORARY STORAGE LOCATION FOR RIP(I) VALUES.  
 RIP(I) = RADIUS TO GAGE POINT I FROM CENTER OF BEST FIT SPHERE  
 RO = RADIUS OF BEST-FIT SPHERE  
 S(I) = TEMPORARY STORAGE LOCATION FOR VARIABLE R(I)  
 THD(I) = CIRCUMFERENTIAL LOCATION OF GAGE POINT I IN DEGREES  
 THE(I) = THD(I) IN RADIAN  
 XO = X-DISTANCE BETWEEN CENTER OF SPHERICAL PIVOT ON  
 EASTERBY APPARATUS AND THE CENTER OF THE BEST-FIT  
 SPHERE

Y0 = Y-DISTANCE BETWEEN CENTER OF SPHERICAL PIVOT ON  
EASTERBY APPARATUS AND THE CENTER OF THE BEST-FIT  
SPHERE  
Z0 = Z-DISTANCE BETWEEN CENTER OF SPHERICAL PIVOT ON  
EASTERBY APPARATUS AND THE CENTER OF THE BEST-FIT  
SPHERE  
Z00(N) = TEMPORARY STORAGE LOCATIONS FOR THE VARIABLES Z0

```

PROGRAM SHELL (INPUT,OUTPUT,TAPE5=INPUT,TAPE6=OUTPUT)
COMMON /IT/ A(300),B(300),C(300),R(300),RIP(300),II
DIMENSION RF(13,300),DEF(300),PR(13),Z00(13),PHI(300),THE(300),
* IP1(100),IP2(100)
DIMENSION PHD(300),THD(300),DIFF(300),IX(300),D(300),
* E(300),F(300),S(300)
1 FORMAT (20(1X,I3))
2 FORMAT (8(4X,I4,F7.4),/)
3 FORMAT (4(1X,I3,1X,F8.3,1X,F9.3,7X)/)
4 FORMAT (*1*)
5 FORMAT(1X,* THIS IS THE *,A4 ,* MODEL. THE PRESSURE IS *,F6.2,
1* PSI*,//)
6 FORMAT (4(1X,* PT PHI THETA *,7X)/)
7 FORMAT (1X,/)
8 FORMAT (4X,10(1X,F6.2,* PSI*))
9 FORMAT(3(1X,I3,2X,F8.4,2X,F6.4,2X,F7.4,7X),/)
13 FORMAT ( 3(* PT R DATA R FINAL DIFF*,8X),//)
15 FORMAT (1X,7F10.6)
23 FORMAT (3(4X, 2F8.2,6X))
PI = 3.14159265
WRITE (6,4)
READ (5,1) KK,II,JJ,JP
WRITE (5,1) KK,II,JJ,JP
READ (5,15) XO,YO,ZO,DXO,DYO,DZO,ESX,ESY,ESZ,ERROR
WRITE (6,15) XO,YO,ZO,DXO,DYO,DZO,ESX,ESY,ESZ,ERROR
READ (5,1) (IP1(K),IP2(K),K=1,JP)
WRITE (5,1) (IP1(K),IP2(K),K=1,JP)
READ (5,29) (PHD(I),THD(I),I=1,JJ)
WRITE (6,4)
WRITE (6,6)
WRITE (5,3) (I,PHD(I),THD(I),I=1,JJ)
DO 103 I=1,JJ
PHI(I) = PHD(I)*PI/180.
THE(I) = THD(I) * PI/180.
J(I) = SIN(PHI(I)) * COS(THE(I))
E(I) = SIN(PHI(I)) * SIN(THE(I))

```



```

103 F(I) = COS(PHI(I))
    WRITE (6,4)
    READ (5,1) (IX(J),J=1,II)
    DO 21 J=1,II
        I = IX(J)
        WRITE (6,1) J,I
        A(J)=D(I)
        B(J)=E(I)
21 C(J)=F(I)
    DO 33 N = 1, KK
        CALL REDUCE (PR,MODEL, JJ,N)
        DO 19 I=1, JJ
19 S(I)=R(I)
        DO 20 J = 1, II
            I=IX(J)
20 R(J)=S(I)
        WRITE (6,4)
        WRITE (6,5) MODEL,PR(N)
        CALL ITER (R0,X0,Y0,Z0,DX0,DY0,DZ0,ESX,ESY,ESZ,ERROR)
        ZOD(N)=Z0
        DO 23 I=1, JJ
23 RIP(I)=SQRT(S(I)**2-2.*S(I)*(X0*D(I)+ Y0*E(I) + Z0*F(I)) + X0**2 +
        ZY0**2 + Z0**2)
        WRITE (6,4)
        WRITE (6,5) MODEL,PR(N)
        DO 30 I=1, JJ
30 DIFF(I) = RIP(I) - R0
        WRITE (6,10)
        DO 32 I=1, JJ
32 RF(N,I) = RIP(I)
33 WRITE (6,9) (I,S(I),RF(N,I),DIFF(I),I=1, JJ)
        DO 35 K=1, JP
            L=IP1(K)
            M=IP2(K)
            DO 34 I=1, JJ
34 DEF(I) = RF(M,I) - RF(L,I) + (ZOD(M)-ZOD(L))*COS(PHI(I))
            WRITE (6,4)
            WRITE (6,8) PR(L),PR(M)
            WRITE (6,7)
35 WRITE (6,2) (I,DEF(I),I=1, JJ)
    END

```

## DEFINITION OF ADDITIONAL VARIABLES IN SUBROUTINE REDUCE

BAD = DIFFERENCE BETWEEN TWO LARGEST DCDT READINGS  
 DELR = DRIFT IN GLO READINGS  
 KI = FLAG FOR FIRST GLO READING  
 OLDR = OLD GLO RADIUS  
 RD = DCDT READING  
 SUM = SUM OF TWO LARGEST DCDT READINGS  
 S1 = DISTANCE DEFINED IN FIGURE A.5  
 S2 = DISTANCE DEFINED IN FIGURE A.5  
 XEWR = NEW GLO RADIUS

```

SUBROUTINE REDUCE (PR,MODEL,JJ,N)
COMMON /IT/ A(300),B(300),C(300),R(300),RIP(300),II
DIMENSION RD(3),PR(10)
2 FORMAT (1X,A4,7X,3(4X,F10.0))
3 FORMAT (18X,I3,4X,F6.0,7X,F6.0,7X,F6.0)
4 FORMAT (*1*)
5 FORMAT(1X,* THIS IS THE *,A4 , *MODEL.    THE PRESSURE IS *,F6.2,
1* PSI*,//)
7 FORMAT (1X,I3,2X,F10.2,1X, *TEN-THOUSANDTHS OF AN INCH-----BAD RE
ADING*,/)
  READ ( 5,2) MODEL, S1,S2,PR(N)
  WRITE (6,4)
  WRITE (6,5) MODEL,PR(N)
  KI = 0      DELR = 0.
  DO 95 I=1,JJ
1: READ ( 5,3) K, (RD(J),J=1,3)
  WRITE(6,3) K, (RD(J),J=1,3)
  SUM = RD(1)+RD(2)+RD(3)-AMIN1(RD(1),RD(2),RD(3))
  R(K) = SUM/50000. - DELR + S1 + S2
  BAD = 2.*ABS(AMAX1(RD(1),RD(2),RD(3)) - SUM/2.) / 2.5
  IF (BAD.GT.2.) WRITE (6,7) K,BAD
9: IF (K-260) 95,91,95
91 IF (KI) 92,92,93
92 OLDR = R(K)
  KI = 1
  GO TO 10
93 XEWR = R(K)
  DELR = XEWR - OLDR + DELR
  OLDR = XEWR
  GO TO 10
95 CONTINUE
  RETURN
  END
  
```

## DEFINITION OF ADDITIONAL VARIABLES IN SUBROUTINE ITER

FACT = SIMPLIFICATION FACTOR IN EQUATIONS A.6 THROUGH A.8  
 AND EQUAL TO  $(R0-RIP(I))/RIP(I)$   
 FSUMX = STORAGE LOCATION FOR SUM OF EQUATION A.6  
 FSUMY = STORAGE LOCATION FOR SUM OF EQUATION A.7  
 FSUMZ = STORAGE LOCATION FOR SUM OF EQUATION A.8  
 ICNT = COUNTER ON NUMBER OF ITERATIONS FOR CONVERGENCE OF  
 SOLUTION  
 KX = CONVERGENCE INDICATOR = 1 UPON CONVERGENCE OF ALL EQUATIONS  
 LX = INDICATOR TO BYPASS ERROR SQUARED CALCULATIONS EXCEPT  
 ON FIRST PASS  
 RA = TRIAL VALUE FOR R0  
 SLX = SLOPE OF SUMX VERSUS X0 CURVE  
 SLY = SLOPE OF SUMY VERSUS Y0 CURVE  
 SLZ = SLOPE OF SUMZ VERSUS Z0 CURVE  
 SUMX = NEW SUMMATION OF EQUATION A.6  
 SUMX1 = PREVIOUS SUMMATION OF EQUATION A.6  
 SUMY = NEW SUMMATION OF EQUATION A.7  
 SUMY1 = PREVIOUS SUMMATION OF EQUATION A.7  
 SUMZ = NEW SUMMATION OF EQUATION A.8  
 SUMZ1 = PREVIOUS SUMMATION OF EQUATION A.8  
 X01 = PREVIOUS VALUE OF X0  
 XX = FIXED POINT NOTATION FOR THE VARIABLE II  
 Y01 = PREVIOUS VALUE OF Y0  
 Z01 = PREVIOUS VALUE OF Z0

```

SUBROUTINE ITER (R0,X0,Y0,Z0,Dx0,Dy0,Dz0,LSX,LSY,LSZ,ERROR)
COMMON /IT/ A(300),B(300),C(300),R(300),RIP(300),II
2 FORMAT (7(2X,F13.6),I6)
3 FORMAT (*1*,1X,*Z0-COUNT = *,I3)
6 FORMAT (1X,*R0 = *,F8.4,7X,*X0 = *,F7.4,6X,*Y0 = *,F7.4,6X,*Z0 = *,
1,F7.4,6X,*COUNT = *,I3,/)
LX = 1 $ KX = 1 $ XX = II
ICNT = 0 $ R0 = 0. $ SUMZ1 = 0. $ SUMX1 = 0. $ SUMY1 = 0.
Z01 = Z0 $ X01 = X0 $ Y01 = Y0
DO 5 I=1,II
RIP(I)=SQRT(R(I)**2-2.*R(I)*(X0*A(I)+ Y0*B(I) + Z0*C(I)) + X0**2 +
1Y0**2 + Z0**2)
5 R0 = R0 + RIP(I)/XX
DO 10 I = 1,II
FACT = (R0-RIP(I))/RIP(I)
SUMX1 = SUMX1 + FACT * (X0-R(I)*A(I))
  
```

```

    SUMY1 = SUMY1 + FACT * (YO-R(I)*B(I))
10 SUMZ1 = SUMZ1 + FACT * (ZO-R(I)*C(I))
    ICNT = ICNT + 1
    FSUMZ = SUMZ1
    FSUMX = SUMX1
    FSUMY = SUMY1
    RA = RO
    WRITE (6,2) RA,XO,YO,ZO,FSUMX,FSUMY,FSUMZ,ICNT
    IF (SUMZ1)1+,14,15
14 ZO = ZO - OZO
    GO TO 45
15 ZO = ZO + OZO
45 IF (SUMX1)4+,44,45
44 XO = XO - DXO
    GO TO 76
45 XO = XO + DXO
76 IF (SUMY1)74,74,75
74 YO = YO - DYO
    GO TO 16
75 YO = YO + DYO
16 RO = 0.
    SUMZ = 0.    $    SUMX = 0.    $    SUMY = 0.
    KX = 1
    DO 18 I=1,II
    RIP(I)=SQRT(R(I)**2-2.*R(I)*(XO*A(I)+ YO*B(I) + ZO*C(I)) + XO**2 +
1YO**2 + ZO**2)
18 RO = RO + RIP(I)/XX
    IF (ICNT - 100) 21,25,17
17 WRITE (6,3) ICNT
    STOP
20 DO 22 I = 1,II
    FACT = (RO-RIP(I))/RIP(I)
    SUMX = SUMX + FACT * (XO-R(I)*A(I))
    SUMY = SUMY + FACT * (YO-R(I)*B(I))
22 SUMZ = SUMZ + FACT * (ZO-R(I)*C(I))
    FSUMZ = SUMZ
    FSUMX = SUMX
    FSUMY = SUMY
    RA = RO
    ICNT = ICNT + 1
    WRITE (6,2) RA,XO,YO,ZO,FSUMX,FSUMY,FSUMZ,ICNT
    IF (ZO-ZO1) 24,23,24
24 SLZ = (SUMZ - SUMZ1) / (ZO - ZO1)
23 IF (XO-XO1) 5+,53,54
54 SLX = (SUMX - SUMX1) / (XO - XO1)

```

```

53 IF (Y0-Y01) 84,83,84
84 SLY = (SUMY - SUMY1) / (Y0 - Y01)
83 GO TO (25,27), LX
25 ESZ = ABS(SLZ)*ERROR
    ESX = ABS(SLX)*ERROR
    ESY = ABS(SLY)*ERROR
    LX = 2
27 IF (ABS(FSUMZ)-ESZ) 57,57,28
28 CX = 2
    ZO1 = ZO
    SUMZ1 = SUMZ
    ZO = ZO - SUMZ/SLZ
57 IF (ABS(FSUMX)-ESX) 67,87,58
58 CX = 2
    XO1 = XO
    SUMX1 = SUMX
    XO = XO - SUMX/SLX
87 IF (ABS(FSUMY)-ESY) 26,26,88
88 CX = 2
    YO1 = YO
    SUMY1 = SUMY
    YO = YO - SUMY/SLY
25 GO TO (29,15), KX
29 WRITE (6,6) RA,XO,YO,ZO,ICNT
    RETURN
    END

```

# INPUT DATA

CARD TYPE 1		1																			
2	202	233																			
CARD TYPE 2		2																			
3.	0.																				
.00029	.0002																				
CARD TYPE 3		3																			
1	2																				
CARD TYPE 4		4																			
1	8.43	0.00																			
4	8.43	180.00																			
ETC.																					
CARD TYPE 5		5																			
233	1	2	3	4	5	6	7	8	9	10	11	12	13	14	15	16	17	18	19		
20	21	22	23	24	25	26	27	28	29	30	31	32	33	34	35	36	37	38	39		
ETC.																					
CARD TYPE 6		6																			
PRET	U																				
CARD TYPE 7		7																			
PRET	.15	001																			
PRET	.15	260																			
PRET	.15	233																			
ETC.																					

## Output Type 1

THIS IS THE FRET MODEL. THE PRESSURE IS .15 PSI

15.588340	0.000000	0.000000	0.000000	-.716792
15.511873	-.100000	.100000	.190000	3.155504
15.536555	-.018511	.055548	.002342	-.230843
15.586361	-.024065	.047973	.002681	.055276
15.504555	-.022827	.051121	.005039	-.037254
15.586127	-.022949	.051240	.002999	-.032588
15.586193	-.023017	.051261	.002915	.000173
RO = 15.5862	XO = -.0230	YO = .0513	ZO = .0025	

1.692049	.005156	1
-1.300253	-.215007	2
-.214293	.000750	3
.124297	.000000	4
.004556	-.004205	5
.001158	-.007167	6
.000110	-.000004	7
COUNT = 7		

Reproduced from  
Best available copy.

Output Type 2

THIS IS THE PRET NODE! . THE PRESSURE IS .15 PSI

PT	R DATA	R FINAL	DIFF	PT	R DATA	R FINAL	DIFF
1	15.4974	15.4980	-.0002	2	15.4966	15.4890	-.0072
4	15.4551	15.4490	-.0061	5	15.5068	15.5068	-.0000
7	15.6267	15.6247	.0020	8	15.6434	15.6391	.0043
10	15.6285	15.6109	.0176	11	15.5740	15.5551	-.0189
13	15.5958	15.5865	.0093	14	15.6510	15.6499	.0011
16	15.6359	15.6481	-.0122	17	15.6089	15.6224	-.0135
19	15.6340	15.6413	-.0073	20	15.6411	15.6404	.0007
22	15.6834	15.6668	.0166	23	15.6672	15.6447	.0225
25	15.6265	15.6001	.0264	26	15.6188	15.5947	.0241
28	15.6363	15.6239	.0124	29	15.6545	15.6502	.0043
31	15.6712	15.6828	-.0116	32	15.6559	15.6742	-.0183
34	15.6061	15.6274	-.0213	35	15.6210	15.6400	-.0190
37	15.5784	15.5889	-.0105	38	15.5724	15.5762	-.0038



Output Type 3

Reproduced from  
best available copy.

.15 PSI 1.00 PSI

1 -.0180	2 -.0184	3 -.0225	4 -.0233	5 -.0164	6 -.0163
9 -.0121	10 -.0394	11 -.0143	12 -.0159	13 -.0193	14 -.0195
17 -.0095	18 -.0124	19 -.0153	20 -.0148	21 -.0160	22 -.0105
25 -.0102	26 -.0137	27 -.0121	28 -.0140	29 -.0145	30 -.0151
33 -.0106	34 -.0120	35 -.0145	36 -.0139	37 -.0142	38 -.0180
41 -.0170	42 -.0149	43 -.0137	44 -.0132	45 -.0126	46 -.0133
49 -.0136	50 -.0138	51 -.0109	52 -.0134	53 -.0170	54 -.0173
57 -.0122	58 -.0131	59 -.0166	60 -.0176	61 -.0167	62 -.0140
65 -.0162	66 -.0169	67 -.0200	68 -.0190	69 -.0186	70 -.0168
73 -.0139	74 -.0154	75 -.0176	76 -.0167	77 -.0164	78 -.0171
81 -.0185	82 -.0132	83 -.0167	84 -.0151	85 -.0132	86 -.0139
89 -.0179	90 -.0130	91 -.0158	92 -.0175	93 -.0169	94 -.0174
97 -.0177	98 -.0161	99 -.0143	100 -.0133	101 -.0132	102 -.0025
105 -.0170	106 -.0184	107 -.0163	108 -.0153	109 -.0177	110 -.0180
113 -.0123	114 -.0132	115 -.0166	116 -.0177	117 -.0167	118 -.0175

REFERENCES

1. Cheng, D. H., "Space Frame Analysis by Flexibility Matrix," International Journal of Mech Sci, Vol 6, Oct 1964, pp 349-360
2. Eisemann, K., Woo, Lin and Manye, S., "Space Frame Analysis by Matrices and Computers," Journal of Structural Division, ASCE, Vol 38, No. ST6, Dec 1962, pp 249-277
3. Jennings, A., and Majid, K. I., "The Computer Analysis of Space Frames Using Sparce Matrix Techniques," Space Structures, Editor R. M. Davies, London, 1966
4. Livesley, R. K., "Matrix Methods of Structural Analysis," Pergamon Press, 1964
5. Tezcan, S. S. and Ovunc, B., "Computer Analysis of Plane and Space Structures," Structural Division Journal, ASCE, Vol 92, April 1966, pp 143-176
6. Weaver, W., "Computer Programs for Structural Analysis," D. Van Nostrand, Inc., Princeton, 1967
7. NASTRAN Computer Program, "The NASTRAN User's Manual," Level 15, NASA SP-221, April 1972
8. IBM Application Program, "IBM 7090/7094 FRAN," Manuals No. 1-4, 7090-EC-01X
9. Haas, A. M., "Design of thin Concrete Shells," Vol I, Positive Curvature Index, John Wiley and Sons, 1962
10. Flugge, W., "Stresses in Shells," Springer-Verlag, Berlin, Germany, 1968
11. Timoshenko, S. and Woinowsky-Krieger, S., "Theory of Plates and Shells," McGraw-Hill, New York, 1959
12. Ramaswamy, G. S., "Design and Construction of Concrete Shell Roofs," McGraw-Hill, New York, 1968
13. Wright, D. T., "Membrane Forces and Buckling in Reticulated Shells," Journal of the ASCE Structural Division, Vol 91, No. ST1, Feb 1965
14. Wright, D. T., "A Continuum Analysis for Double Layer Space Frame Shells," 26th Volume of "Publications" of the Intl Association for Bridge and Structural Engineers
15. Benard, E. F., "A Study of the Relationship Between Continuous and Lattice Structures," PhD Thesis, University of Illinois, 1965

16. Mitchell, L. H., "A Shell Analogy for Framed Domes," Aeronautical Research Labs
17. Lane, James H., "Bar Forces in Latticed Spherical Domes by Means of the Membrane Analogy for Shells," PhD Thesis, North Carolina State University, 1965
18. Lee, W. C., "Validity of Membrane Theory as Applied to Hyperbolic Paraboloid Space Frames," PhD Thesis, Rensselaer Poly Inst, 1964
19. Parikh, K. S. and Norris, C. H., "Analysis of Shells Using Framework Analogy," Proceedings, World Conference on Steel Structures, National Academy of Sciences, Washington, 1964, pp 213-222
20. Buchert, K. P., "Effect of Edge Conditions on Buckling of Stiffened Framed Shells," Engineering Experiment Station Bulletin Series No. 65, University of Missouri, Columbia, Oct 1967
21. Buchert, K. P., "Buckling Considerations in the Design and Construction of Doubly Curved Space Structures," Space Structures, Editor R. M. Davies, London, 1966
22. Lind, N. C., "Stability Analysis of Symmetrical Dome Frameworks," Presented at first joint meeting Structural Engineering, Colegio De Ingenieros Civiles De Mexico/ASCE, Mexico City, Feb 1966
23. Buchert, K., "Space Frame Buckling," Engineering Journal, American Institute of Steel Construction, Vol 5, No. 4, October 1968
24. McCutcheon, J. O. and Dickie, J. F., "The Buckling Stability of Reticulated Domes," Space Structures, Editor R. M. Davies, London, 1966
25. Tezcan, S. S. and Ovunc, B., "An Iteration Method for the Non-Linear Buckling of Framed Structures," Space Structures, Editor R. M. Davies, London, 1966
26. Kolosowski, J., "Model Tests on a Space Grid and Folded Plate Roof," Space Structures, Editor R. M. Davies, London, 1966
27. Makowski, Z. S. and Pippard, A. J. S., "Experimental Analysis of Space Structures with Particular Reference to Braced Domes," Proc I.C.E., Part III, Dec 1952, pp 420-441
28. McCormick, C. W., "The Comparison of a Digital Computer Analysis with Full Scale Tests of a Space Structure," Space Structures, Editor R. M. Davies, London, 1966
29. Bayley, M. J., "An Experimental and Theoretical Investigation into the Behavior of a Three-Way Aluminum Grid Dome," International Conference on Space Structures, University of Surrey, 1966

30. Little, W. A., "Reliability of Shell Buckling Predictions," Research Monograph No. 25, The MIT Press, Cambridge, Massachusetts
31. Geckeler, J. W., "Forschungsarb," No. 276, Berlin, 1926
32. Roark, Raymond J., "Formulas for Stress and Strain," McGraw-Hill, 1965
33. Von Karman, T., and Tsien, H. S., "The Buckling of Spherical Shells by External Pressure," Journal of the Aerospace Sciences, Vol 7, No. 2, 1939
34. Buchert, K., "Buckling of Doubly Curved Orthotropic Shells," Engineering Experiment Station, University of Missouri, Columbia, Missouri, November, 1965
35. Buchert, K., "Zur Stabilitat grosser, doppelt, gekrummter and versteifer Schalen," Der Stahlbau, Feb 1965, pp 55-62
36. Crooker, J. and Buchert, K., "Reticulated Space Structures," ASCE Annual Meeting and National Meeting on Structural Engineering, Pittsburgh, Pennsylvania, Meeting Preprint 731
37. Buchert, K., "Buckling of Shell and Shell-Like Structures," K. P. Buchert & Associates, Columbia, Missouri, 1973